Modeling of leaching and swelling by water uptake of bituminized waste products under different loading conditions

Yujiong Chen

Université Gustave Eiffel

Ecole doctorale Sciences, Ingénierie et Environnement

Laboratoire Navier - Ecole des Ponts ParisTech

Electricité de France

THÈSE

Présentée en vue de l'obtention du grade de

Docteur en Mécanique de l'Université Gustave Eiffel

par

Yujiong CHEN

MODELING OF LEACHING AND SWELLING BY WATER UPTAKE OF BITUMINIZED WASTE PRODUCTS UNDER DIFFERENT LOADING CONDITIONS

Thèse soutenue le 28 septembre 2023 devant le jury composé de :

M. Rudy VALETTE	Rapporteur
M. Sebastia OLIVELLA	Rapporteur
M. Patrick DANGLA	Directeur de thèse
M. Albert GIRAUD	Président du jury
Mme. Nele BLEYEN	Examinatrice
Mme. Sylvie GRANET	Examinatrice
M. Gilles ARMAND	Invité
M. Jean-Baptiste CHAMPENOIS	Invité
M. Geoffroy MELOT	Invité

ABSTRACT

Bituminized Waste Products (BWPs) were produced by conditioning, in bitumen, the co-precipitation sludge resulting from the industrial processing of spent nuclear fuel. Underground geological disposal is one of the considered solutions for the long-term disposal of some intermediate level long-lived (ILW-LL) categorized BWPs in France.

One of the challenges related to BWPs is their swelling behavior due to water uptake in geological disposal conditions. After one or several hundred thousand years, the water from the host rock will indeed fully saturate the disposal cells. By an osmotic phenomenon enabled by the semi-permeable capacity of the bituminous matrix, water in direct contact with BWPs could cause them to swell. This swelling, if sufficiently important, could lead to mechanical coupling with the host rock, resulting in the application of pressure that could damage it. Indeed, on a scale of hundreds of thousands of years, it is assumed that the walls of the storage facility will have disappeared. The penalizing safety scenario is therefore to consider the BWPs in direct contact with the host rock. Consequently, the swelling behavior of BWPs must be taken into account in safety studies for the underground storage facility after site closure.

The objective of this PhD work is to predict the leaching behavior due to water uptake of French BWPs under both free leaching and confined leaching conditions and to better understand the corresponding mechanisms behind. The final goal is to better estimate the maximum stress that French BWPs could generate and apply to the host rock in terms of deformations allowed under geological disposal conditions. The numerical model presented in this work is extended from the MELOT2019 model [1,2]. An innovative formulation of water and salt mass flow with coupled homogenization of transport terms (diffusion, permeation, and osmosis) is proposed to better capture the role of the semi-permeable membrane played by the bitumen and the porosity-dependency of the coupled transport coefficients during the leaching process. A non-linear poro-viscoelastic model taking into account large strains is also proposed to better model the BWPs' leaching behavior under confined conditions. The classic Maxwell viscoelastic model is therefore adapted to poromechanics, and a "viscous Biot-like" coefficient is introduced. The Mori-Tanaka homogenization scheme is applied to model the porosity-dependency of the viscoelastic parameters of the homogenized material.

To support the modeling, a rich experimental program has been conducted at CEA Marcoule to characterize the leaching behaviors of French BWPs, under the BABYLONE joint research program [3]. The experimental results are discussed in this PhD work and used to calibrate the model parameters. The leaching behavior under free leaching, constant counter-pressure, and constant volume conditions are numerically investigated for simplified French BWPs. The fitted parameters are then discussed and compared with the experimental measurements reported in the literature. The role of the poorly soluble salts present in French BWPs is also discussed. Sensitivity studies for composition, material parameters, and sample size are performed to better understand the key parameters of the leaching behavior under free leaching and confined leaching conditions. Finally, the effect of the existing voids on the stress build-up behavior of BWPs under confined leaching conditions is numerically investigated by modeling the case of free leaching followed by leaching under constant volume conditions. This study allows us to obtain a relation between the stress generated under confined leaching conditions and the deformations allowed for BWPs.

Keywords: radioactive wastes, Bituminized Waste Products, chemical-hydro-mechanical modeling, multiphysics modeling, homogenization, leaching

Résumé

Les colis de déchets radioactifs bitumineux ont été produits en conditionnant dans du bitume les boues de co-précipittion résultant du traitement industriel du combustible nucléaire usé. Le stockage géologique souterrain est l'une des potentielles solutions pour le stockage à long terme de certains colis de déchets bitumineux catégorisés moyenne activité à vie longue (MA-VL) en France. Une des problématiques à investiguer pour ces colis de déchets bitumineux est leur comportement de gonflement lié à la reprise en eau dans des conditions de stockage géologique. En effet, après une ou plusieurs centaines de milliers d'années, il est supposé que les parois de l'installation de stockage auront été totalement dégradés et l'eau de la roche hôte du stockage géologique profond saturera complètement les alvéoles de stockage. La présence d'eau, par un phénomène osmotique rendu possible par la capacité semi-perméable de la matrice bitumineuse, va conduire au gonflement des enrobés bitumineux. Ce gonflement, s'il est suffisamment important, pourrait conduire à un couplage mécanique avec la roche hôte qui se traduirait par l'application d'une pression qui pourrait l'endommager. Le scénario de sûreté pénalisant consiste à considérer l'enrobé bitumineux en contact direct avec la roche hôte. Par conséquent, les effets de gonflement des enrobés bitumineux doivent être pris en compte dans les études de sûreté de l'installation de stockage souterrain après fermeture du site.

L'objectif de ce travail de thèse est de prédire le comportement à la lixiviation, dû à la reprise en eau des enrobés bitumineux en milieu libre et en milieu confiné, et de mieux comprendre les mécanismes correspondants, ceci afin de mieux estimer les contraintes maximales que les enrobés bitumineux français pourraient générer sur la roche, en fonction des déformations autorisées dans des conditions de stockage géologique. Le modèle numérique présenté dans ce travail est une extension du modèle MELOT2019 [1,2]. Une formulation novatrice des flux massiques de sel et d'eau avec une homogénéisation couplée des termes de transport (diffusion, perméation et osmose) est proposée pour mieux modéliser le rôle de la membrane semi-perméable jouée par le bitume et la dépendance à la porosité des coefficients de transport couplés pendant le processus de lixiviation. Un modèle poro-viscoélastique non linéaire prenant en compte les grandes déformations est également proposé pour mieux modéliser le comportement à la lixiviation des enrobés bitumineux en milieu confiné. Le modèle viscoélastique classique de Maxwell est ainsi adapté au cas de la poro-mécanique et un coefficient "visqueux de type Biot" est introduit. Le schéma d'homogénéisation Mori-Tanaka est appliqué pour modéliser la dépendance à la porosité des paramètres viscoélastiques du matériau homogénéisé.

Un riche programme expérimental, en soutien à ces travaux de thèse, a été mené par le CEA Marcoule pour caractériser les comportements à la lixiviation des enrobés bitumineux français dans le cadre du programme de recherche BABYLONE [3]. Les résultats expérimentaux sont discutés dans le présent document et utilisés pour calibrer les paramètres du modèle. Le comportement à la lixiviation libre, sous contre-pression constante et à volume constant est étudié numériquement pour des enrobés simplifiés. Les paramètres recalés sont discutés et comparés aux mesures expérimentales publiées dans la littérature. Le rôle des sels peu solubles présents dans les enrobés bitumineux français est également discuté. Des études de sensibilité de la composition, des paramètres matériau et de la taille de l'échantillon sont également réalisées pour mieux comprendre les paramètres clés du comportement à la lixiviation libre et en milieu confiné. Enfin, l'effet des vides existants sur la génération de contraintes des enrobés bitumineux en milieu confiné est étudié numériquement en modélisant le cas d'une lixiviation libre suivie d'une lixiviation en volume constant. Cette dernière étude permet d'obtenir une relation entre contrainte générée en milieu confiné et déformation autorisée des enrobés bitumineux.

Mots clés : déchets radioactifs, enrobés bitumineux, modélisation chimique-hydro-mécanique, modélisation multiphysique, homogénéisation, lixiviation.

Résumé long

Lors du retraitement industriel des combustibles nucléaires usés, certains flux de déchets aqueux contenant principalement des isotopes de césium et de strontium sont produits et doivent être traités afin de réduire la quantité de déchets à gérer. Ce traitement consiste à rendre insoluble ces isotopes à l'aide de réactifs chimiques. Ce processus de coprécipitation conduit à la production d'une boue qui peut être décrite comme une suspension de sels inorganiques peu solubles dans une solution aqueuse contenant principalement des sels de nitrate de sodium très solubles. Pendant de nombreuses décennies et dans plusieurs pays comme la Belgique, le Japon et la France, ce déchet primaire a été conditionné par coextrusion des boues et du bitume à une température proche de 150°C. Tout d'abord, cette température de travail permet l'écoulement du bitume pour faciliter le mélange. Deuxièmement, elle permet la déshydratation de la boue, ce qui entraîne la précipitation des sels solubles de sa fraction aqueuse dans la matrice de bitume. Ce processus de conditionnement produit ainsi ce que l'on appelle des enrobés bitumineux, qui consistent en une dispersion de sels inorganiques solubles et peu solubles dans une matrice de bitume. Dans la plupart des cas, la charge inorganique des enrobés bitumineux est comprise entre 40 et 45 % en masse. Cependant, la composition inorganique des enrobés bitumineux dépend fortement de la période et du pays de production.

En France et à partir des années 1960, environ 75 000 fûts de 220 litres d'enrobés bitumineux ont été produits à Marcoule et à La Hague. Actuellement, quelques dizaines de fûts d'enrobés bitumineux sont encore produits par an. Pour les déchets classés dans la catégorie des déchets de moyenne activité à vie longue (MA-VL), le centre de stockage géologique CIGEO [4] est la solution envisagée pour le stockage. Cette installation doit être construite au sein de la formation argileuse du Callovo-Oxfordien (CoX) située à la limite des départements de la Meuse et de la Haute-Marne. Dans les conditions du stockage géologique, et après environ une ou plusieurs centaines de milliers d'années, l'eau de la roche hôte saturera complètement les alvéoles de stockage contenant ces colis. Par un phénomène osmotique rendu possible par la capacité semi-perméable de la matrice bitumineuse, l'eau en contact direct avec les enrobés bitumineux va provoquer leur gonflement. Le gonflement des enrobés bitumineux sera libre dans un premier temps compte tenu des vides existants dans les conteneurs primaires, entre les conteneurs en béton et le revêtement en béton. Ces vides pourraient être remplis si le gonflement est suffisamment important. Le gonflement des enrobés bitumineux continuerait alors en milieu confiné, entraînant l'application d'une pression sur la roche hôte et pourrait potentiellement endommager localement celle-ci en champ proche d'un alvéole. L'intégrité de la garde saine du Callovo-Oxfordien doit être garantie durant ces processus de lixiviation des enrobés bitumineux. Par conséquent, le gonflement des enrobés bitumineux doit être pris en compte dans les études de sûreté de l'installation de stockage après fermeture du site.

L'objectif de ce travail de thèse est de prédire le comportement à la lixiviation dû à la reprise en eau des enrobés bitumineux en milieu libre et en milieu confinée et de mieux comprendre les mécanismes correspondants. L'objectif final est de mieux estimer les contraintes maximales que les enrobés bitumineux français pourraient générer en fonction des déformations autorisées dans des conditions de stockage géologique. Cette thèse a été menée et financée dans le cadre du volet 3 du programme quadripartite BABYLONE [3] (Andra, CEA, EDF, Orano). Le volet 3 concerne l'étude du comportement à long terme des enrobés bitumineux lors de leur reprise en eau en alvéoles de stockage, afin de répondre aux demandes de l'ASN et l'ASND [5].

De nombreux efforts expérimentaux ont été faits pour caractériser le processus de lixiviation des enrobés bitumineux. La reprise en eau et le gonflement des enrobés bitumineux japonais et belges ont été étudiés en lixiviation libre, à contre-pression constante et aussi à volume constant [6–12]. Cependant, en raison de leur composition différente, les enrobés bitumineux français ont un comportement potentiellement différent. Le comportement à la lixiviation des enrobés bitumineux français a été étudié dans des conditions de lixiviation libre et de volume presque constant [13–17]. Afin d'étudier l'impact spécifique de certains sels, des enrobés simplifiés contenant un ou deux sels ont été produits au CEA Marcoule. Dans le cadre de ce travail de thèse, on s'est intéressé aux enrobés monosel contenant le sel soluble $NaNO_3$ ou le sel peu soluble $BaSO_4$ ainsi que des enrobés bisel contenant à la fois ces deux composés. La résonance magnétique nucléaire (RMN) a été utilisée pour suivre la progression de l'eau à l'intérieur du matériau pendant les essais de lixiviation libre réalisés sur des enrobés bitumineux français simplifiés [18,19]. Récemment, un riche programme expérimental a été mené au CEA Marcoule pour caractériser les comportements à la lixiviation des enrobés bitumineux français simplifiés. Ces données expérimentales sont fournies dans le cadre d'un programme de recherche quadripartite (programme Babylone [3] mené par l'Andra et les trois exploitants nucléaires, CEA, EDF et Orano), projet dans lequel s'insèrent également les travaux de la présente thèse. Des essais de lixiviation libre ont ainsi été réalisés pendant environ 4 ans sur des enrobés bitumineux simplifiés et industriels. Le gonflement en lixiviation libre a été mesuré pour la première fois sur des enrobés bitumineux français. Des essais de lixiviation ont été menés pendant environ 2 ans sur des enrobés bitumineux simplifiés sous une contre-pression constante allant jusqu'à 2,8 MPa. Une phase de consolidation (application de cycles de chargement et de déchargement de la contre-pression à l'échantillon) est précédée à ces essais. Des analyses microstructurales ont été réalisées au CEA à l'aide d'une MEBE (microscope électronique à balayage environnemental). Les résultats expérimentaux utilisés dans cette thèse seront décrits au paragraphe 2.3 et au Chapitre 3.

Comme les caractérisations expérimentales du processus de lixiviation des enrobés bitumineux sont complexes et impliquent un suivi sur plusieurs années, voire des décennies, des modèles numériques sont nécessaires pour étudier le comportement de gonflement à long terme des enrobés bitumineux. Des modèles numériques peuvent également être utilisés pour réaliser des études de sensibilité et conforter la description phénoménologique établie à partir des observations expérimentales. De plus, ces modèles numériques peuvent être combinés à la modélisation des roches hôtes afin d'évaluer les conséquences du gonflement des enrobés bitumineux sur leur environnement de stockage.

Trois modèles numériques dont l'objectif est de représenter le processus de lixiviation des enrobés bitumineux peuvent être trouvés dans la littérature :

- Développé par le CEA, le modèle COLONBO [15,16,20] est focalisé sur les phénomènes chimiques et physico-chimiques (diffusion, dissolution, etc...) afin de prédire la cinétique de relâchement des radionucléides contenus dans les enrobés bitumineux. Le modèle est basé sur des mécanismes diffusifs et est régi par la première loi de diffusion de Fick. Le transport de Darcy et l'osmose ne sont pas pris en compte. Le modèle COLONBO peut décrire l'évolution de la structure des pores, la quantité d'eau absorbée et les ions relâchés pendant la lixiviation des enrobés bitumineux. Toutefois, ce modèle n'intègre pas la prise en compte des conséquences mécaniques.
- Un modèle chimio-hydro-mécanique (CHM) basé sur une approche poromécanique classique et prenant en compte les phénomènes de transport (diffusion, perméation, osmose) a été développé par l'Université Polytechnique de Catalogne (UPC) [10,21–24] et a été implémenté dans CODE_BRIGHT. Le matériau est modélisé comme un mélange d'une matrice poreuse de bitume et de cristaux de sel. La phase liquide (mélange d'eau et de sel dissous) et la phase

gazeuse (mélange d'air sec et de vapeur d'eau) sont également prises en compte. Ce modèle tient compte à la fois de la mécanique et du comportement de transport des différentes espèces chimiques au sein des enrobés bitumineux pendant le processus de lixiviation : l'osmose et la perméation sont prises en compte en plus de la diffusion. Ce modèle a été validé sur l'Eurobitum (enrobés bitumineux belges) [10,21–24], dont la composition en sel et la matrice de bitume diffèrent de ceux des enrobés bitumineux français.

- Basé sur les travaux de l'UPC [10,21–24], G. Melot [1,2] a proposé un modèle poro-viscoélastique avec de nouvelles lois d'évolution en fonction de la porosité pour les paramètres mécaniques et de transport (diffusion et perméation). Une méthode simple par chainage est proposée pour simuler le processus de resaturation en eau des enrobés bitumineux, défini comme le processus de remplissage en eau de la porosité initiale. Ce modèle, appelé MELOT2019 [1,2], a été calibré et validé sur des résultats expérimentaux (quantité de reprise en eau et de sels relâchés) de lixiviation libre réalisés sur des enrobés bitumineux français simplifiés [13] disponibles à la date des travaux de la thèse de G. Melot. Cependant, il faut noter que le modèle MELOT2019 n'est pas validé sur les données de gonflement des enrobés bitumineux français, qui n'étaient pas disponibles à l'époque. L'ensemble de ces différents modèles sera décrit dans la section 2.4.

Le modèle numérique proposé dans cette thèse est une extension du modèle MELOT2019 [1,2] et sera décrit dans le Chapitre 4. Les principales hypothèses de modélisation et les équations gouvernantes du modèle MELOT2019 sont conservées. Le milieu est considéré comme un matériau poreux saturé de fluide. Un seul sel soluble (le plus soluble s'il y en a plusieurs) est pris en compte dans le modèle actuel. Les sels peu solubles contenus dans les enrobés bitumineux ne sont pas traités directement et sont supposés inertes. Il est fait l'hypothèse que leur rôle est pris en compte dans les paramètres du matériau. **Une formulation novatrice des flux massiques d'eau et de sel avec une homogénéisation couplée des termes de transport** (diffusion, perméation et osmose) est proposée pour mieux modéliser le rôle de la membrane semi-perméable joué par le bitume et la dépendance vis-à-vis de la porosité des coefficients de transport couplés pendant le processus de lixiviation. Avec cette approche, on dispose de deux paramètres de recalage qui dépendent des coefficients de diffusion de l'eau et de sel ainsi que la solubilité d'eau et de sel dans le bitume. **Un modèle poro-viscoélastique non linéaire prenant en compte les grandes déformations** est également proposé pour mieux modéliser le comportement à la lixiviation des enrobés bitumineux en milieu confiné. Le modèle viscoélastique classique de Maxwell est ainsi adapté au cas de la poromécanique et un coefficient "visqueux de type Biot" est introduit. Le schéma d'homogénéisation Mori-Tanaka est appliqué pour modéliser la dépendance à la porosité des paramètres viscoélastiques du matériau homogénéisé. Enfin, la cinétique d'hydratation mesurée expérimentalement sur des enrobés bitumineux français est utilisée pour mieux modéliser le remplissage de la porosité initiale (étape d'hydratation). Le modèle numérique développé durant cette thèse est implémenté dans le code d'éléments finis BIL développé par P. Dangla [25].

Le Chapitre 5 est dédié à la modélisation des essais expérimentaux réalisés par le CEA et présentés au Chapitre 3. Le comportement à la lixiviation libre, à contre-pression constante et à volume constant a été étudié numériquement pour des enrobés simplifiés (monosel $NaNO_3$, monosel Na_2SO_4, bisel $NaNO_3/BaSO_4$). Le modèle développé durant la thèse montre sa validité pour l'ensemble du processus de lixiviation en milieu libre et en milieu confinée. La phase de consolidation est bien reproduite par le modèle, et la déformation simulée sous la contrainte de consolidation est cohérente avec les valeurs expérimentales.

Pour les essais de lixiviation libre (section 5.3), le modèle reproduit bien le gonflement et la quantité d'eau reprise mesurés sur des enrobés bitumineux français simplifiés (monosel $NaNO_3$, monosel

Na_2SO_4, bisel $NaNO_3/BaSO_4$). La validité du modèle a été démontrée pour les différents sels solubles pris en compte. Les paramètres matériaux recalés sur les enrobés bitumineux monosel $NaNO_3$ et monosel Na_2SO_4 sont cohérents avec les valeurs publiées dans la littérature. Les paramètres recalés sur les bisels $NaNO_3/BaSO_4$ ont mis en évidence l'effet d'accélération des sels peu solubles $BaSO_4$, ce qui est cohérent avec les observations expérimentales.

Pour les essais de lixiviation sous contre-pression constante (section 5.4), ceux réalisés sous faible contre-pression (176 kPa) sur les enrobés bitumineux monosel $NaNO_3$ et les bisel $NaNO_3/BaSO_4$ sont bien reproduits en utilisant les mêmes paramètres de matériau recalés en lixiviation libre. Il convient de noter que les résultats expérimentaux des bisels $NaNO_3/BaSO_4$ sous 176 kPa ne peuvent être bien reproduits qu'en supposant que les sels peu solubles $BaSO_4$ n'ont pas d'effet dans les enrobés bitumineux consolidés. Cela suggère que l'effet d'accélération du $BaSO_4$ est *a priori* éliminé par la phase de consolidation avant la lixiviation. Cependant, le modèle prédit des valeurs de gonflement plus importantes que les résultats expérimentaux pour des contre-pressions plus importantes (1,4 MPa et 2,8 MPa). L'image acquise par MEBE en fin du test de lixiviation sous 2,8 MPa montre une surface du matériau extrêmement chaotique. Il semble que la lixiviation sous une contre-pression de 2,8 MPa ait suivi un chemin préférentiel à l'intérieur de l'échantillon, ce qui pourrait expliquer les différences entre les résultats expérimentaux et numériques. Des analyses supplémentaires pourraient être entreprises pour déterminer si le comportement de gonflement différent observé sous une contre-pression importante est un biais expérimental ou bien chercher à comprendre son origine si ce n'est pas le cas.

Pour les essais de lixiviation à volume constant (section 5.5), la pression osmotique théorique d'une solution aqueuse de $NaNO_3$ avec une membrane semi-perméable parfaite est utilisée pour valider le modèle, car il n'existe pas encore de résultats expérimentaux d'enrobés bitumineux français simplifiés à volume constant. Le modèle reproduit bien la pression osmotique théorique (environ 41,6 MPa) en utilisant les paramètres de Pitzer appropriés. Des études de sensibilité sur la composition d'enrobés bitumineux, les paramètres des matériaux et la taille de l'échantillon ont été réalisées pour mieux comprendre les paramètres clés du comportement de la génération de contraintes à volume constant.

L'effet des vides existants sur le comportement de la génération de contraintes des enrobés bitumineux en milieu confiné est étudié numériquement en modélisant le cas d'une lixiviation libre suivie d'une lixiviation à volume constant. Les calculs ont été réalisés sur un exemple de bisel $NaNO_3/BaSO_4$. Cette dernière étude permet d'obtenir une relation entre contrainte générée et déformation autorisée. Les résultats numériques confirment que le pic de contrainte diminue quand le gonflement autorisé augmente. Considérant que la contrainte maximale est obtenue lorsqu'aucun gonflement n'est autorisé (volume constant tout le temps), les résultats pourraient être donnés en termes de pourcentage de cette contrainte maximale en fonction de la déformation autorisée. Les résultats numériques montrent que le pourcentage de la contrainte maximale diminue de manière significative avec l'augmentation du gonflement autorisé. Seulement environ 40 % de la contrainte maximale est atteinte lorsqu'un gonflement d'environ 30 % en volume est autorisé pendant la phase de lixiviation libre. **Par ailleurs, l'analyse de sensibilité montre que la hauteur de l'échantillon et les paramètres du matériau ont peu d'impact sur ces résultats numériques de pourcentage de contrainte maximale par rapport aux déformations.** Les résultats numériques pour le cas de la lixiviation libre suivie de la lixiviation à volume constant sont donc *a priori* également valables pour les enrobés bitumineux de taille réelle.

Enfin, le modèle est testé sur des enrobés bitumineux industriels (STE3, STEL) dont la composition est simplifiée (seul le sel le plus soluble est pris en compte, les autres sels étant considérés comme des composants inertes). Les résultats expérimentaux de lixiviation libre et à volume constant peuvent être partiellement reproduits en utilisant des paramètres spécifiquement recalés. Les tendances d'évolu-

tion et les ordres de grandeur des résultats numériques sont cohérents avec des résultats expérimentaux. Cependant, il est difficile d'interpréter ces paramètres recalés. Les comportements à la lixiviation spécifiques observés sur les enrobés industriels (STE3, STEL) sont *a priori* dus aux différents sels peu solubles contenus dans les enrobés industriels et ne peuvent pas être parfaitement reproduits par le modèle en utilisant une composition simplifiée. Des mesures expérimentales complémentaires pourraient être réalisées pour mieux comprendre l'effet des différents sels peu solubles présents dans les enrobés industriels.

En résumé, le modèle numérique développé dans cette thèse permet de prendre en compte les principaux phénomènes physiques impliqués dans le processus de lixiviation des enrobés bitumineux sous différentes conditions de chargement. Une formulation novatrice des flux massiques d'eau et de sel avec une homogénéisation couplée des termes de transport (diffusion, perméation et osmose) est proposée pour mieux modéliser le rôle de la membrane semi-perméable joué par le bitume et la dépendance à la porosité des coefficients de transport couplés pendant le processus de lixiviation. Un modèle poro-viscoélastique non linéaire prenant en compte les grandes déformations est également proposé pour mieux modéliser le comportement à la lixiviation des enrobés bitumineux en milieu confiné. La disponibilité d'un tel modèle est d'un grand intérêt pour l'évaluation du comportement à la lixiviation des enrobés bitumineux dans des conditions de stockage géologique souterrain. Il pourrait fournir des informations pour l'évaluation de l'endommagement potentiel du Callovo-Oxfordien en champ proche des alvéoles et ainsi contribuer aux études de sûreté des installations de stockage après fermeture du site.

<u>Perspectives pour des travaux ultérieurs à cette thèse :</u>

Un seul sel, usuellement le plus soluble ($NaNO_3$), est pris en compte dans le modèle actuel. Les autres sels solubles sont alors considérés comme étant identique au sel le plus soluble, cette approche est conservative. Les sels peu solubles contenus dans les enrobés bitumineux sont eux assimilés à la matrice bitumineuse et l'impact de leur présence sur les mécanismes de transport est pris en compte par des paramètres matériau spécifiques. Cette approche fonctionne bien pour les enrobés bitumineux français simplifiés (monosel $NaNO_3$, monosel Na_2SO_4, bisel $NaNO_3/BaSO_4$). Cependant, il semble que le rôle des diverses espèces de sels minoritaires, notamment les espèces peu solubles, contenues dans les enrobés bitumineux industriels (STE3, STEL) soit plus complexe et ne puisse pas être facilement appréhendé par une telle approche. Des études supplémentaires seront donc nécessaires pour mieux comprendre et modéliser l'effet des différents sels peu solubles présents dans les enrobés bitumineux industriels. L'objectif final, ultérieur à la thèse, sera de trouver un ensemble de paramètres qui donnera un résultat enveloppe en termes de contrainte générée en milieu confiné pour les enrobés bitumineux industriels.

Dans le modèle actuel développé durant la thèse, le remplissage de la porosité initiale par l'eau est modélisé indépendamment des principaux phénomènes de lixiviation (diffusion, perméation et osmose). Cette hypothèse est motivée par les résultats des expériences de H-RMN menées par CEA Marcoule [18,19] sur des enrobés bitumineux simplifiés contenant à la fois des sels solubles et peu solubles, qui montrent que la progression du front d'hydratation est beaucoup plus rapide que celle du front de lixiviation. Des études supplémentaires pourraient être menées pour affiner le modèle et déterminer le domaine de validité de cette hypothèse.

Il y a actuellement peu de résultats expérimentaux qui peuvent être utilisés pour valider le recalage retenu pour les paramètres du modèle. Des études expérimentales supplémentaires sont nécessaires pour mieux interpréter les significations physiques des paramètres recalés. D'autre part, des essais ont

été menés au CEA Saclay pour mesurer les valeurs de coefficient de diffusion effectif du sel dans différents enrobés. Ces résultats pourraient être comparés aux valeurs de coefficient de diffusion effectif simulés (cf. équation (73)) pour consolider le choix des paramètres de recalage.

L'origine des différents comportements à la lixiviation observés sur les enrobés bitumineux à contre-pression constante importante (1,4 et 2,8 MPa) reste mal comprise. En outre, il n'y a pas de résultats expérimentaux d'enrobés simplifiés à volume constant qui peuvent être utilisés pour valider le modèle. Des études expérimentales supplémentaires à contre-pression constante importante et à volume constant pourraient permettre de mieux comprendre les comportements à la lixiviation dans ces conditions et poursuivre l'amélioration du modèle.

Pour se rapprocher le plus possible du cas industriel (enrobés bitumineux placés dans une alvéole creusée dans l'argilite du Callovo-Oxfordien), ce modèle pourrait être couplé à un modèle approprié pour le comportement de la roche hôte comme une loi de comportement viscoplastique telle que celle du modèle LKR [26] utilisé par EDF pour modéliser l'argilite du Callovo-Oxfordien et qui est implémenté dans le code d'éléments finis Codes-Aster [27]. Cela permettrait d'évaluer les éventuelles conséquences mécaniques du gonflement des fûts d'enrobés bitumineux sur le Callovo-Oxfordien en champ proche des alvéoles. Le modèle développé dans cette thèse pourrait aussi être utilisé pour fournir une estimation des contraintes maximales que le Callovo-Oxfordien pourrait subir et qui pourrait être utilisé dans une approche simplifiée pour évaluer l'endommagement du Callovo-Oxfordien en champ proche induit par le gonflement des fûts d'enrobés bitumineux.

Acknowledgments

First of all, I would like to thank my thesis supervisor Patrick Dangla, and my advisors Sylvie Granet and Geoffroy Melot. We have been a great team of bitumen. I learned a lot from them, not only about the thesis but in many aspects, which will be very useful for the rest of my career. Secondly, I would like to thank the Babylone joint research program and all collaborators within the program. The insightful discussions and clear explanations were really helpful. I would like to especially thank Jean-Baptiste Champenois and the whole experimental team at CEA Marcoule for collecting the experimental data on French BWPs, which is crucial for the development and calibration of the numerical model. Finally, I would like to thank my family for their support. Thanks to the support of my wife Dr. Yutong LIU who defended her own thesis 3 days before mine. Thanks to my parents-in-law who flew to France to take care of the baby and allow us to better prepare the thesis defenses. Last but not least, thanks to our son Zhilin CHEN for accepting to be babysitted by someone else from two months and a half and for accepting to sleep the whole night from five months, which is essential for the good preparation of the thesis.

Table of Contents

CHAPTER 1

INTRODUCTION

During the industrial processing of spent nuclear fuels, some aqueous waste streams containing mainly cesium, strontium and ruthenium isotopes are produced and need to be treated to decrease the amount of waste that must be managed. Such a treatment is done by insolubilizing these isotopes using chemical reactants. This co-precipitation process yields a sludge that can be described as a suspension of poorly soluble inorganic salts in an aqueous solution containing mainly highly soluble sodium nitrate salts. For many decades and in several countries such as Belgium, Japan, and France, this primary waste was conditioned by co-extruding the sludge and bitumen at a temperature close to 150 °C - 160 °C. Firstly, this working temperature makes the bitumen more fluid and thus eases the mixing. Secondly, it allows the dehydration of the sludge, which leads to the precipitation of soluble salts from its aqueous fraction within the bitumen matrix. This conditioning process produced so-called Bituminized Waste Products (BWPs), consisting of a dispersion of soluble and poorly soluble inorganic salts into a bitumen matrix. In most cases, the inorganic load of BWPs ranges from 40 to 45 wt. %. However, the inorganic composition of BWPs highly depends on the period and the country of production.

In France and since the 1960s, about 75 000 220-liter drums of BWPs were produced at Marcoule and La Hague. Currently, a few dozen drums of BWPs are still produced per year. For those categorized as intermediate level long-lived waste (ILW-LL), the geological disposal facility CIGEO [4] is the considered disposal solution. This repository is foreseen to be constructed in the Callovo-Oxfordian (CoX) clay formation located between Meuse and Haute-Marne departments in France. One of the challenges with BWPs under geological disposal conditions is their swelling behavior due to water uptake. Indeed, after about one or several hundred thousand years, the water from the host rock will completely saturate the disposal cells containing these packages in the deep geological repository. By an osmotic phenomenon enabled by the semi-permeable capacity of the bitumen matrix, water in direct contact with BWPs will cause their swelling. Free swelling of BWPs will first occur until the existing voids within primary containers, as well as those between the concrete containers and the concrete pavement, are filled. The BWPs swelling will then be under confined conditions, leading to pressure on the host rock which could potentially damage it near the disposal cell. While the above phenomena take place, the integrity of the Callovo-Oxfordian must be guaranteed. Therefore, the BWPs swelling behavior must be considered in disposal facilities' safety studies after geological disposal closure.

Various experimental efforts have been made to characterize the BWPs leaching process. The water-uptake and swelling behavior of Japanese and Belgian BWPs have been investigated under free leaching, constant counter-pressure, and constant volume conditions [6–12]. However, due to a different composition compared to Japanese and Belgian BWPs, French BWPs potentially have a different leaching and swelling behavior. The leaching behavior of French BWPs has been investigated under both free leaching and nearly constant volume conditions [13–17]. Nuclear magnetic resonance (NMR) was used to monitor the water progression inside the material during the free leaching tests carried out on simplified French BWPs [18,19]. The existing experimental investigation of French BWPs will be detailed in 2.3.

As the experimental characterizations of the BWPs leaching process are complex and involve monitoring over several years or even decades, numerical models are necessary for investigating the long-term

swelling behaviors of BWPs. The numerical model can also be used to carry out sensitivity studies and validate the phenomenological description established on experimental observations. Moreover, such models aim to be coupled with the modeling of the host rocks to evaluate the consequences of BWPs swelling on their disposal environment. Various numerical models [1,2,10,15,20–24] have been developed in the past to represent the leaching process of BWPs, they will be briefly introduced in 2.4.

The objective of this PhD work is to predict the leaching behavior due to water uptake of French BWPs under free leaching and confined leaching conditions and better understand the corresponding mechanisms behind. The final goal is to better estimate the maximum stress that French BWPs could generate and apply to the host rock under geological disposal conditions. The numerical model developed in this work can be used to provide the evolution of the generated stress in terms of allowed deformation, which can be coupled with an appropriate host rock model to carry out safety analyses. This thesis was carried out and financed under part 3 of the BABYLONE quadripartite program [3] (Andra, CEA, EDF, Orano), which concerns the study of the long-term behavior of BWPs due to water uptake in storage cells, in response to requests from ASN and ASND [5].

A state of the art is first presented in CHAPTER 2. The production and composition of the French BWPs are described and compared with BWPs produced in other countries. The major physical phenomena involved during the leaching process under geological disposal conditions are introduced. The existing experimental results on French BWPs and existing numerical models are summarized. A significant increase (up to about 60%) in the porosity of the BWPs could occur during the leaching process and will have non-negligible effects on material mechanical and transport properties. Section 2.5 presents a brief literature review of homogenization methods, which can be used to model the porosity-dependency of the material properties.

A rich experimental program has been recently conducted to characterize the leaching behaviors of French BWPs. The experiments were mostly carried out by and at CEA Marcoule in close connection with this thesis. The newly acquired experimental results used for the investigation of French BWPs' leaching behavior and the calibration of the numerical model are presented in CHAPTER 3.

The numerical model proposed in this thesis is presented in detail in CHAPTER 4. The modeling hypotheses and the governing equations kept from the MELOT2019 model [1,2] are recalled. An innovative flux formulation with coupled homogenization of transport terms (diffusion, permeation, and osmosis) is proposed to better capture the role of the semi-permeable membrane played by the bitumen and the porosity-dependency of the coupled transport coefficients during the leaching process. A non-linear poro-viscoelastic model taking into account large strains is proposed to better model the BWPs' leaching behavior under confined conditions. The Mori-Tanaka homogenization scheme is applied to model the porosity-dependency of the viscoelastic parameters of the homogenized material.

The numerical results produced by the new model developed in this PhD work are presented and discussed in CHAPTER 5. The leaching behavior under free leaching, constant counter-pressure, and constant volume conditions are numerically investigated for simplified French BWPs. The fitted parameters are discussed and compared with the experimental measurements reported in the literature. The role of the poorly soluble salts present in French BWPs is also discussed. Sensitivity studies of composition, material parameters, and sample size are realized to better understand the key parameters of the leaching behavior under free leaching and confined leaching conditions. Finally, the effect of the existing voids on the stress build-up behavior of BWPs under confined leaching conditions is numerically investigated by studying the case of free leaching followed by leaching under constant volume conditions.

CHAPTER 2

STATE OF THE ART

As mentioned in the introduction, in the context of deep geological disposal, the BWPs will be in direct contact with the water-saturated host rock after about one or several hundred thousand years. The main objective of this work is to understand the BWPs' leaching behavior due to water uptake. This chapter presents a state of the art of this problematic in five parts. Firstly, the French BWPs are described in 2.1 and are compared with Japanese and Belgian BWPs. Secondly, the physical phenomena involved during the leaching process under geological disposal conditions are explained in 2.2. The existing experimental results on French BWPs and the existing numerical models on BWP's leaching behavior are summarized in 2.3 and 2.4, respectively. Finally, some existing homogenization methods available in the literature are summarized in 2.5.

2.1. Bituminized Waste Products (BWPs)

The term Bituminized Waste Products (BWPs) corresponds to radioactive waste conditioned in a bituminous matrix.

The radioactive wastes studied during this thesis are co-precipitation sludge from the treatment of effluents during the nuclear spent fuel processing process. This co-precipitation sludge comes from aqueous nuclear waste streams that are processed by using inorganic reagents to co-precipitate radionuclides. Due to its strong confining capability (linked to its impermeability), the bitumen was selected as a matrix for the conditioning of this co-precipitation sludge to produce BWPs. The role of the bitumen is to prevent the dispersion of these salts in the environment. Bitumen and sludge are co-extruded at a temperature close to 150°C, leading to the evaporation of the water initially present in the sludge, the precipitation within the bitumen matrix of soluble inorganic salts, and the embedding of insoluble inorganic salts. To summarize, the BWPs are composed of a bitumen matrix containing several salt crystals. These salts could be soluble or poorly soluble.

In France and from the 1960s, about 75 000 drums of 220L of BWPs were produced at Marcoule (80%) and La Hague (20%). The production procedures and the composition of the French BWPs studied in this thesis are presented in 2.1.1. Meanwhile, the use of bitumen as a matrix is not exclusively French. For example, Belgium and Japan also use bitumen as the conditioning matrix for their radioactive wastes [7,28,29]. The comparison between these different BWPs will be detailed in section 2.1.2.

2.1.1. Production and composition of French BWPs

Depending on the co-precipitation sludge used for the production, French BWPs can be categorized into two types: STE3 produced in the Effluent Treatments Station N°3 in La Hague and STEL produced in the Liquid Effluent Treatments Station in Marcoule. In order to study their mechanical behavior, non-radioactive BWPs surrogates are produced in the laboratory. These laboratory-produced non-radioactive BWPs are studied in this thesis, including industrial BWPs and simplified BWPs. The synthetic non-radioactive BWPs are elaborated by co-extruding a pure straight-run bitumen (Azalt 70/100 provided by Total-Energies) and the sludge resulting from the treatment of effluents during the spent fuel processing process.

Fig. 2-1 illustrates a schematic representation of the extrusion process. The pure bitumen was inserted in a co-rotating twin screw extruder along with sludge, toluene and surfactants to ease the sludge-bitumen mixing. Four vapor outlets were used along the screw to enable water evaporation. Consequently, the crystallization of soluble salts occurred during the extrusion process. The residual water content in these non-radioactive BWPs was assessed by using the Karl-Fischer method and found to be systematically lower than the 0.5 wt. % detection limit. The salt content was measured using gravimetry after dissolving the bitumen matrix of BWPs in toluene and drying the corresponding filtrated residue in a 20 % RH chamber. Apparent and intrinsic densities of elaborated BWPs were measured respectively using volumetry and Helium pycnometry.

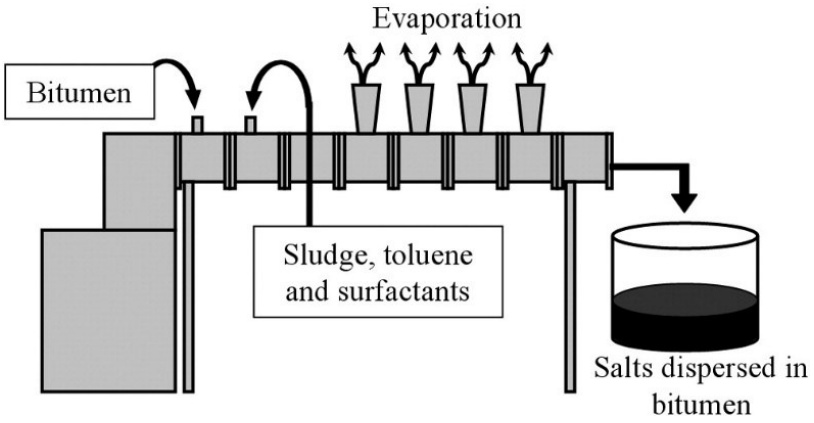

Fig. 2-1 Schematic representation of the extrusion process used to produce the BWPs [18].

Depending on the sludge composition, we can distinguish the industrial BWPs (STE3 and STEL) and the simplified BWPs containing only one or two salts. The non-radioactive industrial BWPs are produced in laboratories and have the mean composition (cf. Table 1) of those produced at La Hague and Marcoule.

Table 1 Composition of non-radioactive industrial BWPs STE3 and STEL [17].

Characteristics	STE3	STEL
Bitumen content (wt. %)	**61**	**54**
Inorganic load (wt. %)	**39**	**46**
Soluble salts	**12.9**	**4.1**
$NaNO_3$	11.1	2.8
Na_2SO_4	1.8	1.4
Insoluble salts	**26**	**41.9**
$BaSO_4$	21.1	14.7
$K_2NiFe(CN)_6$ precipitated	2.4	7.4
$Fe(OH)_3$	-	9.7
$Cu(OH)_2$	-	5.1
$Co(OH)_2$	1.1	-
CoS	1.4	-
$Ca_3(PO_4)_2$	0.1	-
Diatomite	-	5.1
Residual water (wt. %)	**< 1%**	**< 1%**
Density ($g.cm^{-3}$)	**1.39 ± 0.01**	**1.39 ± 0.03**

Given the various salts contained in the industrial BWPs, simplified BWPs containing one or two salts were produced in order to study the specific impact of a given salt. For this purpose, a bitumen identical to that of industrial BWPs is used and the sludge composition is simplified. The notation, composition, density, and porosity of the simplified BWPs are listed in Table 2. The major soluble salts (sodium nitrate $NaNO_3$ and sodium sulfate Na_2SO_4) and a major poorly soluble salt (barium sulfate $BaSO_4$) are selected. Their physical properties are reported in Table 3. The simplified BWPs containing one single salt are named mono-salt BWPs, while those containing two salts are named bi-salt BWPs. These simplified BWPs allow bypassing the couplings of different salts that could take place for the industrial

BWPs and are thus very useful to understand the leaching behavior of the BWPs. The calibration and validation of the numerical models are thus mainly realized on these simplified BWPs.

Table 2 Composition, salt fractions, densities, and apparent porosities of simplified BWPs studied during the thesis.

Notation	Composition	Nominal salt fraction (wt. %)	Measured salt fraction (± 0.1 wt. %)	Expected density ($g.cm^{-3}$)	He density ($g.cm^{-3}$)	Apparent density ($g.cm^{-3}$)	Apparent porosity (vol. %)
M5_NaNO3	$NaNO_3$	5	4.4	1.05	1.10	1.05	4
M10_NaNO3		10	9.0	1.07	1.20	1.08	9
M20_NaNO3		20	18.3	1.13	1.26	1.17	6
M30_NaNO3		30	31.1	1.23	1.29	1.17	8
M10_Na2SO4	Na_2SO_4	10	N/A	N/A	N/A	N/A	N/A
M25_Na2SO4		25					
M40_Na2SO4		40					
M5_BaSO4	$BaSO_4$	5	6.4	1.06	1.12	1.09	3
M10_BaSO4		10	14.3	1.10	1.23	1.08	10
M20_BaSO4		20	24.2	1.21	1.21	1.21	0
M30_BaSO4		30	32.0	1.32	1.39	1.31	6
M40_BaSO4		40	40.1	1.48	1.52	1.37	8
M5_NaNO3_ M35_BaSO4	5 wt. % $NaNO_3$, 35 wt. % $BaSO_4$	40	39.2	1.45	1.46	1.33	7
M10_NaNO3 _M30_BaSO4	10 wt. % $NaNO_3$, 30 wt. % $BaSO_4$	40	39.6	1.43	1.45	1.23	12.3
M20_NaNO3 _M20_BaSO4	20 wt. % $NaNO_3$, 20 wt. % $BaSO_4$	40	39.4	1.39	1.43	1.34	4.5

Table 3 Physical properties of salt contained in simplified French BWPs [30].

	$NaNO_3$	Na_2SO_4	$BaSO_4$
Density ($kg.m^{-3}$)	2260	2660	4500
Molar mass ($g.mol^{-3}$)	85	142	233.4
Water solubility at 25°C ($g.L^{-1}$)	921	195	2.4×10^{-3}

Microstructural analyses were conducted on laboratory-made simplified BWPs to study morphology and the size of the salt crystals. ESEM images and particle size distributions are reported in Fig. 2-2 for mono-salt $NaNO_3$ and mono-salt $BaSO_4$ BWPs [18]. The $NaNO_3$ grains (Fig. 2-2(a)) are single crystals with a size of several tenths of micrometers, which is in good agreement with the distribution centered at 32 ± 13 µm obtained using laser particle analysis. For mono-salt $BaSO_4$ BWPs, the mean grain size and the distance between nearby grains were much smaller (Fig. 2-2(b)). Moreover, high-magnification images of this sample indicate that $BaSO_4$ particles were in fact formed by an agglomeration of nano-metric monocrystals (see insert in Fig. 2-2(b)). Therefore, these results suggest that the $BaSO_4$ size distributions obtained by laser granulometry (5 ± 3 µm) were mainly representative of these agglom-erates, which is an order of magnitude smaller than that of $NaNO_3$ crystals.

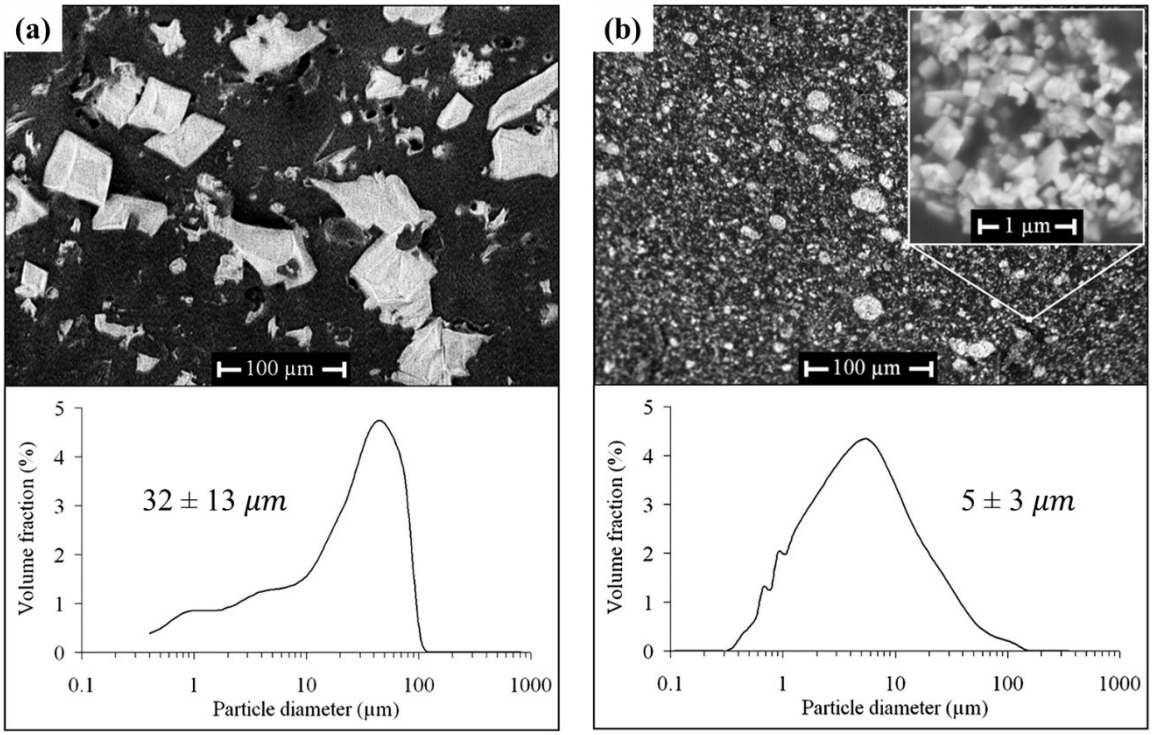

Fig. 2-2 ESEM observation and laser particle size analysis for (a) mono-salt $NaNO_3$; (b) mono-salt $BaSO_4$ BWPs [18].

2.1.2. Comparison with Japanese and Belgian BWPs

BWPs are also produced in other countries in the world besides France. Belgium and Japan, for example, have also used bitumen as the conditioning matrix. The Belgian [7] and Japanese [31] BWPs also contain soluble and insoluble salts, but of different natures and in different proportions compared to French BWPs. Table 4 summarizes the composition of Belgian [7], Japanese [31], and French BWPs. Japanese BWPs are produced from Straight Bitumen grade 60/80 [31]. These BWPs contain 17.5 wt. % sodium nitrate and 20 wt. % barium sulfate. One of the specificities of these Japanese BWPs is their manufacturing process. Unlike Belgian and French BWPs which are produced by extrusion, Japanese BWPs are produced by mixing. In 2003, a Japanese team conducted a study of these BWPs under free leaching conditions [31].

Belgian BWPs are called "Eurobitum" [7]. They are produced by using a different bituminous matrix (Mexphalt R85/70) compared to French BWPs, which leads *a priori* to a different mechanical response. In terms of salt content, Eurobitum contains about 25 to 30 wt. % of soluble salts, while French BWPs contain less than 20 wt. %. For Eurobitum, all soluble salts are sodium nitrate, whereas the French BWPs also contain sodium sulfate. The fraction of poorly soluble salts within Eurobitum varies from 8 to 16 wt. %, while French BWPs contain between 20 to 40 wt. %. The composition of the poorly soluble salts is also different. SCK-CEN is conducting experimental studies on these BWPs in collaboration with UPC [9,10].

Table 4 Composition differences between Belgian [7]*, Japanese* [31]*, and French BWPs.*

	Belgian BWPs [7]	Japanese BWPs [31]	French BWPs
Bitumen	Mexphalt R85/40	Straight Bitumen 60/80	Viatotal 70/100

Soluble salt content (%)	25 – 30 ($NaNO_3$)	17.5 ($NaNO_3$)	1 – 20 ($NaNO_3$ and Na_2SO_4)
Poorly soluble salt content (%)	8 – 16 (mostly $CaSO_4$)	20 ($BaSO_4$)	20 – 40 (mostly $BaSO_4$)

2.2. Main physical phenomena involved during the leaching process under geological disposal

In France and from the 1960s, about 75 000 220-liters drums of BWPs were produced at Marcoule and La Hague. For those classified as intermediate level long-lived waste (ILW-LL), the geological disposal facility CIGEO [4] is the disposal solution. This repository is foreseen to be constructed in the Callovo-Oxfordian (CoX) clay formation. Various coupled physical phenomena occur under long-term geological disposal conditions, mainly diffusion, permeability (Darcy transport), osmosis, and salt dissolution/precipitation. A good understanding of these phenomena, their causes and consequences is an essential prerequisite for the development of a numerical model.

First, it is necessary to give some definitions:

- Solvent: a liquid substance that has the property of dissolving, diluting, or extracting other substances without modifying them chemically and without being modified. The solvent in this study is water.
- Solute: substances dissolved in a solvent.
- Semi-permeable membrane: membrane that only allows solvents to pass through (water in this study) and not substances in solution.

2.2.1. Diffusion

Diffusion is the transport of a chemical compound in a medium under the influence of a gradient of concentration (cf. Equation (131)). The transport is from the most concentrated area to the least concentrated area. The component that diffuses can be solid, liquid, or gas. In the same way, the medium in which the diffusion takes place can be in one of the three states. The kinetics of diffusion depends on the nature of the interactions between the medium and the diffusing material.

In the context of BWP leaching under long-term geological disposal, different diffusions occur:

- Diffusion of water in the bitumen matrix
- Diffusion of dissolved salts in the bitumen matrix
- Diffusion of dissolved salts in water

It should be noted that if the BWPs can be considered as homogeneous material from a macroscopic point of view, especially in terms of salt distribution within the matrix, they are heterogeneous on a smaller scale. BWPs can be considered as a mix of three components: bitumen, salt crystals and pores. The diffusion coefficients of such a material are actually effective diffusion coefficients, which depend on the diffusion coefficient of the species in each of the components and the volume fraction of these components. For example, the effective diffusion coefficient of an ion in the BWPs will depend on the diffusion coefficient in the water-saturated porosity and in the bitumen matrix. Since diffusion is faster

in water than in the bitumen matrix, the effective diffusion coefficient of the ion in the BWP is more important as the porosity increases. This porosity-dependency of the effective diffusion coefficients will be taken into account by a specific coupled homogenization method described in section 4.2.

2.2.2. Permeation

Permeation is governed by Darcy's law [32,33], which describes the transport of a fluid through a porous medium under the influence of a pressure gradient (cf. Equation (132)). The transport is from the zone of high pressure towards the zone of lower pressure. Darcy's law is valid for sufficiently slow flows, i.e., at low Reynolds numbers (Re << 1). This condition is largely fulfilled for flows in BWPs, given the very low permeability of the material.

2.2.3. Osmosis

Osmosis is the transport of a solvent through a semi-permeable membrane separating two solutions under the influence of a solute concentration gradient (cf. Equation (133)). The transport of solvent is from the less concentrated solution to the more concentrated one. The osmotic pressure is defined as the minimum pressure that needs to be applied to a solution to prevent the inward flow of its pure solvent across a semi-permeable membrane. Theoretically, this osmotic pressure, in the case of a perfect semi-permeable membrane, is given by the following relation [34]:

$$\Pi = -\frac{RT\rho_w}{M_w} ln(a_w) \quad (1)$$

where R is the perfect gas constant, T is the temperature, ρ_w is the liquid water density, M_w is the water molar mass, and a_w is the water activity. Water activity is a dimensionless parameter lower or equal to 1. The water activity decreases with an increasing amount of solute contained in the water.

In the case of BWPs, the bituminous matrix acts as a semi-permeable membrane [10]. The presence of soluble salt crystals which are hygroscopic (tendency to absorb water) in the bituminous matrix leads to a pore solution saturated with salt until all the salt crystals are dissolved. On the other hand, the site water in contact with BWPs has a low salt content. The important difference in solute concentrations leads to a significant difference in water activity, and thus an important osmotic pressure difference.

As $NaNO_3$ is the major and the most soluble salt contained in French BWPs, the theoretical osmotic pressure is estimated by using the solubility of sodium nitrate $NaNO_3$, and more exactly the corresponding water activity in a sodium nitrate saturated solution. About 42 MPa was reported in the literature[1,2,21,22] as the theoretical osmotic pressure for $NaNO_3$-saturated aqueous solution at 25 °C, which can be considered as a conservative value. Fig. 2-3 shows the osmotic pressure calculated with equation (1) in terms of different $NaNO_3$ concentrations for a perfect semi-permeable membrane at 25 °C, by using the water activity data reported in [35] and summarized in Table 5. The resulting maximum theoretical osmotic pressure 41.6 MPa (with a solute mass fraction of 10.83 moles of $NaNO_3$ per kilogram of water) is used in the rest of this study.

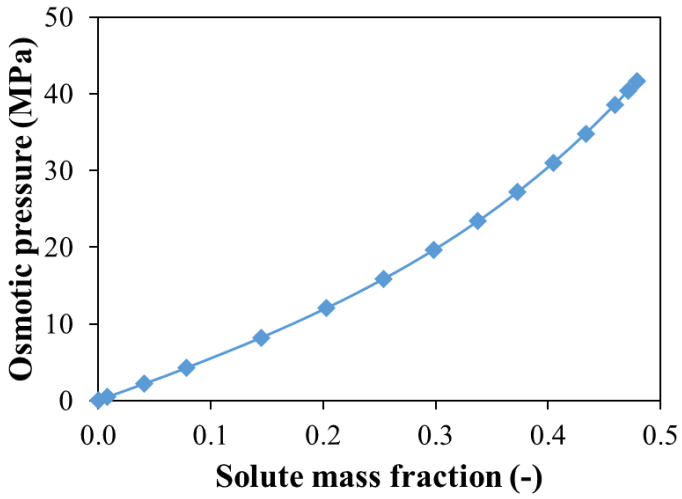

Fig. 2-3 Theoretical osmotic pressure in terms of $NaNO_3$ solute mass fraction (kg/kg) for a perfect semi-permeable membrane at 25 °C.

Table 5 Water activity in terms of solute concentration for an aqueous solution of $NaNO_3$ at 25°C [35].

Solute mole concentration (mol/kg of solvent)	Solute mass concentration (kg/kg)	Water activity (-)
0	0.000	1.000
0.1	0.008	0.997
0.5	0.041	0.984
1	0.078	0.970
2	0.145	0.942
3	0.203	0.916
4	0.254	0.891
5	0.298	0.867
6	0.338	0.844
7	0.373	0.821
8	0.405	0.798
9	0.433	0.777
10	0.459	0.756
10.5	0.472	0.746
10.83	0.479	0.739

It should also be noted that the bituminous matrix is not a perfect semi-permeable membrane. The osmotic efficiency coefficient τ is introduced to take into account the imperfection of the semi-permeable membrane. This parameter is between 0 and 1, and decreases with the ability of the membrane to prevent the transport of solute molecules: 1 for a perfect semi-permeable membrane and 0 when the membrane can no longer prevent the transport of molecules. The modeling of the evolution of the osmotic efficiency coefficient τ will be taken into account by a coupled homogenization of transport terms in 4.2.

2.3. Existing experimental results on French BWPs

A vast experimental program dedicated to characterizing the French BWPs is carried out at the CEA in parallel to this thesis and will be presented in CHAPTER 3. In this section, only the experimental results acquired on French BWPs already existing in the literature are summarized.

2.3.1. Leaching behavior under free leaching conditions

B. Gwinner studied the leaching behavior of industrial BWPs STE3 under free leaching conditions [14–16]. The experiments were conducted using leaching solutions of different water activities ranging from 0.74 to 1. The amount of water uptake and release salt are monitored over a leaching time up to 1000 days. The water uptake and released $NaNO_3$ of STE3 leached by solutions with different water activities are illustrated in Fig. 2-4. The results reveal that the water uptake and released $NaNO_3$ increase with the water activity of the leachate, particularly when the water activity of the leachate exceeds 0.97.

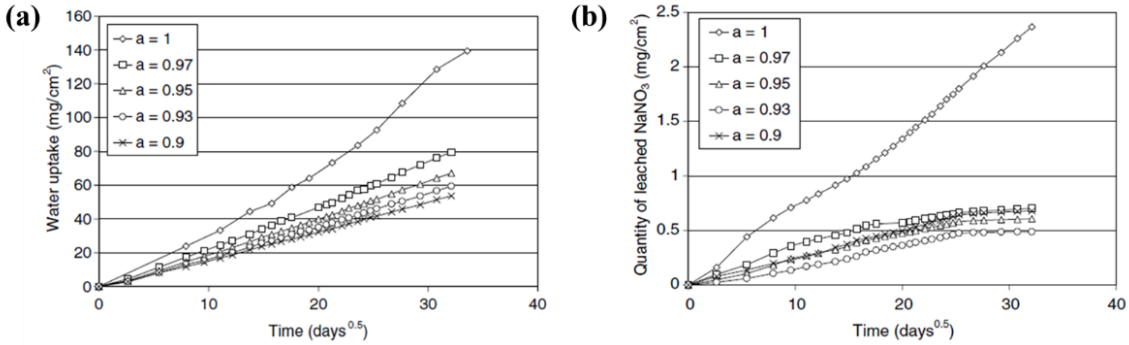

Fig. 2-4 Experimental measurements of (a) water uptake (mg/cm^2); (b) released $NaNO_3$ (mg/cm^2) of STE3 leached by solutions with water activity a ranging from 0.9 to 1 [15].

B. Gwinner investigated the porosity profile evolution of STE3 for different leaching time and leachate water activity [15]. Fig. 2-5 shows the binary images based on ESEM observations performed on STE3 samples leached by pure water (water activity = 1) during 2, 6, 12, 25 and 37 months [15]. The mean porosity profiles reconstructed from these ESEM observations at different leaching time are shown in Fig. 2-6 and share the same trend. The maximum porosity (quite constant in time and about 60%) is located near the leaching surface (depth = 0). The porosity decreases when progressing into the depth of the sample until no significant pore volume is measured. The mean porosity profiles of STE3 samples leached 11 months by solutions of different chemical activities (0.74, 0.89, 0.95 and 1) [15] are shown in Fig. 2-7. The results indicate that the porosity increases overall as the water activity increases.

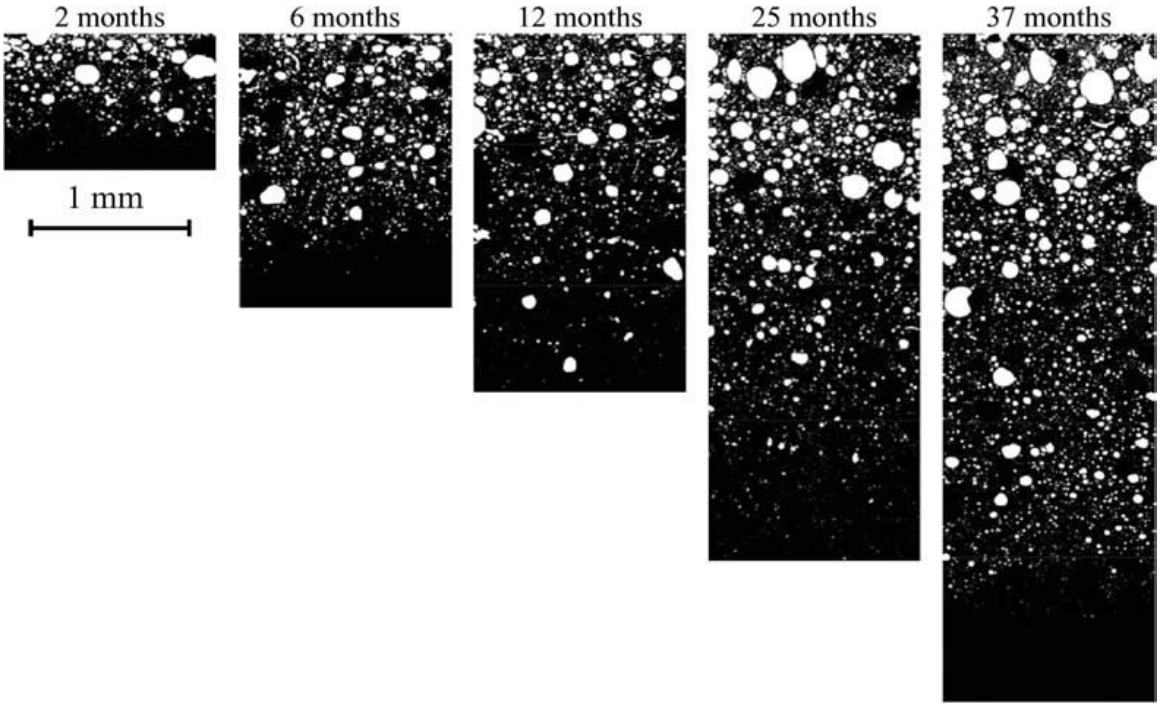

Fig. 2-5 Binary images based on ESEM observations performed on STE3 samples leached by pure water during 2, 6, 12, 25 and 37 months [15].

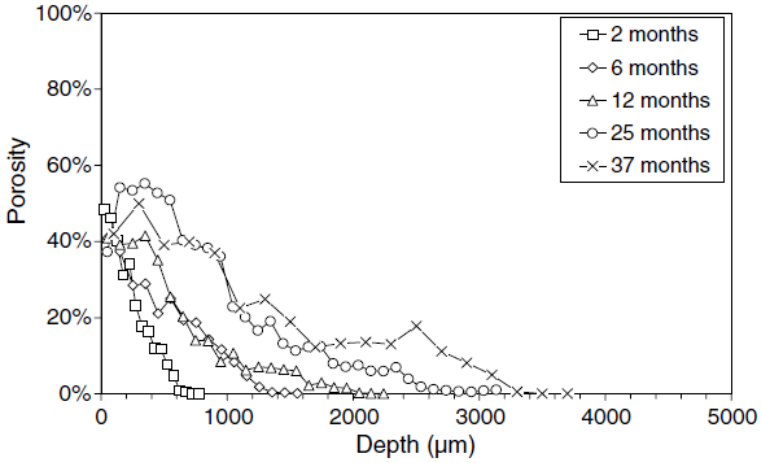

Fig. 2-6 Porosity profiles obtained from ESEM observations of STE3 samples leached by pure water during 2, 6, 12, 25 and 37 months [15].

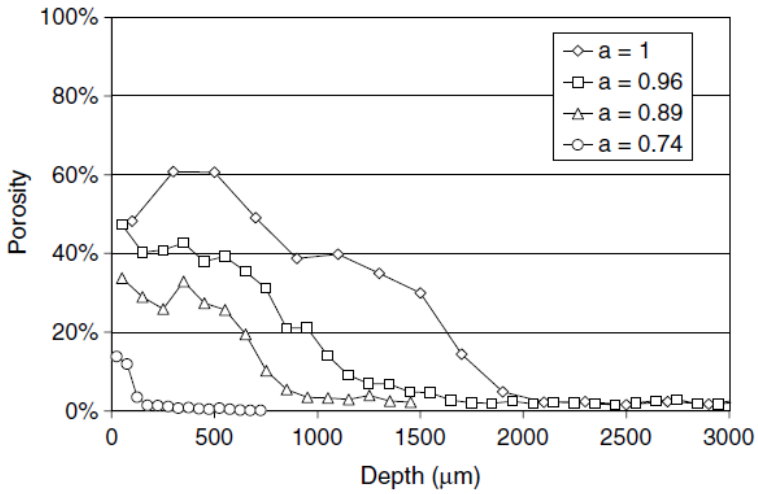

Fig. 2-7 Porosity profiles obtained from ESEM observations performed on STE3 samples leached 11 months by solutions of chemical activities equal to 0.74, 0.89, 0.95 and 1 [15].

B. Gwinner [16] measured the diffusion coefficients of different species in water, pure bitumen and leached BWPs. Table 6 summarizes the diffusion coefficients of tritium water (HTO), cesium and sodium in water and pure bitumen. The diffusion coefficients in pure bitumen are significantly smaller than in water. Furthermore, the diffusion coefficients of the ions in pure bitumen are at least four orders of magnitude smaller than that of tritium water, which is consistent with the semi-permeable nature of the bitumen.

Table 6 Diffusion coefficients of tritium water, cesium and sodium in water and pure bitumen [16].

Species	Diffusion coefficient in water ($m^2 s^{-1}$)	Diffusion coefficient in pure bitumen ($m^2 s^{-1}$)
Tritium water (HTO)	1.93×10^{-9}	$8.6 \pm 1.2 \times 10^{-14}$
Cesium	2.05×10^{-9}	$< 1 \times 10^{-18}$
Sodium	1×10^{-9}	$< 1 \times 10^{-17}$

The effective water diffusion coefficients and the porosity near the leaching surface are estimated for STE3 with different leachate activity (cf. Table 7) [16]. The results reveal logically that the effective water diffusion coefficients increase with the porosity.

Table 7 Estimation of the effective diffusion coefficient of water in STE3 BWPs leached with different leachate activities [16].

Porosity	Effective water diffusion coefficient (m^2/s)
0	3.1×10^{-14}
0.33	5.1×10^{-14}
0.45	8.5×10^{-14}
0.55	2.6×10^{-13}

More recently, J.B. Champenois et al. [13] measured the amount of water uptake and ions released during the free leaching tests conducted on simplified French BWPs incorporating one type of salt (Na_2SO_4 or $BaSO_4$), as shown in Fig. 2-8. They reported that for BWPs containing a single salt, the amount of water uptake and released salts are in general more important for higher salt content and salt solubility. It should be noted that for BWP incorporating poorly soluble salt $BaSO_4$, the amount of water uptake drastically increased for BWPs containing 40 wt. % $BaSO_4$, while the amount of released sulfate remained at a low level.

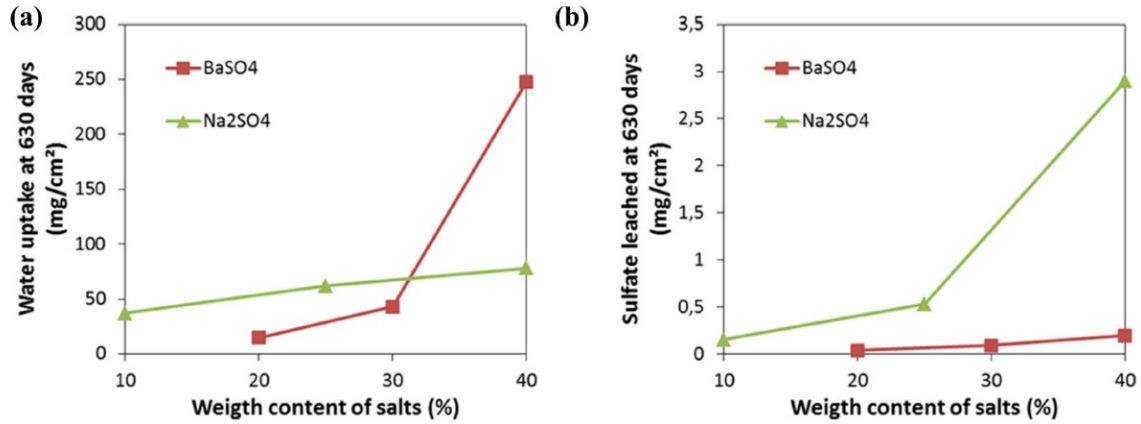

Fig. 2-8 Amount of (a) water uptake; (b) released sulfate after 630 days of leaching by pure water at 25°C for simplified BWPs containing an increasing amount of sodium sulfate Na_2SO_4 and barium sulfate $BaSO_4$ [13].

However, there is currently no existing experimental investigation of French BWPs' swelling behavior under free leaching conditions. Indeed, mechanical behavior is not studied through these tests and no swelling measurement is available.

2.3.2. Leaching under constant volume conditions

N. Bleyen and al. [17] experimentally investigated the swelling and pressure build-up behavior of the French industrial BWPs (STEL and STE3) under nearly constant volume conditions (cf. Fig. 2-9). Due to the very high pressures generated, the strain gauges in the load cells slightly deformed and allowed a slight swelling of the samples (Fig. 2-9(b), (d)).

For both STEL and STE3 samples, the generated pressure increased rapidly during the first ~200 days, as shown in Fig. 2-9 (a), (c). For STEL, the pressure increase rate decreased continuously. A pressure of ~23 MPa was recorded at about 2000 days, and it continues to increase slowly with time. For STE3,

The pressure increase rate decreased significantly after the first 200 days. A maximum pressure between 28 and 34 MPa seems to be reached at about 1000 days. After 1200 days, the generated pressure slightly decreased over time.

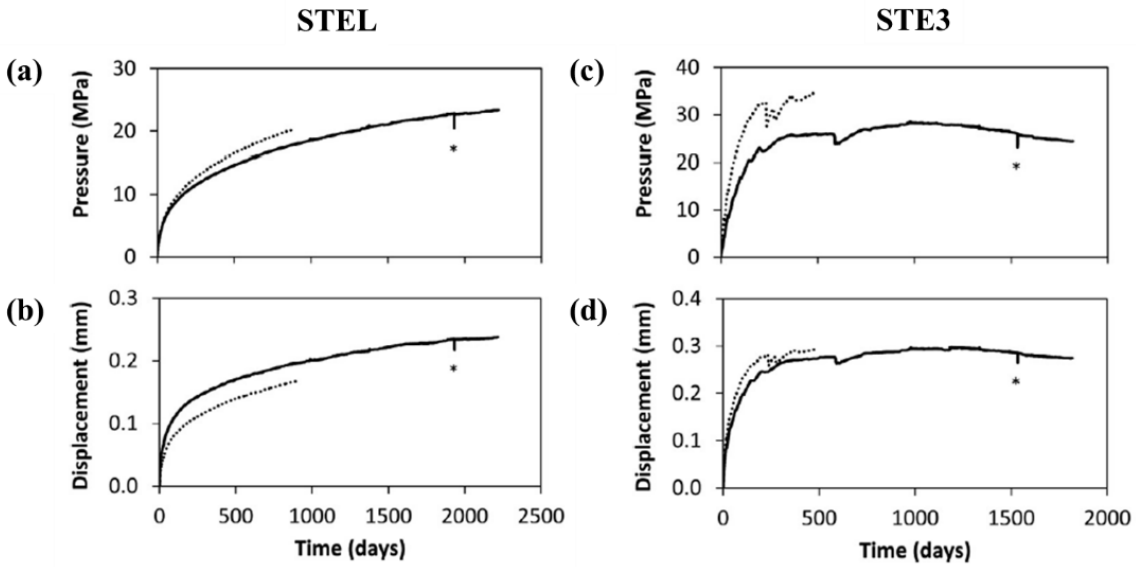

Fig. 2-9 Evolution of the generated pressure and displacement as a function of time after leaching of STEL (a-b) and STE3 (c-d) samples under nearly constant volume conditions. ⁎: pressure and displacement decreases caused by a temperature decrease in the lab during a power failure [17].

2.3.3. Nuclear magnetic resonance (H-NMR)

Nuclear magnetic resonance (NMR) was used to monitor the water progression inside the material during the free leaching tests carried out on simplified French BWPs [18,19]. S. Le Feunteun et al. [18] investigated the 1D profiles of water quantity within the French BWPs (see Table 8 for the chemical composition) after 47 days, 4, 6 and 8 months of leaching using NMR (Fig. 2-10).

Table 8 Chemical composition of the French BWPs samples S, I and B used in [18].

Sample type	Salt total mass fraction (%)	Composition	Salt total volume fraction (%)
S	40.3	40.3% $NaNO_3$	23.3
I	40.8	40.8% $BaSO_4$	13.5
B	40.3	14.3% $NaNO_3$,26.9% $BaSO_4$	16.9

The sample surface in contact with the leaching solution is indicated by the zero value on the abscissa in Fig. 2-10. For S-type samples (Fig. 2-10(a)), all the water remained within the first 2 mm of depth after 8 months of leaching. The water quantity increased in intensity with the water uptake, whereas the leaching front progressed very slowly in depth. For I-type samples (Fig. 2-10(b)), the water quantity in the first millimeters under the sample surface was comparable to that observed for the S-type. However, the water progressed much faster within the sample, as the water already reached the bottom of the NMR tube in less than 8 months. For B-type samples ((Fig. 2-10(c)), the first profile at 47 days is

similar to that observed on S-type samples. However, the profiles with long leaching time became closer to those observed on I-type samples. These results show that $BaSO_4$ salts facilitate the water transport within the BWPs, and thereby increase the water uptake amount.

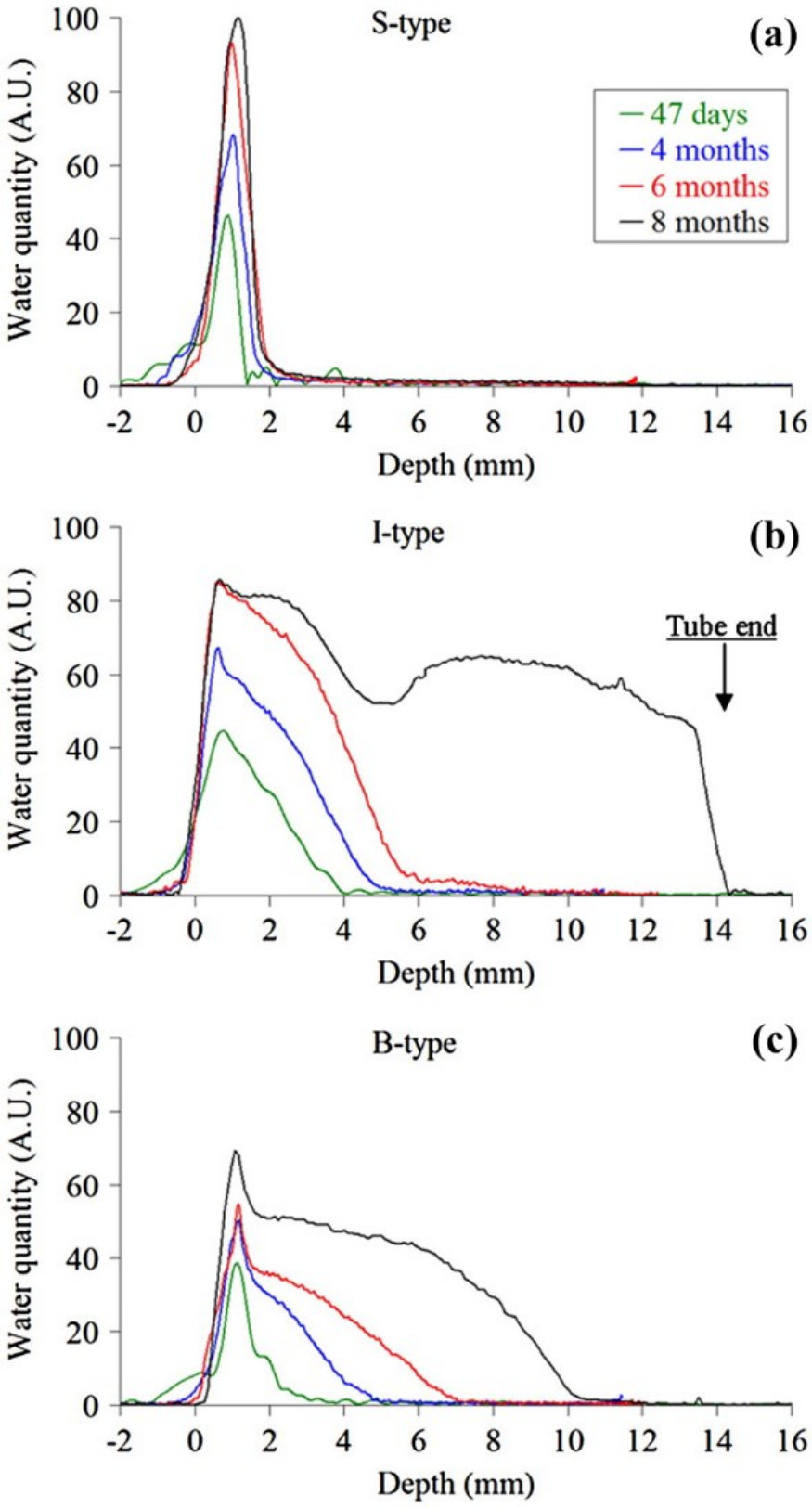

Fig. 2-10 1D profiles of water quantity within the (a) S-type, (b) I-type, (c) B-type samples after 47 days, 4, 6 and 8 months of leaching [18].

More recently, R. Blinder et al. [19] used NMR to monitor the water uptake behavior of simplified French BWPs incorporating 40 wt. % $SrSO_4$ or $MgSO_4$. They reported similar results as the existing one: the insoluble salts dispersed in the bitumen matrix enhance the water progression in the material and thereby increase its water uptake rate.

2.4. Existing numerical models

As the experimental characterizations of the BWPs leaching process are complex and involve monitoring over several years or even decades, numerical models are necessary for investigating the swelling behaviors of BWPs. The numerical model can also be used to carry out sensitivity studies and validate the phenomenological description made based on experimental observations. Moreover, such models could be coupled with the modeling of disposal host rocks to evaluate the consequences of BWPs swelling on the disposal facilities. Various numerical models have been developed to represent the leaching process of BWPs and will be briefly presented in this section.

2.4.1. COLONBO model

Developed by the French Alternative Energies and Atomic Energy Commission (CEA), the COLONBO model [15,16,20] is focused on chemical and physicochemical phenomena (diffusion, dissolution, ...) in order to predict the release kinetics of radionuclides contained in BWPs. The model is based on diffusive mechanisms and is governed by Fick's first diffusion law. The BWPs are considered impermeable, the Darcy transport is neglected. Similarly, osmosis is not taken into account in the model.

The model describes the progression of the dissolution front, which separates the leached and non-leached zones of the BWPs. The dissolution front is defined by the value of the water activity, which tends to increase with the arrival of the 'pure' water from the geological disposal site. When the water activity reaches the threshold, the salt crystals dissolve and lead to pores saturated by saline solution. The COLONBO model can describe the evolution of the pore structure, the amount of water uptake and ions released during the leaching process of BWPs. However, such a model does not consider any mechanical consequences.

2.4.2. Chemo-Hydro-Mechanical model (University Polytechnic of Catalunya)

A Chemo-Hydro-Mechanical (CHM) model based on a classic poromechanical approach and taking into account the transport phenomena (diffusion, permeation, osmosis) was developed by the University Polytechnic of Catalunya (UPC) [10,21–24] and was implemented in CODE_BRIGHT. The material is modeled as a mixture of a porous bitumen matrix and salt crystals (cf. Fig. 2-11). The liquid phase (mixture of water and dissolved salt) and the gas phase (mixture of dry air and water vapor) are also considered.

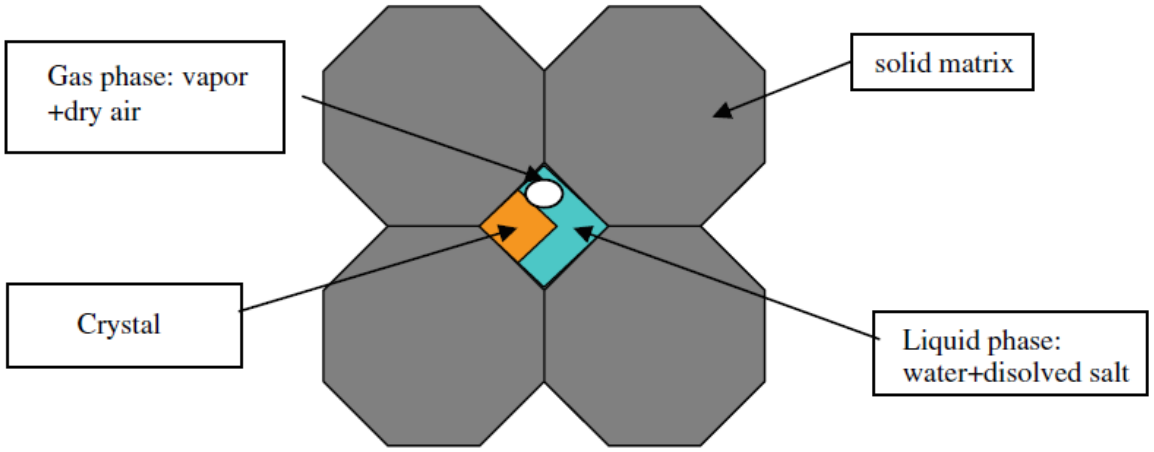

Fig. 2-11 Schematic representation of the medium [22].

The following assumptions are made for the CHM model [10,21–24], which are common to the COLONBO model [15,16,20]:

- The model is homogenized on a macroscopic scale.
- Only one soluble salt (sodium nitrate $NaNO_3$) is considered.
- The poorly soluble salts, particularly barium sulfate ($BaSO_4$), are considered inert. They are considered as part of the solid matrix.

This model considers both mechanics and transport behavior of BWPs during the leaching process: osmosis and permeability are taken into account in addition to the diffusion. Moreover, the parameters governing these transport mechanisms are considered as variables depending on the porosity of the material. The constitutive equations are based on the mass conservation equations (for water, solid matrix, solute, and salt crystals) and the mechanical equilibrium equation. An elasto-viscoplastic model has been developed to describe the creep behavior of the BWP. It should be noted that this model is validated on "Eurobitum" (Belgian BWPs), whose salt composition and bitumen matrix differ from French BWPs.

2.4.3. MELOT2019 model

Based on the work of UPC [10,21–24], G. Melot [1,2] proposed a viscoelastic poromechanical model with novel porosity-dependent evolution laws for mechanical and transport (diffusion and permeation) coefficients. A simple method is proposed to simulate the hydration process of the BWPs, defined as the water-filling process of the initial porosity. This model, called MELOT2019 [1,2], has been calibrated and validated on experimental results (amount of water uptake and released ions) of free leaching tests carried out on simplified French BWPs [13]. However, it should be noted that the MELOT2019 model is not validated on French BWPs swelling data, which was not available at the time. The general framework of the MELOT2019 model is kept in this study and will be recalled in section 4.1.

2.5. Homogenization methods

As shown in 2.3, the porosity of the BWPs could significantly increase (up to about 60%) during the leaching process. Such an increase in porosity has non-negligible effects on material mechanical and transport properties. This porosity-dependency of the material properties can be modeled using homogenization methods. The homogenization schemes proposed in the literature for molecular diffusion (cf. 2.5.1), linear elasticity (cf. 2.5.2), and linear viscoelasticity (cf. 2.5.3) are summarized in this section.

2.5.1. Molecular diffusion problem

In this section, we focus on the estimation of the effective diffusion coefficient within the homogenized material.

The molecular diffusion problem can be defined by the following equations [33]:

$$\mathrm{div}(j) = 0 \quad for\ z \in \Omega \tag{2}$$

$$j = -D(z)\nabla(\rho) \tag{3}$$

$$\rho = H.z \quad when\ z \in \partial\Omega \tag{4}$$

where Ω is a defined area, j is the diffusive flux, ρ is the concentration, D the diffusion coefficient, H the macroscopic concentration gradient.

The local concentration gradient $\nabla(\rho)$ is related to the macroscopic concentration gradient H via a second-order tensor $A(z)$:

$$\nabla(\rho) = A(z).H \tag{5}$$

The local flow can be written as:

$$j = -D(z)\nabla(\rho) = -D(z).A(z).H \tag{6}$$

For a material composed of two homogeneous phases (phase 1 and phase 2), the average of the equation (*6*) on each phase i $(i = 1, 2)$ gives:

$$j_i = -D_i.A_i.H \tag{7}$$

with D_i the diffusion coefficient in the phases i and A_i the average of $A(z)$ over phase i respecting the following relation:

$$\sum_i \varphi_i A_i = 1 \tag{8}$$

where φ_i is the volumetric fraction of the phase i.

The homogenized diffusion coefficient is defined as:

$$D_{hom} = \sum_i \varphi_i A_i D_i \tag{9}$$

In our case, the BWPs can be considered as a material composed of two phases: matrix and pores. It is worth noting that the presence of these pores filled with aqueous solution will accelerate the diffusion of dissolved salt in the material since the diffusion in aqueous solution is much faster than in the bituminous matrix (cf. Table 6).

There are a number of classical homogenization schemes in the literature that can be applied to the diffusion problem. In our case, each scheme leads to an expression of the homogenized diffusion coefficient as a function of the porosity n_l, the diffusion coefficient in the matrix D_M and the diffusion coefficient in aqueous solution-saturated pores D_p. A comparison of these schemes is proposed below.

Maxwell scheme:

Maxwell's homogenization scheme applies to a continuous medium in which there is a "small amount" of unconnected spherical pores sufficiently far from each other [36,37].

$$\frac{D_{Maxwell}}{D_M} = 1 + 3n_l \left(\frac{\frac{D_p}{D_M} + 2}{\frac{D_p}{D_M} - 1} - n_l \right)^{-1} \tag{10}$$

where $D_{Maxwell}$ is the Maxwell homogenized diffusion coefficient.

Since D_p/D_M is greater than 10^4 (cf. Table 6) in considered application, equation (10) can be simplified as:

$$D_{Maxwell} = D_M(1 + \frac{3n_l}{1 - n_l}) \tag{11}$$

Eshelby's problem in linear diffusion:

Instead of solving the molecular diffusion problem defined by equations (2)-(4), Eshelby [33,38] defined an auxiliary problem dealing with an embedded inclusion I in an infinite homogeneous medium ω. Given the assumed infinity of the medium ω, the boundary conditions defined in the original diffusion problem must be replaced by the boundary conditions at infinity. The equations of Eshelby's problem in linear diffusion are therefore:

$$\mathrm{div}(j) = 0 \tag{12}$$

$$j = -D(z)\nabla(\rho) \tag{13}$$

$$\rho \to H.z \quad when\ |z| \to \infty \tag{14}$$

Eshelby showed that for an ellipsoidal inclusion I (in which the diffusion coefficient is equal to D_I) embedded in an infinite medium (in which the diffusion coefficient is equal to of D_0) and subjected to a concentration gradient H, the concentration gradient in the inclusion is constant and equal to (cf. eq 6.50 in [33]):

$$\nabla(\rho) = \left(1 + \left(\frac{D_I}{D_0} - 1\right)P\right)^{-1} H \tag{15}$$

where the second-order tensor $P_{ij} = -\frac{1}{4\pi}\frac{\partial^2}{\partial_{z_i}\partial_{z_j}}\ (\Phi(z))$ with

$$\Phi(z) = \int_I \frac{1}{|z - z'|} d(V_{z'}) \tag{16}$$

In our case where the inclusions are assumed to be spherical pores (of diffusion coefficient D_p), we have $P = \frac{1}{3}\underline{1}$ and the concentration gradient in the pores becomes:

$$\nabla(\rho) = \left(1 + \frac{1}{3}\left(\frac{D_p}{D_0} - 1\right)\right)^{-1} H_0 \tag{17}$$

Let A_p denote the average of the concentration tensor in the pores, equation (9) becomes by using (*8*):

$$D_{hom} = D_0 + \left(D_p - D_0\right) n_l A_p \tag{18}$$

Four schemes based on Eshelby's problem in linear diffusion are studied below.

Dilute scheme:

When the volume fraction of pores is infinitesimal, it is reasonable to neglect the interaction between the pores and to treat the material as a single spherical pore p embedded in an infinite matrix M. In this case, we obtain [33,38]:

$$A_p = \left(1 + \frac{1}{3}\left(\frac{D_p}{D_M} - 1\right)\right)^{-1} \tag{19}$$

$$D_{Dil} = D_M + n_l\left(D_p - D_M\right)\left(1 + \frac{1}{3}\left(\frac{D_p}{D_M} - 1\right)\right)^{-1} \tag{20}$$

where D_{Dil} is diffusion coefficient homogenized using the dilute scheme.

The diluted scheme is valid only for $n_l \ll 1$.

Differential scheme:

Starting from n_l = 0 (matrix without initial porosity), the idea is to introduce the porosity by infinitesimal increments. After each increment j, an estimate of the effective diffusion coefficient D_j^{diff} is re-calculated corresponding to the current value of the porosity n_l. During each step, a volume fraction dv of the homogenized material is removed and replaced by the same pore volume. This process can be described as $d\ (n_l) = (1 - n_l)dv$ in porosity. Replacing D_M by D_j^{diff} and n_l by $dv = \frac{d(n_l)}{1-n_l}$ in equation (20), we obtain:

$$D_{j+1}^{diff} = D_j^{diff} + \frac{d(n_l)}{1 - n_l}\left(D_p - D_j^{diff}\right)\left(1 + \frac{1}{3}\left(\frac{D_p}{D_j^{diff}} - 1\right)\right)^{-1} \tag{21}$$

Replacing D_j^{diff} by D^{diff}, (*21*) can be written as the following equation :

$$\frac{\mathrm{d}\left(D^{diff}\right)}{D_p - D^{diff}}\left(1 + \frac{1}{3}\left(\frac{D_p}{D^{diff}} - 1\right)\right) = \frac{d(n_l)}{1 - n_l} \tag{22}$$

which leads to :

$$\frac{\mathrm{d}\left(D^{diff} - D_p\right)}{D^{diff} - D_p} - \frac{1}{3}\frac{\mathrm{d}(D^{diff})}{D^{diff}} = \frac{d(1 - n_l)}{1 - n_l} \tag{23}$$

By integrating equation (23) with $D^{diff} = D_M$ for $n_l = 0$, we have:

$$\frac{\left(D_p - D^{diff}\right)^3}{D^{diff}} = (1 - n_l)^3 \frac{\left(D_p - D_M\right)^3}{D_M} \tag{24}$$

In our case where $D_M/D_p \ll 1$ and $D^{diff}/D_p \ll 1$, we have:

$$D^{diff} = (1 - n_l)^{-3} D_M \tag{25}$$

The Differential scheme is a way to model the interaction between the inclusions. Also based on Eshelby's problem in linear diffusion, the Mori-Tanaka and Self-Consistent schemes take this interaction into account differently.

For an Eshelby-like morphology (ellipsoidal inclusions embedded in an infinite reference medium of diffusion coefficient D_0), one way to capture the interaction between the inclusions is to change the uniform concentration gradient to infinity: replace the concentration gradient H by H_0 and define H_0 appropriately to satisfy expression (8).

By assuming spherical pores, the average concentration tensor in phase i is [33,38]:

$$A_i = \frac{\left(1 + \frac{1}{3}\left(\frac{D_i}{D_0} - 1\right)\right)^{-1}}{\sum_i \varphi_i \left(1 + \frac{1}{3}\left(\frac{D_i}{D_0} - 1\right)\right)^{-1}} \qquad for\ i = M, p \tag{26}$$

By substituting (26) into (9), the homogenized diffusion coefficient D_{hom} is:

$$D_{hom} = n_l D_p A_p + (1 - n_l) D_M A_M = \frac{D_p D_M + 2D_0\left(n_l D_p + (1 - n_l) D_M\right)}{2D_0 + n_l D_M + (1 - n_l) D_p} \tag{27}$$

Depending on the choice of the reference medium and D_0 in equation (27), two different homogenization schemes can be distinguished.

Mori-Tanaka scheme:

For the Mori-Tanaka scheme, the matrix is chosen as the reference medium:

$$D_0 = D_M, \qquad D_{hom} = D_{MT}$$

where D_{MT} is the diffusion coefficient homogenized using the Mori-Tanaka scheme.

$$D_{MT} = D_M \frac{(1+2n_l)D_p + 2(1-n_l)D_M}{(2+n_l)D_M + (1-n_l)D_p} \tag{28}$$

In our case where $D_M/D_p \ll 1$, we have

$$D_{MT} = D_M \frac{1+2n_l}{1-n_l} \tag{29}$$

Self-Consistent scheme:

For the Self-Consistent scheme, the homogenized material is chosen as the reference medium:

$$D_0 = D_{hom} = D_{SC}$$

where D_{SC} is the diffusion coefficient homogenized using the Self-Consistent scheme.

$$D_{SC} = \frac{D_p D_M + 2D_{SC}(n_l D_p + (1-n_l)D_M)}{2D_{SC} + n_l D_s + (1-n_l)D_p} \tag{30}$$

D_{SC} is given implicitly.

In our case where $D_M/D_p \ll 1$, we have

$$D_{SC} = \frac{D_M}{1-3n_l} \tag{31}$$

Table 9 summarizes the simplified homogenization schemes by assuming spherical pores embedded in the matrix and $D_M/D_p \ll 1$.

Table 9 Simplified homogenization schemes by assuming spherical pores embedded in the matrix and $D_M/D_p \ll 1$.

Homogenization scheme	Simplified homogenized diffusion coefficient
Maxwell scheme	$D_{Maxwell} = D_M(1 + \frac{3n_l}{1-n_l})$
Dilute scheme	$D_{Dil} = D_M + n_l(D_p - D_M)\left(1 + \frac{1}{3}\left(\frac{D_p}{D_M} - 1\right)\right)^{-1}$
Differential scheme	$D_{diff} = (1-n_l)^{-3} D_M$
Mori-Tanaka scheme	$D_{MT} = D_M(1 + \frac{3n_l}{1-n_l})$
Self-Consistent scheme	$D_{SC} = \frac{D_M}{1-3n_l}$

It is worth noting that the Maxwell scheme and the Mori-Tanaka scheme have the same expressions after simplification. In our application, the BWP is chosen as the matrix.

In order to choose a homogenization scheme suitable for French BWPs, the effective diffusion coefficients of HTO in French BWPs at different porosity reported in [16] are used (cf. Table 7). Fig. 2-12 illustrates a comparison of different simplified homogenization schemes in Table 9 applied to the case of diffusion of HTO in BWPs. First, we can quickly notice that the Self-Consistent scheme and the Dilute scheme cannot well reproduce the experimental data. Secondly, the Mori-Tanaka/Maxwell scheme reproduces better the first three experimental points (until a porosity of about 45%), while the sharp increase at the fourth point is less well captured. As a reminder, the porosity of the French BWPs is initially about 7% and may increase up to ~65% during the leaching process. The Mori-Tanaka/Maxwell scheme is finally selected and used in 4.2 because it represents better the experimental data for small porosities and allows to better model the evolution of the diffusion coefficients during the first parts of the leaching process. This choice is made with limited experimental points and needs to be consolidated with more experimental data.

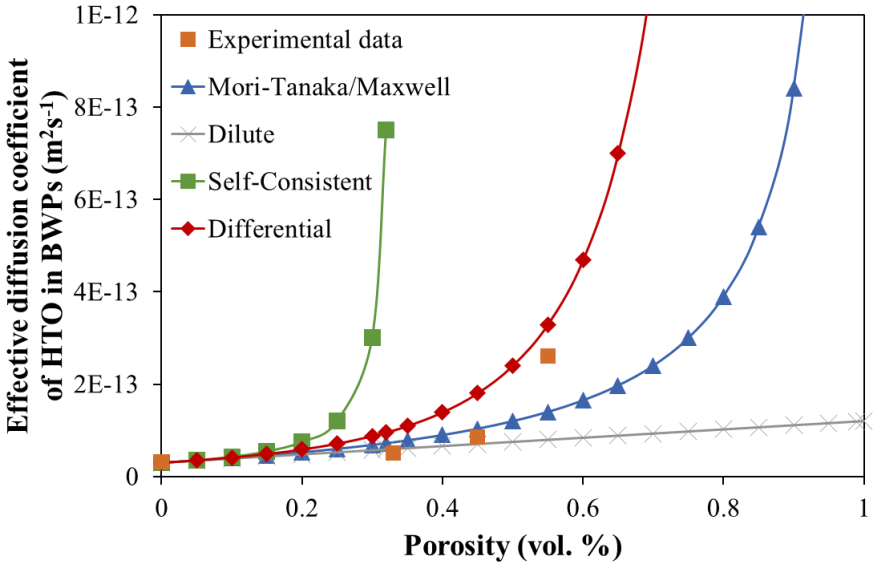

Fig. 2-12 Application of different simplified homogenization schemes in Table 9 to estimate the effective diffusion coefficient of HTO in BWPs. The experimental points are from [16] *(cf. Table 7).*

2.5.2. Linear elasticity

The linear elasticity problem can be defined by the following equations [33,38]:

$$\mathrm{div}(\sigma) = 0 \quad for\ z \in \Omega \tag{32}$$

$$\sigma = C(z) : \varepsilon \quad for\ z \in \Omega \tag{33}$$

$$\sigma(z) \cdot n(z) = \Sigma \cdot n(z) \quad when\ z \in \partial\Omega \tag{34}$$

where σ is the microscopic Cauchy stress tensor, ε is the strain tensor, Σ is the macroscopic Cauchy stress tensor, C is the stiffness tensor, $n(z)$ is the outward unit normal to the boundary at point z.

We can note the similarity between the mathematical equations (32)-(34) and (2)-(4):

$$\sigma \leftrightarrow j$$

$$\varepsilon \leftrightarrow \nabla(\rho)$$

Hooke's law ↔ Fick's law

The homogenization methods developed based on Eshelby's problem in linear diffusion can therefore be applied to the linear elasticity problem [33,38]. K_s and G_s means respectively the bulk and shear modulus of the solid BWP matrix. The expressions of the homogenized bulk $K_{hom}$and shear modulus G_{hom}using four homogenization schemes are summarized below.

Dilute scheme:

$$K_{hom} = K_{Dil} = K_s\left(1 - n_l\left(1 + \frac{3K_s}{4G_s}\right)\right) \tag{35}$$

$$G_{hom} = G_{Dil} = G_s\left(1 - 5n_l\frac{3K_s + 4G_s}{9K_s + 8G_s}\right) \tag{36}$$

Differential scheme:

For the differential scheme, the expressions of the homogenized modulus depend on the Poisson ratio of the solid matrix ν_s. We have to solve the following systems (with $G_{hom} = G_{diff}$ and $K_{hom} = K_{diff}$):

If $\nu_s > 0.2$,

$$\frac{(1 + 4G_s/3K_s)\left(G_{diff}/G_s\right)^3}{2 - (1 - 4G_s/3K_s)\left(G_{diff}/G_s\right)^{3/5}} = (1 - n_l)^6 \tag{37}$$

$$G_{diff} = G_s\frac{\left(1 - 4G_{diff}/3K_{diff}\right)^{5/3}}{(1 - 4G_s/3K_s)^{5/3}} \tag{38}$$

If $\nu_s < 0.2$,

$$\frac{(1 + 4G_s/3K_s)\left(G_{diff}/G_s\right)^3}{2 + (4G_s/3K_s - 1)\left(G_{diff}/G_s\right)^{3/5}} = (1 - n_l)^6 \tag{39}$$

$$G_{diff} = G_s\frac{\left(4G_{diff}/3K_{diff} - 1\right)^{5/3}}{(4G_s/3K_s - 1)^{5/3}} \tag{40}$$

Mori-Tanaka scheme:

$$K_{hom} = K_{MT} = K_s\frac{4(1 - n_l)G_s}{3n_lK_s + 4G_s} \tag{41}$$

$$G_{hom} = G_{MT} = G_s\frac{(1 - n_l)(9K_s + 8G_s)}{9K_s(1 + 2n_l/3) + 8G_s(1 + 3n_l/2)} \tag{42}$$

Self-consistent scheme:

$$K_{hom} = K_{SC} = (1 - n_l)\frac{K_s}{1 + \alpha_{SC}(K_s - K_{SC})/K_{SC}} \tag{43}$$

$$G_{hom} = G_{SC} = (1 - n_l)\frac{G_s}{1 + \beta_{SC}(G_s - G_{SC})/G_{SC}} \quad (44)$$

with

$$\alpha_{SC} = \frac{3K_{SC}}{3K_{SC} + 4G_{SC}}$$

$$\beta_{SC} = \frac{6(K_{SC} + 2G_{SC})}{5(3K_{SC} + 4G_{SC})}$$

Note that in the general cases, equations (43) and (44) are coupled because α_{SC} and β_{SC} both depend on K_{SC} and G_{SC}.

It should be noted that no available experimental data on the mechanical properties of French BWPs with different porosity can be used to determine the homogenization scheme for the mechanical parameters. As a reminder, the Dilute scheme (cf. (35)-(36)) applies only when the porosity is infinitesimal, the Differential scheme (cf. (37)-(40)) and the Self-consistent scheme (cf. (43)-(44)) requires to solve a non-linear system. Therefore, the Mori-Tanaka scheme has been selected and used in 4.3.4 as the homogenization scheme for the mechanical parameters. This choice remains questionable and needs to be consolidated with experimental data.

2.5.3. Linear viscoelasticity

Various investigations of the homogenization of linear viscoelasticity based on Eshelby's problem were reported in the literature [39–42]. The idea is to write the linear viscoelasticity equations in a similar form as in elasticity by using the Laplace transform, thus allowing the use of the existing results established for the linear elasticity problem (cf. 2.5.2).

In a differential form, the hydrostatic and deviatoric parts of the linear viscoelastic constitutive equations of the phase r can be written generally as:

$$R_r(d/dt).\sigma_{kk}^r(t) = S_r(d/dt).\varepsilon_{kk}^r(t) \quad (45)$$

$$P_r(d/dt).s_{ij}^r(t) = Q_r(d/dt).e_{ij}^r(t) \quad (46)$$

where σ_{ij}^r is the coefficient of the stress tensor, s_{ij}^r is the coefficient of the deviatoric stress tensor ($s_{ij}^r = \sigma_{ij}^r - \frac{1}{3}tr(\sigma^r)\delta_{ij}$), ε_{ij}^r is the strain tensor, e_{ij}^r the coefficients of the deviatoric strain tensor ($e_{ij} = \varepsilon_{ij} - \frac{1}{3}tr(\varepsilon)\delta_{ij}$) for the phase r. P_r, Q_r, R_r and S_r are polynomial differential operators with constant coefficients. Their specific forms are dependent upon the viscoelastic models adopted for each phase, and d/dt represents the time differential.

The Laplace transform of a time function $f(t)$ is defined as:

$$\hat{f}(s) = \int_0^{+\infty} f(t)e^{-st}dt \quad (47)$$

By using Laplace transform, equations (*45*)-(*46*) can be written in a similar form as in elasticity in the "transformed domain (TD)" [39–42]:

$$\hat{\sigma}_{kk}^r(s) = 3K_r^{TD}(s)\hat{\varepsilon}_{kk}^r(s) \quad (48)$$

$$\hat{s}_{ij}^{r}(s) = 2G_r^{TD}(s)\hat{e}_{ij}^{r}(s) \tag{49}$$

where $\hat{\sigma}_{kk}^{r}$, $\hat{\varepsilon}_{kk}^{r}$, $\hat{s}_{ij}^{r}$ and $\hat{e}_{ij}^{r}$ are the Laplace transform of their counterparts σ_{kk}^{r}, ε_{kk}^{r}, s_{ij}^{r} and e_{ij}^{r}. $K_r^{TD}(s)$ and $G_r^{TD}(s)$ are the bulk and shear moduli of the phase r in the "transformed domain (TD)", defined as:

$$K_r^{TD}(s) = \frac{S_r(s)}{3R_r(s)} \tag{50}$$

$$G_r^{TD}(s) = \frac{Q_r(s)}{2P_r(s)} \tag{51}$$

The similarity between (*48*)-(*49*) and the elastic stress-strain relations makes it possible to adopt the correspondence principle, with the moduli in the transformed domain replacing their elastic counterparts. The effective moduli of a linear viscoelastic composite in the transformed domain $K^{TD}(s)$ and $G^{TD}(s)$ can be established by using the homogenization methods initially developed for the linear elasticity problem (presented in 2.5.2). Finally, the inverse Laplace transform is applied to $K^{TD}(s)$ and $G^{TD}(s)$ to obtain the effective moduli in the time domain.

The homogenization methods for linear viscoelasticity presented in this section will be applied to BWPs, whose mechanical behavior is modeled by the Maxwell viscoelastic model. More details can be found in 4.3.4 and Appendix B.

CHAPTER 3

EXPERIMENTAL RESULTS

This chapter presents the experimental results studied during this thesis. The experiments were conducted at CEA Marcoule, France. The experimental data is provided within a joint R&D program (Babylone program [3] led by Andra and the three nuclear licensees, CEA, EDF and Orano).

The experimental procedures are described in 3.1. The experimental results of leaching tests conducted on simplified and industrial BWPs under free leaching conditions are presented in 3.2. The experimental results of leaching tests under constant counter-pressure conducted on simplified BWPs are illustrated in 3.3.

3.1. Experimental procedures

The experimental procedures developed at CEA Marcoule for leaching tests under free leaching conditions and constant counter-pressure are described in 3.1.1 and 3.1.2, respectively. The procedures for the ESEM characterization are presented in 3.1.3.

3.1.1. Free leaching tests

Before leaching experiments, samples were cast in a 125 mL polypropylene flask by heating 10 g of BWPs at 50°C for 30 minutes. Leaching experiments were carried out at 22 ± 2°C and started after filling these flasks with 40 g of deionized water. The corresponding initial liquid/surface ratio was 2.12 cm^{-1}. Leachates were renewed regularly with deionized water. During these renewals, BWPs water uptake was first measured using gravimetry and expressed in the following as the water uptake amount divided by the area of the initial leaching surface. Then, the volume of the remaining headspace between the BWP and a calibrated needle set to the plug of the polyethylene flask was measured. The swelling of the BWP was calculated by dividing the leached BWP volume at any given time by the initial BWP volume. Thirdly, the chemical composition of leachates collected at each renewal was measured using ionic chromatography (930 Compact IC Flex, Metrohm). Results were expressed as the cumulative amount of leached salts normalized by the salts contained in the initial BWP. In order to quantify experimental uncertainties, free leaching experiments were repeated independently five times for each BWP composition. For each experiment, swelling measurements were repeated three times to assess uncertainties. Leachate composition analyses were carried out on only two samples among the five repeated samples.

3.1.2. Leaching tests under constant counter-pressure

Fig. 3-1 shows a schematic representation of the experimental setup for leaching tests of BWPs under confined conditions. The cell is made up of three parts:

- a base, with a circuit to bring the leaching solution into contact with the BWPs.
- a liner, allowing to constrain the BWPs' lateral deformations.
- a piston, which also has a circuit to bring the leaching solution into contact with the BWPs.

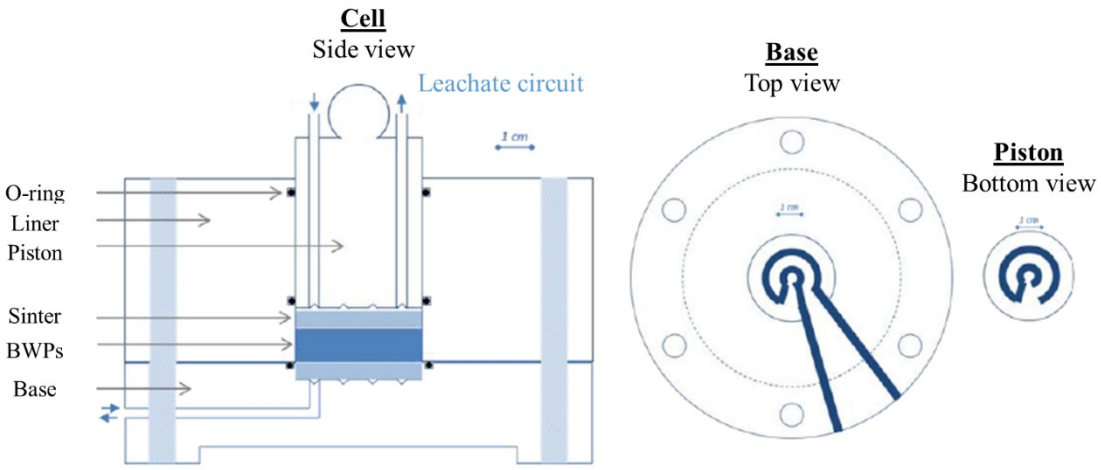

Fig. 3-1 Schematic representation of the experimental setup for leaching tests of BWPs under confined conditions.

Under these conditions, the leaching occurs from both the bottom and top surfaces of the sample. The sample is contained in the leaching chamber by the installation of O-rings and an additional membrane with a cutoff of less than one micrometer between the BWPs and the sinter. Such a design can ensure that the BWPs are maintained in the leaching chamber during experiments.

Before leaching tests under confined conditions, the sample is first placed in the leaching chamber. A consolidation stage in the oedometer, which consists in applying loading and unloading cycles of counter-pressure to the sample in successive steps, is performed. Fig. 3-2 shows a photo of the oedometer benches. The values of counter-pressure applied during these loading/unloading protocols are imposed by the design of the oedometer bench and are ranging from 176 kPa to 2.8 MPa. Different values of counter-pressure were used for consolidation to obtain BWPs with different initial porosities. An example of the deformation curve recorded during the consolidation stage is shown in Fig. 3-14.

Fig. 3-2 Photo of oedometer benches - CEA.

Leaching tests under constant counter-pressure are then conducted on the consolidated BWPs. Fig. 3-3 shows a photo of the experimental setup.

Fig. 3-3 Photo of leaching tests under constant counter-pressure - CEA.

3.1.3. ESEM characterization

Environmental Scanning Electron Microscopy (ESEM) was used to characterize BWPs' microstructure and check salt dispersion in the bitumen matrix before and after leaching. To obtain small pieces of material suitable for ESEM analyses, BWP samples were frozen at −18 °C for 24 h and then cut using a sharp cutting tool, yielding a fresh fracture. ESEM analyses were performed using a FEI Quanta 200 ESEM FEG coupled with a Bruker SDD 5010 X-ray energy dispersive spectrometer, using a 15 kV acceleration voltage and a gas pressure of 70 to 100 Pa. During the observation time, the sample temperature was held at 0.2 °C with a Peltier cooling stage.

3.2. Leaching behavior of simplified and industrial BWPs under free leaching conditions

BWPs of different compositions have been tested under free leaching conditions. The free leaching experiments conducted on mono-salt BWPs containing respectively $NaNO_3$, Na_2SO_4 and $BaSO_4$ are presented in 3.2.1, 3.2.2 and 3.2.3. The free leaching results of bi-salt BWPs (containing both $NaNO_3$ and $BaSO_4$) are shown in 3.2.4 and are compared with the leaching results obtained on mono-salt BWPs in 3.2.5. The microstructures of these simplified BWPs before and after leaching are discussed in 3.2.6. The free leaching results conducted on the industrial BWPs (STE3, STEL) are presented in 3.2.7.

3.2.1. Mono-salt $NaNO_3$ BWPs

In Fig. 3-4, the evolution of swelling, water uptake, and released salt fraction is presented as a function of time for BWPs containing an increasing amount of sodium nitrate ranging from 5 up to 30 wt. % (M5_NaNO3, M10_NaNO3, M20_NaNO3, and M30_NaNO3). As expected [13], the results reveal that the swelling (Fig. 3-4(a)) and water uptake (Fig. 3-4(b)) increase in general as the soluble salt mass fraction increases.

However, from these results, it appears that M30_NaNO3 would swell more than M20_NaNO3 with an approximately equivalent amount of water uptake. Such a result, which seems quite surprising at first glance, could arise from an experimental bias. Indeed, in the case of M30_NaNO3, the water uptake might be underestimated because the water located in the large local porosity caused by swelling near the leaching surface might not be easily captured by the gravimetry method. In the following, the numerical model is thus calibrated on M20_NaNO3 and then tested on M5_NaNO3, M10_NaNO3, and M30_NaNO3.

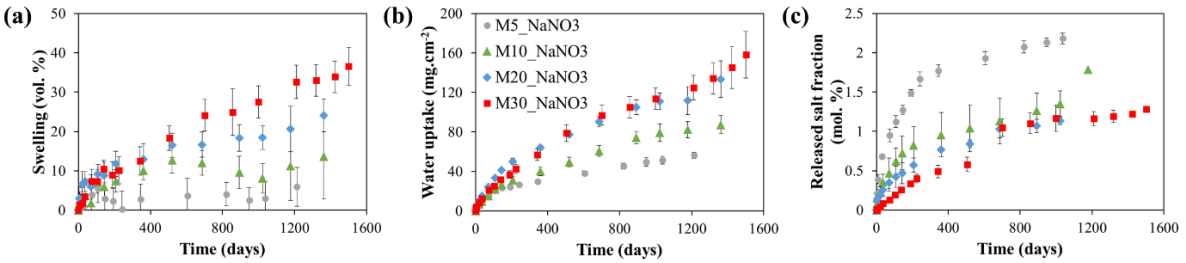

Fig. 3-4 Experimental measurements of (a) swelling (vol. %); (b) water uptake (mg/cm^2); (c) released salt fraction (mol. %) during free leaching tests on mono-salt BWPs containing 5 wt.%, 10 wt.%, 20 wt.% and 30 wt.%. of $NaNO_3$.

3.2.2. Mono-salt Na_2SO_4 BWPs

In Fig. 3-5, the evolution of water uptake is presented as a function of time for BWPs containing an increasing amount of sodium sulfate Na_2SO_4 ranging from 10 up to 40 wt. % (M10_Na2NO4, M25_Na2NO4 and M40_Na2SO4) [13]. Similarly to mono-salt $NaNO_3$ BWPs in 3.2.1, the water uptake increases as the soluble salt mass fraction increases.

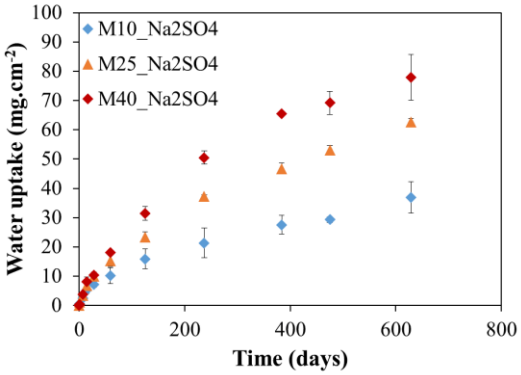

Fig. 3-5 Experimental measurements of water uptake (mg/cm^2) during free leaching tests on mono-salt BWPs containing 10wt.%, 25 wt.% and 40 wt.%. of Na_2SO_4.

3.2.3. Mono-salt $BaSO_4$ BWPs

In Fig. 3-6, the evolution of the swelling and the water uptake is presented as a function of time for BWPs containing an increasing amount of barium sulfate (M5_BaSO4, M10_ BaSO4, M20_ BaSO4, M30_BaSO4 and M40_ BaSO4).

Despite the absence of soluble salt in the sample that would be responsible for any intense osmotic phenomenon, water uptake is observed as a function of time for all samples. No correlation between the water uptake rate and the salt content can be observed in these results for a barium sulfate content lower than 30 wt. %. A slight increase in the water uptake rate can be suspected for simplified BWPs containing 40 wt. % $BaSO_4$ based on these results. After 1200 days, the water uptake tends to stabilize for all samples close to a value of about 30 mg/cm². This value is consistent with the water needed to fill the initial porosity of the samples by considering a value of 7 ± 2 vol. %. The filling of the initial unsaturated pore volume could thus explain the water uptake of these BWPs incorporating $BaSO_4$. This

is moreover consistent with a previous study evidencing the water ingress through similar samples by using ^{1}H-NMR [18], especially for samples containing only barium sulfate.

If only the filling of the initial porosity occurs, no swelling should result from this water uptake. It seems to be actually the case during the first 700 days of leaching. However, despite measurement uncertainties, a slight swelling from 0 up to about 8 vol. % is observed between 750 days and 1250 days. Such an increase is followed by a slight decrease in the swelling of samples down to a value of about 4 vol. % at 1800 days. At present, no plausible explanation can be given for such a swelling behavior.

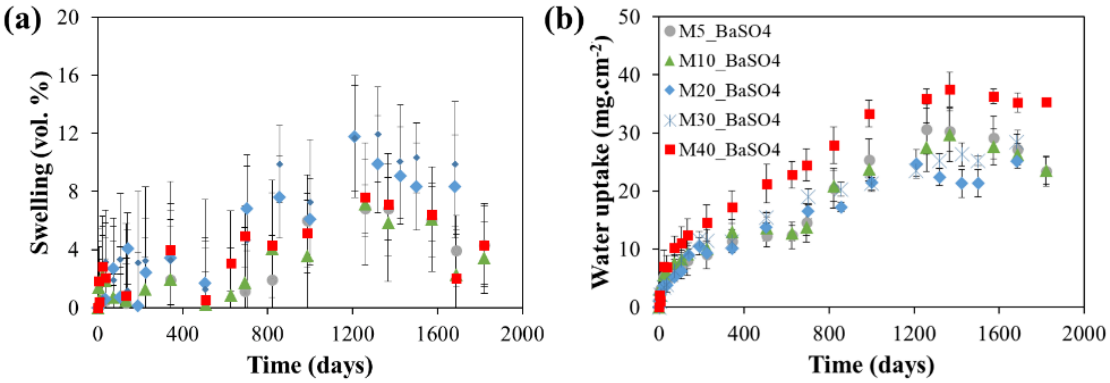

Fig. 3-6 Experimental measurements of (a) swelling (vol. %); (b) water uptake (mg/cm^2) during free leaching tests of mono-salt BWPs containing 5 wt.%, 10 wt.%, 20 wt.%, 30 wt.% and 40 wt.%. of $BaSO_4$.

3.2.4. Bi-salt BWPs incorporating both $NaNO_3$ and $BaSO_4$

In Fig. 3-7, the evolution of swelling, water uptake, and released salt fraction are presented as a function of time for bi-salt BWPs incorporating both $NaNO_3$ and $BaSO_4$ (M5_NaNO3_M35_BaSO4, M10_NaNO3_M30_BaSO4, and M20_NaNO3_M20_BaSO4).

Firstly, a difference in leaching kinetics can be observed for these three bi-salt BWPs. While the growth rate of both swelling (cf. Fig. 3-7(a)) and water uptake (cf. Fig. 3-7(b)) slows down at around 500 days for M5_NaNO3_M35_BaSO4 and M10_NaNO3_M30_BaSO4, both quantities continue to increase for M20_NaNO3_M20_BaSO4. The growth rate of released salt fraction (cf. Fig. 3-7(c)) slowed down at around 150 days for M5_NaNO3_M35_BaSO4 and M10_NaNO3_M30_BaSO4 while it continues to increase for M20_NaNO3_M20_BaSO4.

Moreover, the water uptake and swelling of the bi-salt BWP containing the most $BaSO_4$ (M5_NaNO3_M35_BaSO4) tend to stabilize after 1000 days. Considering that the osmosis-driven mechanism is the primary swelling mechanism, a stabilization phase indicates a significant reduction in the intensity of the osmosis phenomenon and an approach to the end of the leaching process. As no significant difference in leaching kinetics has been observed for BWPs containing different concentrations of $NaNO_3$ (cf. 3.2.1), the presence of poorly soluble salts $BaSO_4$ in the BWP matrix could be one reason for the different leaching kinetics observed for these bi-salt BWPs.

A stabilized swelling of about 150% has been recorded for M5_NaNO3_M35_BaSO4 at about 1330 days. As a reminder, the poorly soluble salt $BaSO_4$ does not *a priori* contribute to the osmosis-driven swelling of the BWPs. Taking into account the swelling of about 10 % observed on mono-salt $BaSO_4$ BWPs (cf. section 3.2.2), only 5 wt.% of $NaNO_3$ would be responsible for about 140% of the swelling. It is worth noting that the released salt fraction tends to stabilize at about 99 mol. % after 150 days for

M5_NaNO3_M35_BaSO4, which is much faster than water uptake and swelling. The reason for this difference in kinetics remains unknown and needs further investigation.

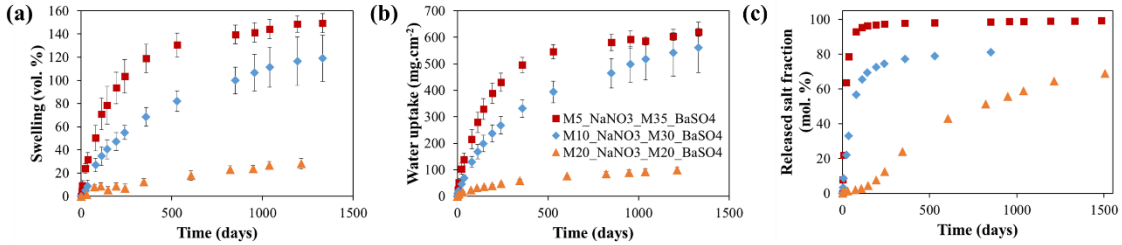

Fig. 3-7 Experimental measurements of (a) swelling (vol. %); (b) water uptake (mg/cm^2); (c) released salt fraction (mol. %) during free leaching tests on bi-salt BWPs incorporating both $NaNO_3$ and $BaSO_4$.

3.2.5. Comparison of free leaching test results between mono-salt and bi-salt BWPs

Fig. 3-8 illustrates a comparison of experimental results between mono-salt BWPs and bi-salt M5_NaNO3_M35_BaSO4 BWP. The effect of $BaSO_4$ presence is highlighted by comparing two BWPs containing the same amount of sodium nitrates, such as M5_NaNO3 and M5_NaNO3_M35_BaSO4. In a first approach, one could expect that $BaSO_4$ plays no significant role in the leaching behavior, given its poor aqueous solubility and thus its poor ability to induce osmotic phenomenon, as illustrated by previously discussed results on M40_BaSO4. However, during the leaching of the bi-salt M5_NaNO3_M35_BaSO4 BWP, water uptake, released ions, and swelling were significantly faster than those observed for both mono-salt BWPs. While all experimental measurements on M5_NaNO3 increase slowly over the leaching time, the bi-salt BWP shows different leaching kinetics. After the first stage of rapid growth, the leaching kinetics of bi-salt BWP significantly slows down and approaches a stabilization phase. At about 1200 leaching days, M5_NaNO3_M35_BaSO4 absorbed 10 times more water, leached 50 times more ions, and swelled 25 times more than M5_NaNO3, which contains the same amount of soluble salts. We can also note that the leaching kinetics during the first leaching stage of bi-salt BWP is much faster than M5_NaNO3. This observation indicates that the presence of the poorly soluble salt $BaSO_4$ accelerates the leaching process and the approach toward the stabilization phase. This observation is consistent with the existing nuclear magnetic resonance (NMR) results in the literature [18,19], which suggests that insoluble salts dispersed in the bitumen matrix enhance the water progression in the material and thereby increase its water uptake rate and the resulting swelling.

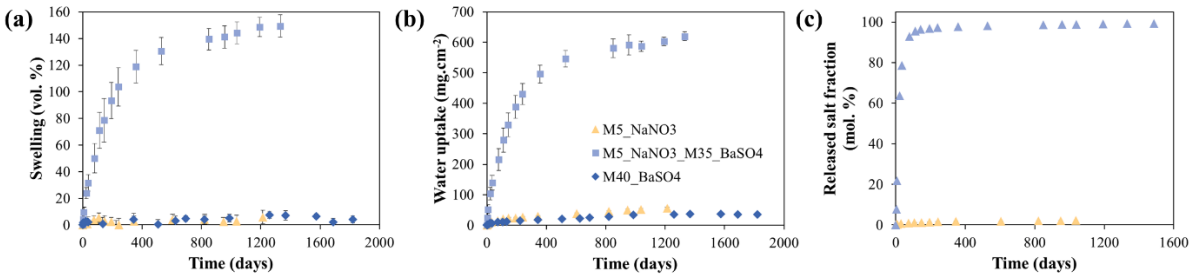

Fig. 3-8 Comparison of (a) swelling (vol. %); (b) water uptake (mg/cm^2); (c) released salt fraction (mol. %) between mono-salt M5_NaNO3 BWP, M40_BaSO4 BWP and bi-salt M5_NaNO3_M35_BaSO4 BWP.

3.2.6. Microstructure of simplified BWPs before and after leaching

ESEM observations of M30_NaNO3, M40_BaSO4 and M5_NaNO3_M35_BaSO4 BWP samples before and after leaching are presented respectively in Fig. 3-9, Fig. 3-10 and Fig. 3-11. For all samples, BWPs' microstructure before leaching can be described as a dispersion of inorganic salts in a bitumen matrix, evidenced on ESEM images by light gray and dark gray respectively. In these images, the presence of pores within the microstructure can be observed. This is consistent with the presence of an initial porous volume of about 7 ± 2 vol. % as evidenced by comparing BWPs' apparent and intrinsic densities (cf. Table 2). The main microstructural difference of the mono-salt simplified BWPs lies in salt crystal sizes. For M30_NaNO3 (Fig. 3-9(a)), the estimated size of sodium nitrate salt crystals is a few tens of micrometers. On the other hand, the size of barium sulfate crystals (Fig. 3-10(a)) is smaller than half a micrometer. Such a difference results in a completely different dispersion of both salts within bitumen since barium sulfate salt is widely dispersed in bitumen due to its tiny crystal size. The microstructure bi-salt BWPs (Fig. 3-11(a)) can be described as a superimposition of both microstructures described previously for single salt BWP.

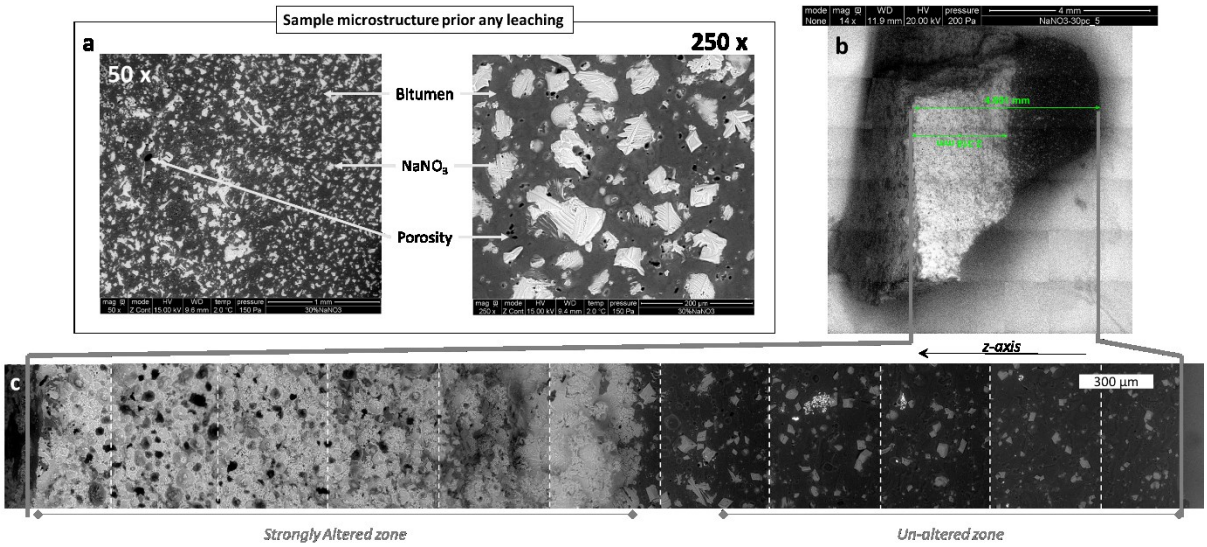

Fig. 3-9 ESEM observation of a BWP containing 30 wt. % $NaNO_3$: (a) Sound before any leaching experiment (50 X and 250 X magnification); (b) Overview of the cross-section of a sample after 1400 days of leaching (14 x magnification); (c) Z profile reconstruction along the leached sample cross section after 1400 days of leaching (200 x magnification).

ESEM observations of a M30_NaNO3 mono-salt BWP sample after 1400 days of leaching are presented in Fig. 3-9 (b-c). After 1400 days of leaching, two main different zones can be distinguished based on ESEM observation: a light gray area on the top of the sample in contact with the leaching solution (left part), and a dark area at the bottom of the sample (right part). In the dark area, the BWP stays in its initial state and remains unaltered by leaching. On the other hand, the BWP in the light area has been strongly altered by leaching. In this zone, pores and bitumen matrix are covered by sodium nitrate crystals, which have reprecipitated from the nearly saturated solution contained in these pores during the ESEM analysis. A transition zone between these two zones can be observed on the z-axis reconstructed profile within which no empty pores are observed. Such a transition zone can be highlighted by plotting the gray shade evolution along the height of the sample(cf. Fig. 5-11(b)). For a M30_NaNO3 mono-salt BWP after 1400 days of leaching, the height of the strongly altered zone has been estimated to be equal to about 2.3 mm (Fig. 3-9(b)). This strongly altered zone within the BWP is characterized by low amounts of soluble sodium nitrate salts and large spherical pores. From a macroscopic point of view, such a microstructure is entirely consistent with the observed swelling of samples.

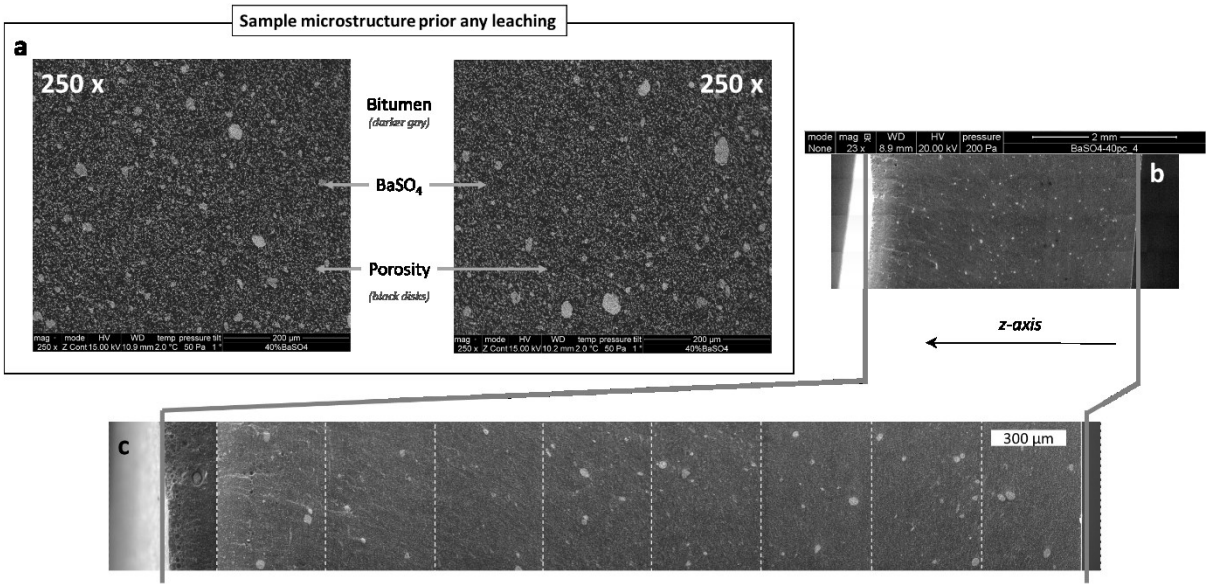

Fig. 3-10 ESEM observation of a BWP sample containing 40 wt. % BaSO4: (a) Sound before any leaching experiment (250 X magnification at two different locations); (b) Overview of the cross-section of a sample after 1400 days of leaching (14 x magnification); (c) Z profile reconstruction along the leached sample cross section after 1400 days of leaching (200 x magnification)

ESEM observations of a M40_BaSO4 BWP sample after 1400 days of leaching are presented in Fig. 3-10 (b-c). As $BaSO_4$ is poorly soluble, there is *a priori* no osmosis phenomenon in mono-salt $BaSO_4$ BWPs. The swelling can hardly be observed using ESEM, despite a suspicion of $BaSO_4$ crystals reorganization within the sample as illustrated by light gray trails. Once again, the mechanisms responsible for these samples' swelling are not yet established.

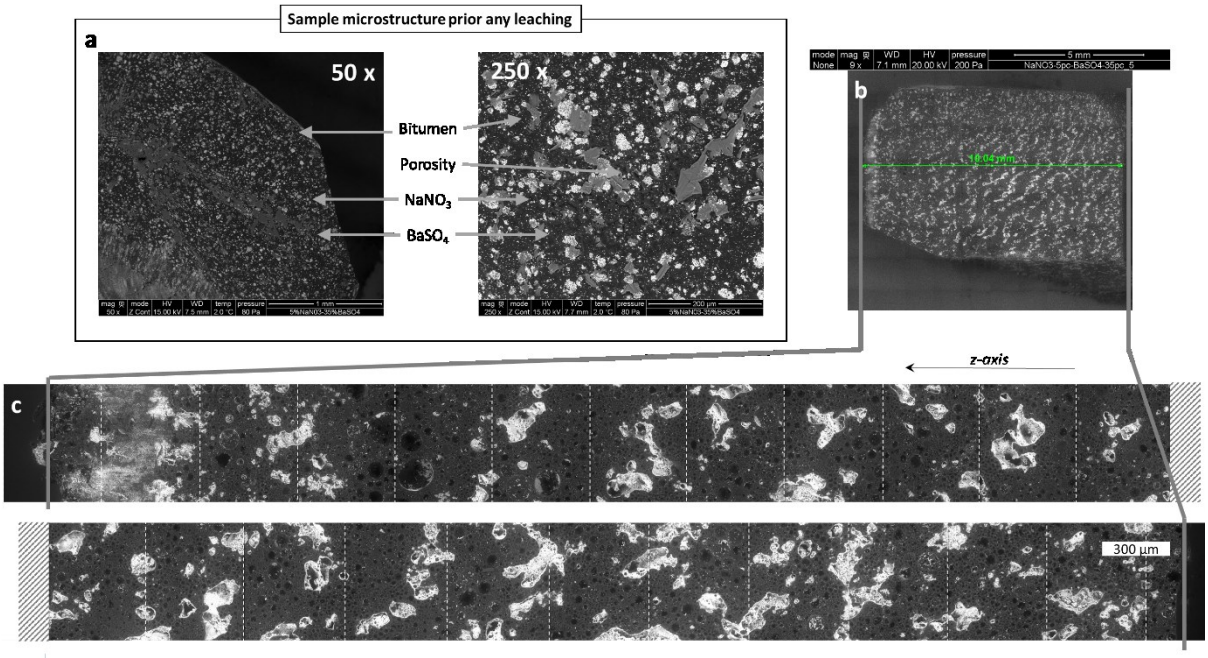

Fig. 3-11 ESEM observation of a BWP sample containing 5 wt. % $NaNO_3$ and 35 wt. % BaSO4: (a) Sound before any leaching experiment (50 x and 250 x magnifications); (b) Overview of the cross-section of a sample after 1000 days of leaching (14 x

magnification); (c) Z profile reconstruction along the leached sample cross section after 1000 days of leaching (200 x magnification)

ESEM observations of a M5_NaNO3_M35_BaSO4 BWP sample after 1000 days of leaching are presented in Fig. 3-11 (b-c). The microstructure of the leached sample was relatively homogeneous over the whole height of the sample, and no separated zones were observed. It is worth noting that the microstructure is drastically different from the one before any leaching (Fig. 3-11 (a)). First, the presence of sodium nitrate crystals has not been evidenced during ESEM analysis, and a high amount of spherical pores can be observed, the same as expected [18]. Secondly, the distribution of barium sulfate is drastically modified compared to the non-leached sample. Indeed, barium sulfate crystals are no longer spread homogeneously and finely over the bitumen matrix. Many barium sulfate aggregates can be observed within the bitumen matrix and even within large non-spherical pores. Finally, it has to be noted that the covering of the sample by sodium nitrate reprecipitation during ESEM analysis is not as significant as in the case of the M30_NaNO3 sample (Fig. 3-9 (b), (c)).

From these microstructural analyses, it can be concluded that the leaching process of this M5_NaNO3_M35_BaSO4 sample was much faster than the one occurring for M30_NaNO3 BWP, which incorporates only soluble sodium nitrate salt, as evidenced by swelling and water uptake measurements (Fig. 3-7). After only about 1000 days, almost all sodium nitrate was leached out, and the leaching front had already crossed the full height of the sample, yielding a fast swelling of the BWP up to its maximum swelling ability. The presence of $BaSO_4$, which could be suggested as being an inert component at first glance, seems to play a critical role in transport kinetics, as already observed in previous studies [18,19]. The restructuration of barium sulfate particles into aggregates needs to be further investigated to identify its trigger and associated phenomena.

3.2.7. Industrial BWPs (STE3, STEL)

The water uptake and the swelling are presented as a function of time for industrial BWPs STE3 and STEL in Fig. 3-12 and Fig. 3-13 respectively. It is worth noting that the leaching kinetics of these two industrial BWPs are quite different from the mono-salt and bi-salt BWPs presented in the previous sections. For STE3, a significant increase in swelling and water uptake rate occurred after 1000 leaching days. No sign of stabilization can be observed until 1650 leaching days.

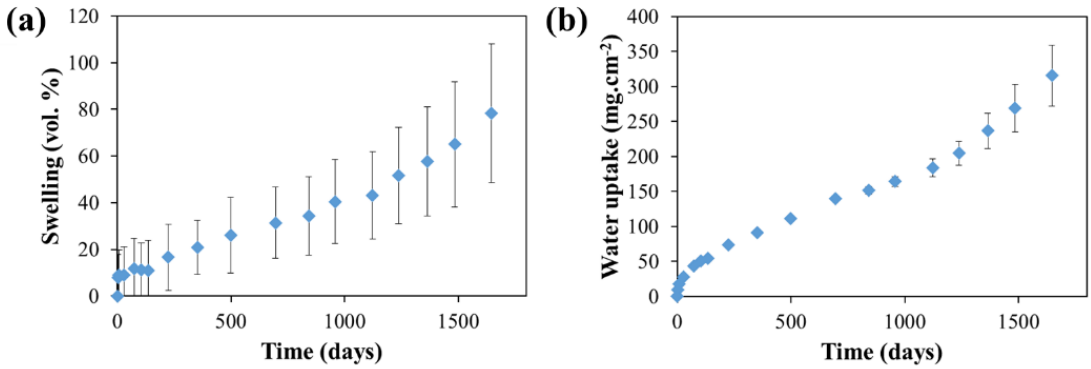

Fig. 3-12 Experimental measurements of (a) swelling (vol. %); (b) water uptake (mg/cm^2) during free leaching tests on industrial BWP STE3.

For STEL, the water uptake and swelling reached values of about 267 vol. % and 1080 mg/cm^2 after about 1500 days of leaching. Despite important experimental values, the swelling and water uptake

rates seem quite stable over leaching time, no sign of stabilization can be observed until 1500 days. Moreover, it should be noted that STEL contains only 4.1 wt.% of soluble salts (cf. Table 1) but swells much more than M5_NaNO3_M35_BaSO4 bi-salt BWPs which contains 5 wt.% of soluble salts (cf. 3.2.4). This suggests that various poorly soluble salts present in the bituminous matrix (cf. Table 1) may also be involved in the leaching process. The mechanisms of these different leaching behaviors of the industrial BWPs remain unknown and need further investigation.

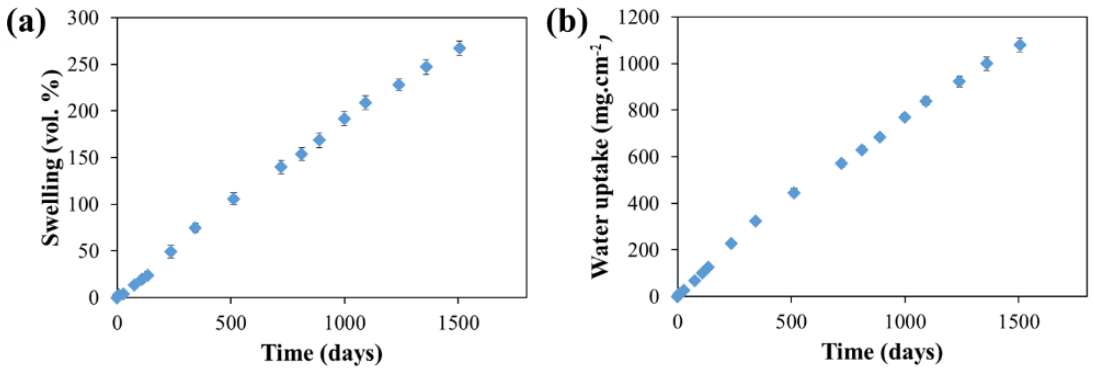

Fig. 3-13 Experimental measurements of (a) swelling (vol. %); (b) water uptake (mg/cm^2) during free leaching tests on industrial BWP STEL.

3.3. Leaching behavior of simplified BWPs under constant counter-pressure

This section presents the experimental results of leaching tests under constant counter-pressure conducted on simplified BWPs. The consolidation curves are first presented in 3.3.1. The leaching results of mono-salt M30_NaNO3 BWPs and bi-salt M10_NaNO_M30_BaSO4 BWPs are illustrated in 3.3.2 and 3.3.3, respectively.

3.3.1. Consolidation

As described in section 3.1.2, BWP samples are consolidated with loading and unloading cycles of counter-pressure ranging between 176 kPa and 2.8 MPa before leaching tests under constant counter-pressure. An example of the strain curve recorded during the consolidation process is shown in Fig. 3-14. After a short sample set-up phase, the applied counter-pressure increased successively to the maximum value (2.8 MPa in the example) and then decreased to 176 KPa. After the first loading/unloading cycle, the applied counter-pressure increased again to the maximum value and decreased to the constant counter-pressure used for the leaching tests (here 176 kPa). The strain curve is repeatable during two cycles of load/unload, which indicates that the initial porosity is almost completely removed. It should be noted that the observed strain is actually the superposition of the removed porosity and elastic deformation of the BWP matrix. By using the values of the stabilized strain during the second loading cycle, the initial porosity within the sample can be estimated as about 7%, which is consistent

with the values reported in [1,2]. Different maximum values of counter-pressure were used for consolidation, which led to BWPs with different initial porosities.

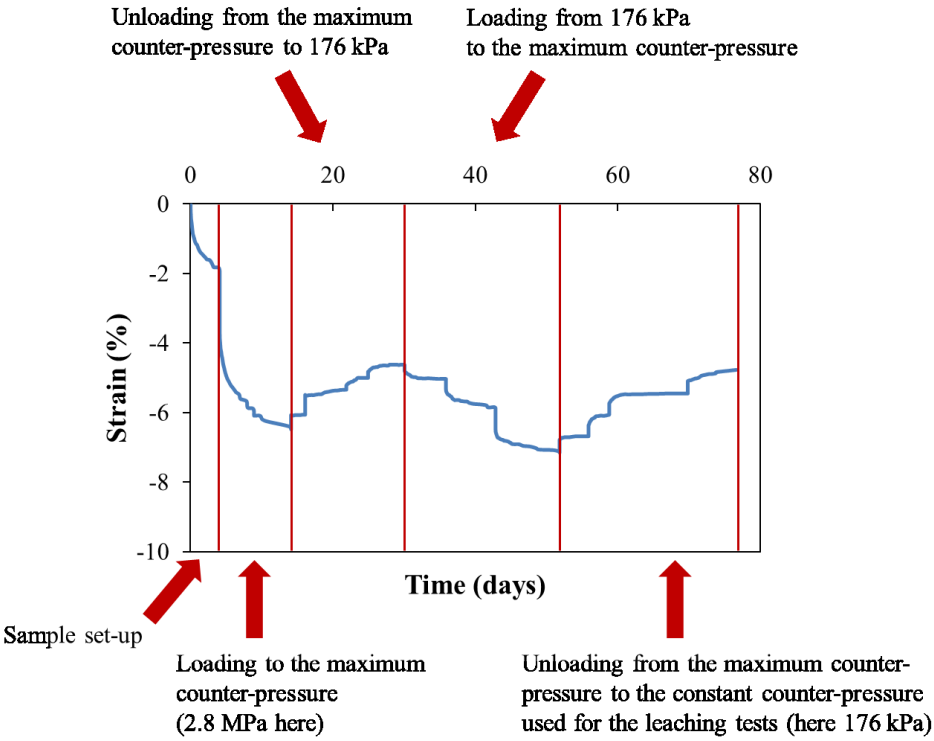

Fig. 3-14 Example of strain curve recorded during the consolidation process.

3.3.2. Mono-salt BWPs M30_NaNO3

In Fig. 3-15, the evolution of swelling is presented as a function of time for BWPs containing 30 wt. % of sodium nitrates (M30_NaNO3) under different constant counter-pressure (176kPa, 1.4 MPa, 2.8 MPa). It should be noted that only one test is performed for each constant counter-pressure. The swelling decreases with increasing counter-pressure.

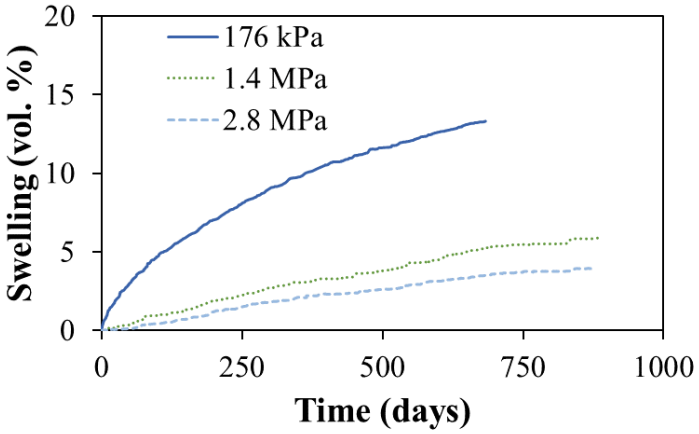

Fig. 3-15 Experimental measurements of swelling) on mono-salt BWPs containing 30 wt.%. of NaNO3 under different constant counter-pressure (176 kPa, 1.4 MPa, 2.8 MPa).

ESEM observations of M30_NaNO3 mono-salt BWP samples leached under 176 kPa and 2.8 MPa are presented in Fig. 3-16 (a) and (b). Two main different zones can be clearly distinguished for M30_NaNO3 leached under 176 kPa counter-pressure (Fig. 3-16(a)): light gray areas on the top and the bottom of the sample in contact with the leaching solution, and a dark area in the middle of the sample. The light gray areas correspond to the zones strongly altered by leaching while the BWP stays in its initial state and remains unaltered by leaching in the dark zone. It is worth noting that the strongly altered zone (gray areas) expands towards the sample center over the entire cross-section. Moreover, this distinction of strongly altered and unaltered zones on M30_NaNO3 under 176 kPa counter-pressure is consistent with previous ESEM observations conducted on M30_NaNO3 under free leaching conditions [43]. This consistency suggests that M30_NaNO3 has a similar leaching behavior under free leaching conditions and 176 kPa counter-pressure.

On the other hand, the M30_NaNO3 BWP leached under 2.8 MPa counter-pressure (Fig. *3-16*(b)) displays a very different leaching behavior. The strongly altered zone (gray areas) and the unaltered zone (dark areas) are mixed. Moreover, the strongly altered zones (gray areas) did not expand toward the sample center over the entire cross-section. It seems that the leaching under 2.8 MPa counter-pressure followed some preferential path within the sample. The reason for this different leaching behavior is still under investigation.

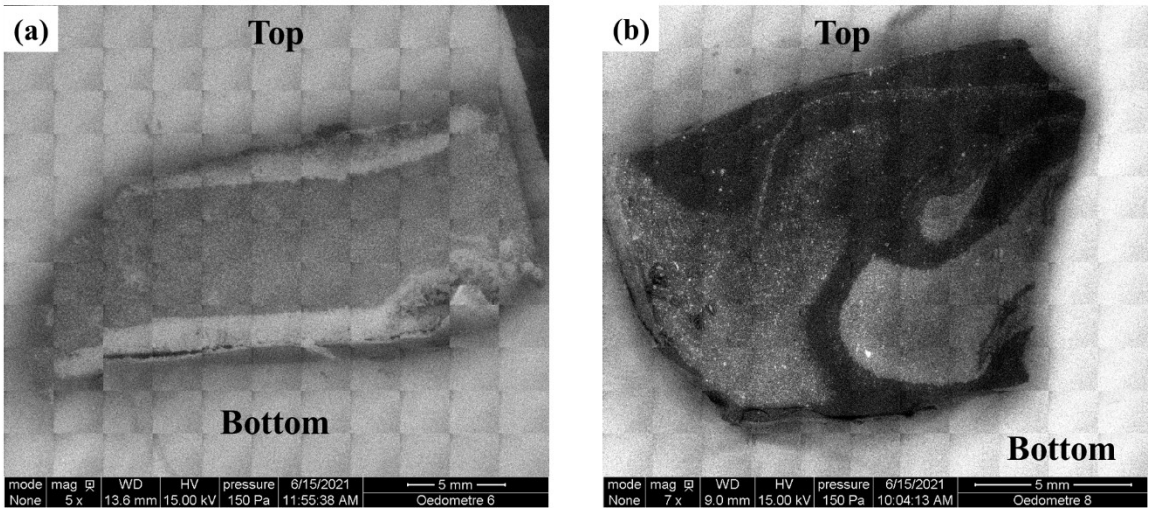

Fig. 3-16 ESEM observation of the cross-sections of BWPs containing 30 wt. % $NaNO_3$ under constant counter-pressure of (a): 176kPa (5 x magnification) after 683 days of leaching; (b) 2.8 MPa (7 x magnification) after 683 days of leaching.

3.3.3. Bi-salt BWPs M10_NaNO3_M30_BaSO4

In Fig. 3-17, the evolution of swelling under 176 kPa counter-pressure is presented as a function of time for BWPs containing 10 wt.% $NaNO_3$ and 30 wt.%. of $BaSO_4$ (M10_NaNO3_M30_BaSO4) consolidated with different levels of stress (therefore with different initial porosities). It seems that the experimental swelling behaviors of these BWPs are quite similar, which suggests that the initial porosity

has no significant effect on the swelling behavior of the consolidated BWPs under constant counter-pressure.

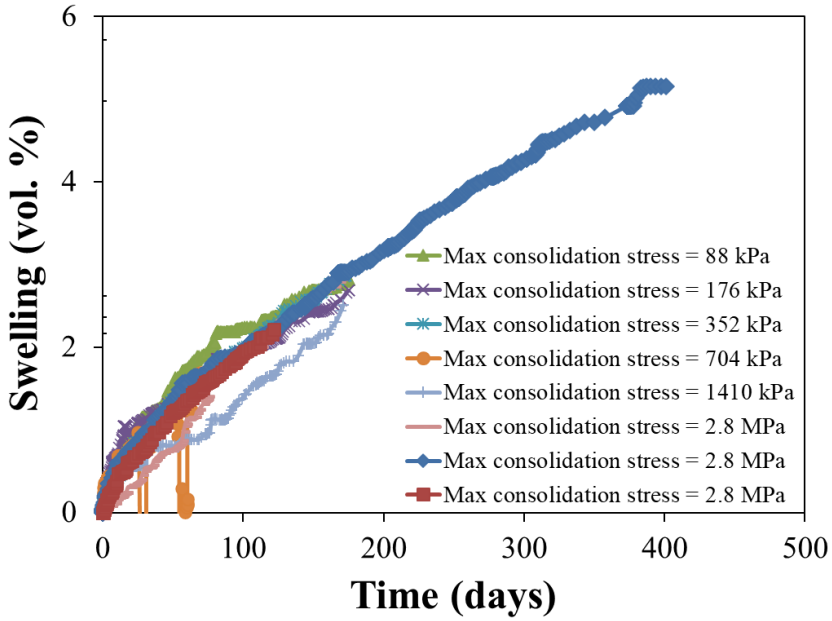

Fig. 3-17 Experimental measurements of swelling (vol. %) under 176 kPa counter-pressure on bi-salt BWPs containing 10 wt.% $NaNO_3$ and 30 wt.%. of $BaSO_4$ consolidated with different level of stress.

CHAPTER 4

NUMERICAL MODELING

The model presented in this chapter is extended from an existing work of G. Mélot [1,2] and aims at representing the water uptake, the poromechanical behavior and the salt leaching of BWPs during the leaching process under free and confined conditions (constant counter-pressure and constant volume conditions).

The general framework of the model developed by G. Mélot [1,2] (referenced as MELOT2019 model hereafter) is recalled in section 4.1. As the MELOT2019 model has not been able to reproduce the newly acquired experimental data (detailed in section 5.2), two extensions have been proposed. Firstly, an innovative coupled homogenization of transport terms is proposed in section 4.2 to better capture the role of the semi-permeable membrane played by the BWP matrix and the porosity-dependency of the transport coefficients during leaching. Secondly, a large-strain viscoelastic model and a homogenization of viscoelastic parameters are proposed in section 4.3 to better model the leaching process under confined conditions.

4.1. General framework of the model MELOT2019

The general framework of the model MELOT2019 [1,2] is kept in this work and recalled in this section. The modeling hypotheses are presented in 4.1.1. The governing equations are recalled in 4.1.2. The complementary laws kept from [1,2] are recalled in 4.1.3, 4.1.4 and 4.1.5.

4.1.1. Modeling hypotheses

The following simplifying hypotheses are made to allow the modeling:

Hypothesis N°1: Only the most soluble salt in the BWPs is modeled.

The BWPs can contain both soluble salts (ex. $NaNO_3$) and poorly soluble salts (ex. $BaSO_4$). The poorly soluble salts have significantly lower aqueous solubility than soluble salts. For example, the aqueous solubility of $BaSO_4$ ($2.5 \times 10^{-4}\ g.L^{-1}$ at 25°C) is 400 000 times less soluble than $NaNO_3$ (921 $g.L^{-1}$ at 25°C). For mechanisms such as diffusion and osmosis, the aqueous solubility of salt plays a dominant role through salt concentration gradients. The diffusive fluxes and osmotic pressures due to these poorly soluble salts can thus be neglected. The poorly soluble salts are therefore considered as part of the homogenized BWP matrix. However, regarding experimental observations, they may impact the BWPs matrix's mechanical and transport properties. This aspect will be detailed in the rest of this work.

French BWPs contain mostly two soluble salts: $NaNO_3$ and Na_2SO_4. These two salts have an aqueous solubility of 921 $g.L^{-1}$ and 195 $g.L^{-1}$ at 25°C, which corresponds to a mass fraction of dissolved salt in a saturated aqueous solution of 0.479 and 0.17 g of salt/g of saturated solutions. Moreover, the theoretical maximum osmotic pressure generated by these two salts is about 42 MPa for $NaNO_3$ (cf. 2.2.3) and 5 MPa for Na_2SO_4 [2]. Assimilating Na_2SO_4 to $NaNO_3$ is *a priori* conservative for the modeling of the BWPs leaching process. For the rest of this work, only the most soluble salt in the BWPs ($NaNO_3$) is modeled.

Hypothesis N°2: The material is considered as a fluid-saturated porous material.

The BWPs have an initial porosity so that a filling of the initial pores (referred to as the hydration stage hereafter) takes place during the early stage of the leaching process. This hydration stage is treated separately by assuming that the contribution of the water uptake due to this filling of the initial pores follows a simple square root of time kinetics [1,2] (see details in section 4.1.5). The model presented hereafter does not consider this hydration process but starts once the initial porosity is totally saturated by the liquid. Thus, the material is regarded as a fluid-saturated porous material composed of 2 phases: the solid BWP matrix, composed of bitumen and salt crystals, and the liquid phase, a mixture of water and dissolved salt (cf. Fig. 4-1). ϕ_b, ϕ_l, ϕ_c are respectively the volumetric fraction of the bitumen, liquid, and salt crystals within the material. ϕ_l is also named Lagrangian porosity hereafter (cf. 4.3.1 for more details). We have thus $\phi_b + \phi_l + \phi_c = 1$.

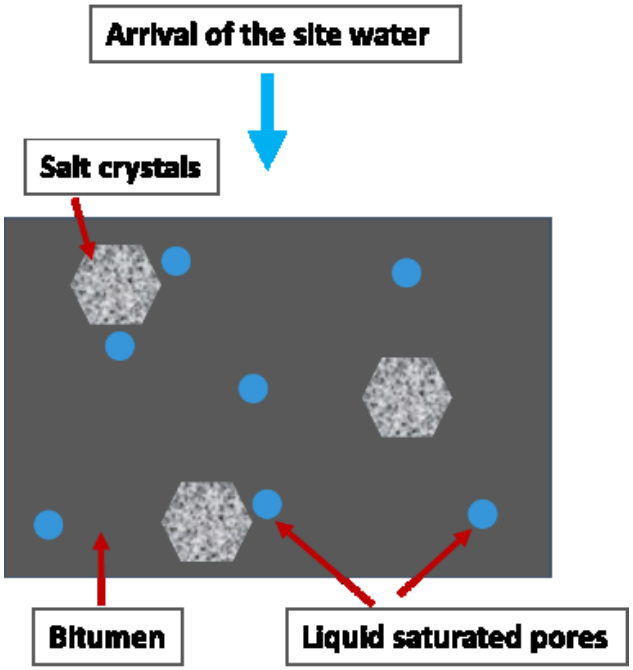

Fig. 4-1 Schematic representation of BWPs.

Hypothesis N°3: The BWP matrix is assumed to be isotropic and viscously incompressible (no viscous volumetric strain).

The BWPs can be considered as isotropic materials. The BWPs are assumed to be viscously incompressible, the BWPs' viscous volumetric strain is therefore assumed to be constantly zero.

4.1.2. Governing equations

The mass balance equations for the total mass (water and salt) and the salt are written under the form:

$$\frac{\partial}{\partial t}(\rho_l \phi_l + \rho_c \phi_c) + \nabla . \boldsymbol{W_l} = 0 \tag{52}$$

$$\frac{\partial}{\partial t}(\rho_l \phi_l \omega_s + \rho_c \phi_c) + \nabla . \boldsymbol{W_s} = 0 \tag{53}$$

where ρ_l is the liquid density, ϕ_l the Lagrangian porosity, ρ_c the crystal density, ϕ_c the volume fraction of salt crystal, ω_s the solute mass fraction in the liquid phase, $\boldsymbol{W_l}$ and $\boldsymbol{W_s}$ the mass flux of the liquid phase and the mass flux of salt. In order to simplify the equations and to get rid of the expression of the mass flux of water, the conservation of the sum of salt and water was treated in MELOT2019 instead of the conservation of water. This choice is kept in the current model. The fluxes $\boldsymbol{W_l}$ and $\boldsymbol{W_s}$ are written classically in terms of permeability, diffusion, and osmosis coefficients in MELOT2019 [1,2] and are not recalled here. A new formulation of these fluxes is proposed in section 4.2.

By neglecting gravity, the mechanical equilibrium writes:

$$\nabla \cdot \boldsymbol{\sigma} = \boldsymbol{0} \tag{54}$$

where $\boldsymbol{\sigma}$ denotes the total stress tensor.

4.1.3. Dissolution kinetics

The dissolution/precipitation law is kept from [1,2], which is a simplified version of N. Mokni's work [24]:

$$\frac{d\phi_c}{dt}\rho_c = \phi_c \sigma_c \beta \left[\left(\frac{\omega_s}{\omega_{sat}}\right) - 1\right] \quad (55)$$

where ϕ_c is the volume fraction of salt crystal, σ_c is the specific surface (m^{-1}), β is the dissolution rate constant ($kg.s^{-1}.m^{-3}$) and ω_{sat} is the solute mass fraction in the liquid phase at saturation.

4.1.4. Evolution of the liquid phase density

The evolution of the liquid phase density ρ_l is kept from [1,2]:

$$\frac{d\rho_l}{\rho_l} = C_w dp - \rho_l v^r d\omega_s \quad (56)$$

where C_w is the compressibility of the liquid water, p is the pore pressure and $v^r = \frac{V_w}{M_w} - \frac{V_s}{M_s}$ with V_w, V_s, M_w, M_s respectively the molar volume and molar mass of the liquid water and dissolved salt.

4.1.5. Filling of the initial porosity (hydration stage)

As shown in 2.1, the French BWPs have an initial porosity of about 7 vol. %. With such an important value, the filling of the initial porosity within the BWPs (hydration stage), highlighted in [6], is not negligible. In fact, a significant amount of the water absorbed by the sample during the leaching test is used to fill the porosity initially present in the material. This amount of water (named hydration water hereafter) needs therefore to be taken into account in the modeling. Moreover, the hydration solution is not initially saturated with salt. It will be loaded with salt as it penetrates through the BWPs and encounters the soluble salt crystals. The amount of salt needed to saturate the hydration water (named hydration salt hereafter) must therefore also be considered in the modeling.

We define the hydration front as the place where the filling of the initial porosity takes place. It must be distinguished from the leaching front, defined as the place where the leaching phenomena described in 2.2 take place. For I-type ($BaSO_4$ only) samples (Fig. 2-10(b)), the H-NMR results (cf. 2.3.3) show that the water already reached the bottom of the NMR tube in less than 8 months. As a reminder, there is *a priori* no leaching phenomenon for BWPs containing only poorly soluble salt $BaSO_4$. The water profile recorded on I-type samples (cf. Fig. 2-10(b)) is actually the profile of the hydration front. For profiles recorded on B-type (bi-salt) samples (Fig. 2-10(c)), two parts can be distinguished: a localized water distribution within the first 2 mm of depth after 8 months of leaching and a more dispersed water distribution along the depth. The dispersed water distributions along the depth are similar to those recorded on B-type (bi-salt) samples and can be recognized as the hydration front. The localized water distributions within the first 2 mm of depth are similar to those recorded on S-type ($NaNO_3$ only) samples (Fig. 2-10(a)) and are actually the leaching front. This suggests that the hydration front progresses much faster than the leaching front for BWPs containing both soluble salt $NaNO_3$ and poorly soluble salt $BaSO_4$. However, the progression of the hydration front seems not significantly faster than

the leaching front for S-type ($NaNO_3$ only) samples (Fig. 2-10(a)). More recently, R. Blinder et al. [19] used NMR to monitor the water uptake behavior of simplified French BWPs incorporating 40 wt. % $SrSO_4$ or $MgSO_4$. They reported similar results as the existing one: the insoluble salts dispersed in the bitumen matrix enhance the water progression in the material.

Generally speaking, the hydration front progresses much faster than the leaching front for BWPs containing both soluble and poorly soluble salts. We assume this is true for all BWPs considered in this work for simplicity. We can therefore model the progression of the hydration front independently from the leaching phenomena described in 2.2. This hypothesis is questionable but seems reasonable considering the previous observations.

N. Bleyen [6] conducted free leaching tests on Eurobitum (Belgian BWPs, cf. 2.1.2) and reported that the quantity of the water uptake and the leached $NaNO_3$ shows mainly three stages. The first stage (about 50 days) consists of an initial fast ingress of water into and leaching of $NaNO_3$ from pores close to the surface. During the second stage (about 800 days), the progression of the hydration front, the swelling, and the leaching of $NaNO_3$ slowed down but behaved linearly with the square root of time, indicating that these processes are mainly controlled by diffusion. An acceleration of the various mechanisms is observed during the last stage (after 2 or 3 years), which can be explained *a priori* by the reaching of a porosity threshold.

Based on the reported experimental results [6], we assume the progression of the hydration front is mainly diffusive within the BWPs: the quantity of the hydration water evolves linearly as a function of the square root of time. The filling of the initial pores (hydration stage) is therefore modeled as follows:

$$m_{hydration\ water}(t) = Vn_{l_i}.\sqrt{t/t_f} \tag{57}$$

$$m_{hydration\ salt}(t) = m_{hydration\ water}(t) \times S \tag{58}$$

where t is the leaching time, t_f is the time needed to hydrate the whole BWP sample, $m_{hydration\ water}(t)$ and $m_{hydration\ salt}(t)$ are respectively the mass flux of water and salt at time t due to the hydration stages, V is the volume of the BWP sample, n_{l_i} is the initial porosity, S is the water solubility of soluble salt. The sample dimensions listed in Table 14 and Table 15 are used to calculate V. The initial porosities listed in Table 1 are used for n_{l_i}. t_f is estimated by using the hydration kinetics experimentally measured on French BWPs and will be detailed in CHAPTER 5 for each composition.

4.2. Flux formulation with coupled homogenization of transport

The porosity of the BWPs samples may significantly increase during the leaching process (cf. 3.2) and thus has an important impact on transport terms (diffusion, permeation, and osmosis). The evolution laws proposed for each transport coefficient (permeability k, osmotic efficiency τ and effective diffusion D_{eff}) in [1,2] have not been able to reproduce the newly acquired experimental data (detailed in 5.2). Describing the porosity-dependent evolution of these coefficients is thus a major challenge of this work. To achieve this goal, an innovative coupled homogenization of transport terms is proposed in this section.

The temperature is assumed to be uniform and constant in the material. Assuming the thermodynamic equilibrium at the macroscopic scale, the chemical potential of species i ($i = w$ for water and $i = s$ for salt) is uniform at the macroscopic scale and thus takes the same value in the bitumen and the pore

solution. By neglecting gravity, the overall dissipation associated with water and salt transport phenomena is positive and can be expressed as [44,45]:

$$-\boldsymbol{W_w}\cdot\nabla(\mu_w)-\boldsymbol{W_s}\cdot\nabla(\mu_s)\geq 0 \tag{59}$$

where $\boldsymbol{W_w}$ and $\boldsymbol{W_s}$ are respectively the mass flux ($kg.m^{-2}.s^{-1}$) of water and salt, μ_w and μ_s respectively the chemical potential ($J.kg^{-1}$) of water and dissolved salt. Note that $\boldsymbol{W_l}=\boldsymbol{W_s}+\boldsymbol{W_w}$ where $\boldsymbol{W_l}$ is the mass flux of the liquid phase.

The inequality (59) can be always satisfied if $\boldsymbol{W_w}$ and $\boldsymbol{W_s}$ are written in terms of μ_w and μ_s as [46]:

$$\boldsymbol{W_w}=-D_{ww}\nabla(\mu_w)-D_{ws}\nabla(\mu_s) \tag{60}$$

$$\boldsymbol{W_s}=-D_{sw}\nabla(\mu_w)-D_{ss}\nabla(\mu_s) \tag{61}$$

where the diffusion matrix $\begin{bmatrix}D_{ww} & D_{ws}\\ D_{sw} & D_{ss}\end{bmatrix}$ is symmetric positive definite. D_{ws} and D_{sw} describe the coupled diffusion of salt and water in the medium, they are assumed to be neglected ($D_{ws}=D_{sw}=0$).

From (*60*) and (*61*), $\boldsymbol{W_l}$ and $\boldsymbol{W_s}$ can be derived as (see the demonstration in Appendix A):

$$\boldsymbol{W_l}=-\rho_l k\nabla(p)+\rho_l\tau_{max}\tau\rho_l k\frac{RT}{M_s}\nabla(\omega_s) \tag{62}$$

$$\boldsymbol{W_s}=\omega_s\left[1-\frac{1-\omega_s}{R(\omega_s)}(\tau_{max}\tau-a)\right]\boldsymbol{W_l}-\rho_l D_{eff}\nabla(\omega_s) \tag{63}$$

where p is the pore pressure, M_s ($kg.mol^{-1}$) is the molar mass of salt, R ($J.mol^{-1}.K^{-1}$) is the ideal gas constant, $T(K)$ is the temperature, τ_{max} is a normalization parameter, a is a coupling parameter, k ($m^2.Pa^{-1}.s^{-1}$), τ(-) and $D_{eff}(m^2.s^{-1})$ are respectively the effective permeability coefficient, osmotic efficiency coefficient, and effective diffusion coefficient. It is worth noting that the effective permeability coefficient k is defined as the ratio of the intrinsic permeability (m^2) and the water viscosity ($Pa.s$).

$R(\omega_s)$ is a function depending on the soluble salts taken into account in the model. For 1-1 electrolytes (such as $NaNO_3$), we have (cf. Appendix A for calculation details):

$$R(\omega_s)=\frac{\nu_N\omega_s}{M_s(1-\omega_s)^2}\left[\frac{-A_\phi}{2\sqrt{m}}\frac{3+2b\sqrt{m}}{\left(1+b\sqrt{m}\right)^2}+2\beta_0+\frac{2\beta_1}{\alpha^2}\exp\left(-\alpha\sqrt{m}\right)\left(\alpha^2-\frac{\alpha^3}{4}\sqrt{m}\right)+2mC^\gamma\right]+\frac{\nu_N}{1-\omega_s}$$

where ν_N is the stoichiometric number of moles of ions per one mole of salt, A_ϕ, b, α, β_0, β_1, C_ϕ are Pitzer's model parameters [47]. In the case of $NaNO_3$, we have $\nu_N=2$. The Pitzer's model parameters for the aqueous solution of $NaNO_3$ at 25℃ are fitted and listed in Table 10 (find more details about the fitting in 5.5.1). The expressions of $R(\omega_s)$ for 2-1 electrolytes (such as Na_2SO_4) and the Pitzer's model parameters for Na_2SO_4 are given in Appendix A.

Table 10 Fitted Pitzer's model parameters for an aqueous solution of $NaNO_3$ at 25℃.

Parameter	Value
A_ϕ	$0.392\ kg^{1/2}mol^{-1/2}$
b	$1.2\ kg^{1/2}mol^{-1/2}$
α	$2\ kg^{1/2}mol^{-1/2}$
β_0	$0.0068\ kg.mol^{-1}$
β_1	$0.1783\ kg.mol^{-1}$
C_ϕ	$-0.000267\ kg^2.mol^{-2}$

Fig. 4-2 shows the profile of $R(\omega_s)$ for $\omega_s \in [0, \omega_{sat}]$ calculated with Pitzer's model parameters for $NaNO_3$ listed in Table 10. ω_{sat} denotes the solute mass fraction in the liquid phase at saturation.

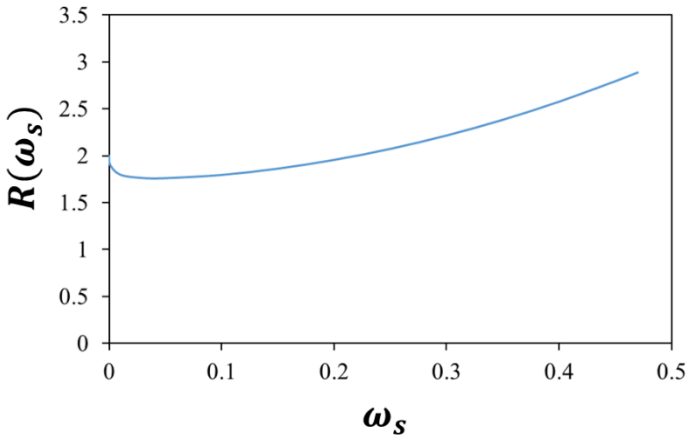

Fig. 4-2 Profile of $R(\omega_s)$ for $\omega_s \in [0, \omega_{sat}]$ calculated with Pitzer's model parameters listed in Table 10.

It should be mentioned that the transport mechanisms for water and salt are assumed to be governed essentially by diffusion through the BWP matrix and the pore solution. In other words, the permeability is actually an apparent permeability since the material's porosity is hardly connected, so Darcian flow in the porosity is highly improbable. The pore pressure generated in the material primarily results from an osmotic effect. The transport parameters $k, \tau \; and \; D_{eff}$ actually originate from the diffusion of water and salt through the BWP matrix and the pore solution.

The transport coefficients k, τ, D_{eff} can be written in terms of D_{ww} and D_{ss} as (see the demonstration in Appendix A):

$$\rho_l^2 k = (1 + \rho_w v_s')D_{ss} + (1 - \rho_s v_s')D_{ww} \tag{64}$$

$$\tau = \frac{\tau_0}{\tau_{max}}\left[1 - \frac{\frac{\rho_l}{\rho_s}D_{ss}}{\rho_l^2 k}\right] \tag{65}$$

$$\rho_l D_{eff} = \frac{R(\omega_s)}{1-\omega_s}\frac{RT}{M_s}(1 - \frac{\tau_{max}\tau}{\tau_0})D_{ww} \tag{66}$$

where ρ_w and ρ_s $(kg.m^{-3})$ are the mass concentration of water and dissolved salt in the liquid phase, respectively, $v_s' = v_s - v_w$ $(m^3.kg^{-1})$ is the difference between the specific partial volumes of water and dissolved salt and $\tau_0 = \frac{R(\omega_s)}{(1-\omega_s)(1-\rho_s v_s')}$.

D_{ww} and D_{ss} are the diffusion coefficients of water and dissolved salt in the homogenized material. By assuming spherical pores embedded in the BWP matrix, the Mori-Tanaka homogenization scheme [33,48] (cf. 2.5.1) can be applied. Considering the diffusion in the pores is much larger than in the BWP matrix, we have:

$$D_{ww} = \frac{1 + 2n_l}{1 - n_l} D_{ww}^{mat} \tag{67}$$

$$D_{ss} = \frac{1 + 2n_l}{1 - n_l} D_{ss}^{mat} \tag{68}$$

where D_{ww}^{mat} and $D_{ss}^{mat}(kg.s.m^{-3})$ are the diffusion coefficients in the BWP matrix, n_l is the Eulerian porosity of the liquid phase.

It is worth noting that D_{ww}^{mat} and D_{ss}^{mat} are the diffusion coefficients related to $(\nabla\mu_w, \nabla\mu_s)$. We propose to note D_w^{mat} and D_s^{mat} $(m^2.s^{-1})$ the diffusion coefficients of water and dissolved salt in the BWP matrix related to $(\nabla\rho_w^{mat}, \nabla\rho_s^{mat})$, where $\rho_w^{mat} = \alpha_w\rho_w$ is the solubility of water in the BWP matrix $(kg.m^{-3})$ and $\rho_s^{mat} = \alpha_s\rho_s$ is the solubility of salt in the BWP matrix $(kg.m^{-3})$ with α_w and α_s two solubility factors (-).

The links between $(D_{ww}^{mat}, D_{ss}^{mat})$ and (D_w^{mat}, D_s^{mat}) are derived in Appendix A:

$$D_{ww}^{mat} = \rho_w^{mat}\frac{M_w}{RT}D_w^{mat} \tag{69}$$

$$D_{ss}^{mat} = \rho_s^{mat}\frac{M_s}{\nu_N RT}D_s^{mat} \tag{70}$$

By substituting (69)-(70) into (64)-(66), the transport coefficients k, τ, D_{eff} can be finally written in terms of four material parameters ($\alpha_w, \alpha_s, D_w^{mat}$ and D_s^{mat}):

$$\rho_l^2 k = \frac{1+2n_l}{1-n_l}\frac{\rho_l}{RT}\left[(1+\rho_w v_s')\frac{\omega_s M_s}{\nu_N}\alpha_s D_s^{mat} + (1-\rho_s v_s')M_w(1-\omega_s)\alpha_w D_w^{mat}\right] \tag{71}$$

$$\tau = \frac{\tau_0}{\tau_{max}}\left[1 - \frac{1}{(1+(1-\omega_s)\rho_l v_s')\omega_s + (1-\omega_s\rho_l v_s')\nu_N\frac{M_w(1-\omega_s)\alpha_w D_w^{mat}}{M_s\alpha_s D_s^{mat}}}\right] \tag{72}$$

$$D_{eff} = \frac{1+2n_l}{1-n_l}\frac{R(\omega_s)}{1-\omega_s}\left(1-\frac{\tau_{max}\tau}{\tau_0}\right)\frac{M_w}{M_s}(1-\omega_s)\alpha_w D_w^{mat} \tag{73}$$

Although there are four material parameters for the BWP matrix ($\alpha_w, \alpha_s, D_w^{mat}$ and D_s^{mat}), these four parameters always appear in the form of two products $\alpha_w D_w^{mat}$ and $\alpha_s D_s^{mat}$. In CHAPTER 5, these two products will be calibrated based on the experimental results shown in CHAPTER 3.

4.3. Large-strain viscoelastic model and homogenization of viscoelastic parameters

Bitumen is a material whose mechanical behavior is difficult to qualify. It is a fluid so viscous that it seems solid. Its time-dependent strains (or delayed strains) are important. It has the particularity to flow under its own weight. This behavior is demonstrated by the "pitch drop experiment" which shows the fluidity of a bitumen, through a long-term test started in 1927 [49]. A sample of bitumen is placed in a funnel, and a drop forms and falls out of the funnel about every decade. The mechanical behavior of French BWPs is strongly dependent on the mechanical behavior of the bitumen it contains. On the one hand, because bitumen is the main component (about 60% in mass fraction), and on the other hand because the strains of the salt crystals are negligible compared to those of the bitumen. For the above reasons, the mechanical behavior of the French BWPs is assumed to be viscoelastic, as proposed in MELOT2019 [1,2]. The total strain is the sum of the instantaneous elastic strain and the time-dependent viscous strain.

Also, it is worth noting that the swelling of French BWPs can reach about 150 vol. % for simplified BWPs (cf. 3.2.4) and about 270 vol. % for industrial ones (cf. 3.2.7). The maximum porosity can reach about 60 vol.% (cf. 2.3.1). As such large strains are not considered in the Maxwell viscoelastic poromechanical

model proposed in MELOT2019 [1,2], numerical convergence problems were observed at this level. Such large porosities (large strains) exceed the validity domain of the MELOT2019 model.

To tackle this problem, a non-linear poro-viscoelastic model taking into account large strains is proposed in this section. The thermodynamics of large strain poromechanics and the notations are developed in 4.3.1. A nonlinear poro-viscoelastic model is developed in 4.3.3 based on poro-elasticity developed in 4.3.2. A homogenization of the viscoelastic parameters using the Mori-Tanaka homogenization scheme [33,39,48] is proposed in section 4.3.4. In the following, tensile stresses are considered positive for sign convention.

4.3.1. Thermodynamics of large strain poromechanics

Consider the deformation tensor $\boldsymbol{F}$ linking the initial configuration κ_0 and the current configuration κ. The deformation tensor $\boldsymbol{F}$ can be decomposed into an inelastic deformation (here viscoelastic, linking the initial configuration κ_0 and an intermediate configuration $\tilde{\kappa}$) and an instantaneous elastic deformation (linking the intermediate configuration and the current configuration κ). The intermediate configuration $\tilde{\kappa}$ is obtained from instantaneous elastic unloading from the current configuration κ. We can note $\boldsymbol{F^e}$ and $\boldsymbol{F^v}$ respectively the deformation tensors for elastic and viscoelastic deformation. We have therefore $\boldsymbol{F} = \boldsymbol{F^e} \cdot \boldsymbol{F^v}$.

The deformation of a volume element from its initial configuration V_0 to its current configuration V through an intermediate configuration $\tilde{V}$ ($V_0 \rightarrow \tilde{V} \rightarrow V$) can be described by the determinant of $\boldsymbol{F}$ (noted as $J = \det(\boldsymbol{F})$). J can be decomposed as a product of elastic and viscoelastic contributions: $J = J^e J^v$, where $J^e = V/\tilde{V}$ and $J^v = \tilde{V}/V_0$. Similarly, the pore volume is subjected to the deformation $V_{0,p} \rightarrow \tilde{V}_p \rightarrow V_p$. The current Lagrangian porosity is defined as $\phi_l = V_p/V_0$, the initial lagrangian porosity is $\phi_0 = V_{0,p}/V_0$. We can define the elastic deformation of the pore as $\varphi^e = (V_p - \tilde{V}_p)/\tilde{V}$ and the viscoelastic deformation of the pore as $\varphi^v = (\tilde{V}_p - V_{0,p})/V_0$. We have therefore:

$$\phi_l = \phi_0 + J^v \varphi^e + \varphi^v \tag{74}$$

The Eulerian porosity is defined as $n_l = V^p/V = \phi_l/J$.

Consider in the current configuration, a representative volume, V, of the porous material, which can be considered as a homogeneous medium at the macroscopic scale. The total stresses and pore pressure can thus be considered homogeneous within V. This volume is composed of the volume of the solid V_s and the volume of the porous space V_p : $V = V_s + V_p$. We note F_s and S_s the free energy and the entropy of the solid contained in V_s. The two first laws of thermodynamics in Eulerian description entail (cf. equations 2.46 and 3.33 in [45]):

$$\boldsymbol{\sigma}\!:\! V\boldsymbol{d} + p\frac{\mathrm{d}}{\mathrm{dt}}(V_p) - S_s\frac{\mathrm{d}}{\mathrm{dt}}(T) - \frac{\mathrm{d}}{\mathrm{dt}}(F_s) \geq 0 \tag{75}$$

where $\boldsymbol{\sigma}$ is the total stress tensor, p is the pore pressure and T is the temperature. The Eulerian strain rate $\boldsymbol{d}$ is defined as the symmetric part of $\frac{\mathrm{d}}{\mathrm{dt}}(\boldsymbol{F}) \cdot \boldsymbol{F^{-1}}$:

$$\boldsymbol{d} = \left\{\frac{\mathrm{d}}{\mathrm{dt}}(\boldsymbol{F}) \cdot \boldsymbol{F^{-1}}\right\}^{sym} = \frac{1}{2}\left(\frac{\mathrm{d}}{\mathrm{dt}}(\boldsymbol{F}) \cdot \boldsymbol{F^{-1}} + \left(\frac{\mathrm{d}}{\mathrm{dt}}(\boldsymbol{F}) \cdot \boldsymbol{F^{-1}}\right)^T\right) \tag{76}$$

$$\frac{\mathrm{d}}{\mathrm{dt}}(\boldsymbol{F}) \cdot \boldsymbol{F^{-1}} = \frac{\mathrm{d}}{\mathrm{dt}}(\boldsymbol{F^e}) \cdot (\boldsymbol{F^e})^{-1} + \boldsymbol{F^e} \cdot (\frac{\mathrm{d}}{\mathrm{dt}}(\boldsymbol{F^v}) \cdot (\boldsymbol{F^v})^{-1}) \cdot (\boldsymbol{F^e})^{-1} \tag{77}$$

We can link the volumetric strain rate $tr(\boldsymbol{d})$ with J as:

$$tr(\boldsymbol{d}) = \frac{dJ/dt}{J} \tag{78}$$

Let $f_s = F_s/V_0$ denote the free energy density and the entropy density $s_s = S_s/V_0$, (*75*) becomes:

$$J\boldsymbol{\sigma}\colon \boldsymbol{d} + p\frac{\mathrm{d}}{\mathrm{dt}}(\phi) - s_s\frac{\mathrm{d}}{\mathrm{dt}}(T) - \frac{\mathrm{d}}{\mathrm{dt}}(f_s) \geq 0 \tag{79}$$

At constant temperature, we get:

$$J\boldsymbol{\sigma}\colon \boldsymbol{d} + p\frac{\mathrm{d}}{\mathrm{dt}}(\phi) - \frac{\mathrm{d}}{\mathrm{dt}}(f_s) \geq 0 \tag{80}$$

It should be noted that the large porosities and large strains experimentally observed on BWPs (cf. 2.3.1, 3.2.4 and 3.2.7) are mostly due to viscosity but not elasticity. We can therefore assume the elastic deformation is infinitesimal, i.e., $\boldsymbol{F^e} \cong 1, J \cong J^v$. Equation (*76*) then becomes:

$$\boldsymbol{d} = \frac{\mathrm{d}}{\mathrm{dt}}(\boldsymbol{\varepsilon^e}) + \boldsymbol{d^v} \tag{81}$$

with

$$\boldsymbol{\varepsilon^e} = \{\boldsymbol{F^e}\}^{sym} - 1 \tag{82}$$

$$\boldsymbol{d^v} = \left\{\frac{\mathrm{d}}{\mathrm{dt}}(\boldsymbol{F^v}) \cdot (\boldsymbol{F^v})^{-1}\right\}^{sym} \tag{83}$$

Similarly to (78), we can link the viscous volumetric strain rate $tr(\boldsymbol{d^v})$ with J^v as:

$$tr(\boldsymbol{d^v}) = \frac{dJ^v/dt}{J^v} \tag{84}$$

By substituting equations (*74*) and (*81*) into (*80*), we have:

$$J^v\boldsymbol{\sigma}\colon\left(\frac{\mathrm{d}}{\mathrm{dt}}(\boldsymbol{\varepsilon^e}) + \boldsymbol{d^v}\right) + p\frac{\mathrm{d}}{\mathrm{dt}}(J^v\varphi^e + \varphi^v) - \frac{\mathrm{d}}{\mathrm{dt}}(f_s) \geq 0 \tag{85}$$

We can assume that f_s depends on the viscoelastic deformation and pore volume change: $f_s = f_s(\boldsymbol{\varepsilon^e}, \varphi^e, \boldsymbol{F^v}, \varphi^v)$. For a purely reversible elastic deformation (where $\boldsymbol{F^v}, \varphi^v$ remain constant), the inequality (*85*) turns into equality:

$$J^v\boldsymbol{\sigma}\colon\frac{\mathrm{d}}{\mathrm{dt}}(\boldsymbol{\varepsilon^e}) + pJ^v\frac{\mathrm{d}}{\mathrm{dt}}(\varphi^e) - \left(\frac{\mathrm{d}}{\mathrm{dt}}(f_s)\right)_{\boldsymbol{F^v},\varphi^v} = 0 \tag{86}$$

By replacing (*86*) in (*85*), the dissipation reads finally:

$$J^v\boldsymbol{\sigma}\colon\boldsymbol{d^v} + p\left(\frac{\mathrm{d}}{\mathrm{dt}}(J^v)\varphi^e + \frac{\mathrm{d}}{\mathrm{dt}}(\varphi^v)\right) - \left(\frac{\mathrm{d}}{\mathrm{dt}}(f_s)\right)_{\boldsymbol{\varepsilon^e},\varphi^e} \geq 0 \tag{87}$$

4.3.2. Nonlinear poro-elasticity

In this section, we study the case of nonlinear poro-elasticity. Although the results are well-known, the nonlinear poro-elasticity case is developed in detail in this section to facilitate the comprehension of the nonlinear poro-viscoelasticity, which will be developed similarly in 4.3.3.

Nonlinear poro-elasticity writes in the isotropic case as [45]:

$$d(\sigma_m) = Kd(tr(\boldsymbol{\varepsilon^e})) - bdp \tag{88}$$

$$d(\varphi^e) = bd(tr(\boldsymbol{\varepsilon^e})) + d(p)/N \tag{89}$$

$$ds_{ij} = 2Gd(dev(\varepsilon^e_{ij})) \tag{90}$$

where $\sigma_m = \frac{1}{3}tr(\boldsymbol{\sigma})$, $s_{ij} = \sigma_{ij} - \sigma_m\delta_{ij}$ are the coefficients of the deviatoric total stress tensor, $dev(\varepsilon^e_{ij}) = \varepsilon^e_{ij} - \frac{1}{3}tr(\boldsymbol{\varepsilon^e})\delta_{ij}$ are the coefficients of the deviatoric strain tensor. K, G, b and N are respectively drained bulk and shear modulus, Biot's coefficient, and Biot's modulus of the homogenized material.

Considering in the current state an instantaneous and elastic incremental confining stress loading, $d\sigma_m = -dp$, (*88*) gives thus:

$$b = 1 + \frac{Kd(tr(\boldsymbol{\varepsilon^e}))}{dp} \tag{91}$$

During such loading, the mechanical response under confining stress test is given by $dV/V = d\phi_l/\phi_l = d\sigma_m/K_s = -dp/K_s$. With $d(J^v) = 0$ and $d(\varphi^v) = 0$, we have:

$$d(J^e)/J^e = J^v d(\varphi^e)/\phi_l = -dp/K_s \tag{92}$$

where K_s is the bulk modulus of the BWP matrix.

Under infinitesimal elastic deformation, we have $\boldsymbol{F^e} \cong 1$ and $J^e \cong 1$, equation (*92*) becomes:

$$d(tr(\boldsymbol{\varepsilon^e})) = J^v d(\varphi^e)/\phi_l = -dp/K_s \tag{93}$$

Equation (*93*) gives:

$$\frac{d(tr(\boldsymbol{\varepsilon^e}))}{dp} = -\frac{1}{K_s} \tag{94}$$

$$d(\varphi^e) = n_l d(tr(\boldsymbol{\varepsilon^e})) \tag{95}$$

By substituting (*94*) into (*91*), we have

$$b = 1 - \frac{K}{K_s} \tag{96}$$

By substituting (*95*) into (*89*), we have

$$n_l d(tr(\boldsymbol{\varepsilon^e})) = bd(tr(\boldsymbol{\varepsilon^e})) + \frac{dp}{N} \Rightarrow \frac{1}{N} = (n_l - b)\frac{d(tr(\boldsymbol{\varepsilon^e}))}{dp} \tag{97}$$

By substituting (*94*) into (*97*), we get

$$\frac{1}{N} = \frac{b - n_l}{K_s} \tag{98}$$

4.3.3. Nonlinear poro-viscoelasticity

In this section, we consider the case of non-linear poro-viscoelasticity. The objective is to adapt the classic Maxwell viscoelastic model to our poro-mechanical case.

Let J_s denote the volume deformation of the solid matrix from its initial configuration to its current configuration, we have:

$$J = J_s(1 - \phi_0) + \phi_l \tag{99}$$

J_s can be written as a product of its elastic and viscous parts: $J_s = J_s^e J_s^v$.

We use the temporal derivatives to describe the time-dependent viscous strains. Using (*74*), we can identify the elastic and the viscous increments as:

$$J^v d(J^e) = J_s^v d(J_s^e)(1 - \phi_0) + J^v d(\varphi^e) \tag{100}$$

$$\frac{\mathrm{d}}{\mathrm{dt}}(J^v) = \frac{\mathrm{d}}{\mathrm{dt}}(J_s^v)(1 - \phi_0) + \frac{\mathrm{d}}{\mathrm{dt}}(\varphi^v) + \frac{\mathrm{d}}{\mathrm{dt}}(J^v)\varphi^e \tag{101}$$

By analogy to (*89*), we can assume that the viscous pore volume change rate $\frac{\mathrm{d}}{\mathrm{dt}}(\varphi^v) + \frac{\mathrm{d}}{\mathrm{dt}}(J^v)\varphi^e$ is equal to :

$$\frac{d}{dt}(\varphi^v) + \frac{d}{dt}(J^v)\varphi^e = b^v \frac{\mathrm{d}}{\mathrm{dt}}(J^v) + \frac{p}{N^v} \tag{102}$$

where b^v is a "viscous Biot-like" coefficient, N^v is a "viscous Biot-like" modulus. Note that N^v is positive.

By substituting (84) into (102), we have:

$$\frac{d}{dt}(\varphi^v) + \frac{d}{dt}(J^v)\varphi^e = b^v J^v tr(\boldsymbol{d^v}) + \frac{p}{N^v} \tag{103}$$

By using (*102*)(*103*), the dissipation (*87*) then becomes:

$$J^v(\boldsymbol{\sigma} + b^v p\mathbf{1}) : \boldsymbol{d^v} + \frac{p^2}{N^v} - \left(\frac{\mathrm{d}}{\mathrm{dt}}(f_s)\right)_{\boldsymbol{\varepsilon^e}, \varphi^e} \geq 0 \tag{104}$$

By assuming that f_s does not depend on $\boldsymbol{F^v}$ and φ^v, we have $\left(\mathrm{d}/\mathrm{dt}\ (f_s)\right)_{\boldsymbol{\varepsilon^e}, \varphi^e} = 0$. Note that $\frac{p^2}{N^v}$ is positive. One way to ensure the inequality (*104*) is true for all cases is to have the volumetric and deviatoric parts of $\boldsymbol{d^v}$ proportional to those of $\boldsymbol{\sigma} + b^v p\mathbf{1}$. We can thus formulate the viscoelastic law as follows:

$$tr(\boldsymbol{d^v}) = \frac{1}{\eta_v}(\sigma_m + b^v p) \tag{105}$$

$$dev(\boldsymbol{d^v}) = \frac{1}{2\eta_d} dev(\boldsymbol{\sigma}) \tag{106}$$

where η_v and η_d are respectively the volumetric viscosity and the deviatoric viscosity of the homogenized material.

By using (*102*), equation (*101*) can be transformed to:

$$(1-b^v)\frac{\mathrm{d}}{\mathrm{dt}}(J^v)=\frac{\mathrm{d}}{\mathrm{dt}}(J_s^v)(1-\phi_0)+\frac{p}{N^v} \tag{107}$$

Combining (*84*) and (*105*), we get:

$$\frac{\mathrm{d}}{\mathrm{dt}}(J^v)=J^v\frac{1}{\eta_v}(\sigma_m+b^v p) \tag{108}$$

Similarly, we can write:

$$\frac{\mathrm{d}}{\mathrm{dt}}(J_s^v)=J_s^v\frac{1}{\eta_{v,s}}\sigma_{m,s} \tag{109}$$

where $\sigma_{m,s}$ is the mean stress within the solid matrix and $\eta_{v,s}$ is the volumetric viscosity of the solid matrix.

Note that $\sigma_{m,s}$ and σ_m satisfy $\sigma_m=\sigma_{m,s}(1-n_l)-pn_l$, entailing $\sigma_{m,s}=(\sigma_m+pn_l)/(1-n_l)$.

By assuming $J_s\cong J_s^v$ and by substituting (*99*), (*108*)-(*109*) into (*107*), we get:

$$(1-b^v)J^v\frac{\sigma_m+b^v p}{\eta_v}=J\frac{\sigma_m+pn_l}{\eta_{v,s}}+\frac{p}{N^v} \tag{110}$$

where we can identify:

$$b^v=1-\frac{J}{J^v}\frac{\eta_v}{\eta_{v,s}} \tag{111}$$

$$\frac{1}{N^v}=\frac{J}{\eta_{v,s}}(b^v-n_l) \tag{112}$$

By assuming $J^e\cong 1$ and thus $J\cong J^v$, equation (*110*) becomes:

$$b^v=1-\frac{\eta_v}{\eta_{v,s}} \tag{113}$$

It is worth noting that the expression of b^v is analogous to its elastic counterpart b (cf. equation (96)).

The poro-viscoelastic behavior is given by combining elasticity equations (*88*), (*90*) and viscosity equations (*105*)-(*106*):

$$tr(\boldsymbol{d})=\frac{1}{K}\left(\frac{d\sigma_m}{dt}+b\frac{dp}{dt}\right)+\frac{1}{\eta_v}(\sigma_m+b^v p) \tag{114}$$

$$dev(\boldsymbol{d})=\frac{1}{2G}\frac{ds_{ij}}{dt}+\frac{1}{2\eta_d}s_{ij} \tag{115}$$

The Lagrangian porosity change rate $d\phi_l/dt$ is given by using equations (74), (88)-(89), (102), (105) and (112):

$$\frac{d\phi_l}{dt}=J^v\left[\left(\frac{d\sigma_m}{dt}+\frac{bdp}{dt}\right)\frac{b}{K}+\frac{1}{N}\frac{dp}{dt}+\frac{b^v}{\eta_v}(\sigma_m+b^v p)\right]+Jp\frac{b^v-n_l}{\eta_{v,s}} \tag{116}$$

In our case where the BWP matrix is assumed to be viscously incompressible (cf. 4.1.1), the term $Jp\frac{b^v-n_l}{\eta_{v,s}}$ can be neglected due to the extremely large volumetric viscosity of the BWP matrix $\eta_{v,s}$ (cf. 5.1 for numerical value of $\eta_{v,s}$).

By assuming $J^e \cong 1$ and thus $J \cong J^v$, (*116*) becomes:

$$\frac{d\phi_l}{dt} = J\left[\left(\frac{d\sigma_m}{dt} + \frac{bdp}{dt}\right)\frac{b}{K} + \frac{1}{N}\frac{dp}{dt} + \frac{b^v}{\eta_v}(\sigma_m + b^v p)\right] \tag{117}$$

Due to the complexity of the numerical implementation of equations (*114*)-(*115*) and (*117*), the following assumptions are made for simplicity:

$$\boldsymbol{d} \cong \frac{d\boldsymbol{\varepsilon}}{dt}$$

$$dev(\boldsymbol{d}) \cong \frac{de_{ij}}{dt}$$

$$J \cong 1 + \varepsilon_v$$

$$tr(\boldsymbol{d}) = \frac{dJ/dt}{J} \cong \frac{d\varepsilon_v}{dt}\frac{1}{1+\varepsilon_v}$$

where $\boldsymbol{\varepsilon}$ is the strain tensor, $\varepsilon_v = tr(\boldsymbol{\varepsilon})$, e_{ij} are the coefficients of the deviatoric strain tensor ($e_{ij} = \varepsilon_{ij} - \frac{1}{3}\varepsilon_v\delta_{ij}$).

Equations (*114*), (*115*) and (*117*) then become:

$$\frac{1}{1+\varepsilon_v}\frac{d\varepsilon_v}{dt} = \frac{1}{K}\left(\frac{d\sigma_m}{dt} + b\frac{dp}{dt}\right) + \frac{1}{\eta_v}(\sigma_m + b^v p) \tag{118}$$

$$\frac{de_{ij}}{dt} = \frac{1}{2G}\frac{ds_{ij}}{dt} + \frac{1}{2\eta_d}s_{ij} \tag{119}$$

$$\frac{d\phi_l}{dt} = (1+\varepsilon_v)\left[\left(\frac{d\sigma_m}{dt} + \frac{bdp}{dt}\right)\frac{b}{K} + \frac{1}{N}\frac{dp}{dt} + \frac{b^v}{\eta_v}(\sigma_m + b^v p)\right] \tag{120}$$

It is worth noting that (*120*) describes the porosity variation due to mechanical loading. The pore volume change due to salt crystal dissolution should also be taken into account. We have therefore:

$$\frac{d\phi_l}{dt} = (1+\varepsilon_v)\left[\left(\frac{d\sigma_m}{dt} + \frac{bdp}{dt}\right)\frac{b}{K} + \frac{1}{N}\frac{dp}{dt} + \frac{b^v}{\eta_v}(\sigma_m + b^v p)\right] - \frac{d\phi_c}{dt} \tag{121}$$

The complete model is summarized as:

$$\frac{1}{1+\varepsilon_v}\frac{d\varepsilon_v}{dt} = \frac{1}{K}\left(\frac{d\sigma_m}{dt} + b\frac{dp}{dt}\right) + \frac{1}{\eta_v}(\sigma_m + b^v p) \tag{118}$$

$$\frac{de_{ij}}{dt} = \frac{1}{2G}\frac{ds_{ij}}{dt} + \frac{1}{2\eta_d}s_{ij} \tag{119}$$

$$\frac{d\phi_l}{dt} = (1+\varepsilon_v)\left[\left(\frac{d\sigma_m}{dt} + \frac{bdp}{dt}\right)\frac{b}{K} + \frac{1}{N}\frac{dp}{dt} + \frac{b^v}{\eta_v}(\sigma_m + b^v p)\right] - \frac{d\phi_c}{dt} \tag{121}$$

$$b = 1 - \frac{K}{K_s} \tag{96}$$

$$b^v = 1 - \frac{\eta_v}{\eta_{v,s}} \tag{111}$$

The temporal discretization of these equations for numerical resolution is detailed in Appendix C.

4.3.4. Homogenization of viscoelastic parameters

By considering the case of a single family of spherical pores embedded in an isotropic solid phase (BWP matrix), the Mori-Tanaka homogenization scheme [33,48] is applied to model the viscoelastic parameters of the homogenized material [39] (cf. 2.5.3 and Appendix B):

$$K = K(n_l) = K_s \frac{\left(4G_s(1-n_l)\right)}{3n_l K_s + 4G_s} \tag{122}$$

$$G = G(n_l) = G_s \frac{1-n_l}{1+\frac{2}{3}n_l} \tag{123}$$

$$\eta_v = \eta_v(n_l) = \eta_{v,s} \frac{\left(4\eta_{d,s}(1-n_l)\right)}{3n_l\eta_{v,s} + 4\eta_{d,s}} \tag{124}$$

$$\eta_d = \eta_d(n_l) = \eta_{d,s} \frac{1-n_1}{1+\frac{2}{3}n_1} \tag{125}$$

$$b = b(n_l) = 1 - \frac{4G_s(1-n_l)}{3n_l K_s + 4G_s} \tag{126}$$

$$b^v = b^v(n_l) = 1 - \frac{4\eta_{d,s}(1-n_l)}{3n_l\eta_{v,s} + 4\eta_{d,s}} \tag{127}$$

where $K_s = \frac{E_s}{3(1-2\nu_s)}$ and $G_s = \frac{E_s}{2(1+\nu_s)}$ are the bulk and the shear modulus of the matrix respectively, $\eta_{v,s}$ and $\eta_{d,s}$ are the volumetric and the deviatoric viscosity of the matrix respectively, E_s is the Young's modulus of the matrix and ν_s is the Poisson's ratio of the matrix.

Fig. 4-3 shows the evolution in terms of porosity of the homogenized viscoelastic parameters using equations (122)-(127). The numerical values summarized in Table 11 will be used for the viscoelastic parameters of the BWP matrix K_s, G_s, $\eta_{v,s}$, $\eta_{d,s}$. The evolution curve of η_v is plotted in Fig. 4-3(c) in logarithmic scale of 10. As a reminder, The BWP matrix is assumed to be viscously incompressible (cf. 4.1.1). To be consistent with this hypothesis, the volumetric viscosity of the BWP matrix $\eta_{v,s}$ is taken as $10^{30}\ Pa.s$ (cf. Table 11). Due to the important value of $\eta_{v,s}$, we can note that $b^v = 0$ for $n_l = 0$ and b^v almost constantly equals to 1 for all other values of porosity.

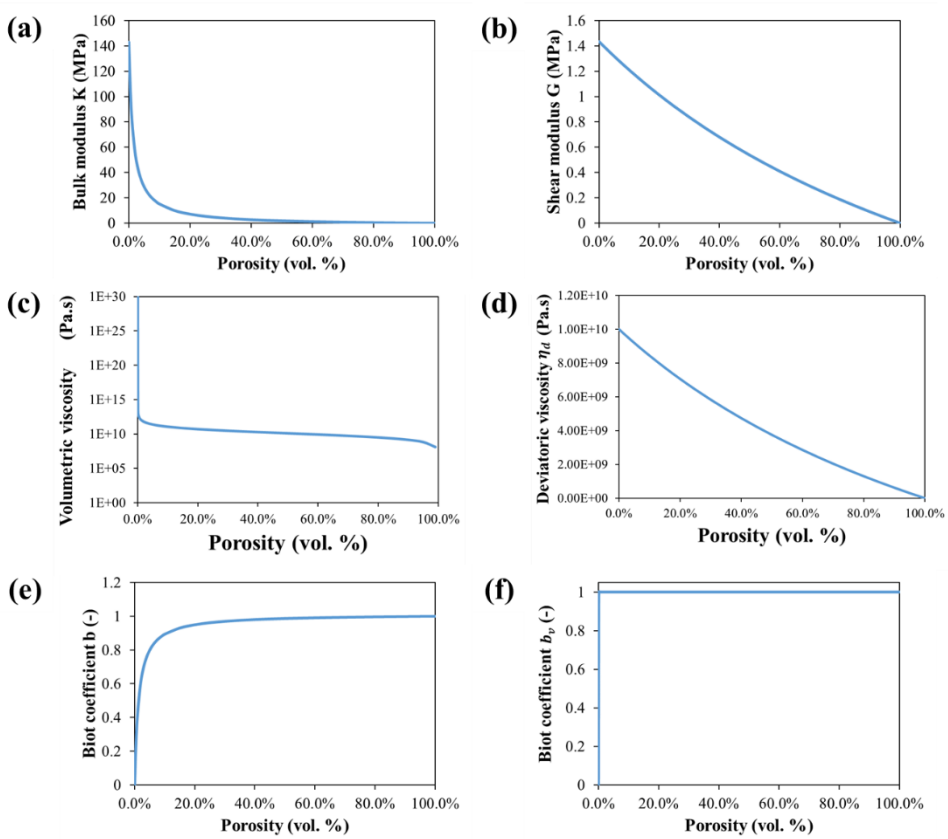

Fig. 4-3 Evolution in terms of porosity of (a) bulk modulus K; (b) shear modulus G; (c) volumetric viscosity η_v (plotted in logarithmic scale of 10); (d) deviatoric viscosity η_d; (e) Biot coefficient b; (f) viscous Biot coefficient b^v.

4.4. Numerical Implementation

The numerical model presented in this chapter is implemented in the Finite Element code BIL developed by P. Dangla [25]. The main unknowns are the displacement u , the pore pressure p and the mass fraction of dissolved salt ω_s. The temporal discretization follows the implicit Euler scheme. The time step is adaptively managed by the code. The Newton-Raphson method is used to solve the nonlinear matrix system obtained after discretization. The FEM simulations were mainly completed in 1D using quadratic 3-node elements. 2D simulations using quadratic 8-node elements were also realized for several typical cases for verification (cf. Appendix F).

CHAPTER 5

NUMERICAL RESULTS

In this section, the model is used to represent leaching tests under different loading conditions. The general material parameters and the modeling description for three types of leaching tests (under free leaching, under constant counter-pressure, and under constant volume conditions) are first presented in section 5.1. The limits of the MELOT2019 model [1,2] are evidenced in 5.2 by the new experimental data. The numerical results of simplified BWPs under free leaching, under constant counter-pressure, and under constant volume conditions are shown respectively in sections 5.3, 5.4 and 5.5. The effect of the existing voids on the stress build-up behavior of BWPs under confined conditions is numerically investigated in section 5.6 by studying the case of free leaching followed by leaching under constant volume conditions. Finally, the leaching behavior of industrial BWPs STE3 and STEL under free leaching and constant volume conditions are presented in section 5.7. The conclusions and perspectives of the numerical results are discussed in 5.8.

5.1. Material parameters and modeling descriptions

The material parameters used in the model are listed in Table 11. The Young's modulus and the Poisson's ratio of the BWP matrix are calculated based on the oedometric results acquired at CEA Marcoule (cf. Appendix D). The deviatoric viscosity of the BWP matrix $\eta_{d,s}$ depends *a priori* on amount of salt crystals contained in BWP matrix. The value used in the model $\eta_{d,s} = 1 \times 10^{10}\ Pa.s$ is determined based on a sensitivity study (cf. Appendix E). All other numerical values listed in Table 11 are kept from [1,2]. The initial porosity n_{l_i} for non-consolidated BWPs is kept as 7% from [1,2]. As the consolidation process eliminates the porosity within the samples (cf. 3.3.1), the initial porosity n_{l_i} is *a priori* infinitesimal for the consolidated BWPs. Sensitivity studies on initial porosity of the consolidated BWPs (cf. 5.4.3) indicate that n_{l_i} has no significant impact on numerical results when n_{l_i} is less than 1%. Finally, $n_{l\_i} = 0.1\%$ is set for the consolidated BWPs. The initial volume fraction of salt crystals ϕ_{c_i} are calculated for each composition based on nominal massive fraction of salt listed in Table 2.

Table 11 Numerical values of material parameters used in the model.

Parameter	Notation	Value
Deviatoric viscosity of BWP matrix	$\eta_{d,s}$	$1 \times 10^{10}\ Pa.s$
Volumetric viscosity of BWP matrix	$\eta_{v,s}$	$1 \times 10^{30}\ Pa.s$
Young's modulus of BWP matrix	E_s	$4.3 \times 10^{6}\ Pa$
Poisson's ratio of BWP matrix	ν_s	0.495
Initial liquid density	ρ_l	$1000\ kg.m^{-3}$
Salt crystal dissolution rate	β	$10^{-5}\ kg.s^{-1}.m^{-3}$
Specific surface of salt crystal	σ_c	$148 m^{-1}$
Specific partial volume of water	v_w	$1 \times 10^{-3}\ m^3.kg^{-1}$

The material parameters concerning salt crystal and dissolved salt for $NaNO_3$ are summarized in Table 12 and for Na_2SO_4 in Table 13. The specific partial volume of dissolved salt v_s are calculated based on data of aqueous solutions of $NaNO_3$ and Na_2SO_4 published in [30].

Table 12 Numerical values of material parameters for $NaNO_3$.

Parameter	Notation	Value
Salt crystal density	ρ_c	$2260\ kg.m^{-3}$
Molar mass of salt	M_s	$85 \times 10^{-3}\ kg.mol^{-1}$
Stoichiometric number of moles of ions in one mole of salt	ν_N	2
Specific partial volume of dissolved salt	v_s	$5 \times 10^{-4}\ m^3.kg^{-1}$
Water solubility of salt at 25℃	S	$0.912\ kg.kg^{-1}$

Table 13 Numerical values of material parameters for Na_2SO_4.

Parameter	Notation	Value
Salt crystal density	ρ_c	$2660\ kg.m^{-3}$
Molar mass of salt	M_s	$142 \times 10^{-3}\ kg.mol^{-1}$
Stoichiometric number of moles of ions in one mole of salt	ν_N	3
Specific partial volume of dissolved salt	v_s	$2 \times 10^{-4}\ m^3.kg^{-1}$
Water solubility of salt at 25℃	S	$0.195\ kg.kg^{-1}$

The geometry is one-dimensional plane strain modeling. Simulations in two-dimensional plane strain modeling are also performed to verify the independence of the numerical results with respect to the dimension (cf. Appendix F). The initial and boundary conditions for tests under free leaching conditions, under constant counter-pressure, and under constant volume conditions are respectively shown in Fig. 5-1, Fig. 5-2 and Fig. 5-3. The weight, height and cross-section of the BWP samples used for leaching tests under free and constant counter-pressure conditions are summarized respectively in Table 14 and Table 15.

Fig. 5-1 Geometry and boundary conditions of the numerical problem under free leaching conditions.

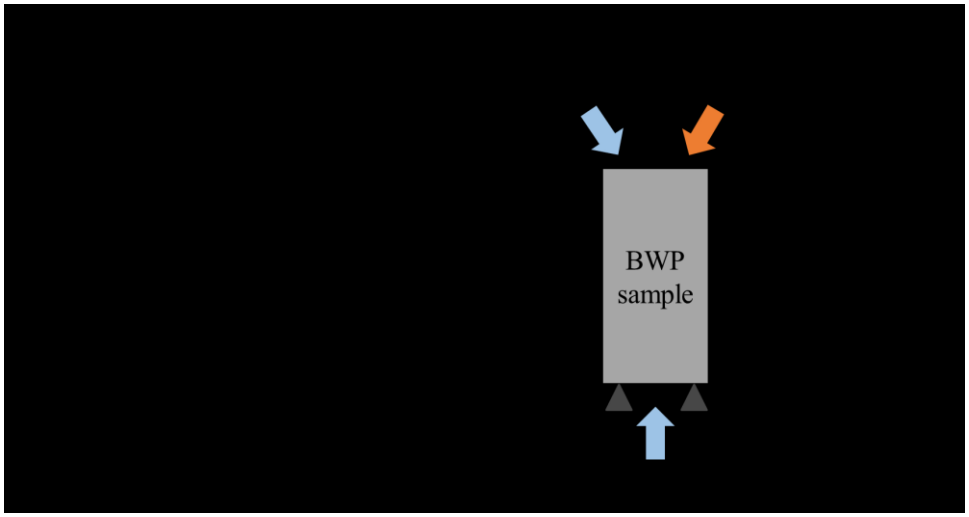

Fig. 5-2 Geometry and boundary conditions of the numerical problem under constant counter-pressure.

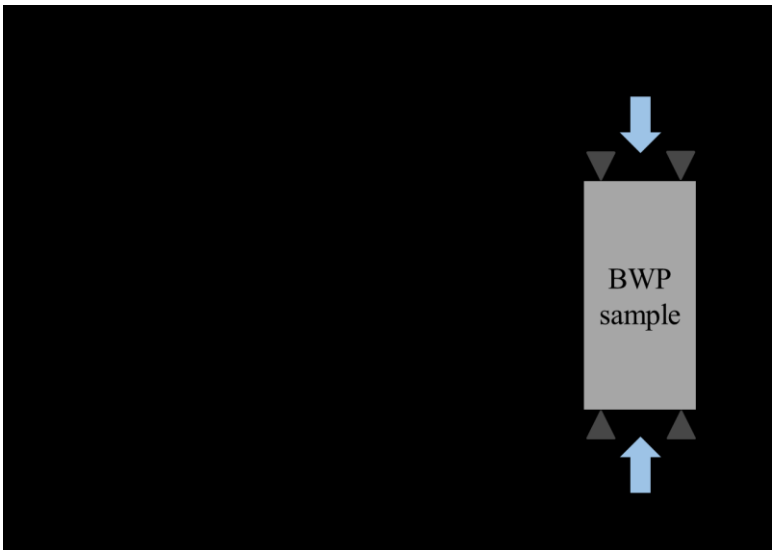

Fig. 5-3 Geometry and boundary conditions of the numerical problem under constant volume conditions

Table 14 Weight, height and cross-section of the BWP samples used for free leaching tests.

Sample	Weight (g)	Height (mm)	Cross-section (cm^2)
M5_NaNO3	10.06 ± 0.11	5.1 ± 0.05	18.85
M10_NaNO3	10.00 ± 0.05	5.0 ± 0.02	
M20_NaNO3	10.02 ± 0.03	4.6 ± 0.01	
M30_NaNO3	10.05 ± 0.07	4.6 ± 0.03	
M10_Na2SO4			
M25_Na2SO4	N/A	N/A	13.6
M40_Na2SO4			
M5_BaSO4	10.04 ± 0.05	4.9 ± 0.02	
M10_BaSO4	10.05 ± 0.04	4.9 ± 0.02	
M20_BaSO4	10.03 ± 0.06	4.4 ± 0.03	18.85
M30_BaSO4	10.03 ± 0.05	4.1 ± 0.02	
M40_BaSO4	10.04 ± 0.03	3.9 ± 0.01	
M5_NaNO3_M35_BaSO4	9.91 ± 0.27	4 ± 0.1	
M10_NaNO3_M30_BaSO4	10.02 ± 0.06	4.3 ± 0.03	18.85
M20_NaNO3_M20_BaSO4	9.97 ± 0.08	4.0 ± 0.03	
STEL	10.06 ± 0.07	3.8 ± 0.02	18.85
STE3	10.01 ± 0.06	3.7 ± 0.02	

Table 15 Weight, height after consolidation, and cross-section of the BWP samples used for leaching tests under constant counter-pressure.

Sample	Weight (g)	Height after consolidation (mm)	Cross-section (cm^{-2})
M30_NaNO3	13.59 ± 0.30	9.9 ± 0.03	11.34
M10_NaNO3_M30_BaSO4	13.96 ± 0.003	9.393 ± 0.135	

As mentioned in section 4.2, the four material parameters, $\alpha_w, \alpha_s, D_w^{mat}, D_s^{mat}$, appear in the form of two products $\alpha_w D_w^{mat}$ and $\alpha_s D_s^{mat}$. Therefore, $\alpha_w D_w^{mat}$ and $\alpha_s D_s^{mat}$ are chosen to be the two fitting parameters of the numerical model. For each BWPs composition, the parameters are first calibrated based on experimental results (water uptake and sample swelling) of free leaching tests. The fitted parameters are then tested for leaching under constant counter-pressure or constant volume conditions.

5.2. Limits of the MELOT2019 model evidenced by the new experimental data

In this section, the limits of the MELOT2019 [1,2] model are illustrated by comparing the numerical results produced using MELOT2019 with the newly acquired experimental data, especially the BWPs' swelling data under free leaching conditions.

As a reminder, the transport terms (diffusion, permeation, osmosis) are modeled by separate laws in the MELOT2019 model [1,2]:

$$D_{eff} = D_i \left(1 + \frac{3n_l}{1 - n_l}\right) \tag{128}$$

$$k = k_i \left(1 + \frac{3n_l}{1 - n_l}\right) \tag{129}$$

$$\tau = \tau_0 \frac{n_{l\_i}}{n_l} \tag{130}$$

$$W_{Fick} = -\rho_l D_{eff} \nabla \omega_s \tag{131}$$

$$W_{Darcy} == -\rho_l k \nabla p \tag{132}$$

$$W_{Osmosis} = \rho_l k \frac{RT}{M_s} \rho_l \tau \nabla \omega_s \tag{133}$$

where D_{eff} is the salt effective diffusion coefficient, k is the effective permeability coefficient, τ is the osmotic efficiency coefficient, W_{Fick}, W_{Darcy} and $W_{Osmosis}$ are respectively the massive flux due to diffusion, permeation, and osmosis (cf. 2.2). The initial permeability coefficient k_i, the initial salt effective diffusion coefficient d_i and the initial osmotic efficiency coefficient τ_i are the fitting parameters.

The parameters k_i, d_i and τ_i fitted on the amount of water uptake and released salts of mono-salt $NaNO_3$ BWPs [1,2] are summarized in Table 16. It should be emphasized that the experimental data on BWP swelling were not available during the development of the MELOT2019 model. Fig. 5-4 shows the numerical predictions of water uptake and swelling of M20_NaNO3 mono-salt BWP using the

MELOT2019 model and parameters reported in [1,2]. The numerical results are significantly lower than the experimental values.

Table 16 Parameters of the MELOT2019 model fitted on the amount of water uptake and released salts of mono-salt $NaNO_3$ BWPs [1,2].

Parameter	Value
k_i	$5 \times 10^{-22}\ m^2.Pa^{-1}.s^{-1}$
d_i	$2 \times 10^{-15}\ m^2.s^{-1}$
τ_i	0.135

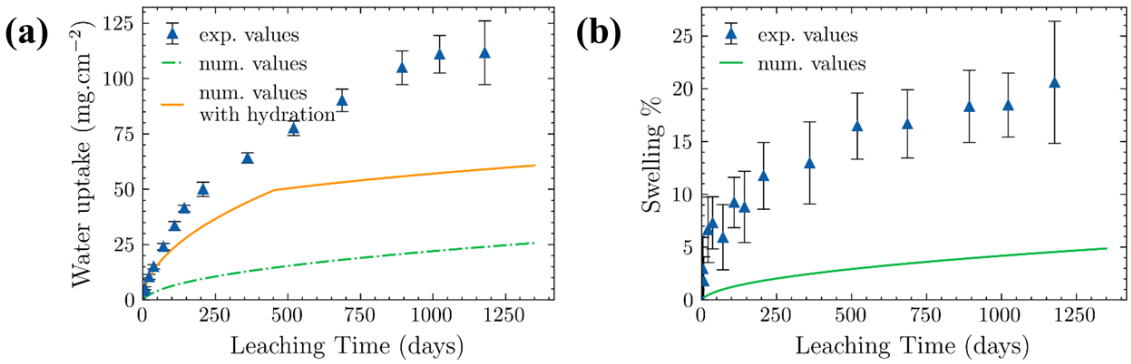

Fig. 5-4 Numerical and experimental results of the temporal evolution of (a) absorbed water; (b) swelling of M20_NaNO3 mono-salt BWP using the MELOT2019 model and parameters reported in [1,2].

In order to reproduce numerical results in the same order of magnitude as the experimental results using the MELOT2019 model, we need to set the osmotic efficiency coefficient τ constantly equal to its initial value ($\tau = \tau_i$). The fitted parameters and the resulting numerical results are shown in Table 17 and Fig. 5-5. The experimental results are well reproduced. However, a constant osmotic efficiency coefficient τ means that the osmotic capacity of the BWP matrix remains unchanged over leaching time, even with a possible significant increase in porosity (from ~7% up to ~65%). Such a hypothesis of a constant osmotic efficiency coefficient is unlikely consistent with the real physical phenomena involved in the BWP leaching process. Moreover, since the three transport terms (diffusion, permeation, osmosis) are in fact deeply coupled, separately modeling them could lead to non-physical fitting results exceeding the validity domain of the MELOT2019 model.

Table 17 Parameters fitted on water uptake and swelling of mono-salt M20_NaNO3 BWPs using MELOT2019 model with constant osmotic efficiency coefficient τ.

Parameter	Value
k_i	$1.2 \times 10^{-22}\ m^2.Pa^{-1}.s^{-1}$
d_i	$0.4 \times 10^{-15}\ m^2.s^{-1}$
τ_i	0.9

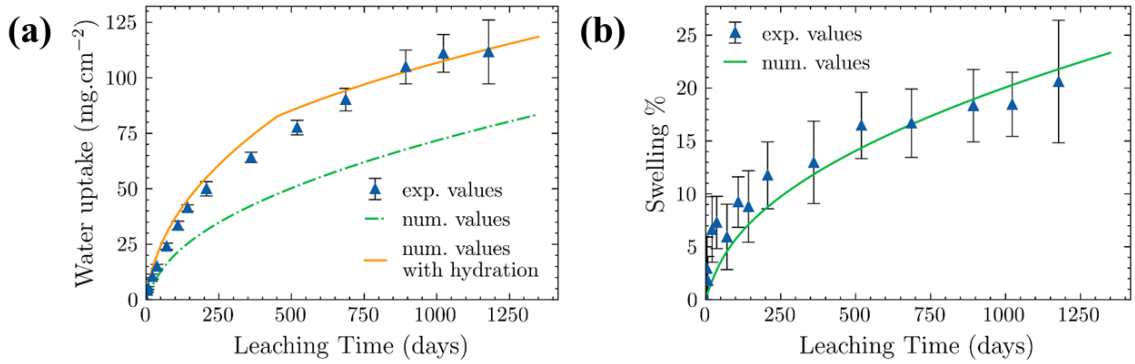

Fig. 5-5 Numerical and experimental results of the temporal evolution of (a) absorbed water; (b) swelling of M20_NaNO3 mono-salt BWP using MELOT2019 model with constant osmotic efficiency coefficient τ.

Furthermore, while the MELOT2019 model gives consistent results for free leaching tests, it has not been able to model the leaching tests under confined conditions. In this case, numerical divergences appear, and the mechanical model is suspected. Indeed, under free leaching without mechanical loading, constitutive mechanical law plays a minor role, which is not the case in confined conditions.

Therefore, an innovative flux formulation with coupled homogenization of transport terms (diffusion, permeation, and osmosis) is proposed in 4.2 to better capture the role of the semi-permeable membrane played by the bitumen and the porosity-dependency of the coupled transport coefficients during the leaching process. A non-linear poro-viscoelastic model taken into account large strains along with a homogenization of the viscoelastic parameters is proposed in 4.3. In the rest of this chapter, the model presented in CHAPTER 4 is applied to the numerical calculations.

5.3. Simplified BWPs under free leaching conditions

This section shows the numerical results of simplified BWPs under free leaching conditions. The model parameters are fitted for mono-salt $NaNO_3$ BWPs (5.3.1), mono-salt Na_2SO_4 BWPs (5.3.2), and bi-salt BWPs (5.3.3) by using the experimental results presented in 3.2. The fitted parameters are discussed in 5.3.4. The simulated released salt fractions are discussed in 5.3.5.

5.3.1. Mono-salt $NaNO_3$ BWPs

In this section, the model parameters are first calibrated on mono-salt M20_NaNO3 BWPs. The obtained parameters are then tested on other mono-salt BWPs incorporating different concentrations of $NaNO_3$ (M5_NaNO3, M10_NaNO3, and M30_NaNO3).

The hydration kinetics, defined as the progression of the hydration front that would lead to the filling of initial pores, is assumed to be identical for all mono-salt $NaNO_3$ BWPs. About 2.3 mm of hydration is experimentally observed at 1400 leaching days on M30_NaNO3 BWPs (cf. Fig. 3-9(c)). By assuming the progression of the hydration front behaves linearly with the square root of time (cf. 4.1.5), we have $t_f = 5520$ days by using the height of the M20_NaNO3 BWP sample listed in Table 14. Different values of t_f are estimated for other mono-salt $NaNO_3$ by using their heights listed in Table 14.

The parameters calibrated on experimental results of M20_NaNO3 mono-salt BWPs are shown in Table 18. The numerical and experimental results of water uptake amount and swelling are presented in

Fig. 5-6. The present model shows the ability to well reproduce all experimental results acquired during free leaching tests conducted on M20_NaNO3 mono-salt BWPs with the calibrated parameters.

Table 18 Parameters calibrated on experimental results of M20_NaNO3 mono-salt BWP.

Parameter	Value
$\alpha_w D_w^{mat}$	$8 \times 10^{-15}\ m^2.s^{-1}$
$\alpha_s D_s^{mat}$	$4.4 \times 10^{-16}\ m^2.s^{-1}$

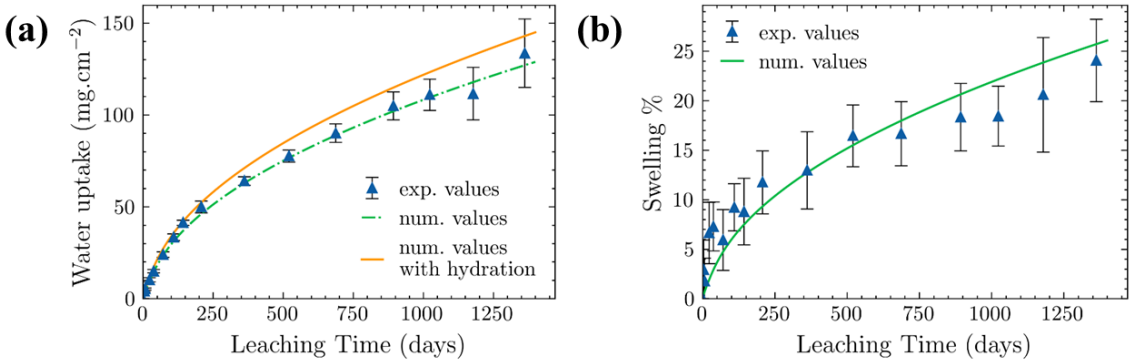

Fig. 5-6 Numerical and experimental results of the temporal evolution of (a) absorbed water; (b) swelling of M20_NaNO3 mono-salt BWP.

Fig. 5-7 shows the profiles along the sample of the Eulerian porosity and the transport coefficients at different leaching times. At the leaching border (position = 0 m), the porosity significantly increases from 7 % to a maximum of about 65 % and remains almost constant for increasing leaching time. The increase in the porosity propagates toward the bottom of the sample over leaching time. The effective permeability coefficient k, the effective diffusion coefficient of dissolved salt D_{eff} and the osmotic efficiency coefficient τ take their extreme value logically at the leaching border, located at 0 m, due to the important porosity.

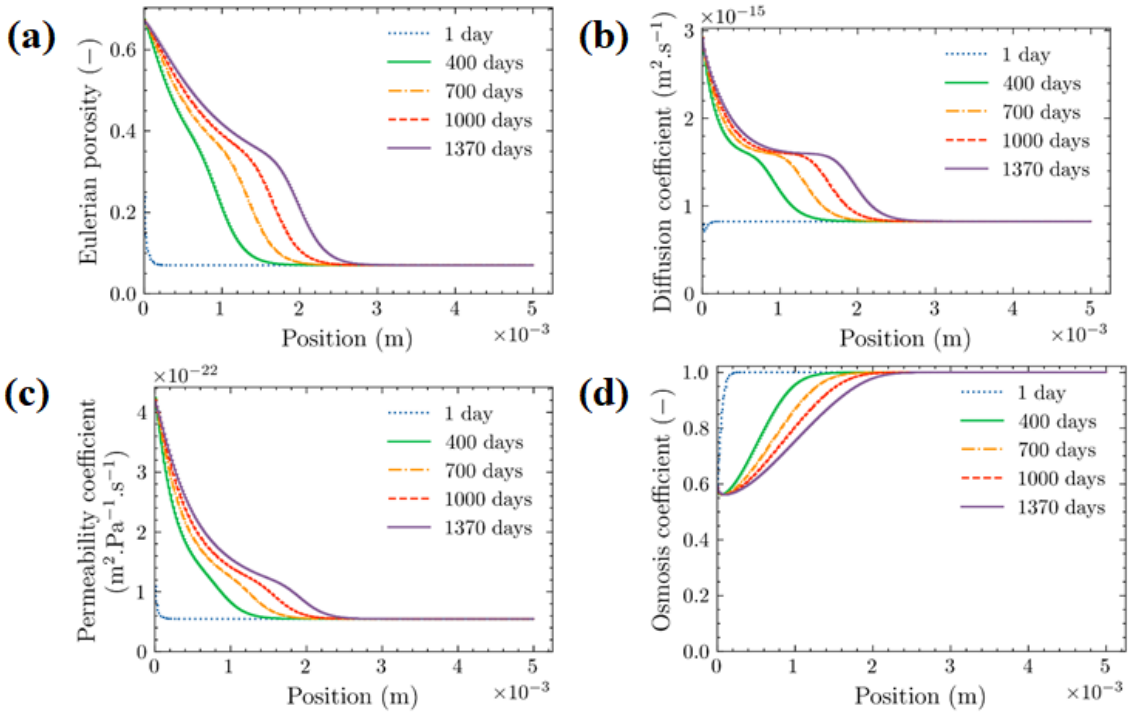

Fig. 5-7 Profile along the sample of (a) Eulerian porosity; (b) effective diffusion coefficient of dissolved salt; (c) effective permeability coefficient; (d) osmotic efficiency coefficient at different leaching times of M20_NaNO3 mono-salt BWP.

By varying ϕ_{c_i} for different compositions, the fitted parameters are then used to reproduce the experimental results obtained from M5_NaNO3 (Fig. 5-8) and M10_NaNO3 (Fig. 5-9) mono-salt BWPs. Given the important measurement uncertainties, the model prediction is successful for these two compositions. The parameters calibrated on M20_NaNO3 mono-salt BWP are thus consistent on M5_NaNO3 and M10_NaNO3 mono-salt BWPs.

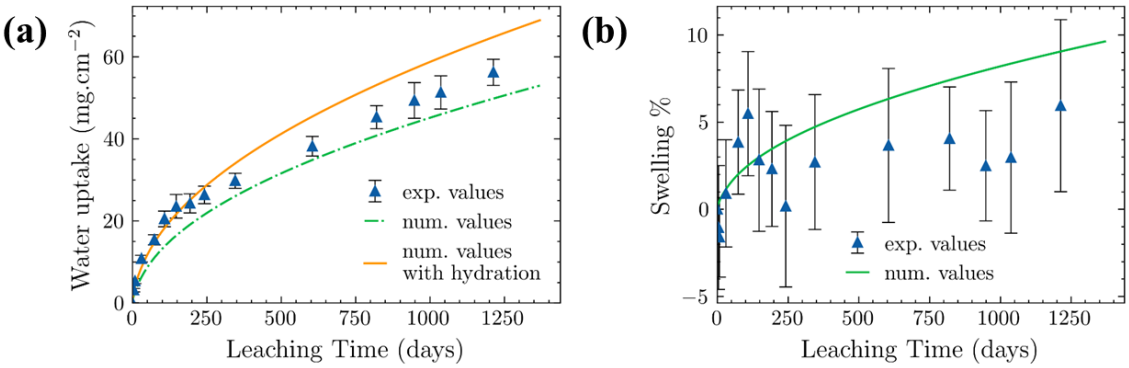

Fig. 5-8 Numerical and experimental results of the temporal evolution of (a) absorbed water; (b) swelling of M5_NaNO3 mono-salt BWP.

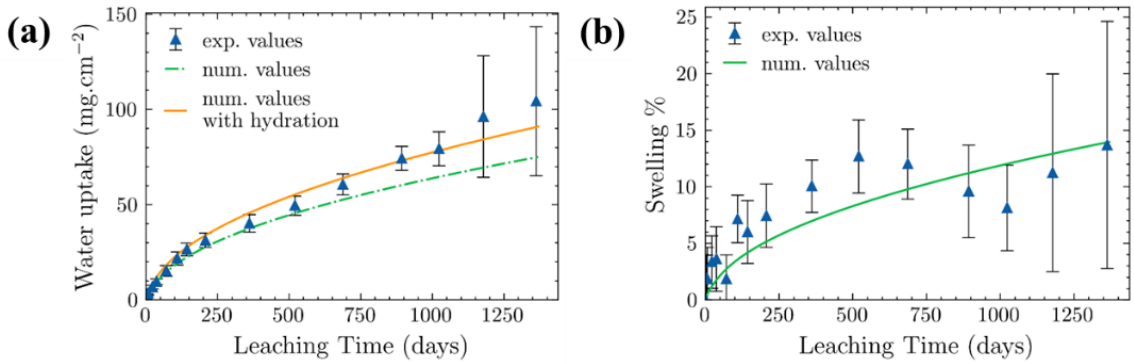

Fig. 5-9 Numerical and experimental results of the temporal evolution of (a) absorbed water; (b) swelling of M10_NaNO3 mono-salt BWP.

Fig. 5-10 (b) and (c) illustrate a comparison of numerical results reproduced using the above fitted parameters and experimental results of M30_NaNO3. The swelling (Fig. 5-10 (c)) is well reproduced while the numerical values of water uptake (Fig. 5-10 (b)) exceed the experimental measurements. Profiles of porosity along the sample at different leaching times (Fig. 5-10 (a)) indicate a porosity of about 75 vol. % near the leaching surface (Position = 0 m). As shown in section 3.2, the water uptake of M30_NaNO3 might be underestimated due to the large local porosity near the leaching surface. The important porosity predicted near the leaching surface is consistent with this hypothesis. The parameters calibrated on M20_NaNO3 BWPs are thus validated on M5_NaNO3, M10_NaNO3, and M30_NaNO3. They can therefore be considered as parameters for mono-salt $NaNO_3$ BWPs.

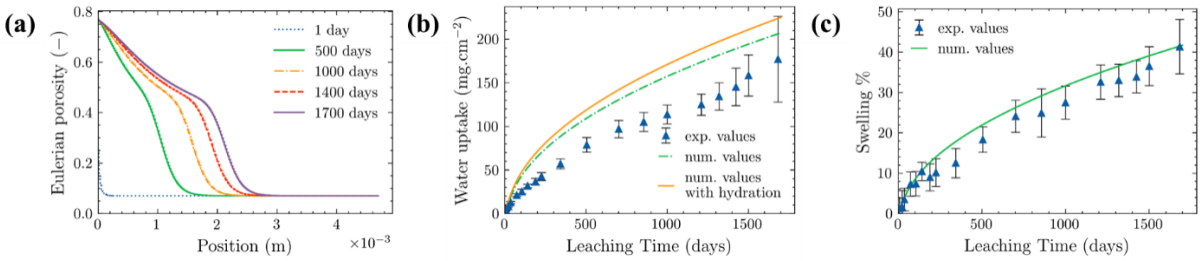

Fig. 5-10 (a) Profile along the sample of porosity at different leaching times. Numerical and experimental results of the temporal evolution of (b) absorbed water; (c) swelling of M30_NaNO3 mono-salt BWP.

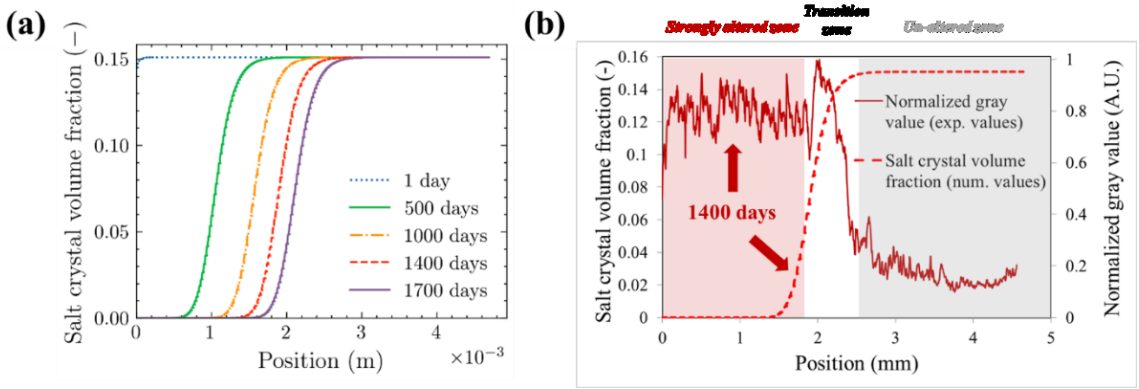

Fig. 5-11 (a) Profile along the sample of salt crystal volume fraction at different leaching times; (b) profiles along the sample of salt crystal volume fraction and normalized gray shade value at 1400 days of leaching for M30_NaNO3 mono-salt BWP.

The profile along the sample of salt crystal volume fraction ϕ_c at different leaching times is presented in Fig. 5-11 (a). At each leaching time, three different zones can be identified: the strongly altered zone where $\phi_c \cong 0$, the un-altered zone where ϕ_c remains at its initial value, and a transition zone between

the two previous areas. The transition zone propagates toward the bottom of the sample over leaching time, enlarging the strongly altered zone and reducing the unaltered zone. Gray shade profiles measured on ESEM images along the M30_NaNO3 sample after 1400 days of leaching were evaluated based on the reconstructed profile (Fig. 3-9(c)) and normalized by the brightest point. The obtained normalized gray shades profile at 1400 leaching days is presented in Fig. 5-11 (b). Three zones can be identified as well: (i) a first zone corresponding to a strongly altered zone, wherein the normalized gray shade value is noisy and ranges between 0.7 and 0.9, reflecting the presence of pores; (ii) A second zone corresponding to an un-altered zone where gray value is about 0.2, (iii) a transition zone between the two previous areas, where a hump in the gray shade values is observed, without any empty pores. It is worth noting that these zones, identified from the experimental normalized gray value profile, are consistent with those determined from the numerically simulated profile of salt crystal volume fraction.

5.3.2. Mono-salt Na_2SO_4 BWPs

In this section, the parameters calibrated on mono-salt $NaNO_3$ BWPs (cf. Table 18) are tested on mono-salt Na_2SO_4 BWPs (M10_Na2SO4, M25_Na2SO4, and M40_Na2SO4).

Due to the lack of experimental data on hydration kinetics for mono-salt Na_2SO_4 BWPs, the hydration kinetics used for the mono-salt $NaNO_3$ BWPs in 5.3.1 are kept in this section. As mentioned in 3.2.2, the water uptake amount is the only available data for the free leaching tests on mono-salt Na_2SO_4 BWPs.

It should be emphasized that the experimental water uptake is well reproduced for M10_Na2SO4 (Fig. 5-12) and M25_Na2SO4 (Fig. 5-13) by using the same parameters calibrated on mono-salt $NaNO_3$ BWPs. However, a gap has been observed between the numerical and experimental values of water uptake for M40_Na2SO4 (Fig. 5-14). Similarly to M30_NaNO3 (cf. section 3.2), the experimental water uptake amount of M40_Na2SO4 might be underestimated due to the large local porosity near the leaching surface.

The model can well reproduce in general the experimental results of mono-salt Na_2SO_4 BWPs, which shows the validity of the model for BWPs containing different soluble salts. As a reminder, the calibration parameters $\alpha_w, \alpha_s, D_w^{mat}$, D_s^{mat} characterize the transport properties of the BWP matrix, composed of pure bitumen and salt crystals. The fact that the parameters calibrated on mono-salt $NaNO_3$ BWPs can well reproduce the experimental results of mono-salt Na_2SO_4 BWPs indicates that the type of soluble salt (sodium nitrate and sodium sulfate) has *a priori* no significant impact on the transport properties of the BWP matrix.

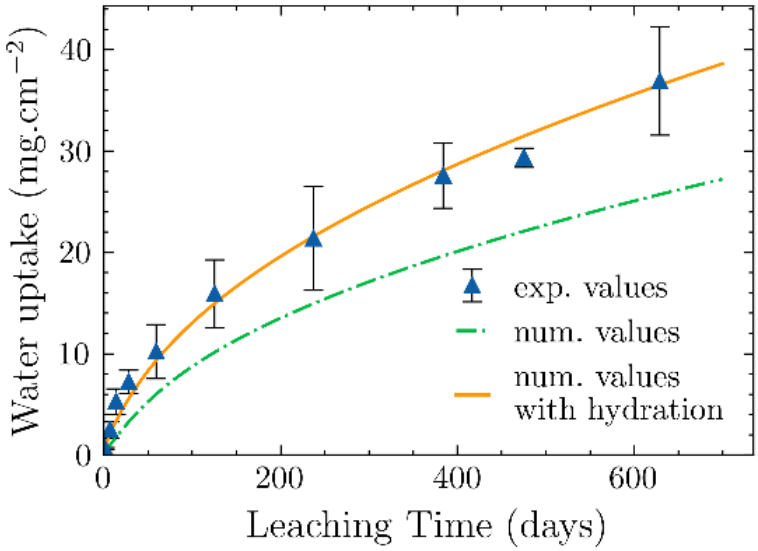

Fig. 5-12 Numerical and experimental results of the temporal evolution of absorbed water of M10_Na2SO4 mono-salt BWP.

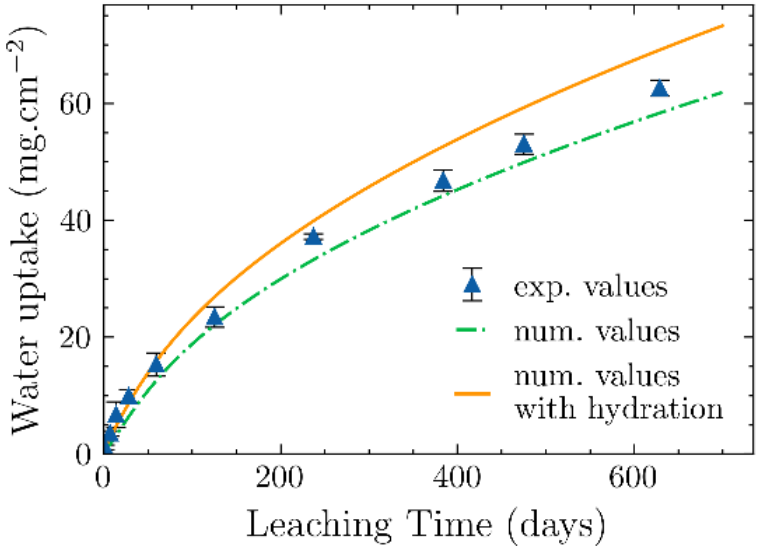

Fig. 5-13 Numerical and experimental results of the temporal evolution of absorbed water of M25_Na2SO4 mono-salt BWP.

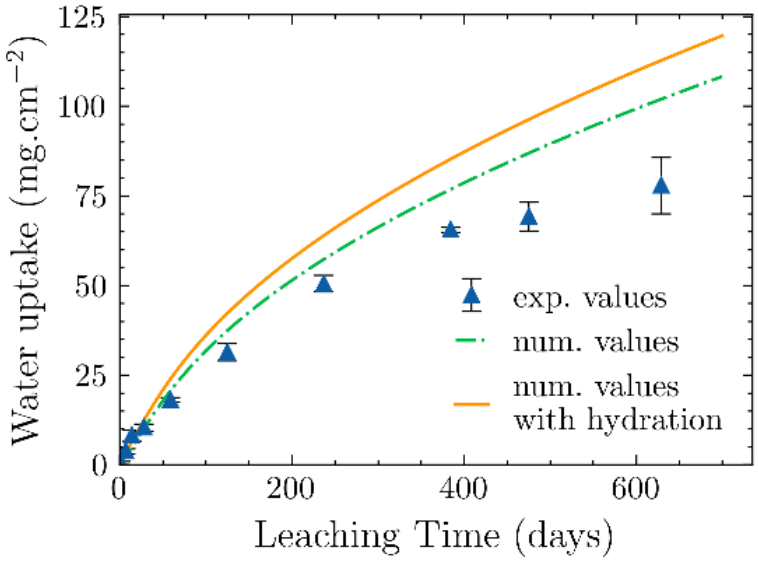

Fig. 5-14 Numerical and experimental results of the temporal evolution of absorbed water of M40_Na2SO4 mono-salt BWP.

5.3.3. Bi-salt $NaNO_3/BaSO_4$ BWPs

Table 19 summarizes the model parameters calibrated for three bi-salt BWPs: M5_NaNO3_M35_BaSO4, M10_NaNO3_M30_BaSO4 and M20_NaNO3_M20_BaSO4.

Table 19 Parameters calibrated on experimental results of bi-salt BWPs M5_NaNO3_M35_BaSO4, M10_NaNO3_M30_BaSO4, and M20_NaNO3_M20_BaSO4.

Composition	$\alpha_w D_w^{mat}(m^2.s^{-1})$	$\alpha_s D_s^{mat}(m^2.s^{-1})$
M5_NaNO3_M35_BaSO4	2×10^{-12}	6.3×10^{-14}
M10_NaNO3_M30_BaSO4	3×10^{-13}	1.35×10^{-14}
M20_NaNO3_M20_BaSO4	1.5×10^{-14}	1.6×10^{-15}

Due to a lack of experimental data, the hydration kinetics of bi-salt BWPs is estimated from [18]: 0.5 mm of hydration at 120 leaching days. The numerical and experimental results of the amount of water uptake and swelling are presented in Fig. 5-15, Fig. 5-16 and Fig. 5-17 for M5_NaNO3_M35_BaSO4, M10_NaNO3_M30_BaSO4 and M20_NaNO3_M20_BaSO4 respectively. The stabilization stage observed at about 1330 leaching days on the M5_NaNO3_M35_BaSO4 bi-salt BWP is well reproduced by the present model, which shows that the model is valid for the entire leaching process. The amount of water uptake and swelling are well reproduced for M5_NaNO3_M35_BaSO4 (Fig. 5-15 (a), (b)) and M10_NaNO3_M30_BaSO4 (Fig. 5-16(a), (b)).

The swelling results are well reproduced for M20_NaNO3_M20_BaSO4 (Fig. 5-17(b)) while a gap between the experimental and numerical values of water uptake amount (Fig. 5-17(a)) has been observed. Similarly to M30_NaNO3 (cf. section 3.2), the experimental water uptake amount of M20_NaNO3_M20_BaSO4 might be underestimated due to the large local porosity near the leaching surface.

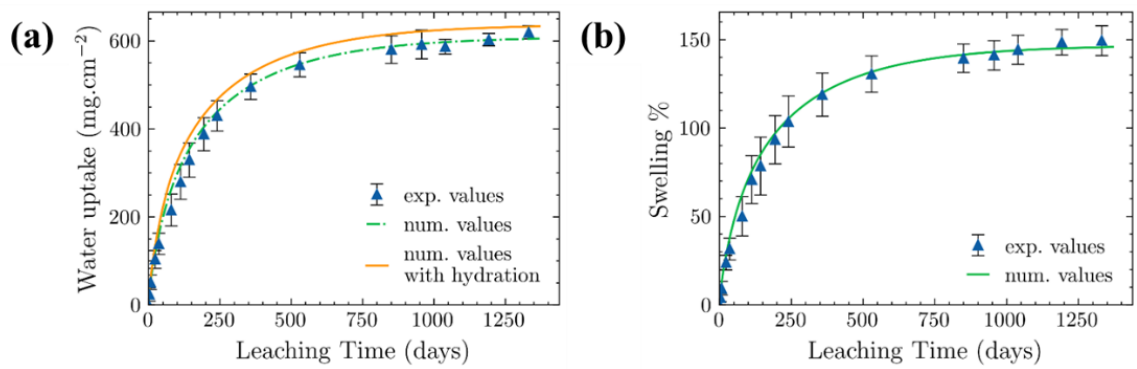

Fig. 5-15 Numerical and experimental results of the temporal evolution of (a) absorbed water; (b) swelling of M5_NaNO3_M35_BaSO4 bi-salt BWP.

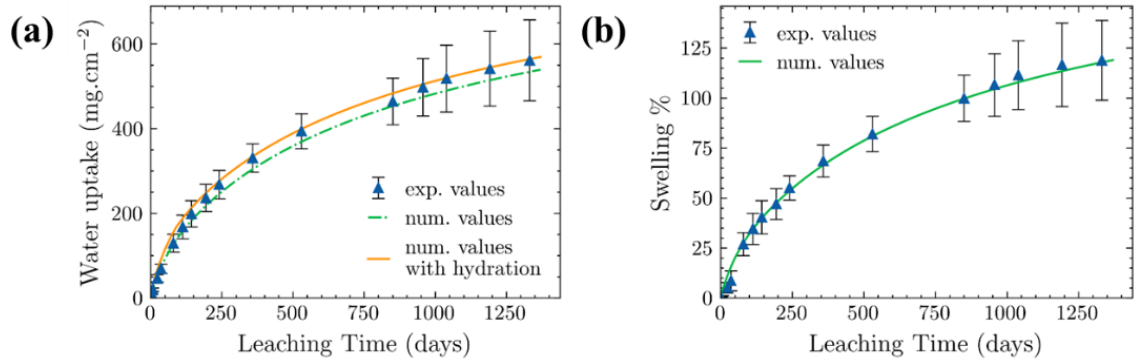

Fig. 5-16 Numerical and experimental results of the temporal evolution of (a) absorbed water; (b) swelling of M10_NaNO3_M30_BaSO4 bi-salt BWP.

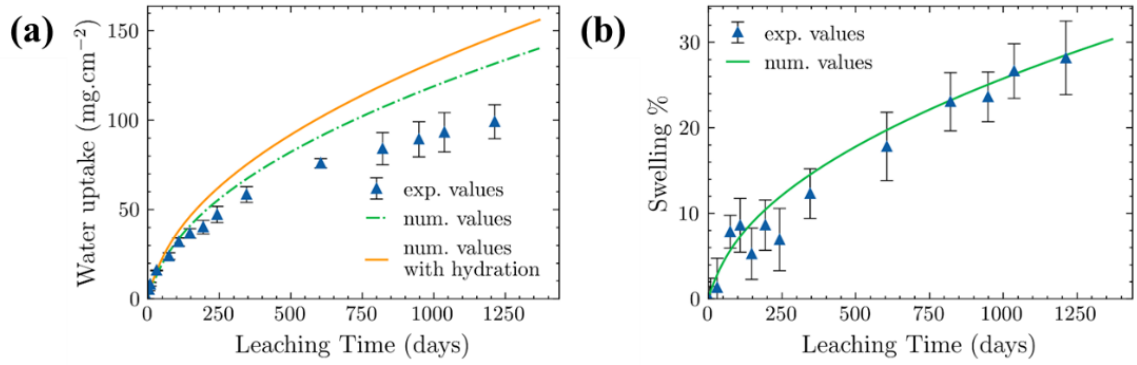

Fig. 5-17 Numerical and experimental results of the temporal evolution of (a) absorbed water; (b) swelling of M20_NaNO3_M20_BaSO4 bi-salt BWP.

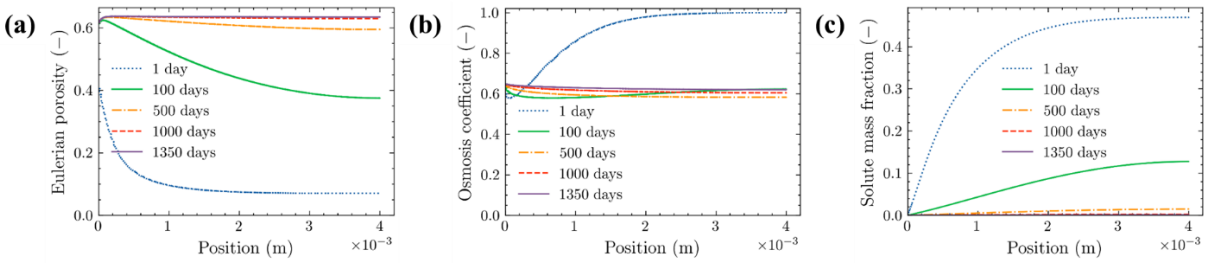

Fig. 5-18 Profile along the sample of (a) Eulerian porosity; (b) osmotic efficiency coefficient; (c) solute mass fraction of M5_NaNO3_M35_BaSO4 bi-salt BWP.

Fig. 5-18 shows the profile of the Eulerian porosity, the osmotic efficiency coefficient τ, and the solute mass fraction ω_s along the M5_NaNO3_M35_BaSO4 bi-salt BWP. The Eulerian porosity (Fig. 5-18 (a)) has significantly increased to ~ 62% in the whole sample after 1350 days of leaching. However, the osmotic efficiency coefficient τ (Fig. 5-18 (b)) stabilized at about 0.6 in the entire sample, indicating that the bituminous matrix's semi-permeable capacity is partially kept even at large porosity. Therefore, the reduction of the osmosis intensity and thus the stabilization stage is actually due to the significant decrease of ω_s (Fig. 5-18 (c)) and $\nabla\omega_s$ in the whole sample.

5.3.4. Discussions about fitted parameters

Table 20 summarizes the model parameters for mono-salt $NaNO_3$ BWPs, mono-salt Na_2SO_4 BWPs and bi-salt $NaNO_3$/$BaSO_4$ BWPs.

Table 20 Parameters calibrated on experimental results of mono-salt $NaNO_3$ BWPs and bi-salt $NaNO_3$/$BaSO_4$ BWPs.

Composition	$\alpha_w D_w^{mat} (m^2.s^{-1})$	$\alpha_s D_s^{mat} (m^2.s^{-1})$
M5_NaNO3		
M10_NaNO3		
M20_NaNO3		
M30_NaNO3	8×10^{-15}	4.4×10^{-16}
M10_Na2SO4		
M25_Na2SO4		
M40_Na2SO4		
M5_NaNO3_M35_BaSO4	2×10^{-12}	6.3×10^{-14}
M10_NaNO3_M30_BaSO4	3×10^{-13}	1.35×10^{-14}
M20_NaNO3_M20_BaSO4	1.5×10^{-14}	1.6×10^{-15}

B. Gwinner [16] experimentally measured the solubility of pure water in a straight run 70/100 bitumen, as the one used in this study to elaborate BWPs, and reported a value of $\alpha_w = 5.6\% \pm 1.2\%$. Values for the water diffusion coefficient in bitumen D_w^{mat} reported in the literature range between 2.5×10^{-14} and $2.3 \times 10^{-12}\ m^2.s^{-1}$ [16,50–53]. The value $8.6 \pm 1.2 \times 10^{-14}\ m^2.s^{-1}$ [16], experimentally measured in 70/100 bitumen (the one used in this study to elaborate BWPs), is consistent with the values reported in the literature and is used for D_w^{mat}. The value of the product $\alpha_w D_w^{mat}$ calculated from previous experimental results reported by B. Gwinner [16] is equal to $4.8 \times 10^{-15}\ m^2.s^{-1}$. Such a value is of the same order of magnitude as the one calibrated on mono-salt $NaNO_3$ BWPs and validated on mono-salt Na_2SO_4 BWPs in this work ($8 \times 10^{-15}\ m^2.s^{-1}$). This consistency reveals that the sodium nitrate and sodium sulfate soluble salt has *a priori* no effect on α_w and D_w^{mat}.

On the other hand, parameters calibrated on bi-salt BWPs lead to higher values than those calibrated on mono-salt $NaNO_3$ BWPs. Table 21 summarizes the growth rate of $\alpha_w D_w^{mat}$ and $\alpha_s D_s^{mat}$ for three bi-salt $NaNO_3$/ $BaSO_4$ BWPs compared to the parameters fitted on mono-salt $NaNO_3$ BWPs.$\alpha_w D_w^{mat}$ and $\alpha_s D_s^{mat}$ calibrated on M20_NaNO3_M20_BaSO4 are 2 and 4 times larger than those calibrated on M20_NaNO3. As $BaSO_4$ crystals represent about 5.7 vol. % in M20_NaNO3_M20_BaSO4, they have *a priori* no significant impact on the solubility factor of water α_w and dissolved salt α_s in the bi-salt BWP matrix. By assuming this, the difference in calibrated parameters is therefore solely due to the difference in diffusion coefficients of water D_w^{mat} and dissolved salt D_s^{mat} in the BWP matrix.

The present model allows therefore to roughly quantify the impact of $BaSO_4$ on the diffusion coefficients of water and dissolved salt in the BWP matrix. D_w^{mat} and D_s^{mat} calibrated on M20_NaNO3_M20_BaSO4 are 2 and 4 times larger than those in the mono-salt $NaNO_3$ matrix, respectively. This increase of diffusion coefficients in the presence of poorly soluble salts is consistent with the existing results in the literature [17–19], which reported that the insoluble salts finely dispersed in a bitumen matrix enhance the water progression in the material. The experimentally observed acceleration effect in the presence of $BaSO_4$ crystals (cf. section 3.2.5) could be explained by the increased water and salt diffusion coefficients in the BWP matrix. Moreover, this increase of D_w^{mat} and D_s^{mat} becomes larger as the mass concentration of $BaSO_4$ crystals increases. The parameters calibrated on M5_NaNO3_M35_BaSO4 are 250 and 140 times larger than those for mono-salt $NaNO_3$ matrix. The mechanisms behind this increase in diffusion coefficients remain unknown and need further investigation. The network formed by small porosities near the highly dispersed $BaSO_4$ crystals could be one reason.

Table 21 Growth rate of $\alpha_w D_w^{mat}$ and $\alpha_s D_s^{mat}$ for three bi-salt $NaNO_3$/ $BaSO_4$ BWPs compared to the parameters fitted on mono-salt $NaNO_3$ BWPs.

Composition	Growth rate of $\alpha_w D_w^{mat}$	Growth rate of $\alpha_s D_s^{mat}$
M5_NaNO3_M35_BaSO4	250	140
M10_NaNO3_M30_BaSO4	37	30
M20_NaNO3_M20_BaSO4	2	4

5.3.5. Discussions about released salt fraction

Fig. 5-19 compares the numerical and experimental results of released salt fraction for mono-salt $NaNO_3$ and bi-salt M5_NaNO3_M35_BaSO4 BWPs. We must point out that the illustrated numerical results take into account the hydration stage (cf. section 5.1) and thus depend on the hydration kinetics as well as the initial porosity of the samples. The experimentally observed value on M30_NaNO3 (2.3 mm of hydration at 1400 leaching days, cf. Fig. 3-9(b)) is used for all mono-salt $NaNO_3$ BWPs as hydration kinetics. Due to a lack of experimental data, the hydration kinetics of M5_NaNO3_M35_BaSO4 is estimated from [18]: 0.5 mm of hydration at 120 leaching days. The initial porosity reported in Table 2 is used for calculations.

By taking into account the hydration stage, the numerical values of released salt fractions are zero until 1380 leaching days for M5_NaNO3 (Fig. 5-19(a)), M10_NaNO3 (Fig. 5-19(b)) and during the first 100 leaching days for M20_NaNO3 (Fig. 5-19(c)), M5_NaNO3_M35_BaSO4 (Fig. 5-19(e)). A numerical value of zero means that the model predicts no salt diffusion toward the outside and that all dissolved salts remain in the liquid phase within the material. A small quantity of leached salts$\sim 0.5\ mg.cm^{-2}$ at 1000 days is experimentally measured for M5_NaNO3 and M10_NaNO3. This quantity could be due to the salt diffusion in the leached zone near the sample surface, where the porosity has significantly increased during leaching and made the outward salt diffusion process possible. The experimental results of M20_NaNO3 are pretty well reproduced (Fig. 5-19(c)) despite zero values during the first 100 leaching days. However, differences have been observed between the numerical values and the experimental results for M30_NaNO3 (Fig. 5-19(d)) and M5_NaNO3_M35_BaSO4 (Fig. 5-19(e)). The

measurement uncertainties of initial porosity and hydration kinetics would be responsible for the observed differences.

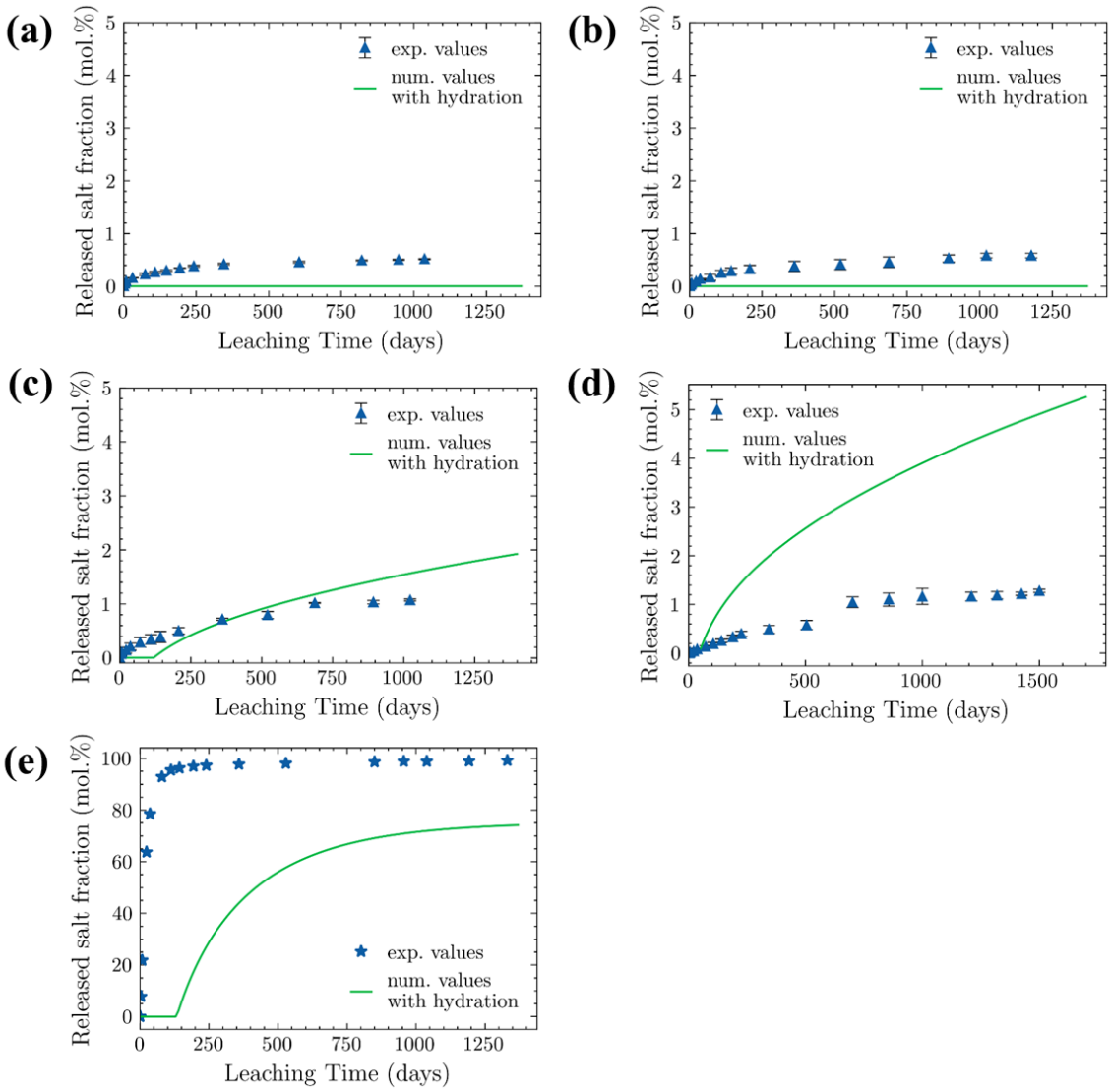

Fig. 5-19 Numerical and experimental results of the amount of leached salts for (a) M5_NaNO3; (b) M10_NaNO3 ; (c) M20_NaNO3; (d) M30_NaNO3 BWPs; (e) M5_NaNO3_M35_BaSO4.

5.3.6. Sensitivity analysis of sample height for free leaching tests

In this section, the sensitivity of sample height is analyzed for free leaching tests. The simulations are performed for M10_NaNO3_M30_BaSO4 BWPs using the corresponding parameters listed in Table 19. Fig. 5-20 illustrates the temporal evolution of swelling and displacement of M10_NaNO3_M30_BaSO4 BWPs simulated with sample heights ranging from 5 mm to 20 mm. The simulated swelling values decrease as the sample height increases (cf. Fig. 5-20(a)).

As the swelling depends on the sample height, it would be more intuitive to compare the displacement at the sample border (at $x = 0$ in Fig. 5-1) shown in Fig. 5-20(b). First, we can notice that the displacements simulated with four different heights are totally overlapped until about 500 days. This is because the progression of the leaching front within the sample, which is the origin of the swelling, is actually

independent of the sample height at the beginning of the leaching process, where the solute concentration gradient is the same regardless of the sample height. However, as the total amount of soluble salt depends on the volume (thus the height) of the sample, the solute concentration in the smaller samples will decrease more quickly than in larger samples when the leaching front progresses further within the sample. This decrease in solute concentration will lead to reduced intensity of the osmosis and thus reduced swelling. This explains why the displacement curve for the 5mm-high sample is separated at about 500 days from the other curves, which remain overlapped until about 1500 days. Due to the same reason, the displacement curve for the 10mm-high sample separated with another two curves after 1500 days.

To summarize, the swelling under free leaching conditions depends strongly on the sample height. Appropriate sample heights consistent with the experimental setup need to be used for simulations.

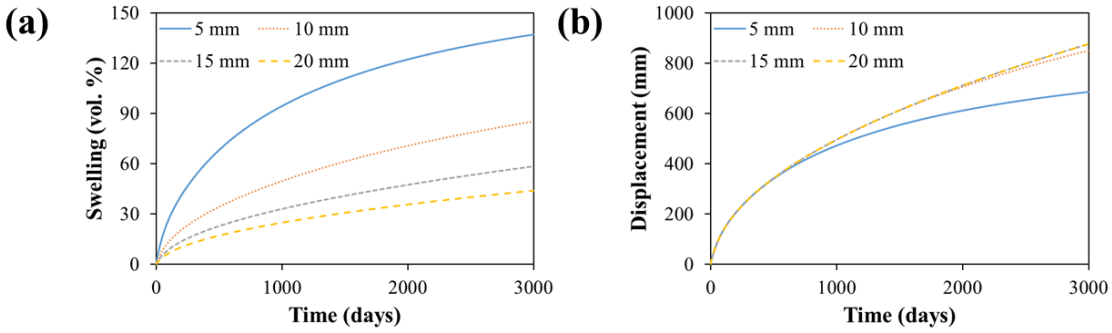

Fig. 5-20 Temporal evolution of (a) swelling ; (b) displacement of M10_NaNO3_M30_BaSO4 BWPs simulated with sample height ranging from 5 mm to 20 mm.

5.4. Simplified BWPs under constant counter-pressure

In this section, the consolidation stage is first simulated in 5.4.1. The numerical results of M30_NaNO3 and M10_NaNO3_M30_BaSO4 BWPs leached under constant counter-pressure conditions are presented in 5.4.2 and 5.4.3, respectively.

5.4.1. Modeling of consolidation

As a reminder, BWPs are consolidated in oedometer priori to leaching tests under constant counter-pressure (cf. 3.1.2). As shown in 3.3.1, we remain in the elasticity range with the applied counter-pressure. The objective of this section is to verify if the model can reproduce the experimental consolidation data with appropriate parameters.

Fig. 5-21 illustrates the geometry and boundary conditions of the consolidation problem. It should be noted that the BWPs are not in contact with water during the consolidation. Different physical phenomena (diffusion, permeability, and osmosis) presented in 2.2 are therefore not involved during the consolidation. The following conditions are used to build an equivalent configuration consistent with the experimental conditions:

- No initial salt crystals in the sample: initial volume fraction of salt crystal $\phi_{c,i} = 0$

- No initial dissolved salt in the sample: initial value of the solute mass fraction $(\omega_s)_{t=0} = 0$ in the whole sample
- No salt from outside: solute mass fraction $(\omega_s)_{x=0} = 0$ at the leaching border $x = 0$
- Pressure $p = 0.1\ MPa$ imposed in the whole sample
- Pressure $p_{x=0} = 0.1\ MPa$ at the leaching border $x = 0$

With these conditions, we have constantly $\omega_s = 0$ and $p = 0.1\ MPa$ in the whole sample, which makes sure that the diffusion, permeability, and osmosis are not involved during the consolidation process since there is neither solute concentration gradient $\nabla\omega_s$ nor pressure gradient ∇p in the sample.

The simulated volumetric deformation of BWPs under a consolidation stress of 2.8 MPa stabilized at about -8.9% (cf. Fig. 5-22). The volumetric deformation can be decomposed into two parts: the elimination of the initial porosity and the elastic deformation of the BWP matrix. Taking into account the initial porosity of 7%, the BWP matrix has a simulated elastic deformation of about -1.9% under 2.8 MPa. As the consolidation experiments are performed under oedometric conditions, the elastic volumetric deformation of the BWP matrix can be estimated by using the oedometric modulus of the BWP matrix $E_{s,oed} = 144 \pm 12\ MPa$ (cf. Appendix D). The elastic volumetric deformation under 2.8 MPa is therefore estimated as $2.8/144 = 1.94\%$, which is consistent with the simulated value. The model is thus valid for the consolidation case.

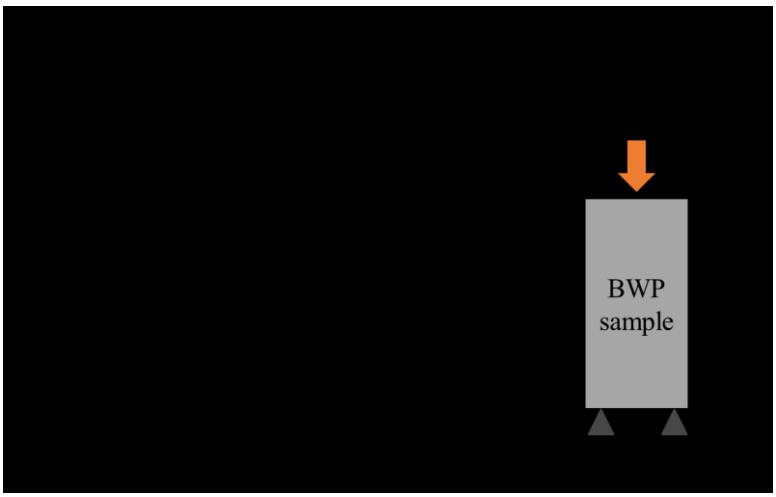

Fig. 5-21 Geometry and boundary conditions of the consolidation problem.

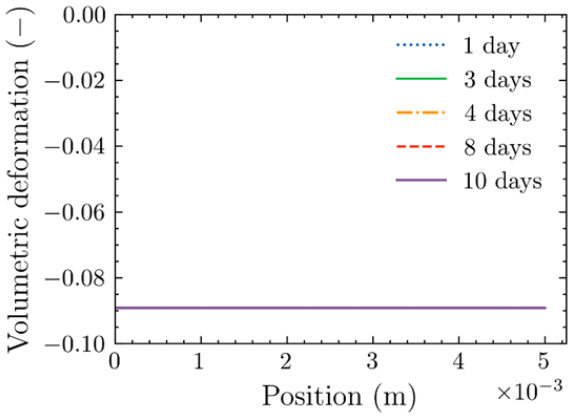

Fig. 5-22 Volumetric deformations of BWPs with an initial porosity of 7% and consolidated under 2.8 MPa.

5.4.2. Mono-salt BWPs M30_NaNO3

In this section, the parameters calibrated in 5.3.1 on mono-salt $NaNO_3$ BWPs under free leaching conditions (cf. Table 18) are tested on M30_NaNO3 under different constant counter-pressure. The results under 176 kPa, 1.4 MPa and 2.8 MPa constant counter-pressure are respectively presented in Fig. 5-23, Fig. 5-25, and Fig. 5-26.

It should be emphasized that the experimental results of M30_NaNO3 under 176 kPa constant counter-pressure (Fig. 5-23) are well reproduced using parameters calibrated on free leaching test results (cf. Table 18), which validates therefore the present numerical model under constant counter-pressure. Moreover, this consistency also suggests that the consolidated M30_NaNO3 BWPs have a leaching behavior under 176 kPa constant counter-pressure similar to that under free leaching conditions.

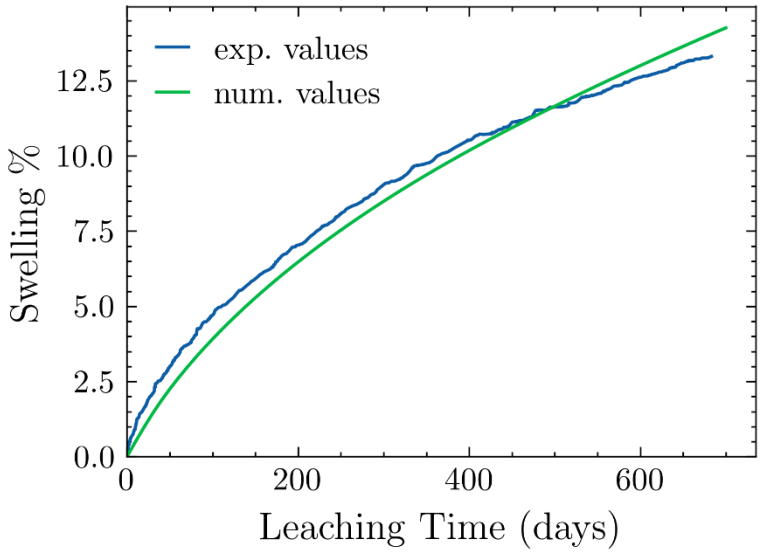

Fig. 5-23 Numerical and experimental results of the temporal evolution of swelling of M30_NaNO3 mono-salt BWP under 176 kPa constant counter-pressure.

It should be noted that the progression of the leaching front for M30_NaNO3 under 176 kPa constant counter-pressure can be estimated by measuring the thickness of the strongly altered zone (gray areas) in Fig. 3-16(a): about 1.6 mm at 683 days. Fig. 5-24 shows the simulated profile along the sample of salt crystal volume fraction at different leaching times. The progression of the simulated leaching front

can be determined by identifying the position where the salt crystal volume fraction starts to decrease. About 1.5 mm after 680 days is therefore estimated, which is consistent with the value estimated on the ESEM image Fig. 3-16(a).

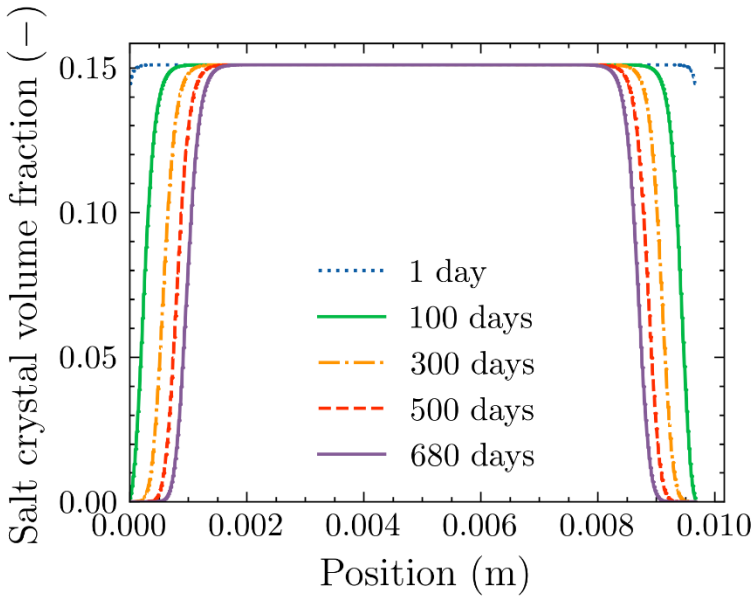

Fig. 5-24 Simulated profile along the sample of salt crystal volume fraction at different leaching times.

However, for M30_NaNO3 under constant counter-pressure of 1.4 MPa (Fig. 5-25) and 2.8 MPa (Fig. 5-26), the numerical predictions with parameters calibrated on free leaching tests (cf. Table 18) far exceed the experimental results (approximately twice). This difference is still under investigation, a different leaching behavior under important counter-pressure could be one reason. As a reminder, a different leaching behavior of M30_NaNO3 under 2.8 MPa counter-pressure, with *a priori* a preferential path within the sample, has been observed in ESEM images (cf. Fig. 3-16). As only one experimental curve exists for this leaching test, we cannot conclude whether the observed different leaching behavior under 2.8 MPa counter-pressure is repeatable. Moreover, due to the lack of the ESEM images for M30_NaNO3 leached under 1.4 MPa counter-pressure, it is difficult to conclude the leaching behavior under important counter-pressure. More experiments are needed for further investigation. However, it is worth noting that the model predicts swelling values more important than the experimental data

for M30_NaNO3 leached under 1.4 and 2.8 MPa counter-pressure and remains thus conservative in terms of swelling.

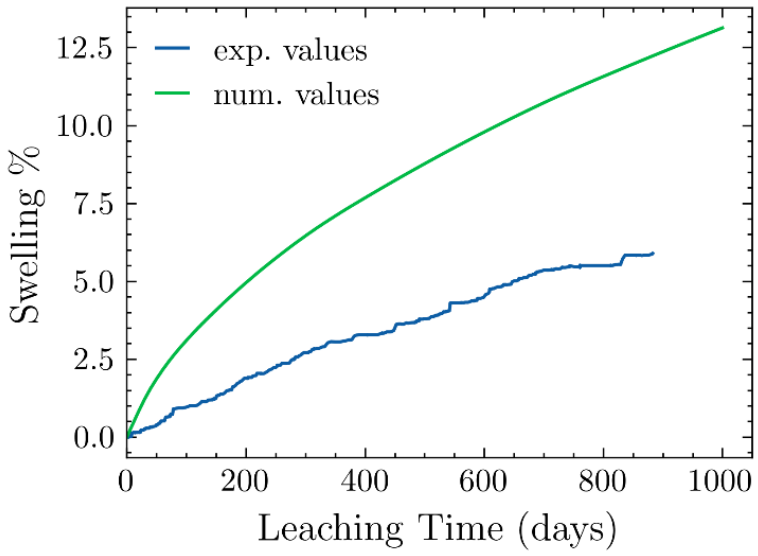

Fig. 5-25 Numerical and experimental results of the temporal evolution of swelling of M30_NaNO3 mono-salt BWP under 1.4 MPa constant counter-pressure.

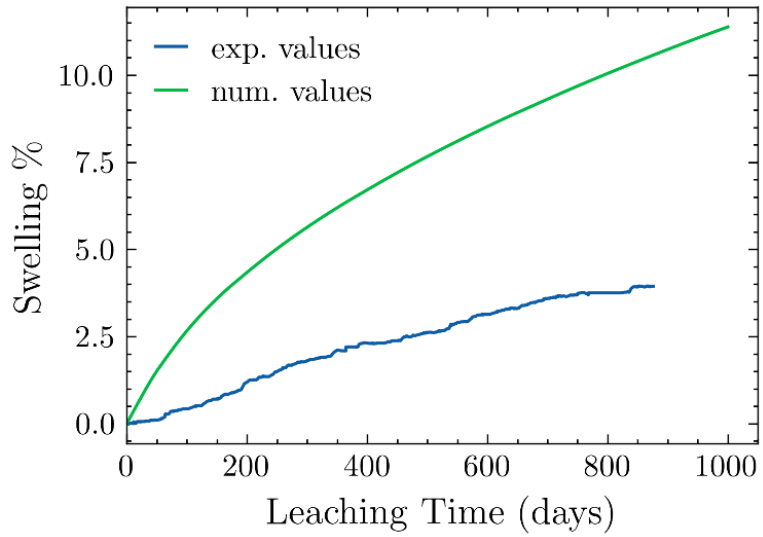

Fig. 5-26 Numerical and experimental results of the temporal evolution of swelling of M30_NaNO3 mono-salt BWP under 2.8 MPa constant counter-pressure.

5.4.3. Bi-salt BWPs M10_NaNO3_M30_BaSO4

Fig. 5-27 shows the numerical results for consolidated M10_NaNO3_M30_BaSO4 BWPs leached under 176 kPa constant counter-pressure, by using respectively the parameters calibrated on M10_NaNO3_M30_BaSO4 BWPs (Table 19) and mono-salt $NaNO_3$ BWPs (Table 18) under free leaching conditions.

With the parameters calibrated on M10_NaNO3_M30_BaSO4 BWPs (Fig. 5-27(a)), the model predicts a swelling significantly larger than the experimental value. However, with the parameters calibrated

on mono-salt $NaNO_3$ BWPs (Fig. 5-27(b)), the experimental swelling is well produced. This could indicate that the consolidated M10_NaNO3_M30_BaSO4 BWPs have a leaching behavior similar to mono-salt $NaNO_3$ BWPs. It seems that the elimination of the initial porosity during the consolidation phase has also eliminated the acceleration effect due to the presence of $BaSO_4$, which further supports the hypothesis that the acceleration effect of $BaSO_4$ originates from the network formed by small porosities near the highly dispersed $BaSO_4$ crystals.

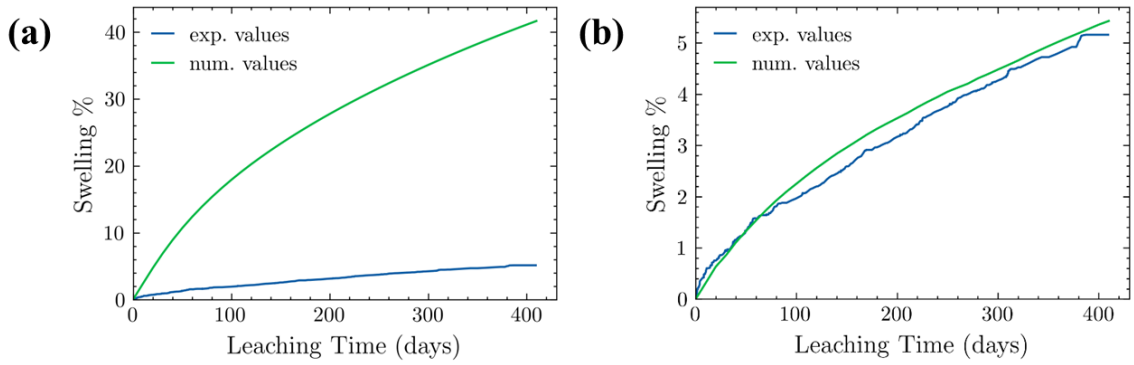

Fig. 5-27 Comparison of numerical results of M10_NaNO3_M30_BaSO4 BWP swelling under 176 kPa constant counter-pressure by using parameters calibrated on (a) M10_NaNO3_M30_BaSO4 BWPs (cf. Table 19) ; (b) mono-salt $NaNO_3$ BWPs (cf. Table 18) under free leaching conditions.

In order to study the sensitivity of the initial porosity, the swelling behavior under 176 kPa constant counter-pressure of consolidated M10_NaNO3_M30_BaSO4 BWPs are simulated with an initial porosity n_{l_i} ranging from 0.1% to 8%. The parameters in Table 18 are used for simulations. As shown in Fig. 3-17, the swelling under 176 kPa counter-pressure was experimentally measured on M10_NaNO3_M30_BaSO4 BWPs consolidated with different levels of stress (therefore with different initial porosity). Since the experimental results in Fig. 3-17 are quite close, an average of the experimental data is calculated using OriginLab and is compared to the numerical results in Fig. 5-28. The simulated swelling values are in general more important as the initial porosity increases and are slightly

higher than the averaged experimental data. Given the important measurement uncertainties at low swelling values, the model prediction is rather satisfactory.

It should also be noted that the numerical results simulated with initial porosities less than 1% are quite close. It seems that when the initial porosity is less than 1%, it has little impact on numerical results. Based on these results, the initial porosity of the consolidated BWPs is set as 0.1% (cf. 5.1).

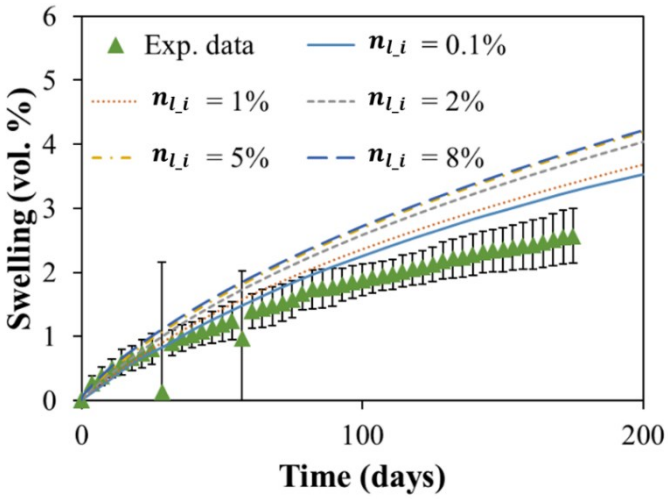

Fig. 5-28 Swelling behavior under 176 kPa constant counter-pressure of M10_NaNO3_M30_BaSO4 BWP with different initial porosity n_{l_i}. The numerical results are compared with the average of the experimental results shown in Fig. 3-17.

5.5. Simplified BWPs under constant volume conditions

It should be noted that the leaching tests under constant volume conditions are only conducted on industrial BWPs STEL and STE3 (cf. 2.3.2) for French BWPs. As there are currently no leaching test results under constant volume conditions for simplified French BWPs, the theoretical osmotic pressure in the case of a perfect semi-permeable membrane (cf. 2.2.3) is used to validate the numerical model. In section 5.5.1, the case of a perfect semi-permeable bitumen matrix is numerically investigated for mono-salt $NaNO_3$ BWPs. The Pitzer's model parameters are fitted to reproduce the theoretical osmotic pressure.

The stress build-up behaviors under constant volume conditions are studied for mono-salt (cf. 5.5.2) and bi-salt (cf. 5.5.3) simplified BWPs by using the parameters calibrated under free leaching conditions in 5.3. A parameter sensitivity study is realized in 5.5.4 to better understand the key parameters of the stress build-up behavior under constant volume conditions.

5.5.1. Case of perfect semi-permeable membrane

In this section, the stress build-up behavior under constant volume conditions with a perfect semi-permeable membrane is numerically investigated for mono-salt $NaNO_3$ BWPs. The salt diffusion in the BWP matrix is completely blocked to simulate a perfect semi-permeable membrane: $D_s^{mat} = 0\ m^2.s^{-1}$.

First, it should be emphasized that the simulated maximum stress is very sensitive to the Pitzer's model parameters. In fact, the osmotic pressure Π is proportional to $-ln(a_w)$ (cf. Equation (*1*)). To estimate the simulated values of water activity a_w, we can link a_w to salt activity a_s from (A.*15*):

$$d\big(ln(a_w)\big) = -\frac{M_w}{M_s}\frac{\rho_s \nu_N}{\rho_w} d\big(ln(a_s)\big) \tag{134}$$

By using (A.*20*), (134) becomes

$$d\big(ln(a_w)\big) = -\frac{M_w}{M_s}\frac{\rho_s \nu_N}{\rho_w}\frac{d(\omega_s)}{\nu_N \omega_s} R(\omega_s) = -\frac{M_w}{M_s}\frac{R(\omega_s)}{1-\omega_s} d(\omega_s) \tag{135}$$

As $a_w = 1$ and $ln(a_w) = 0$ for $\omega_s = 0$, we can integrate (135) and obtain:

$$ln(a_w) = \frac{-M_w}{M_s}\int_0^{\omega_s} \frac{R(\omega_s)}{1-\omega_s} d(\omega_s) \tag{136}$$

As $R(\omega_s)$ depends on Pitzer's model parameters A_ϕ, b, α, β_0, β_1, C_ϕ (cf. Appendix A), so does $ln(a_w)$ and thus the osmotic pressure. The integral in (136) can be numerically estimated by using the expression of $R(\omega_s)$ for $NaNO_3$ (cf. (A.*21*)).

As a reminder, the Pitzer's model is initially developed to model the salt activity coefficient γ (cf. (A.*19*)). In our case where we are interested in the maximum osmotic pressure for mono-salt $NaNO_3$ BWPs, the Pitzer's model parameters need to be fitted on both experimental data of salt activity coefficient γ and water activity a_w for the aqueous solution of $NaNO_3$.

The fitted Pitzer's model parameters are listed in Table 10 and are used for simulations. The stress build-up behavior under constant volume conditions (see Fig. 5-3 for corresponding geometry and boundary conditions) with a perfect semi-permeable membrane is simulated for mono-salt $NaNO_3$ BWPs and is shown in Fig. 5-29. The generated stress stabilized at about 41.5 MPa and remains constant after, no stress relief stage has been observed. The evolution over different leaching time of the solute mass fraction ω_s and osmotic efficiency coefficient τ is shown in Fig. 5-30. After about 2000 leaching days, the solute mass fraction stabilized in the whole sample at 0.479 (except the two ends in contact with the leaching solution), which indicates that the pore solution within the sample is all saturated in $NaNO_3$. Meanwhile, the osmotic efficiency coefficient is stabilized in the whole sample at 1 after 2000 leaching days (except the two ends in contact with the leaching solution), which shows the BWP matrix acts indeed as a perfect semi-permeable membrane. The stress of about 41.5 MPa, reached at about 2000 leaching days and remained constant after, is, therefore, the maximum osmotic stress under constant volume conditions with a perfect semi-permeable membrane simulated by using Pitzer's model parameters in Table 10. The generated maximum stress of about 41.5 MPa is consistent with the theoretical value calculated in 2.2.3 (41.6 MPa). The numerical model is therefore validated for leaching under constant volume conditions. These fitted Pizer's model parameters (listed in Table 10) are used for all numerical results presented in this work.

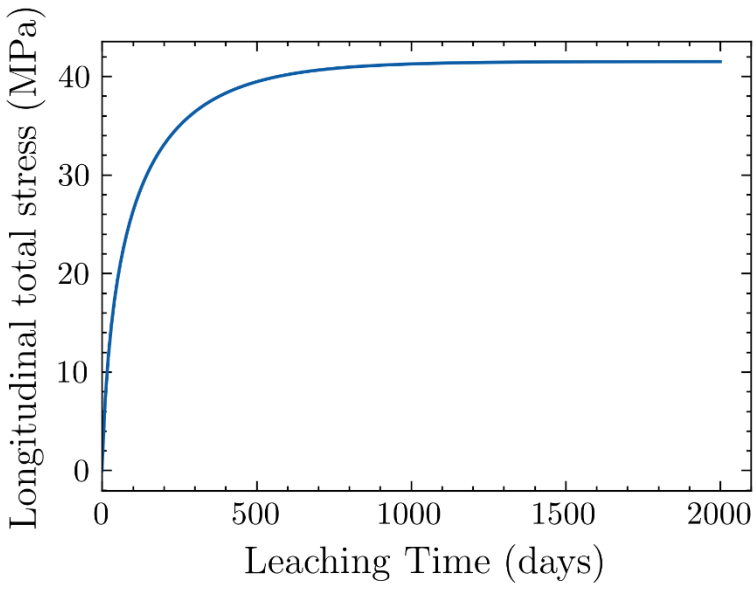

Fig. 5-29 Stress build-up behavior of mono-salt $NaNO_3$ BWPs under constant volume conditions with a perfect semi-permeable membrane simulated with the fitted Pitzer's model parameters listed in Table 10.

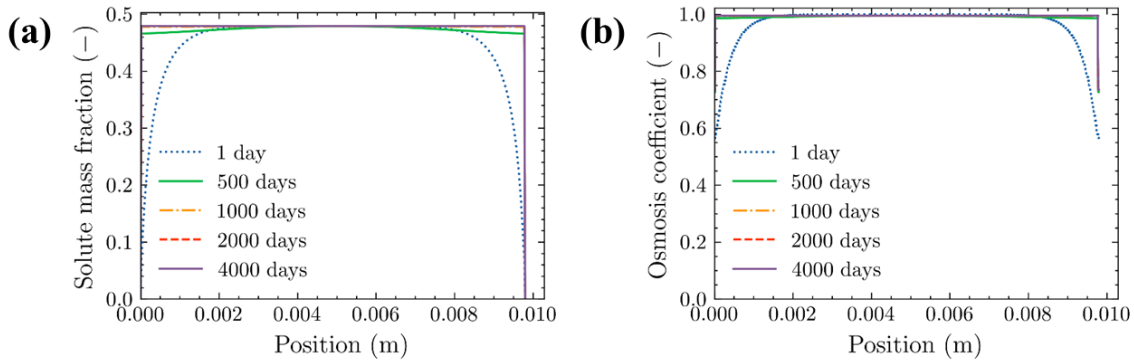

Fig. 5-30 Evolution of (a) solute mass fraction; (b) osmotic efficiency coefficient over different leaching time under constant volume conditions with a perfect semi-permeable membrane simulated with Pitzer's model parameters in Table 10.

Fig. 5-31 shows the numerical values of the salt activity coefficient and $-ln(a_w)$ simulated with the fitted Pitzer's model parameters in Table 10. Both quantities are well reproduced.

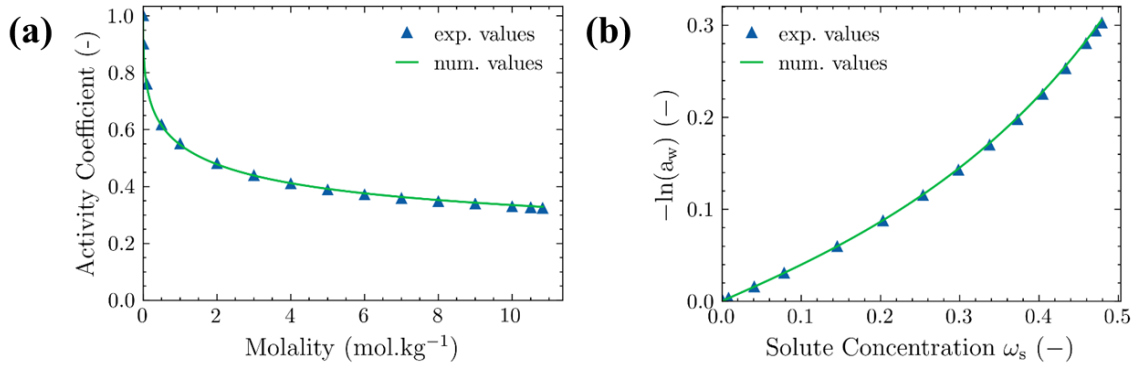

Fig. 5-31 Numerical values of (a) salt activity coefficient; (b) $-ln(a_w)$ simulated with the fitted Pitzer's model parameters listed in Table 10. The experimental values are respectively from [47] *and* [35].

To show the sensitivity of the maximum osmotic stress to the Pitzer's model parameters, the parameters reported in [47] for the aqueous solution of $NaNO_3$ at 25℃ are used as an example. The fitted

Pitzer's model parameters are compared in Table 22 with the values reported in [47], the difference lies only in the parameter C_ϕ.

Fig. 5-32 shows the stress build-up behavior under constant volume conditions with a perfect semi-permeable membrane simulated with parameters reported in [47]. The resulting maximum osmotic stress stabilized at about 38.2 MPa, which is slightly lower than the theoretical value calculated in 2.2.3 (41.6 MPa). Fig. 5-33 shows the numerical values of the salt activity coefficient and $-ln(a_w)$ simulated with the Pitzer's model parameters reported in [47]. The salt activity coefficient γ is in general well reproduced despite a slight difference for large molality (cf. Fig. 5-33(a)). The numerical values of $-ln(a_w)$ ((cf. Fig. 5-33(b)) are smaller than the experimental values [35] at large solute concentrations. As a reminder, the maximum osmotic pressure is generated at the saturated solute concentration ω_{sat}. The underestimation of $-ln(a_w)$ at ω_{sat} in the numerical model leads therefore to the difference between the simulated maximum osmotic pressure (about 38.2 MPa) and the theoretical value (41.6 MPa).

Table 22 Comparison of fitted Pitzer's model parameters and values reported in [47].

	Fitted parameters	Values reported in [47]
A_ϕ	$0.392\ kg^{1/2}mol^{-1/2}$	$0.392\ kg^{1/2}mol^{-1/2}$
b	$1.2\ kg^{1/2}mol^{-1/2}$	$1.2\ kg^{1/2}mol^{-1/2}$
α	$2\ kg^{1/2}mol^{-1/2}$	$2\ kg^{1/2}mol^{-1/2}$
β_0	$0.0068\ kg.mol^{-1}$	$0.0068\ kg.mol^{-1}$
β_1	$0.1783\ kg.mol^{-1}$	$0.1783\ kg.mol^{-1}$
C_ϕ	$-0.000267\ kg^2.mol^{-2}$	$-0.00072\ kg^2.mol^{-2}$

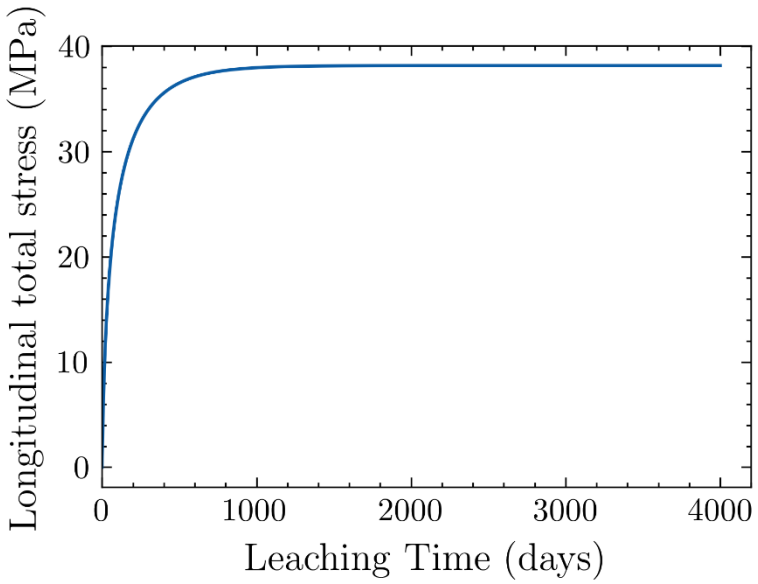

Fig. 5-32 Stress build-up behavior of mono-salt $NaNO_3$ BWPs under constant volume conditions with a perfect semi-permeable membrane simulated with Pitzer's model parameters reported in [47] *and listed in Table 22.*

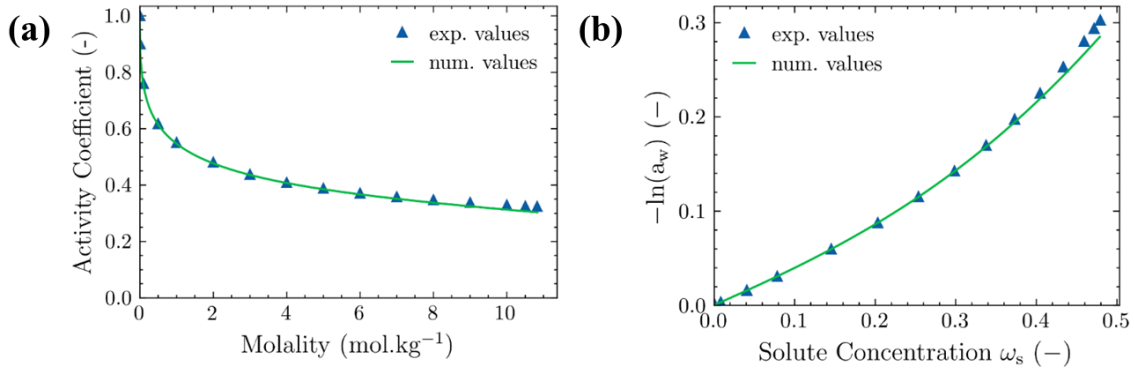

Fig. 5-33 Numerical values of (a) salt activity coefficient; (b) $-ln(a_w)$ simulated with the fitted Pitzer's model parameters reported in [47] *and listed in Table 22. The experimental values are respectively from* [47] *and* [35].

5.5.2. Mono-salt $NaNO_3$ BWPs

The parameters calibrated under free leaching conditions for mono-salt $NaNO_3$ BWPs (cf. 5.3.1) are used to study the stress build-up behavior under constant volume conditions for mono-salt $NaNO_3$ BWPs containing 5, 10, 20 and 30 wt. % of $NaNO_3$. The parameters calibrated in Table 18 are used for simulation. It should be noted that there are no available experimental results.

Fig. 5-34 shows that the stress build-up behaviors of these four BWPs share the same trend. We can note that the maximum stress is reached for all four BWPs. The stress peak is reached at about 850 days for M5_NaNO3, 1100 days for M10_NaNO3, 1500 days for M20_NaNO3, and 2000 days for M30_NaNO3. The time needed to reach the stress peak increases as the salt content increases. The maximum stresses reached are about 10 MPa for M5_NaNO3, 15 MPa for M10_NaNO3, 23 MPa for M20_NaNO3 and 28 MPa for M30_NaNO3. The maximum stress is more important for BWPs containing more soluble salts.

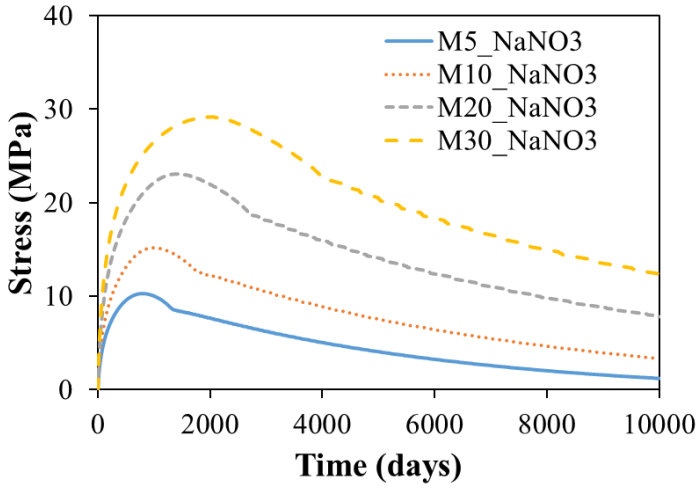

Fig. 5-34 Evolution of stress generated over leaching time within mono-salt $NaNO_3$ BWPs containing 5, 10, 20 and 30 wt. % of $NaNO_3$.

5.5.3. Bi-salt $NaNO_3/BaSO_4$ BWPs

The parameters calibrated under free leaching conditions for bi-salt BWPs (cf. 5.3.3) are used to study the stress build-up behavior under constant volume conditions for M5_NaNO3_M35_BaSO4, M10_NaNO3_M30_BaSO4 and M20_NaNO3_M20_BaSO4 (cf. Fig. 5-35). It should be noted that there are no available experimental results.

First, we can note that the maximum stress is reached for all three bi-salt BWPs. The stress peak is reached at about 20 days for M5_NaNO3_M35_BaSO4, 100 days for M10_NaNO3_M30_BaSO4 and 800 days for M20_NaNO3_M20_BaSO4. Moreover, the stress decreases to zero at about 200 days for M5_NaNO3_M35_BaSO4 and 1000 days for M10_NaNO3_M30_BaSO4, which indicates there is no more leaching within the BWPs. For all three bi-salt BWPs, the stress peak is reached more quickly than the mono-salt BWPs containing the same amount of soluble salts (cf. 5.5.2). For example, the stress peak is reached at about only 20 days for M5_NaNO3_M35_BaSO4 while it is reached at about 850 days for M5_NaNO3. The difference in stress build-up kinetics for bi-salt BWPs is *a priori* due to the presence of the poorly soluble salts $BaSO_4$. The increased water and salt diffusion coefficients in the BWP matrix due to $BaSO_4$ (cf. 5.3.4) accelerate the leaching process and thus also the stress build-up behavior: the stress reaches its maximum and decreases to zero more quickly.

On the other hand, the maximum stresses reached are about 8 MPa for M5_NaNO3_M35_BaSO4, 15 MPa for M10_NaNO3_M30_BaSO4 and 20 MPa for M20_NaNO3_M20_BaSO4. Despite a significantly accelerated kinetics, the maximum stresses reached for these three bi-salt BWPs are consistent with the mono salt BWPs containing the same amount of soluble salts (cf. 5.5.2), which suggests that the poorly soluble salts $BaSO_4$ affect essentially the kinetics but not the magnitude of the stress build-up behavior.

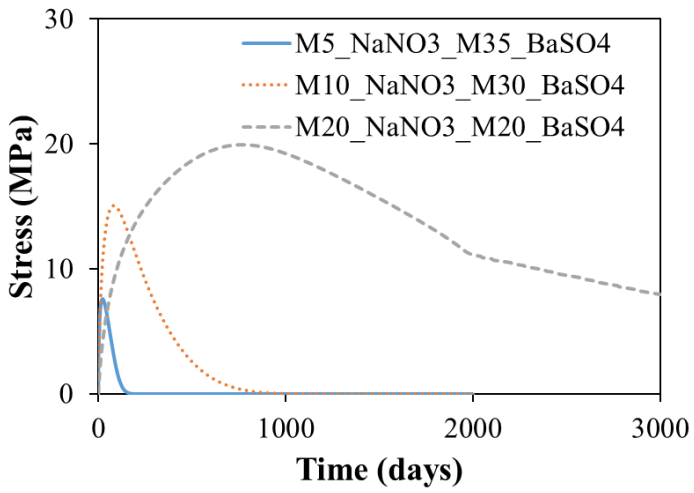

Fig. 5-35 Evolution of stress generated over leaching time within bi-salt BWPs (M5_NaNO3_M35_BaSO4, M10_NaNO3_M30_BaSO4, M20_NaNO3_M20_BaSO4).

5.5.4. Parametric study

In this section, a parametric study is realized for M10_NaNO3_M30_BaSO4 BWPs under constant volume conditions. The tested parameters are summarized in Table 23. All other parameters are kept

from those listed in 5.1. The role of the parameters $\alpha_w D_w^{mat}$ and $\alpha_s D_s^{mat}$ are respectively investigated in Fig. 5-36 (simulated with parameter set 0, 1, 2, 3) and Fig. 5-37 (simulated with parameter set 0, 4, 5, 6).

Table 23 Parameters tested under constant volume conditions for parametric studies.

	$\alpha_w D_w^{mat}(m^2.s^{-1})$	$\alpha_s D_s^{mat}(m^2.s^{-1})$
Set 0	8×10^{-14}	6×10^{-15}
Set 1	8×10^{-13}	6×10^{-15}
Set 2	8×10^{-12}	6×10^{-15}
Set 3	8×10^{-15}	6×10^{-15}
Set 4	8×10^{-14}	6×10^{-16}
Set 5	8×10^{-14}	6×10^{-17}
Set 6	8×10^{-14}	6×10^{-14}

Four values of $\alpha_w D_w^{mat}$ are tested for fixed $\alpha_s D_s^{mat}$ (Fig. 5-36). The numerical results show that the maximum generated stress under constant volume conditions is more important as $\alpha_w D_w^{mat}$ increases. The stress peak is reached quicker with increased $\alpha_w D_w^{mat}$. This could be explained by an enhanced water transport in the BWP matrix, which accelerates the penetration of the leaching front within the sample. The salt crystals are more quickly dissolved, resulting in a larger concentration gradient and thus an amplified osmosis-induced stress build-up.

On the other hand, four values of $\alpha_s D_s^{mat}$ are tested for fixed $\alpha_w D_w^{mat}$ (Fig. 5-37). The maximum generated stress decreases as $\alpha_s D_s^{mat}$ increases. The stress peak is reached more quickly with increased $\alpha_s D_s^{mat}$. This is actually due to an enhanced salt transport in the BWP matrix. The salt concentration within the pore solution decreased more quickly due to enhanced outward transport of the dissolved salt, resulting in a smaller concentration gradient and thus a reduced osmosis-induced stress build-up.

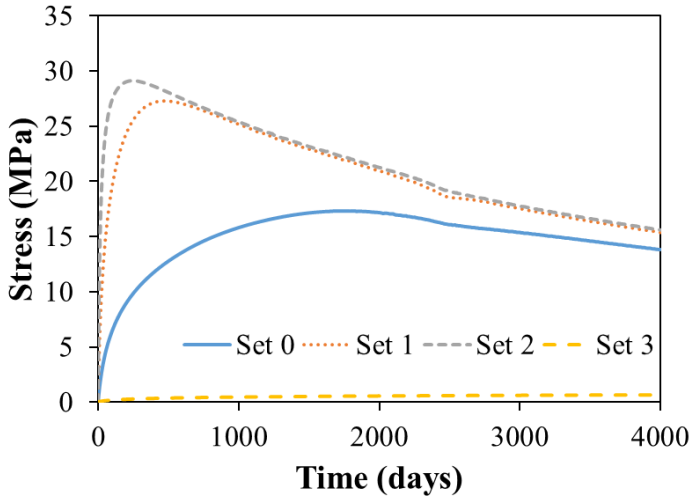

Fig. 5-36 Stress build-up behavior of BWPs under constant volume conditions simulated with different $\alpha_w D_w^{mat}$ (parameter set 0, 1, 2, 3 in Table 23).

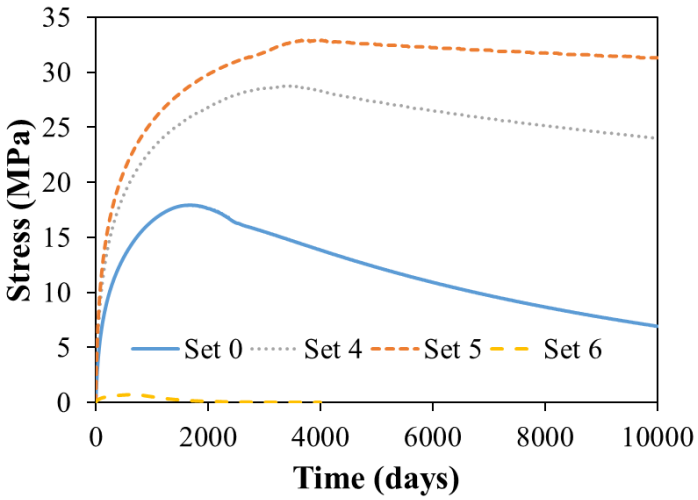

Fig. 5-37 Stress build-up behavior of BWPs under constant volume conditions simulated with different $\alpha_s D_s^{mat}$ (parameter set 0, 4, 5, 6 in Table 23).

5.5.5. Sensitivity analysis of sample height for leaching tests under constant volume conditions

In this section, the sensitivity of sample height is analyzed for leaching tests under constant volume conditions. The simulations are performed for mono-salt $NaNO_3$ BWPs under constant volume conditions with a perfect semi-permeable membrane. Fig. 5-38 illustrates the stress build-up behavior of mono-salt $NaNO_3$ BWPs under constant volume conditions with a perfect semi-permeable membrane simulated with sample height ranging from 5mm to 20mm.

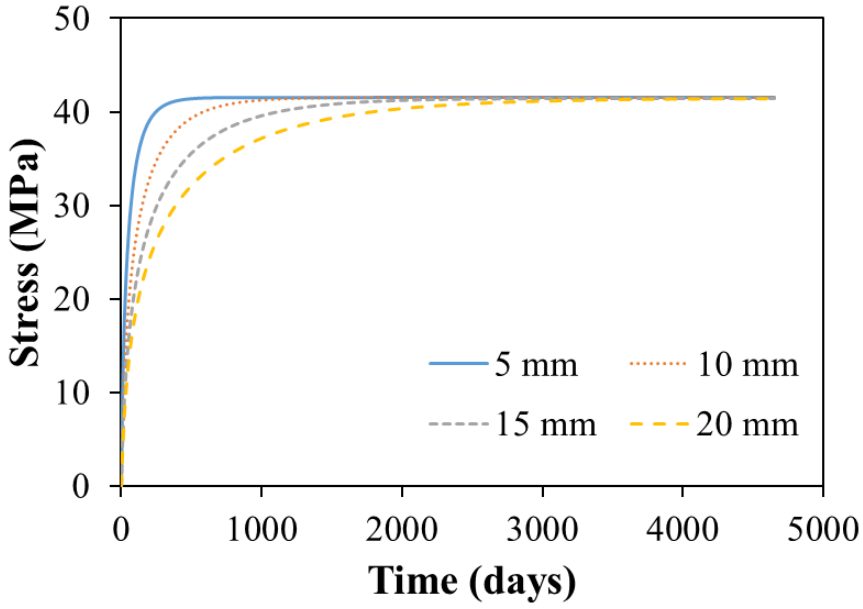

Fig. 5-38 Stress build-up behavior of mono-salt $NaNO_3$ BWPs under constant volume conditions with a perfect semi-permeable membrane simulated with sample height ranging from 5mm to 20mm.

The numerical results indicate that the generated maximum stress is independent of the sample height, which is logical since the maximum stress depends only on the soluble salt taken into account (cf. 2.2.3). On the other hand, the time needed to reach the maximum stress increases as the sample height increases. As shown in 5.5.1, the maximum stress is reached when the solute mass fraction and the osmotic efficiency coefficient stabilized respectively in the whole sample at 0.479 and 1 (except the two ends in contact with the leaching solution). The higher the sample, the longer it takes to satisfy such conditions.

5.6. Free leaching followed by leaching under constant volume conditions

As a reminder, the swelling of BWPs in underground geological disposal conditions will be free in the first place until the existing voids (within primary canisters, concrete containers, and rock vaults) are filled. The BWPs will then swell under confined conditions, leading to pressure on the host rock. It is therefore important to understand the relaxing effect of the existing voids on the stress build-up behavior of the BWPs. This point can be used for the safety study of the disposal facility.

In this section, we investigate the case of free leaching followed by leaching under constant volume conditions. Since in the real case, the rocks surrounding the BWPs will not be completely rigid and can allow a certain strain of the BWPs, the case of free leaching followed by leaching under constant volume conditions remains conservative with regards to the real case.

The BWPs' stress build-up behaviors under constant volume conditions are investigated after different values of swelling allowed during the free leaching stage. It is worth noting that there are currently no experimental results of free leaching tests followed by leaching under constant volume conditions. The numerical results will provide great insight into understanding the role of the existing voids on stress build-up behaviors.

Fig. 5-39 shows the geometry and boundary conditions of free leaching followed by leaching under constant volume conditions. The leaching will first be free until a given value of swelling is reached. The displacement of the sample is then completely blocked to prevent further swelling, the leaching is thus under constant volume conditions.

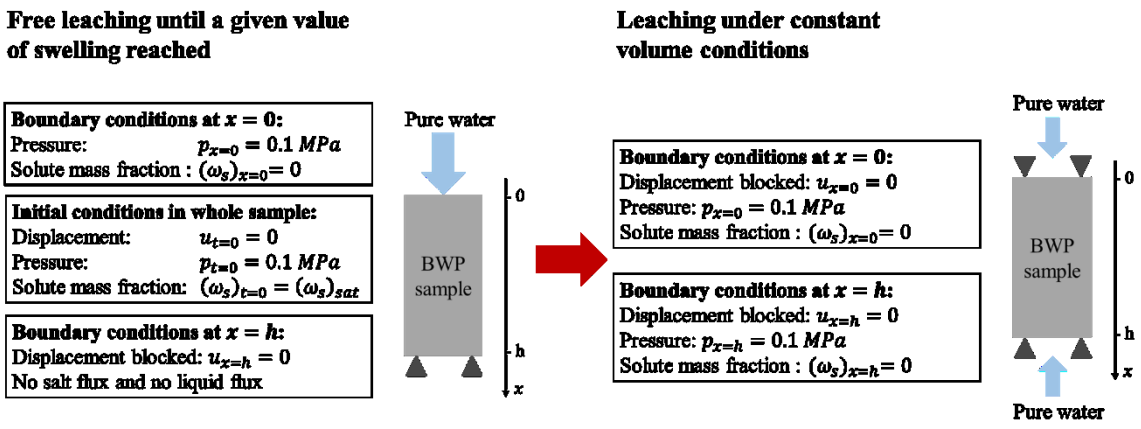

Fig. 5-39 Geometry and boundary conditions of free leaching followed by leaching under constant volume conditions.

The composition first used for simulations is bi-salt M10_NaNO3_M30_BaSO4. As shown in 5.4.3, the consolidated M10_NaNO3_M30_BaSO4 BWPs have a leaching behavior similar to mono-salt $NaNO_3$ BWPs. In real cases, the BWPs might be partly consolidated due to the generated stress within the sample. The mono-salt parameters (cf. Table 18) and the bi-salt parameters fitted on M10_NaNO3_M30_BaSO4 under free leaching conditions (cf. Table 19) are therefore two boundaries of the real leaching behavior and are both tested.

Fig. 5-40 and Fig. 5-41 illustrate the temporal evolutions of swelling and stress build-up behaviors for the case of free leaching followed by leaching under constant volume conditions, simulated respectively with the mono-salt parameters (cf. Table 18) and the bi-salt parameters fitted on M10_NaNO3_M30_BaSO4 under free leaching conditions (cf. Table 19). A swelling of about 20 vol. % is first allowed under free leaching conditions, no stress was generated. The swelling is then fixed at about 20 vol. % and the stress within the sample starts to increase. The stress peak is reached respectively at 6000 days for mono-salt parameters and 250 days for bi-salt parameters. Despite very different kinetics, the stress peaks are almost the same between these two cases (9.8 MPa for mono-salt parameters and 10.4 MPa for bi-salt parameters). This consistency shows again that the poorly soluble salts $BaSO_4$ affect essentially the kinetics but not the magnitude of the stress build-up behavior (cf. 5.5.3).

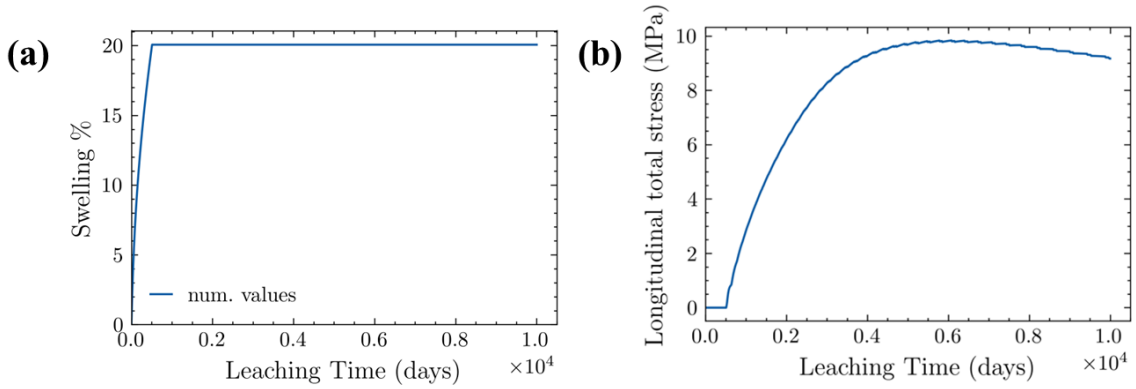

Fig. 5-40 (a) Temporal evolution of swelling ; (b) stress build-up behavior for the case of free leaching followed by leaching under constant volume conditions simulated on a 2.5 mm high bi-salt M10_NaNO3_M30_BaSO4. A swelling of 20 vol. % is allowed under free leaching conditions. The mono-salt parameters (cf. Table 18) are used.

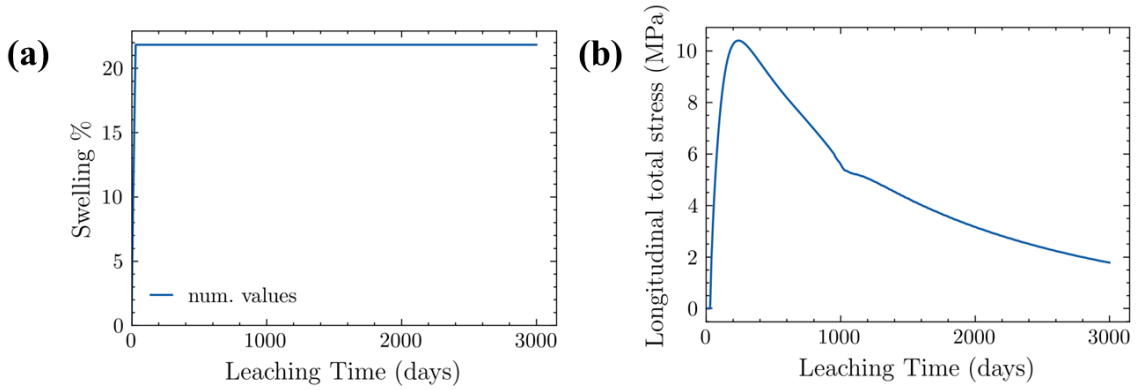

Fig. 5-41 (a) Temporal evolution of swelling ; (b) stress build-up behavior for the case of free leaching followed by leaching under constant volume conditions simulated on a 2.5 mm high bi-salt M10_NaNO3_M30_BaSO4. A swelling of 22 vol. % is allowed under free leaching conditions. The bi-salt parameters fitted on M10_NaNO3_M30_BaSO4 under free leaching conditions (cf. Table 19) are used.

The simulations shown in Fig. 5-40 and Fig. 5-41 are repeated for different values of swelling allowed under free leaching conditions. The simulation time is long enough to ensure that the stress peak under constant volume conditions is reached. The stress peak is then normalized by the maximum stress simulated allowing 0 vol. % of swelling under free leaching conditions (i.e., under constant volume conditions from the beginning of the leaching). It should be noted that this maximum stress (about 19 MPa here for M10_NaNO3_M30_BaSO4) is less than the theoretical osmotic pressure in the case of a perfect semi-permeable membrane (41.6 MPa, cf. 2.2.3). We can thus study the effect of the existing voids on the stress build-up behavior under constant volume conditions. Fig. 5-42 shows the evolution of this percentage of maximum stress reached under constant volume conditions in terms of swelling allowed under free leaching conditions. The numerical results show that the percentage of maximum stress decreases significantly as the allowed swelling increases. Only about 40% of the maximum stress is kept when about 30 vol. % of the swelling is allowed during the free leaching stage. This can be explained by the dissolution of the salt crystals and the outward salt diffusion that occurred during the free leaching stage, which leads to a reduced solute concentration within the sample and thus a reduced osmotic pressure under constant volume conditions. Moreover, the numerical results simulated using the mono-salt parameters (cf. Table 18) and the bi-salt parameters (cf. Table 19) are quite close. It seems that the parameters $\alpha_w D_w^{mat}$ and $\alpha_s D_s^{mat}$ has no significant impact on the stress build-up behavior for the case of free leaching followed by leaching under constant volume conditions. These results are quite meaningful given the uncertainties of determining these parameters.

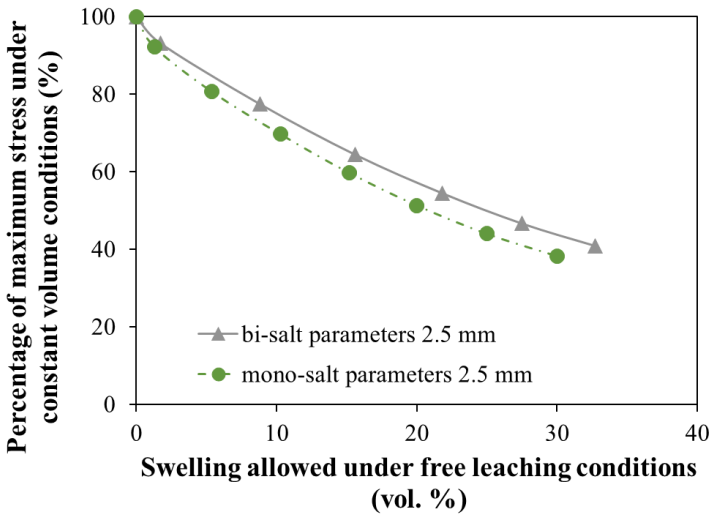

Fig. 5-42 Percentage of maximum stress under constant volume conditions VS swelling allowed under free leaching conditions simulated with the mono-salt parameters (cf. Table 18) and the bi-salt parameters fitted on M10_NaNO3_M30_BaSO4 under free leaching conditions (cf. Table 19) for a 2.5 mm high M10_NaNO3_M30_BaSO4.

It should be noted that although the sample height has no effect on the maximum stress under constant volume conditions (cf. 5.5.5), it has an effect on the swelling value during the free leaching stage since the calculation of swelling depends on the sample height. As the real size of the BWP packages is significantly larger than the laboratory-made simplified BWPs, a sensitivity analysis of sample height is necessary to investigate if the stress build-up behavior for the case of free leaching followed by leaching under constant volume conditions is height-dependent.

Fig. 5-43 illustrates the stress build-up behaviors for the case of free leaching followed by leaching under constant volume conditions simulated with sample heights ranging from 2.5 mm to 20 mm. The numerical results are quite well overlapped, which indicates that the stress build-up behavior seems

to be independent of the sample height. The numerical results presented in this study case are *a priori* also valid for simplified BWPs of real size.

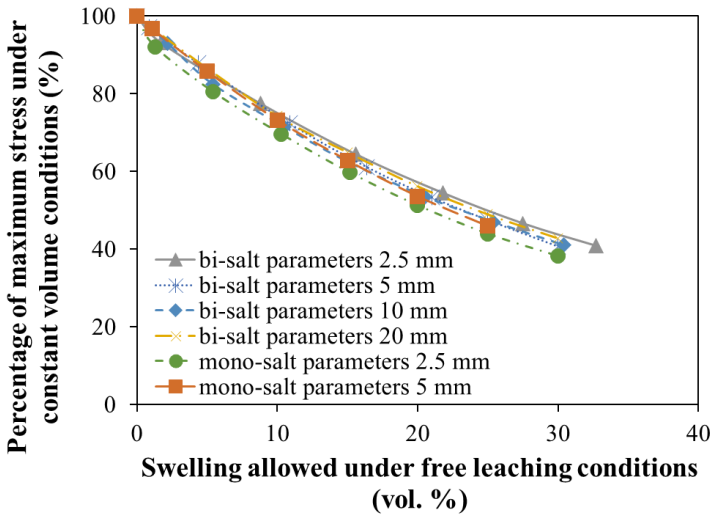

Fig. 5-43 Percentage of maximum stress under constant volume conditions VS swelling allowed under free leaching conditions simulated with the mono-salt parameters (cf. Table 18) and the bi-salt parameters fitted on M10_NaNO3_M30_BaSO4 under free leaching conditions (cf. Table 19). Sample heights ranging from 2.5 mm to 20 mm are used for simulation.

In conclusion, the effect of the existing voids on the stress build-up behavior of BWPs under confined conditions is numerically investigated in this section by studying the case of free leaching followed by leaching under constant volume conditions. The numerical results show that the percentage of maximum stress significantly decreases as the allowed swelling increases. Only about 40% of the maximum stress is reached when about 30 vol. % of the swelling is allowed during the free leaching stage (i.e. when there is 30 vol. % of existing voids). Moreover, the sensitivity analysis shows that the sample height and the material parameters have little impact on the numerical results for the case of free leaching followed by leaching under constant volume conditions. This result is quite encouraging. Therefore, the evolution of the percentage of maximum stress under constant volume conditions in terms of swelling allowed under free leaching conditions (cf. Fig. 5-43) is *a priori* also valid for simplified BWPs of real size.

5.7. Leaching behavior of industrial BWPs (STE3, STEL)

The experimental results of the industrial BWPs (STE3 and STEL) are only available under free leaching (cf. 3.2.7) and constant volume (cf. 2.3.2) conditions. As a reminder, only one salt (the most soluble one) in BWPs is considered in the numerical model. In order to apply the model, the compositions of STE3 and STEL are simplified and compared with their real compositions in Table 24. The soluble salts contained in STE3 and STEL are all assimilated to $NaNO_3$. Since $NaNO_3$ has an aqueous solubility significantly larger than Na_2SO_4 (cf. Table 3) and thus can lead to larger osmosis-induced swelling, this hypothesis remains conservative. The various poorly soluble salts are all assimilated to $BaSO_4$, whose acceleration effect of transport phenomena can be taken into account by transport parameters (cf. 5.3.4 and 5.4.3). This last point is of course an important simplification hypothesis.

Table 24 Simplified compositions of STE3 and STEL compared with their real compositions [17].

Characteristics	STE3 (real)	STE3 (simplified)	STEL (real)	STEL (simplified)
Bitumen content (wt. %)	**61**	**61**	**54**	**54**
Inorganic load (wt. %)	**39**	**39**	**46**	**46**
Soluble salts	**12.9**	**12.9**	**4.1**	**4.1**
$NaNO_3$	11.1	12.9	2.8	4.1
Na_2SO_4	1.8	-	1.4	-
Insoluble salts	**26**	**26**	**41.9**	**41.9**
$BaSO_4$	21.1	26	14.7	41.9
$K_2NiFe(CN)_6$ precipitated	2.4	-	7.4	-
$Fe(OH)_3$	-	-	9.7	-
$Cu(OH)_2$	-	-	5.1	-
$Co(OH)_2$	1.1	-	-	-
CoS	1.4	-	-	-
$Ca_3(PO_4)_2$	0.1	-	-	-
Diatomite	-	-	5.1	-

The model parameters of STE3 and STEL are fitted on experimental results under free leaching conditions in 5.7.1 and then applied on constant volume conditions in 5.7.2. However, the fitted parameters under free leaching conditions are not able to reproduce the experimentally measured stress build-up behavior under constant volume conditions (cf. 5.7.2). Finally, 5.7.3 shows the attempts to fit the experimental results of STE3 and STEL under constant volume conditions.

5.7.1. STE3 and STEL under free leaching conditions

In this section, the model parameters are calibrated on free leaching test results of STE3 and STEL (cf. 3.2.7). As a reminder, a significant increase of swelling and water uptake rate occurred after 1000 leaching days for STE3 under free leaching conditions. The mechanism behind this different leaching behavior remains unknown.

The model cannot reproduce entirely the experimental results. Two fittings are realized (shown in Table 25): the set 1 fits the first 1000 days of leaching (Fig. 5-44), the set 2 fits the final points at 1650 leaching days (Fig. 5-45). The change in leaching kinetics observed at about 1000 days cannot be reproduced by the current numerical model. The various poorly soluble salts present in STE3 could be one reason for this different leaching behavior.

Table 25 Parameter sets calibrated on experimental results of industrial BWP STE3 under free leaching conditions.

	$\alpha_w D_w^{mat} (m^2.s^{-1})$	$\alpha_s D_s^{mat} (m^2.s^{-1})$
Set 1	8×10^{-14}	1.2×10^{-14}
Set 2	8×10^{-14}	6×10^{-15}

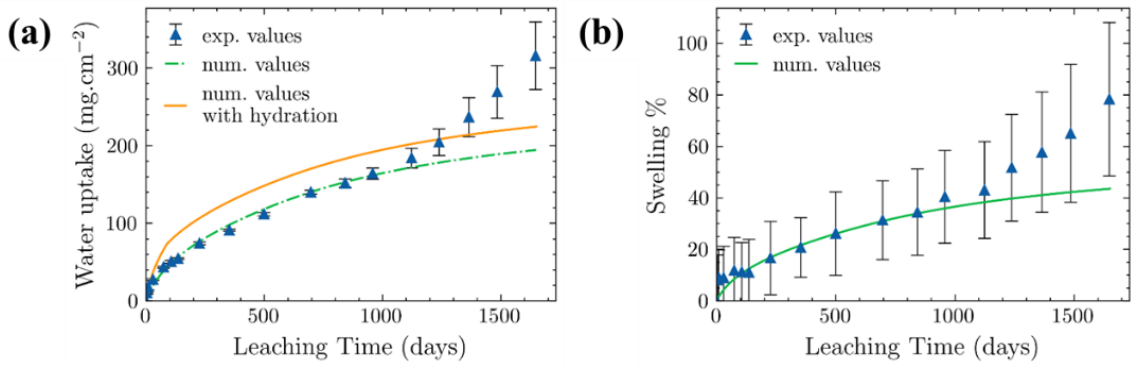

Fig. 5-44 Temporal evolution of (a) absorbed water; (b) swelling of industrial BWP STE3 under free leaching conditions simulated using parameter set 1 in Table 25.

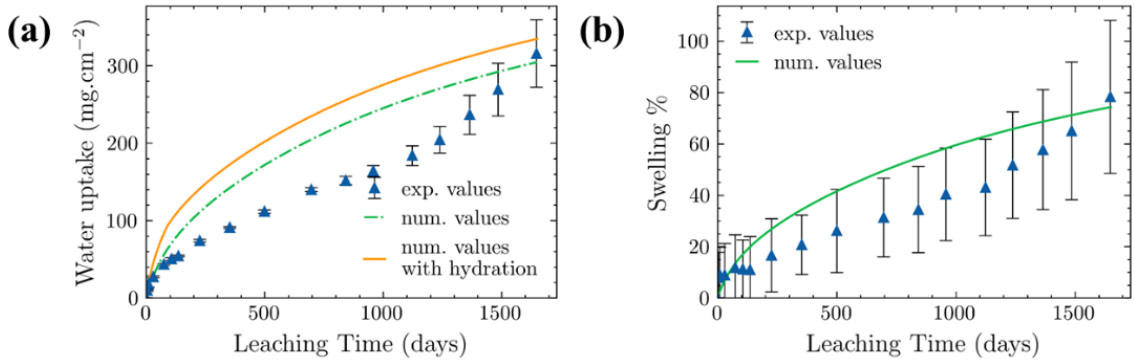

Fig. 5-45 Temporal evolution of (a) absorbed water; (b) swelling of industrial BWP STE3 under free leaching conditions simulated using parameter set 2 in Table 25.

The model parameters fitted on the experimental results of STEL under free leaching conditions are summarized in Table 26. The resulting numerical results are shown in Fig. 5-46. As indicated in 3.2.7, the experimental swelling and water uptake rates seem quite stable over leaching time for STEL despite important experimental values. No sign of stabilization can be observed until 1500 days. Such leaching behavior cannot be reproduced by the current model. However, it is worth noting that the final points at 1500 days of water uptake and swelling can be simultaneously reproduced.

Table 26 Parameters calibrated on experimental results of industrial BWP STEL under free leaching conditions.

Parameter	Value
$\alpha_w D_w^{mat}$	$2 \times 10^{-13}\ m^2.s^{-1}$
$\alpha_s D_s^{mat}$	$8.5 \times 10^{-16}\ m^2.s^{-1}$

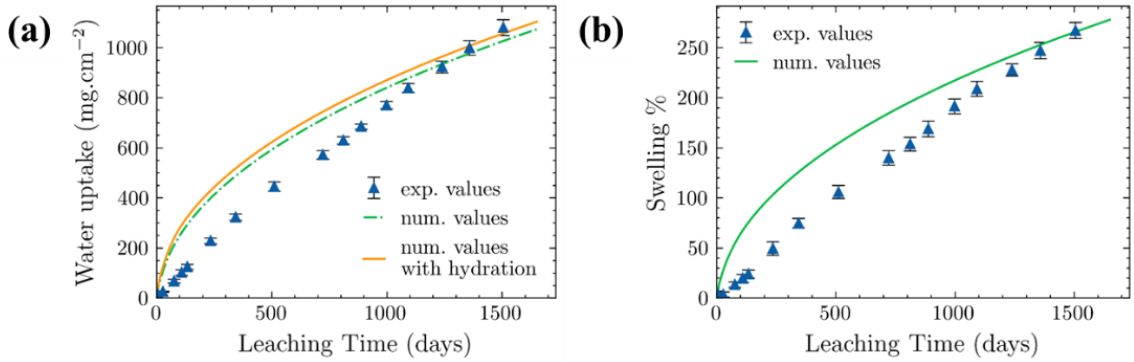

Fig. 5-46 Temporal evolution of (a) absorbed water; (b) swelling of industrial BWP STEL under free leaching conditions simulated using parameters in Table 26.

5.7.2. Application of parameters fitted under free leaching conditions to constant volume conditions

In this section, the parameters calibrated in 5.7.1 on STE3 and STEL under free leaching conditions are applied to leaching tests under constant volume conditions.

The stress build-up behavior of STE3 simulated with the parameter sets in Table 25 is compared with the experimental results [17] in Fig. 5-47. The experimentally observed stress relief stage is well reproduced, which shows that the model is valid for the entire leaching process under constant volume conditions. However, both parameter sets fitted under free leaching conditions cannot reproduce the experimental stress build-up behavior under constant volume conditions. Depending on the used parameter set, the numerical maximum pressure is about 12 and 18 MPa, which is nevertheless of the same order of magnitude as the experimental value (about 30 MPa by averaging two experimental measurements).

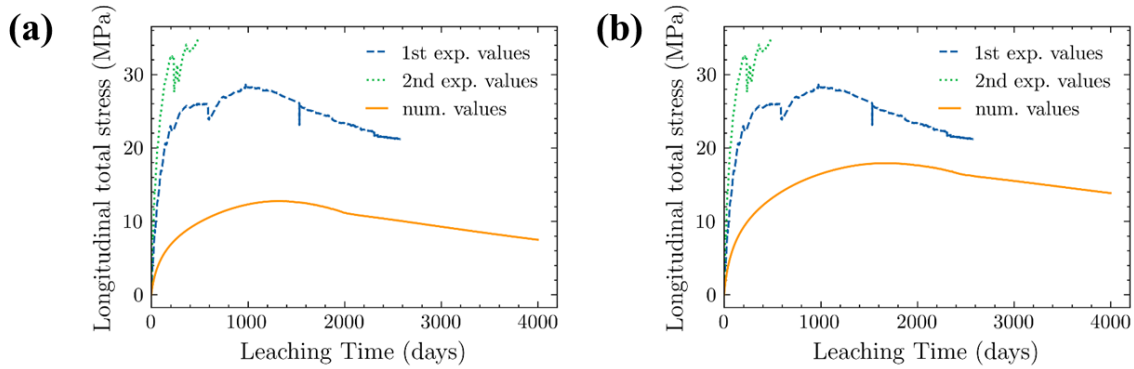

Fig. 5-47 Comparison of experimental results from [17] *and numerical simulation of the stress build-up behavior of STE3 under constant volume conditions using (a) parameter set 1 ; (b) parameter set 2 in Table 25.*

The stress build-up behavior of STEL simulated with the parameters in Table 26 is compared with the experimental results [17] in Fig. 5-48. The parameters fitted under free leaching conditions cannot reproduce the experimental stress build-up behavior under constant volume conditions. The experimental stress values continue to increase until 3000 days while the numerical simulation reaches its maximum of about 17.7 MPa at 900 days.

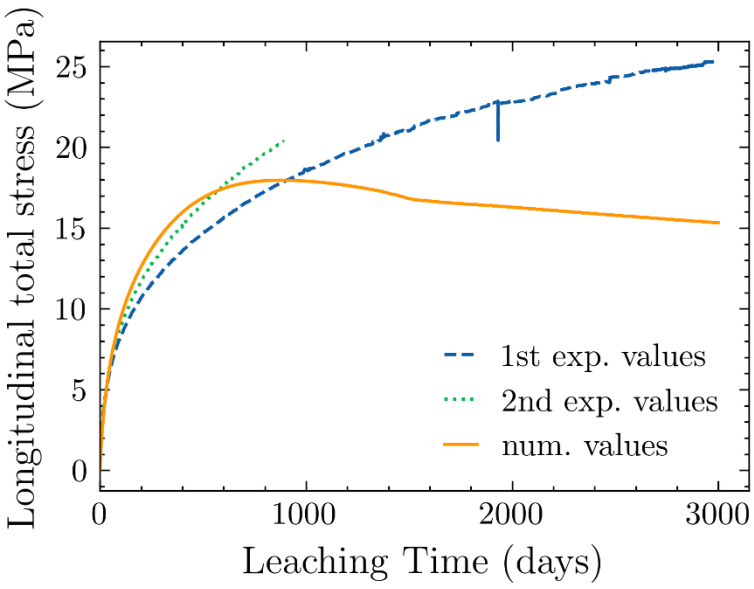

Fig. 5-48 Comparison of experimental results from [17] *and numerical simulation of the stress build-up behavior of STEL under constant volume conditions using parameters in Table 26.*

The differences in leaching kinetics and maximum pressure between the experimental data and the numerical results are *a priori* due to a simplified composition used for simulation. The important volumetric expansion (3.2 times larger) due to the recrystallization of anhydrous Na_2SO_4 (thenardite) into its decahydrate form $Na_2SO_4 \cdot 10H_2O$ (mirabilite) [17] is not taken into account and could contribute to the difference of the generated stress. Moreover, various poorly soluble salts present in STE3 and STEL (cf. Table 1), which are currently all assimilated to $BaSO_4$, could actually have a more complex effect on the leaching behavior.

5.7.3. Fitting of stress build-up behavior of STE3 and STEL under constant volume conditions

In this section, we try to fit the experimental stress build-up behaviors of STE3 and STEL under constant volume conditions [17] (cf. 2.3.2).

With specifically fitted parameters (listed in Table 27), the experimental stress build-up behavior of STE3 can be quite well reproduced by the numerical model (cf. Fig. 5-49). The simulated maximum stress is about 32.3 MPa.

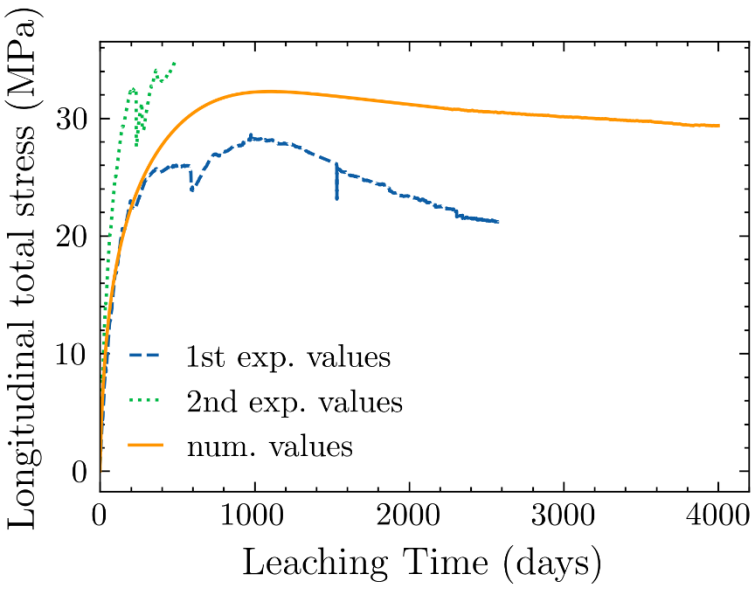

Fig. 5-49 Comparison of experimental results from [17] *and numerical simulation of the stress build-up behavior of STE3 under constant volume conditions using parameters in Table 27.*

Table 27 Parameters calibrated on experimental results of STE3 [17] *under constant volume conditions.*

Parameter	Value
$\alpha_w D_w^{mat}$	$3 \times 10^{-13}\ m^2.s^{-1}$
$\alpha_s D_s^{mat}$	$6 \times 10^{-16}\ m^2.s^{-1}$

Fig. 5-50 shows one fitting of the stress build-up behavior of STEL, the parameters are listed in Table 28. The stress build-up behavior is quite well reproduced until about 1000 days. The simulated stress stabilized at about 21 MPa after 1000 days while the experimental stress values continued to increase until 3000 days.

Table 28 Parameters calibrated on experimental results of STEL under constant volume conditions.

Parameter	Value
$\alpha_w D_w^{mat}$	$1 \times 10^{-13}\ m^2.s^{-1}$
$\alpha_s D_s^{mat}$	$1 \times 10^{-18}\ m^2.s^{-1}$

As a reminder, STEL contains only 4.1 wt.% of soluble salts (cf. Table 1) but swells much more under free leaching conditions than M5_NaNO3_M35_BaSO4 bi-salt BWPs containing 5 wt.% of soluble salts (cf. 3.2.7). It seems that various poorly soluble salts present in the bituminous matrix (cf. Table 1) may also be involved in the leaching process. It is not known yet which poorly soluble salts are involved, nor how they are involved. The simulation presented in Fig. 5-50 is performed with a simplified composition containing 4.1 wt.% of soluble salt $NaNO_3$ (cf. Table 24), the possible participation of the various poorly soluble salts to the stress build-up behavior is not considered. With this simplified composition, the model cannot reproduce the experimental results acquired on STEL. It is also worth noting that the simplified composition of STE3 (cf. Table 24) works relatively well because there are only 26 wt.% of poorly soluble salts, of which $BaSO_4$ accounts for 21 wt.%. However, STEL contains 41.9 wt.% of poorly soluble salts with only 14.7 wt.% $BaSO_4$. While the role of the $BaSO_4$ is studied via the existing experimental results and the fitted parameters (cf. 3.2.5 and 5.3.4), the effect of other poorly soluble salts (massively present in STEL) remains unknown. More experimental investigations are needed to

better understand the effect of the poorly soluble salts contained in these industrial BWPs on their stress build-up behavior under constant volume conditions.

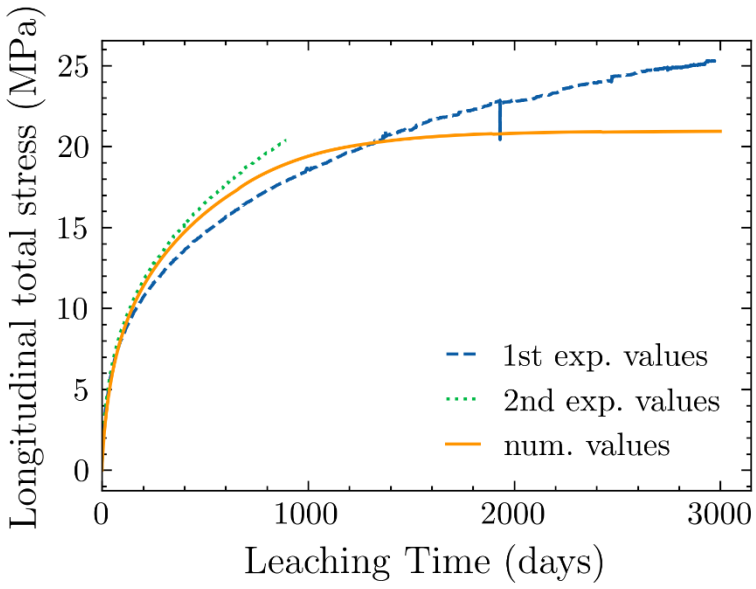

Fig. 5-50 Comparison of experimental results from [17] *and numerical simulation of the stress build-up behavior of STEL under constant volume conditions using parameters in Table 28.*

To summarize, despite the simplified compositions used for simulation, the model can partly reproduce the experimental stress build-up behaviors of industrial BWPs (STE3, STEL) by using specifically fitted parameters. However, it is difficult to interpret these fitted parameters. Further investigations are needed to better understand the stress build-up behaviors of these industrial BWPs.

5.8. Conclusion and perspectives of numerical results

In this chapter, the numerical model presented in CHAPTER 4 has been applied to the consolidation problem as well as leaching tests under free leaching, constant counter-pressure, and constant volume conditions on different simplified and industrial BWPs.

The model shows its validity for the entire leaching process. The consolidation stage is well reproduced by the model, and the simulated deformation under consolidation stress is consistent with the experimental values. For leaching tests under free leaching and constant counter-pressure conditions, the conclusions are summarized according to the composition of the BWPs for clarity.

For simplified mono-salt $NaNO_3$ BWPs :

- The free leaching tests were well reproduced, and a set of material parameters was fitted and validated on BWPs containing different $NaNO_3$ concentrations. The fitted parameters are consistent with the values reported in the literature.
- For leaching under constant counter-pressure, the test under low counter-pressure (176 kPa) was well reproduced with the same set of material parameters used for free leaching, which validates the model for leaching under constant counter-pressure. For larger counter-pressures (1.4 MPa and 2.8 MPa), the model predicts swelling values more important than experimental data and remains conservative. The ESEM image acquired during the leaching test under 2.8 MPa shows an extremely chaotic pattern. It seems that the leaching under 2.8 MPa

counter-pressure followed some preferential path within the sample, which could explain the differences between experimental and numerical results. Further investigations are needed to understand the origin of the different swelling behavior observed under important counter-pressure.

For simplified mono-salt Na_2SO_4 BWPs :

- The free leaching tests were well reproduced using the set of material parameters fitted and validated on mono-salt $NaNO_3$ BWPs, which shows that the model is valid for different soluble salts taken into account.

For simplified bi-salt $NaNO_3/BaSO_4$ BWPs :

- The free leaching tests were well reproduced. The fitted parameters highlighted the acceleration effect of the poorly soluble salts $BaSO_4$, which is consistent with the experimental observation.
- The experimental results under 176 kPa of counter-pressure can only be well reproduced by assuming that the poorly soluble salts $BaSO_4$ have no effect within the consolidated BWPs. This suggests that the acceleration effect of the $BaSO_4$ is *a priori* eliminated by the consolidation phase before leaching.

Due to the lack of experimental results under constant volume conditions for simplified French BWPs, the theoretical osmotic pressure for an aqueous solution of $NaNO_3$ with a perfect semi-permeable membrane is used to validate the numerical model under constant volume conditions. The model can well reproduce the theoretical osmotic pressure (about 41.6 MPa) by using appropriate Pitzer parameters. Sensitivity studies of BWP composition, material parameters, and sample size were realized to better understand the key parameters of the stress build-up behavior under constant volume conditions. The numerical results show that the maximum stress is more important for BWPs containing more soluble salts. The maximum stress increases as $\alpha_w D_w^{mat}$ increases or $\alpha_s D_s^{mat}$ decreases. The stress peak is reached more quickly with increased $\alpha_w D_w^{mat}$ or $\alpha_s D_s^{mat}$. The sample size has no significant impact on the maximum stress but can affect the stress build-up kinetics. Ideally, the model should be validated on experimental results of simplified BWPs under constant volume conditions.

The effect of the existing voids on the stress build-up behavior of BWPs under confined conditions is numerically investigated by studying the case of free leaching followed by leaching under constant volume conditions. The numerical results show that the percentage of maximum stress significantly decreases as the allowed swelling increases. Only about 40% of the maximum stress is reached when 30 vol. % of the swelling is allowed during the free leaching stage. Moreover, the sensitivity analysis shows that the sample height and the material parameters have little impact on the numerical results for the case of free leaching followed by leaching under constant volume conditions. The numerical results obtained are *a priori* also valid for simplified BWPs of real size.

The model is finally applied to the industrial BWPs (STE3, STEL) :

- The free leaching tests can be partly reproduced by the model.
- With specifically fitted parameters, the experimental stress build-up behavior of STE3 can be quite well reproduced. However, it is difficult to interpret the fitted parameters.
- The simplified composition used for simulation could *a priori* explain the differences between the numerical and experimental results under free leaching and constant volume conditions. Further experimental investigations are needed to better understand the effect of various poorly soluble salts present in the industrial BWPs

CHAPTER 6

CONCLUSIONS AND PERSPECTIVES

Conclusions :

Bituminized Waste Products (BWPs) were produced by conditioning in bitumen the co-precipitation sludge resulting from the industrial processing of spent nuclear fuel. In France and from the 1960s, about 75000 220-liter drums of BWPs were produced at Marcoule and La Hague. Currently, a few dozen drums of BWPs are still produced per year. For those categorized as intermediate level long-lived waste (ILW-LL), the geological disposal facility CIGEO [4] is the considered disposal solution

. This repository is foreseen to be constructed in the Callovo-Oxfordian (CoX) clay formation.

One of the challenges related to BWPs is their swelling behavior in geological disposal conditions due to water uptake. Under geological disposal conditions, and after about one or several hundred thousand years, the water from the host rock will indeed completely saturate the disposal cells containing these packages in the deep geological repository. By an osmotic phenomenon enabled by the semi-permeable capacity of the bitumen matrix, water in direct contact with BWPs will cause their swelling. Free swelling of BWPs will first occur until the existing voids within primary containers, as well as those between the concrete containers and the concrete pavement, are filled with site water. The BWPs swelling will then be under confined conditions, leading to pressure on the host rock which could potentially damage it near the disposal cell. While the above phenomena take place, the integrity of the Callovo-Oxfordian must be guaranteed. Therefore, the BWPs swelling behavior must be considered for the safety studies of deep geological disposal facilities after site closure. The objective of this PhD work is to predict the leaching behavior due to water uptake of French BWPs and to better understand the corresponding mechanisms behind it. The final goal is to better estimate the maximum stress that French BWPs could generate and apply to the host rock in terms of allowed deformation under geological disposal conditions.

Various experimental efforts have been made at CEA Marcoule to characterize the French BWPs leaching process. Leaching tests under different loading conditions have been conducted on industrial BWPs (STE3, STEL) and simplified BWPs (containing only soluble salt $NaNO_3$ and/or poorly soluble salt $BaSO_4$). The experimental data was provided within a joint R&D program (Babylone program [3] led by Andra and the three nuclear licensees, CEA, EDF and Orano). Free leaching tests were carried out for about 4 years on simplified and industrial BWPs. The swelling under free leaching conditions was measured for the first time on French BWPs. Leaching tests were conducted for about 2 years on simplified BWPs under constant counter-pressure up to 2.8 MPa. A consolidation stage, consistent with applying loading and unloading cycles of counter-pressure to the sample in successive steps, was conducted before the under constant counter-pressure. Microstructural analyses were realized by using ESEM.

As the experimental characterizations of the BWPs leaching process are complex and involve monitoring over several years or even decades, numerical models are necessary for investigating the long-term swelling behaviors of BWPs. The numerical models can also be used to carry out sensitivity studies and validate the phenomenological description established on experimental observations.

The main modeling hypotheses and the governing equations of the model developed during this PhD work are kept from the MELOT2019 model [1,2], which is a poro-mechanical model taking into account

the transport terms (diffusion, permeation, and osmosis). The limits of the MELOT2019 [1,2] model have been highlighted by the newly acquired experimental data, especially the simplified BWPs' swelling measurements**. An innovative flux formulation with coupled homogenization of transport terms** (diffusion, permeation, and osmosis) is proposed to better capture the role of the semi-permeable membrane played by the bitumen and the porosity-dependency of the coupled transport coefficients during the leaching process. **A non-linear poro-viscoelastic model taking into account large strains** is proposed to better model the BWPs' leaching behavior under confined conditions. The Mori-Tanaka homogenization scheme is applied to model the porosity-dependency of the viscoelastic parameters of the homogenized material. The hydration kinetics experimentally measured on French BWPs are used to better model the filling of the initial porosity (hydration stage). The resulting numerical model is implemented in the Finite Element code BIL developed by P. Dangla [25].

The leaching behavior under free leaching, constant counter-pressure, and constant volume conditions are numerically investigated for simplified French BWPs. The model shows its validity for the entire leaching process under both free and confined leaching conditions. The consolidation stage is well reproduced by the model, and the simulated deformation under consolidation stress is consistent with the experimental values. For free leaching tests, the model can well reproduce the experimental results collected on simplified French BWPs (mono-salt $NaNO_3$, mono-salt Na_2SO_4, bi-salt $NaNO_3$/$BaSO_4$ BWPs). The model has shown its validity for different soluble salts taken into account. The material parameters fitted on mono-salt $NaNO_3$ and mono-salt Na_2SO_4 BWPs are consistent with the values reported in the literature. The parameters fitted on bi-salt $NaNO_3$/$BaSO_4$ BWPs highlighted the acceleration effect of the poorly soluble salts $BaSO_4$, which is consistent with the experimental observation. For leaching tests under constant counter-pressure, the tests conducted under low counter-pressure (176 kPa) on mono-salt $NaNO_3$ BWPs and bi-salt $NaNO_3$/$BaSO_4$ BWPs are well reproduced by using the same material parameters fitted under free leaching conditions. It should be noted that the experimental results of bi-salt $NaNO_3$/$BaSO_4$ BWPs under 176 kPa can only be well reproduced by assuming that the poorly soluble salts $BaSO_4$ have no effect within the consolidated BWPs. This suggests that the acceleration effect of the $BaSO_4$ is *a priori* eliminated by the consolidation phase before leaching. However, the model predicts swelling values higher than the experimental data for larger counter-pressures (1.4 MPa and 2.8 MPa). The ESEM image acquired during the leaching test under 2.8 MPa shows an extremely chaotic pattern. It seems that the leaching under 2.8 MPa counter-pressure followed some preferential path within the sample, which could explain the differences between experimental and numerical results. Further investigations are needed to determine if the different swelling behavior observed under important counter-pressure is an experimental bias or to understand its origin if it is not the case. For leaching tests under constant volume conditions, the theoretical osmotic pressure for an aqueous solution of $NaNO_3$ with a perfect semi-permeable membrane is used to validate the model as there are currently no existing experimental results of simplified French BWPs under constant volume conditions. The model can well reproduce the theoretical osmotic pressure (about 41.6 MPa) by using appropriate Pitzer parameters. Sensitivity studies of BWP composition, material parameters, and sample size were realized to better understand the key parameters of the stress build-up behavior under constant volume conditions.

The effect of the existing voids on the stress build-up behavior of BWPs under confined conditions is numerically investigated by studying the case of free leaching followed by leaching under constant volume conditions. The numerical results show logically that the stress peak decreases as the allowed swelling increases. Considering that the stress maximum is obtained when no swelling is allowed (constant volume all the time), results could be given in terms of percentage of this maximum stress versus allowed deformation. The numerical results show that the percentage of maximum stress significantly decreases as the allowed swelling increases. Only about 40% of the maximum stress is reached when

about 30 vol. % of the swelling is allowed during the free leaching stage**. Moreover, the sensitivity analysis shows that the sample height and the material parameters have little impact on these numerical results of percentage of maximum stress VS allowed deformation**. The numerical results for the case of free leaching followed by leaching under constant volume conditions are *a priori* also valid for BWPs of real size.

Finally, the model is tested on industrial BWPs (STE3, STEL) with a simplified composition (only the most soluble salt is taken into account, other salts are considered as inert components). The experimental results under either free leaching or constant volume conditions can be partly reproduced by using specifically fitted parameters. The evolution trends and orders of magnitude of numerical results are consistent with the experimental results. However, it is difficult to interpret these fitted parameters. The specific leaching behaviors observed on industrial BWPs (STE3, STEL) are *a priori* due to various poorly soluble salts contained in the industrial BWPs and cannot be perfectly reproduced by the model using a simplified composition. Further experimental investigations are needed to better understand the effect of various poorly soluble salts present in the industrial BWPs.

In summary, the numerical model developed in this thesis can capture quite well the main physical phenomena involved during the leaching process of BWPs under geological disposal conditions. The availability of such a model is of great interest for evaluating the leaching behavior of BWPs in underground geological disposal conditions. It could provide information for assessing potential damage to the Callovo-Oxfordian in the near-field of the disposal cells and thus contribute to the disposal facilities' safety studies after site closure.

Perspectives :

It should be noted that only one salt (the most soluble one, $NaNO_3$ in this work) is considered in the current model. The poorly soluble salts contained in the BWPs are assimilated as part of the bitumen matrix, their role is expected to be captured by the material parameters. This approach worked well for the simplified French BWPs (mono-salt $NaNO_3$, mono-salt Na_2SO_4, bi-salt $NaNO_3$/$BaSO_4$ BWPs). However, it seems that the role of various poorly soluble salts contained in the industrial BWPs (STE3, STEL) is more complex and cannot be easily captured by such an approach. Further investigations will be needed to better understand and model the effect of various poorly soluble salts present in the industrial BWPs. The final objective, beyond the thesis, is to find a set of parameters that will give an enveloping result in terms of stress for industrial BWPs.

In the model developed during this PhD work, the filling of the initial porosity by water (hydration stage) is modeled independently from the main leaching phenomena (diffusion, permeation, and osmosis). Such a hypothesis is supported by the H-NMR experiments conducted by CEA Marcoule [18,19] on simplified BWPs containing both soluble and poorly soluble salts, which shows that the progression of the hydration front is much faster than the leaching front. Further investigations are needed to refine the model and determine the validity domain of this hypothesis.

$\alpha_w, \alpha_s, D_w^{mat}$ and D_s^{mat} are four material parameters of the BWP matrix, their products $\alpha_w D_w^{mat}$ and $\alpha_s D_s^{mat}$ are used as the fitting parameters in the numerical model. D_w^{mat} and D_s^{mat} ($m^2.s^{-1}$) are the diffusion coefficients of water and dissolved salt in the BWP matrix. α_w and α_s are two solubility factors (-) of water and dissolved salt in the BWP matrix. For now, only the values of α_w and D_w^{mat} reported by B. Gwinner [16] can be used to compare with the fitted parameters (cf. 5.3.4). Further experimental investigations are needed to better understand the physical meanings of the fitted parameters. On the other hand, experiments have been conducted at CEA Saclay to measure the values of the effective diffusion coefficient of salt within different BWPs. These results could be compared with

the simulated values of the effective diffusion coefficient (cf. equation (73)) to consolidate the choice of the material parameters $\alpha_w, \alpha_s, D_w^{mat}$ and D_s^{mat}.

Due to the limited experimental data, the origin of the different leaching behaviors observed on BWPs under large constant counter-pressure (1.4 and 2.8 MPa) remains unknown. Besides, no experimental results of simplified BWPs under constant volume conditions can be used to validate the model. Further experimental investigations under large constant counter-pressure and constant volume conditions are therefore needed to better understand the leaching behaviors of BWPs and to improve the model.

To get as close as possible to the industrial case (BWPs placed in a cell excavated in the Callovo-Oxfordian argillite), this model could be coupled to an appropriate model for the behavior of the host rock, such as a viscoplastic behavior law like the LKR model [26] used by EDF to model the Callovo-Oxfordian argillite and implemented in the Codes-Aster finite element code [27]. This would allow us to assess the possible mechanical consequences of the BWPs' swelling on the Callovo-Oxfordian in the near field of the disposal cells. The model developed in this thesis could also be used to provide an estimate of the maximum stress that the Callovo-Oxfordian could undergo, which could be used in a simplified approach to assess near-field Callovo-Oxfordian damage induced by BWPs' swelling.

APPENDIX A

COUPLED HOMOGENIZATION OF TRANSPORT TERMS

In this appendix, we show the demonstration for equations (62)-(63) and (71)-(73) in section 4.2.

The temperature is assumed to be uniform and constant in the material. Assuming the thermodynamic equilibrium at the macroscopic scale, the chemical potential of species i ($i = w$ for water and $i = s$ for salt) are uniform at the macroscopic scale and thus take the same value in the bitumen and the pore solution. By neglecting gravity, the overall dissipation associated with water and salt transport phenomena is positive and can be expressed as [44,45]:

$$-\boldsymbol{W_w} \cdot \nabla(\mu_w) - \boldsymbol{W_s} \cdot \nabla(\mu_s) \geq 0 \tag{59}$$

where $\boldsymbol{W_w}$ and $\boldsymbol{W_s}$ are respectively the mass flux ($kg.m^{-2}.s^{-1}$) of water and salt, μ_w and μ_s respectively the chemical potential ($J.kg^{-1}$) of water and dissolved salt.

Equation (59) can be transformed to:

$$-\boldsymbol{W_l} \cdot \nabla(\mu_w) - \boldsymbol{W_s} \cdot \nabla(\mu_s{}') \geq 0 \tag{A.1}$$

where we defined the liquid flux $\boldsymbol{W_l} = \boldsymbol{W_s} + \boldsymbol{W_w}$ and $\mu_s' = \mu_s - \mu_w$.

The Gibbs-Duhem equation writes:

$$\rho_w d(\mu_w) + \rho_s d(\mu_s) = d(p) \tag{A.2}$$

where ρ_w and ρ_s ($kg.m^{-3}$) are the mass concentration of water and dissolved salt in the liquid phase, respectively.

Equation (A.*2*) can be rewritten as $\rho_l \mathrm{d}(\mu_w) + \rho_s \mathrm{d}(\mu_s{}') = d(p)$ by introducing liquid density $\rho_l = \rho_w + \rho_s$. We have therefore:

$$\nabla(\mu_w) = \frac{\nabla(p) - \rho_s \nabla(\mu_s{}')}{\rho_l} \tag{A.3}$$

By substituting equation (A.*3*) into equation (A.*1*), we have:

$$-\frac{1}{\rho_l}\boldsymbol{W_l} \cdot \nabla(p) - \boldsymbol{j_s} \cdot \nabla(\mu_s') \geq 0 \tag{A.4}$$

where we defined water and salt diffusive flux $\boldsymbol{j_w} = \boldsymbol{W_w} - \frac{\rho_w}{\rho_l}\boldsymbol{W_l}$ and $\boldsymbol{j_s} = \boldsymbol{W_s} - \frac{\rho_s}{\rho_l}\boldsymbol{W_l}$ with the property $\boldsymbol{j_s} + \boldsymbol{j_w} = 0$.

The inequality (59) can always be satisfied if $\boldsymbol{W_w}$ and $\boldsymbol{W_s}$ are written in terms of μ_w and μ_s as [46]:

$$\boldsymbol{W_w} = -D_{ww}\nabla(\mu_w) - D_{ws}\nabla(\mu_s) \tag{60}$$

$$\boldsymbol{W_s} = -D_{sw}\nabla(\mu_w) - D_{ss}\nabla(\mu_s) \tag{61}$$

where the diffusion matrix $\begin{bmatrix} D_{ww} & D_{ws} \\ D_{sw} & D_{ss} \end{bmatrix}$ is symmetric positive definite, entailing $D_{ww} > 0, D_{ss} > 0, D_{ww}D_{ss} - D_{sw}D_{ws} > 0$. D_{ws} and D_{sw} describe the coupled diffusion of salt and water in the medium, they are assumed to be equal ($D_{ws} = D_{sw}$).

With the same approach, the inequality (A.*4*) can be always satisfied by writing $\boldsymbol{W_l}$ and $\boldsymbol{j_s}$ in terms of p and μ_s' as:

$$\frac{1}{\rho_l}\boldsymbol{W_l} = -A\nabla(p) - C\nabla(\mu_s') \tag{A.5}$$

$$\boldsymbol{j_s} = -C\nabla(p) - B\nabla(\mu_s') \tag{A.6}$$

where the matrix $\begin{bmatrix} A & C \\ C & B \end{bmatrix}$ is symmetric positive definite, entailing $A > 0, B > 0, AB - C^2 > 0$. We can also check that $\rho_l^2(AB - C^2) = D_{ww}D_{ss} - D_{sw}^2$.

The link between the two sets of coefficients(D_{ww}, D_{ws}, D_{sw} and D_{ss}) and $(A, B, C)$are given by:

$$\rho_l^2 A = D_{ww} + D_{sw} + D_{ws} + D_{ss} \tag{A.7}$$

$$\rho_l C = \frac{\rho_w}{\rho_l}(D_{ss} + D_{ws}) - \frac{\rho_s}{\rho_l}(D_{ww} + D_{sw}) \tag{A.8}$$

$$B = \frac{\rho_w^2}{\rho_l^2}D_{ss} + \frac{\rho_s^2}{\rho_l^2}D_{ww} - \frac{\rho_s\rho_w}{\rho_l^2}(D_{sw} + D_{ws}) \tag{A.9}$$

The chemical potential of water μ_w and dissolved salt μ_s are written as [54]:

$$\mu_w = \mu_w^0 + \frac{RT}{M_w}ln(a_w) \tag{A.10}$$

$$d(\mu_w) = v_w d(p) + \frac{RT}{M_w}d(ln(a_w)) \tag{A.11}$$

$$\mu_s = \mu_s^0 + \frac{\nu_N RT}{M_s}ln(a_s) \tag{A.12}$$

$$d(\mu_s) = v_s d(p) + \frac{\nu_N RT}{M_s}d(ln(a_s)) \tag{A.13}$$

where μ_w^0 and μ_s^0 $(J.kg^{-1})$ are respectively the reference chemical potential at the standard state for water and dissolved salt, a_w and a_s (-) respectively the activity of water and dissolved salt, v_w and v_s $(m^3.kg^{-1})$ respectively the specific partial volume of water and dissolved salt, M_w and M_s $(kg.mol^{-1})$ respectively the molar mass of water and salt and ν_N the stoichiometric number of moles of ions per one mole of salt.

By substituting equations (A.*11*) and (A.*13*) into equation (A.*2*), we obtain:

$$\rho_s v_s + \rho_w v_w = 1 \tag{A.14}$$

$$\rho_s \frac{\nu_N RT}{M_s}d\big(ln(a_s)\big) + \rho_w \frac{RT}{M_w}d\big(ln(a_w)\big) = 0 \tag{A.15}$$

which results in

$$d(\mu_s') = v_s' d(p) + \frac{\nu_N RT}{M_s}\frac{\rho_l}{\rho_w}d\big(ln(a_s)\big) \tag{A.16}$$

where we defined $v_s' = v_s - v_w$.

Therefore, equations (A.*5*)-(A.*6*) can be transformed to:

$$\frac{\boldsymbol{W_l}}{\rho_l} = -(A + Cv_s')\nabla(p) - C\frac{\nu_N RT}{M_s}\frac{\rho_l}{\rho_w}\nabla\big(ln(a_s)\big) \tag{A.17}$$

$$\boldsymbol{j_s} = -(C + Bv_s')\nabla(p) - B\frac{\nu_N RT}{M_s}\frac{\rho_l}{\rho_w}\nabla\big(ln(a_s)\big) \tag{A.18}$$

The salt activity a_s can be defined as:

$$a_s = \gamma\frac{m}{m_0}$$

where γ is the mean activity coefficient, m is the molality (moles of solute per kilo of solvent, $mol.kg^{-1}$) and m_0 is the unit molality ($1\ mol.kg^{-1}$). The molality m can be expressed in terms of ω_s as $m = \frac{\omega_s}{(1-\omega_s)M_s}$.

Pitzer's model [47] is widely used to model the mean activity coefficient γ in terms of solute molality m.

For 1-1 electrolytes (such as $NaNO_3$), we have [47]:

$$\ln(\gamma) = f^\gamma + mB^\gamma + m^2C^\gamma \tag{A.19}$$

with

$$f^\gamma = -A_\phi\left(\frac{\sqrt{m}}{1+b\sqrt{m}} + \frac{2}{b}\ln\big(1+b\sqrt{m}\big)\right)$$

$$B^\gamma = 2\beta_0 + \frac{2\beta_1}{\alpha^2 m}\left[1-(1+\alpha\sqrt{m}-0.5\alpha^2 m)\exp(-\alpha\sqrt{m})\right]$$

$$C^\gamma = \frac{3}{2}C^\phi$$

where $A_\phi, b, \alpha, \beta_0, \beta_1$ and C^ϕ are model parameters. The activity coefficients calculated with Pitzer's model and the fitted parameters in Table 10 are compared with the experimental data [35] in Fig. A - 1.

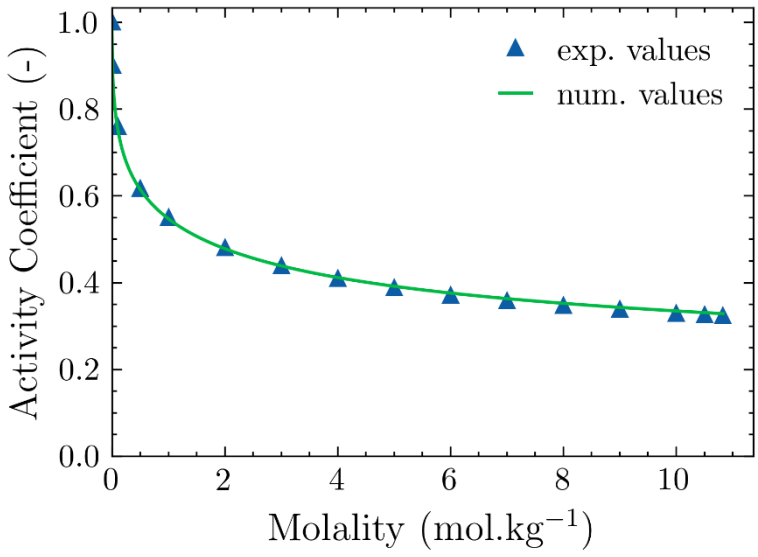

Fig. A - 1 Comparison of experimental data [35] *and activity coefficients calculated with Pitzer's model and the fitted parameters in Table 10.*

$\nabla(\ln(a_s))$ can then be expressed in terms of $\nabla(\omega_s)$ as:

$$\nabla(\ln(a_s)) = \frac{\nabla(\ln(\omega_s))}{\nu_N} R(\omega_s) = \frac{\nabla(\omega_s)}{\nu_N \omega_s} R(\omega_s) \tag{A.20}$$

with

$$R(\omega_s) = \frac{\nu_N \omega_s}{M_s(1-\omega_s)^2}\left[\frac{-A_\phi}{2\sqrt{m}}\frac{3+2b\sqrt{m}}{\left(1+b\sqrt{m}\right)^2} + 2\beta_0 + \frac{2\beta_1}{\alpha^2}\exp\left(-\alpha\sqrt{m}\right)\left(\alpha^2 - \frac{\alpha^3}{4}\sqrt{m}\right) + 2mC^\gamma\right] + \frac{\nu_N}{1-\omega_s} \tag{A.21}$$

For 2-1 electrolytes (such as Na_2SO_4), we have [47]:

$$\ln(\gamma) = 2f^\gamma + 4^{1/3} m B_\pm^\gamma + 4^{2/3} m^2 C_\pm^\gamma \tag{A.22}$$

with

$$f^\gamma = -A_\phi\left(\frac{\sqrt{3}\sqrt{m}}{1+\sqrt{3}b\sqrt{m}} + \frac{2}{b}\ln\left(1+\sqrt{3}b\sqrt{m}\right)\right)$$

$$B_\pm^\gamma = 2\beta_0^\pm + \frac{2\beta_1^\pm}{3\alpha^2 m}\left[1 - \left(1+\sqrt{3}\alpha\sqrt{m} - \frac{3}{2}\alpha^2 m\right)exp\left(-\sqrt{3}\alpha\sqrt{m}\right)\right]$$

where $A_\phi, b, \alpha, \beta_0, \beta_1$ are model parameters. The Pitzer's model parameters reported for the aqueous solution of Na_2SO_4 at 25°C [55] are listed in Table A. 1.

Table A. 1 Pitzer's model parameters for an aqueous solution of Na_2SO_4 at 25°C [55].

Parameter	Value
A_ϕ	$0.392\ kg^{1/2}mol^{-1/2}$
b	$1.2\ kg^{1/2}mol^{-1/2}$
α	$2\ kg^{1/2}mol^{-1/2}$
$\beta_0^\pm$	$0.0261\ kg.mol^{-1}$
$\beta_1^\pm$	$1.484\ kg.mol^{-1}$
$C_\pm^\gamma$	$0.01075\ kg^2.mol^{-2}$

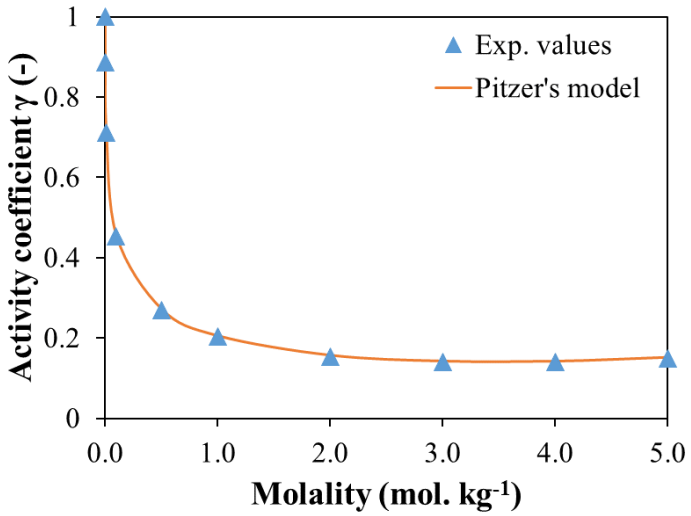

Fig. A - 2 Comparison of experimental data [56] and activity coefficients calculated with Pitzer's model and parameters reported for the aqueous solution of Na_2SO_4 at 25°C (cf. Table A. 1).

$\nabla(\ln(a_s))$ can then be expressed in terms of $\nabla(\omega_s)$ as:

$$\nabla(\ln(a_s)) = \frac{\nabla(\ln(\omega_s))}{\nu_N} R(\omega_s) = \frac{\nabla(\omega_s)}{\nu_N \omega_s} R(\omega_s) \tag{A.23}$$

with

$$R(\omega_s) = \frac{\nu_N \omega_s}{M_s(1-\omega_s)^2}\left[-\frac{A_\phi}{\sqrt{m}}\frac{3\sqrt{3}+6b\sqrt{m}}{\left(1+\sqrt{3}b\sqrt{m}\right)^2} + 2^{\frac{5}{3}}\beta_0^{\pm} + \frac{2^{\frac{5}{3}}\beta_1^{\pm}}{3\alpha^2}\exp\left(-\sqrt{3}\alpha\sqrt{m}\right)\left(3\alpha^2 - \frac{3\sqrt{3}}{4}\alpha^3\sqrt{m}\right) + 2^{\frac{7}{3}}C_{\pm}^{\gamma} m\right] + \frac{\nu_N}{1-\omega_s} \tag{A.24}$$

By substituting equation (A.*20*) into equations (A.*17*) and (A.*18*), we get flux written in terms of p and ω_s:

$$\frac{\boldsymbol{W_l}}{\rho_l} = -(A + Cv_s')\nabla(p) - C\frac{RT}{M_s}\frac{\rho_l}{\rho_w \omega_s} R(\omega_s)\nabla(\omega_s) \tag{A.25}$$

$$\boldsymbol{j_s} = -(C + Bv_s')\nabla(p) - B\frac{RT}{M_s}\frac{\rho_l}{\rho_w \omega_s} R(\omega_s)\nabla(\omega_s) \tag{A.26}$$

Equation (A.*25*) can be written as:

$$\boldsymbol{W_l} = -\rho_l k\nabla(p) + \rho_l \tau' \rho_l k\frac{RT}{M_s}\nabla(\omega_s) \tag{A.27}$$

by introducing effective permeability coefficient k ($m^2.Pa^{-1}.s^{-1}$), osmotic coefficient τ' (-) and diffusion coefficient D ($m^2.s^{-1}$):

$$k = A + Cv_s' \tag{A.28}$$

$$D = \frac{R(\omega_s)}{\rho_w \omega_s} B\frac{RT}{M_s} \tag{A.29}$$

$$\tau' \rho_l k = \frac{-R(\omega_s)\rho_l}{\rho_w \omega_s} C \tag{A.30}$$

Equation (A.*26*) then becomes:

$$\boldsymbol{j_s} = \frac{\omega_s \rho_w}{\rho_l R(\omega_s)}(\tau' - a)\rho_l k\nabla(p) - \rho_l D\nabla(\omega_s) \tag{A.31}$$

with $a = \frac{M_s}{RT}\frac{D}{k}v_s'$

Note that $\boldsymbol{W_s} = \boldsymbol{j_s} + \frac{\rho_s}{\rho_l}\boldsymbol{W_l}$. By using equations (A.*27*) and (A.*31*), $\boldsymbol{W_s}$ writes:

$$\boldsymbol{W_s} = \omega_s\left[1 - \frac{1-\omega_s}{R(\omega_s)}(\tau' - a)\right]\boldsymbol{W_l} - \rho_l\left(D - \frac{\omega_s \rho_w}{\rho_l R(\omega_s)}(\tau' - a)\frac{RT}{M_s}\tau' \rho_l k\right)\nabla(\omega_s) \tag{A.32}$$

For a perfect semi-impermeable porous medium, the salt transport is completely blocked. Therefore, $\boldsymbol{W_s} = 0$ should be satisfied for all values of $\boldsymbol{W_l}$ and $\nabla(\omega_s)$. This can be retrieved for $\tau' = \tau_0 = \frac{R(\omega_s)}{(1-\omega_s)(1-\rho_s v_s')}$, $a = a_0 = \tau_0 \rho_s v_s'$ and $D = D_0 = \frac{RT}{M_s}\tau_0 k_0 \rho_s$.

Equation (A.*32*) can be written as:

$$\boldsymbol{W_s} = \omega_s\left[1 - \frac{1-\omega_s}{R(\omega_s)}(\tau' - a)\right]\boldsymbol{W_l} - \rho_l D_{eff}\nabla(\omega_s) \tag{A.33}$$

by introducing an effective diffusion coefficient D_{eff}:

$$D_{eff}(\tau') = D - \frac{\omega_s \rho_w}{\rho_l R(\omega_s)} \frac{RT}{M_s} \tau' \rho_l k(\tau' - a) \tag{A.34}$$

Note that $AB - C^2 = \frac{\omega_s \rho_w}{\rho_l R(\omega_s)} \rho_l k \frac{M_s}{RT} D_{eff}$. Since $AB - C^2 > 0$ and $R(\omega_s) > 0$ for $\omega_s \in [0, \omega_{sat}]$ for $NaNO_3$, D_{eff} is assumed to be positive. The latter point is also numerically verified.

We can define the osmotic efficiency coefficient $\tau = \tau'/\tau_{max}$, where $\tau_{max}$is a normalization parameter. We can link $(k,\ \tau,\ D_{eff})$ to (D_{ww}, D_{ws}, D_{ss}) by using equations (A.*7*)-(A.*9*) and (A.*28*)-(A.*30*) :

$$\rho_l^2 k = (1 + \rho_w v_s')(D_{ss} + D_{ws}) + (1 - \rho_s v_s')(D_{ww} + D_{sw}) \tag{A.35}$$

$$\tau = \frac{\tau_0}{\tau_{max}} \left[1 - \frac{\frac{\rho_l}{\rho_s}(D_{ss} + D_{ws})}{\rho_l^2 k} \right] \tag{A.36}$$

$$\rho_l D_{eff} = \frac{R(\omega_s)}{1 - \omega_s} \frac{RT}{M_s} (1 - \frac{\tau_{max}\tau}{\tau_0}) \left[D_{ww} - \frac{D_{sw}^2 + D_{ww} D_{ws}}{D_{ss} + D_{ws}} \right] \tag{A.37}$$

with $\tau_0 = \frac{R(\omega_s)}{(1-\omega_s)(1-\rho_s v_s')}$.

By assuming $D_{sw} = D_{ws} = 0$, we get:

$$\rho_l^2 k = (1 + \rho_w v_s')D_{ss} + (1 - \rho_s v_s')D_{ww} \tag{64}$$

$$\tau = \frac{\tau_0}{\tau_{max}} \left[1 - \frac{\frac{\rho_l}{\rho_s} D_{ss}}{\rho_l^2 k} \right] \tag{65}$$

$$\rho_l D_{eff} = \frac{R(\omega_s)}{1 - \omega_s} \frac{RT}{M_s} (1 - \frac{\tau_{max}\tau}{\tau_0}) D_{ww} \tag{66}$$

D_{ww} and D_{ss} are the diffusion coefficients of water and dissolved salt in the homogenized material. By applying the Mori-Tanaka homogenization scheme [33,48] and by assuming that the diffusion in the pores is much larger than in the BWP matrix, we obtain

$$D_{ww} = \frac{1 + 2n_l}{1 - n_l} D_{ww}^{mat} \tag{67}$$

$$D_{ss} = \frac{1 + 2n_l}{1 - n_l} D_{ss}^{mat} \tag{68}$$

where D_{ww}^{mat} and $D_{ss}^{mat}(kg.s.m^{-3})$ are the diffusion coefficients in the BWP matrix, n_l is the Eulerian porosity of the liquid phase.

It is worth noting that D_{ww}^{mat} and D_{ss}^{mat} are diffusion coefficients related to $(\nabla\mu_w, \nabla\mu_s)$. We propose to note D_w^{mat} and D_s^{mat} $(m^2.s^{-1})$ the diffusion coefficients of water and dissolved salt in the BWP matrix related to $(\nabla\rho_w^{mat}, \nabla\rho_s^{mat})$, where $\rho_w^{mat} = \alpha_w \rho_w$ the solubility of water in the BWP matrix $(kg.m^{-3})$ and $\rho_s^{mat} = \alpha_s \rho_s$ the solubility of salt in the BWP matrix $(kg.m^{-3})$ with α_w and α_s two solubility factors (-).

By deriving the equation $\omega_s = \rho_s/\rho_l$, we get:

$$\nabla\omega_s = \frac{\omega_s}{1 + \omega_s \rho_l'/\rho_l} \frac{\nabla\rho_s}{\rho_s} \tag{A.38}$$

where we note $\rho_l' = \partial\rho_l/\partial\omega_s$. By substituting $\rho_s^{mat} = \alpha_s \rho_s$ into (A.*38*), we get:

$$\nabla\omega_s = \frac{\omega_s}{1 + \omega_s \rho_l'/\rho_l} \frac{\nabla\rho_s^{mat}}{\rho_s^{mat}} \tag{A.39}$$

The derivative of (A.*12*) gives $\nabla\mu_s = \frac{\nu_N RT}{M_s}\nabla(ln(a_s))$. By using (A.*20*) and (A.*39*), we have:

$$\nabla\mu_s = \frac{RT}{M_s}\frac{R(\omega_s)}{\omega_s}\frac{\omega_s}{1+\omega_s\rho_l'/\rho_l}\frac{\nabla\rho_s^{mat}}{\rho_s^{mat}} \tag{A.40}$$

The equivalence of salt diffusive flux due to $\nabla\mu_s$ and $\nabla\rho_s^{mat}$ gives:

$$D_{ss}^{mat}\nabla\mu_s = D_s^{mat}\nabla\rho_s^{mat} \tag{A.41}$$

By substituting (A.*40*) into (A.*41*), we get:

$$D_{ss}^{mat} = \rho_s^{mat}\frac{M_s}{\nu_N RT}\frac{1+\omega_s\rho_l'/\rho_l}{R(\omega_s)/\nu_N}D_s^{mat} \tag{A.42}$$

The term $\frac{1+\omega_s\rho_l'/\rho_l}{R(\omega_s)/\nu_N}$ is numerically evaluated for $\omega_s \in [0, \omega_{sat}]$ by using the evolution law of ρ_l in [1,2]. This term is found almost constant and equal to 1 and is therefore omitted for simplicity. With a similar approach, we can link D_{ww}^{mat} to D_w^{mat}.

Finally, we have:

$$D_{ww}^{mat} = \rho_w^{mat}\frac{M_w}{RT}D_w^{mat} \tag{69}$$

$$D_{ss}^{mat} = \rho_s^{mat}\frac{M_s}{\nu_N RT}D_s^{mat} \tag{70}$$

By substituting (*69*)-(*70*) into (*64*)-(*66*), the transport coefficients k, τ, D_{eff} can be finally written in terms of four material parameters ($\rho_w^{mat}, \alpha_s, D_w^{mat}$ and D_s^{mat}):

$$\rho_l^2 k = \frac{1+2n_l}{1-n_l}\frac{\rho_l}{RT}\left[(1+\rho_w v_s')\frac{\omega_s M_s}{\nu_N}\alpha_s D_s^{mat} + (1-\rho_s v_s')M_w(1-\omega_s)\alpha_w D_w^{mat}\right] \tag{71}$$

$$\tau = \frac{\tau_0}{\tau_{max}}\left[1 - \frac{1}{(1+(1-\omega_s)\rho_l v_s')\omega_s + (1-\omega_s\rho_l v_s')\nu_N\frac{M_w(1-\omega_s)\alpha_w D_w^{mat}}{M_s\alpha_s D_s^{mat}}}\right] \tag{72}$$

$$D_{eff} = \frac{1+2n_l}{1-n_l}\frac{R(\omega_s)}{1-\omega_s}\left(1-\frac{\tau_{max}\tau}{\tau_0}\right)\frac{M_w}{M_s}(1-\omega_s)\alpha_w D_w^{mat} \tag{73}$$

with $\tau_0 = \frac{R(\omega_s)}{(1-\omega_s)(1-\omega_s\rho_l v_s')}$ and

$$\tau_{max} = \frac{R(\omega_{sat})}{(1-\omega_{sat})(1-\omega_{sat}\rho_{sat}v_s')}\left[1 - \frac{1}{(1+(1-\omega_{sat})\rho_{sat}v_s')\omega_{sat}+(1-\omega_{sat}\rho_{sat}v_s')\nu_N\frac{M_W(1-\omega_{sat})\alpha_w D_w^{mat}}{M_s\alpha_s D_s^{mat}}}\right].$$

ω_{sat} is the solute mass fraction in the liquid phase at saturation and ρ_{sat} is the density of the saturated aqueous solution of dissolved salt.

In the end, the liquid and salt flux write:

$$\boldsymbol{W_l} = -\rho_l k\nabla(p) + \rho_l\tau_{max}\tau\rho_l k\frac{RT}{M_s}\nabla(\omega_s) \tag{62}$$

$$\boldsymbol{W_s} = \omega_s\left[1 - \frac{1-\omega_s}{R(\omega_s)}(\tau_{max}\tau - a)\right]\boldsymbol{W_l} - \rho_l D_{eff}\nabla(\omega_s) \tag{63}$$

with $a = \frac{\frac{D_{eff}M_s}{k\ RT}+\frac{\omega_s(1-\omega_s)\rho_l}{R(\omega_s)}\tau_{max}^2\tau^2}{\frac{1}{v_s'}+\frac{\omega_s(1-\omega_s)\rho_l}{R(\omega_s)}\tau_{max}\tau}$ a coupling parameter.

APPENDIX B

HOMOGENIZATION OF VISCOELASTICITY PARAMETERS

In this section, based on results in [39], we show the demonstration for equations (122)-(126) in section 4.3.

BWPs are considered as a porous material composed of BWPs matrix (phase 0) and pores (phase 1). Note n_r the volume fraction of the phase r with $n_1 + n_0 = 1$. In a differential form, the hydrostatic and deviatoric parts of the linear viscoelastic constitutive equations of the phase r can be written as:

$$R_r(d/dt).\sigma_{kk}^r(t) = S_r(d/dt).\varepsilon_{kk}^r(t) \tag{B.1}$$

$$P_r(d/dt).\boldsymbol{s_{ij}^r}(t) = Q_r(d/dt).\boldsymbol{e_{ij}^r}(t) \tag{B.2}$$

where σ_{ij}^r is the coefficient of the total stress tensor, s_{ij}^r is the coefficient of the deviatoric stress tensor ($s_{ij}^r = \sigma_{ij}^r - \frac{1}{3}tr(\sigma^r)\delta_{ij}$), ε_{ij}^r is the strain tensor, $\boldsymbol{e_{ij}^r}$ the coefficients of the deviatoric strain tensor ($\boldsymbol{e_{ij}} = \boldsymbol{\varepsilon_{ij}} - \frac{1}{3}tr(\varepsilon)\delta_{ij}$) for the phase r. P_r, Q_r, R_r and S_r are polynomial differential operators with constant coefficients, their specific forms being dependent upon the viscoelastic models adopted for each phase, and d/dt represents the time differential.

The Laplace transform of a time function $f(t)$ is defined as:

$$\hat{f}(s) = \int_0^{+\infty} f(t)e^{-st}dt \tag{B.3}$$

By using Laplace transform, equations (B.*1*)-(B.*2*) can be written in a similar form as in elasticity in the "transformed domain (TD)":

$$\hat{\sigma}_{kk}^r(s) = 3K_r^{TD}(s)\hat{\varepsilon}_{kk}^r(s) \tag{B.4}$$

$$\hat{\boldsymbol{s}}_{\boldsymbol{ij}}^{\boldsymbol{r}}(s) = 2G_r^{TD}(s)\hat{\boldsymbol{e}}_{\boldsymbol{ij}}^{\boldsymbol{r}}(s) \tag{B.5}$$

where $\hat{\sigma}_{kk}^r$, $\hat{\varepsilon}_{kk}^r$, $\hat{\boldsymbol{s}}_{\boldsymbol{ij}}^{\boldsymbol{r}}$ and $\hat{\boldsymbol{e}}_{\boldsymbol{ij}}^{\boldsymbol{r}}$ are the Laplace transform of their counterparts σ_{kk}^r, ε_{kk}^r, $\boldsymbol{s}_{\boldsymbol{ij}}^{\boldsymbol{r}}$ and $\boldsymbol{e}_{\boldsymbol{ij}}^{\boldsymbol{r}}$. $K_r^{TD}(s)$ and $G_r^{TD}(\mathrm{s})$ are the bulk and shear moduli of the phase r in the "transformed domain (TD)", defined as:

$$K_r^{TD}(s) = \frac{S_r(s)}{3R_r(s)} \tag{B.6}$$

$$G_r^{TD}(s) = \frac{Q_r(s)}{2P_r(s)} \tag{B.7}$$

The similarity between (B.*4*)-(B.*5*) and the elastic stress-strain relations makes it possible to adopt the correspondence principle, with the moduli in the transformed domain replacing their elastic counterparts. The effective moduli of a linear viscoelastic composite in the transformed domain $K_r^{TD}(s)$ and $G_r^{TD}(s)$ can be established by using the homogenization methods initially developed for the elasticity problem.

By using the Mori-Tanaka scheme [33,48] for the case of spherical inclusions (phase 1) in a matrix (phase 0), $K^{TD}(s)$ and $G^{TD}(s)$ write:

$$\frac{K^{TD}}{K_0^{TD}} = 1 + \frac{n_1(K_1^{TD} - K_0^{TD})}{n_0\alpha_0^{TD}(K_1^{TD} - K_0^{TD}) + K_0^{TD}} \tag{B.8}$$

$$\frac{G^{TD}}{G_0^{TD}} = 1 + \frac{n_1(G_1^{TD} - G_0^{TD})}{n_0\beta_0^{TD}(G_1^{TD} - G_0^{TD}) + G_0^{TD}} \tag{B.9}$$

where

$$\alpha_0^{TD} = \frac{3K_0^{TD}}{3K_0^{TD} + 4G_0^{TD}} \tag{B.10}$$

$$\beta_0^{TD} = \frac{6}{5}\frac{K_0^{TD} + 2G_0^{TD}}{3K_0^{TD} + 4G_0^{TD}} \tag{B.11}$$

The viscoelastic behavior of the composite writes in the transformed domain as:

$$\hat{\sigma}_{kk}(s) = 3K^{TD}(s).\hat{\varepsilon}_{kk}(s) \tag{B.12}$$

$$\hat{s}_{ij}(s) = 2G^{TD}(s).\hat{e}_{ij}(s) \tag{B.13}$$

In the following, we assume the BWPs matrix (phase 0) has a Maxwell viscoelastic behavior and the pores (phase 1) have an elastic behavior with elastic moduli equal to zero.

The viscoelastic behavior writes for the BWPs matrix (phase 0) as:

$$\dot{\boldsymbol{\varepsilon}}_{\boldsymbol{v}}^{\boldsymbol{0}} = \frac{1}{\eta_{v,0}}\sigma_m^0 + \frac{1}{K_0}\dot{\sigma}_m^0 \tag{B.14}$$

$$\dot{\boldsymbol{e}}_{\boldsymbol{ij}}^{\boldsymbol{0}} = \frac{1}{2\eta_{d,0}}\boldsymbol{s}_{\boldsymbol{ij}}^{\boldsymbol{0}} + \frac{1}{2G_0}\dot{\boldsymbol{s}}_{\boldsymbol{ij}}^{\boldsymbol{0}} \tag{B.15}$$

where $\varepsilon_v^0 = tr(\varepsilon^0)$, $\sigma_m^0 = \frac{1}{3}tr(\sigma^0)$, K_0 and G_0 are the bulk and shear moduli, $\eta_{v,0}$ and $\eta_{d,0}$ are the volumetric and deviatoric viscosity.

We have therefore,

$$\frac{s}{K_0^{TD}} = \frac{s}{K_0} + \frac{1}{\eta_{v,0}} \tag{B.16}$$

$$\frac{s}{G_0^{TD}} = \frac{s}{G_0} + \frac{1}{\eta_{d,0}} \tag{B.17}$$

The porosity (phase 1) is considered as elastic inclusion with

$$G_1^{TD} = G_1 = 0 \tag{B.18}$$

$$K_1^{TD} = K_1 = 0 \tag{B.19}$$

By substituting equations (B.*10*)-(B.*11*), (B.*16*)-(B.*17*) and (B.*18*)-(B.*19*) into (B.*8*)-(B.*9*), $K^{TD}(s)$ and $G^{TD}(s)$ write:

$$\frac{s}{K^{TD}} = \frac{1}{1-n_1}\left[\left(\frac{1}{K_0}+\frac{3n_1}{4G_0}\right)s + \left(\frac{1}{\eta_{v,0}}+\frac{3n_1}{4\eta_{d,0}}\right)\right] \tag{B.20}$$

$$\frac{s}{G^{TD}} = \frac{1}{1-n_1}\left(\frac{s}{G_s}+\frac{1}{\eta_d}\right)\left[1+6n_1\frac{\frac{s}{G_s}+\frac{1}{\eta_{d,0}}+\frac{2s}{K_s}+\frac{2}{\eta_{v,0}}}{P_1 s + P_2}\right] \tag{B.21}$$

with

$$P_1 = \frac{9}{G_0}+\frac{8}{K_0} \tag{B.22}$$

$$P_2 = \frac{9}{\eta_{d,0}}+\frac{8}{\eta_{v,0}} \tag{B.23}$$

The inverse Laplace transform of equation (B.*12*) using equation (B.*20*) gives:

$$\dot{\varepsilon_v} = \frac{3n_1K_0+4G_0}{4(1-n_1)K_0G_0}\dot{\sigma_m} + \frac{3n_1\eta_{v,0}+4\eta_{d,0}}{4(1-n_1)\eta_{v,0}\eta_{d,0}}\sigma_m \tag{B.24}$$

From (B.*24*), we can identify the effective elastic bulk moduli K and the effective volumetric viscosity η_v of the composite:

$$K = \frac{4(1-n_1)K_0G_0}{3n_1K_0+4G_0} \tag{B.25}$$

$$\eta_v = \frac{4(1-n_1)\eta_{v,0}\eta_{d,0}}{3n_1\eta_{v,0}+4\eta_{d,0}} \tag{B.26}$$

The Biot's coefficient b writes:

$$b = 1-\frac{K}{K_0} = 1-\frac{4(1-n_1)G_0}{3n_1K_0+4G_0} \tag{B.27}$$

By using equation (*111*), we have:

$$b^v = 1-\frac{\eta_v}{\eta_{v,0}} = 1-\frac{4(1-n_1)\eta_{d,0}}{3n_1\eta_{v,0}+4\eta_{d,0}} \tag{B.28}$$

The inverse Laplace transform of equation (B.*13*) using (B.*21*) gives:

$$P_1\ddot{e}_{ij}+P_2\dot{e}_{ij} = \frac{1}{1-n_1}\left(P_1(1+P_3)\left(\frac{\ddot{s}_{ij}}{G_0}+\frac{\dot{s}_{ij}}{\eta_{d,0}}\right)+P_2(1+P_4)\left(\frac{\dot{s}_{ij}}{G_0}+\frac{s_{ij}}{\eta_{d,0}}\right)\right) \tag{B.29}$$

with

$$P_3 = 6n_1\frac{K_0+2G_0}{9K_0+8G_0} \tag{B.30}$$

$$P_4 = 6n_1\frac{\eta_{v,0}+2\eta_{d,0}}{9\eta_{v,0}+8\eta_{d,0}} \tag{B.31}$$

(B.*29*) can be written as:

$$P_1\left[\ddot{e}_{ij}-\frac{1+P_3}{1-n_1}\left(\frac{\ddot{s}_{ij}}{G_0}+\frac{\dot{s}_{ij}}{\eta_{d,0}}\right)\right]+P_2\left[\dot{e}_{ij}-\frac{1+P_4}{1-n_1}\left(\frac{\dot{s}_{ij}}{G_0}+\frac{s_{ij}}{\eta_{d,0}}\right)\right]=0 \tag{B.32}$$

By using the values in Table 12, we have $K_0 \gg G_0$ and $\eta_{v,0} \gg \eta_{d,0}$, (B.*30*) and (B.*31*) become therefore:

$$P_3 = P_4 = \frac{2n_1}{3} \tag{B.33}$$

(B.*32*) can be written as:

$$P_1\dot{Q} + P_2 Q = 0 \tag{B.34}$$

with

$$Q = \dot{e}_{ij} - \frac{1+\frac{2n_1}{3}}{1-n_1}\left(\frac{\dot{s}_{ij}}{G_0}+\frac{s_{ij}}{\eta_{d,0}}\right) \tag{B.35}$$

The solution of (B.*34*) can be given as:

$$Q(t) = Q_0 \exp(-\frac{P_2}{P_1}t)$$

with Q_0 a constant. Since $Q(t=0)=0$, we have $Q_0 = 0$ and therefore $Q = 0$.

(B.*35*) becomes then:

$$\dot{e}_{ij} = \frac{1+\frac{2n_1}{3}}{1-n_1}\left(\frac{\dot{s}_{ij}}{G_0}+\frac{s_{ij}}{\eta_{d,0}}\right) \tag{B.36}$$

where we can identify

$$\eta_d = \eta_{d,0}\frac{1-n_1}{1+\frac{2}{3}n_1} \tag{B.37}$$

$$G = G_0\frac{1-n_1}{1+\frac{2}{3}n_1} \tag{B.38}$$

Finally, by taking into account $K_0 \gg G_0$ and $\eta_{v,0} \gg \eta_{d,0}$ and by noting $K_s = K_0$ and $G_s = G_0$ the bulk and the shear modulus of the BWPs matrix respectively, $\eta_{v,s} = \eta_{v,0}$ and $\eta_{d,s} = \eta_{d,0}$ the volumetric and the deviatoric viscosity of the BWP matrix respectively, $n_l = n_1$ the Eulerian porosity, we have:

$$K = K^s\frac{\left(4G^s(1-n_l)\right)}{3n_lK^s+4G^s} \tag{122}$$

$$G = G^s\frac{1-n_l}{1+\frac{2}{3}n_l} \tag{123}$$

$$\eta_v = \eta_{v,s}\frac{\left(4\eta_{d,s}(1-n_l)\right)}{3n_l\eta_{v,s}+4\eta_{d,s}} \tag{124}$$

$$\eta_d = \eta_{d,s} \frac{1 - n_1}{1 + \frac{2}{3} n_1} \tag{125}$$

$$b = 1 - \frac{4G^s(1 - n_l)}{3n_l K^s + 4G^s} \tag{126}$$

$$b^v = 1 - \frac{4\eta_{d,s}(1 - n_l)}{3n_l \eta_{v,s} + 4\eta_{d,s}} \tag{127}$$

APPENDIX C

TEMPORAL DISCRETIZATION FOR NUMERICAL RESOLUTION

In this appendix, the temporal discretization of equations (118), (119) and (121) for numerical resolution is detailed.

By using subscripts n and $n-1$ to represent respectively the current time step and the previous time step, we have:

$$\frac{d\varepsilon_v}{dt} = \frac{\Delta\varepsilon_v}{dt} = \frac{\varepsilon_{v_n} - \varepsilon_{v_{n-1}}}{dt} \tag{C.1}$$

$$\frac{d\sigma_m}{dt} = \frac{\Delta\sigma_m}{dt} = \frac{\sigma_{m_n} - \sigma_{m_{n-1}}}{dt} \tag{C.2}$$

$$\frac{dp}{dt} = \frac{\Delta \mathrm{p}}{dt} = \frac{p_n - p_{n-1}}{dt} \tag{C.3}$$

$$\frac{de_{ij}}{dt} = \frac{\Delta e_{ij}}{dt} = \frac{{e_{ij}}_n - {e_{ij}}_{n-1}}{dt} \tag{C.4}$$

$$\frac{ds_{ij}}{dt} = \frac{{s_{ij}}_n - {s_{ij}}_{n-1}}{dt} \tag{C.5}$$

By using equations (C.*1*)-(C.*5*), (*118*) and (*119*) can be discretized as follows:

$$\sigma_{m_n} + b^v p_n = \frac{\left[\frac{K\Delta\varepsilon_v}{1+\varepsilon_{v_n}} + (b^v - b)\Delta p + \sigma_{m_{n-1}} + b^v p_{n-1}\right]}{1 + \frac{Kdt}{\eta_v}} \tag{C.6}$$

$${s_{ij}}_n = \frac{2G\Delta e_{ij} + {s_{ij}}_{n-1}}{1 + Gdt/\eta_d} \tag{C.7}$$

The porosity evolution due to mechanical loading is described by equation (*120*), which can be transformed to:

$$\frac{dln\phi}{dt} = \frac{b}{n}\frac{d\,ln(1+\varepsilon_v)}{dt} + \frac{b^v - b}{\eta_v n}(\sigma_m + b^v p) + \frac{1}{nN}\frac{dp}{dt} \tag{C.8}$$

By using subscripts n and $n-1$ to represent respectively the current time step and the previous time step, we have:

$$\frac{dln\phi}{dt} = \frac{\Delta ln\phi}{dt} = \frac{ln\phi_n - ln\,\phi_{n-1}}{dt} \tag{C.9}$$

$$\frac{d\,ln(1+\varepsilon_v)}{dt} = \frac{\Delta\,ln(1+\varepsilon_v)}{dt} = \frac{ln\left(1+\varepsilon_{v,n}\right) - ln\left(1+\varepsilon_{v,n-1}\right)}{dt} \tag{C.10}$$

(C.*8*) can thus be discretized as:

$$ln\phi_n = ln\,\phi_{n-1} + \frac{b}{n}\Delta\ln(1+\varepsilon_v) + \frac{b^v - b}{\eta_v n}(\sigma_m + b^v p)dt + \frac{\Delta p}{nN} \quad \text{(C.11)}$$

The porosity evolution due to mechanical loading is therefore described as:

$$\phi_n = \phi_{n-1} \times \exp\left(\frac{b}{n}\Delta\ln(1+\varepsilon_v) + \frac{b^v - b}{\eta_v n}(\sigma_m + b^v p)dt + \frac{\Delta p}{nN}\right) \quad \text{(C.12)}$$

Let $d\phi_{salt} = \phi_{c_{n-1}} - \phi_{c_n}$ denote the volume change associated with salt crystal dissolution, we have finally:

$$\phi_n = \phi_{n-1} \times \exp\left(\frac{b}{n}\Delta\ln(1+\varepsilon_v) + \frac{b^v - b}{\eta_v n}(\sigma_m + b^v p)dt + \frac{\Delta p}{nN}\right) + d\phi_{salt} \quad \text{(C.13)}$$

Equations (C.*6*), (C.*7*) and (C.*13*) are implemented in the model.

APPENDIX D

RESULTS OF OEDOMETER TESTS AND ESTIMATION OF BWPS' ELASTIC PARAMETERS

The consolidation results of simplified French BWPs presented in 3.3.1 are used in this section to estimate their elastic parameters. As shown in 3.3.1, multiple loading and unloading were conducted during the consolidation process. By assuming that the samples have an elastic behavior during the unloading, the oedometer modulus can be estimated by calculating the slope of the stress-strain curves recorded during the unloading. Fig. D - 1 summarizes the experimental results recorded during the unloading stage conducted on mono-salt and bi-salt French simplified BWPs. Table D - 1 summarizes the fitted oedometer modulus and the corresponding coefficients of determination. The average value 144 ± 12 MPa is used as the oedometer modulus of the French simplified BWPs.

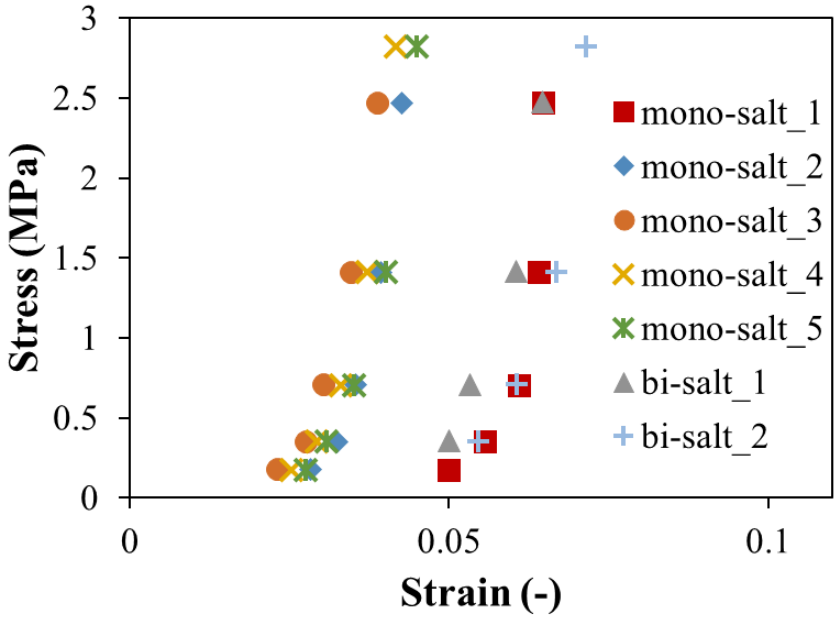

Fig. D - 1 Experimental points of stress VS strain recorded during the unloading stage conducted on mono-salt and bi-salt French simplified BWPs.

Table D - 1 Summary of oedometer modulus fitted on experimental results in Fig. D - 1.

	Fitted oedometer modulus (MPa)	Coefficient of determination R^2 (-)
mono-salt_1	126	0.7068
mono-salt_2	158	0.9018
mono-salt_3	146	0.9183
mono-salt_4	159	0.8947
mono-salt_5	146	0.909
bi-salt_1	136	0.9505
bi-salt_2	139	0.8853
Average	144 ± 12	

The oedometer modulus $E_{s,oed}$ is linked to Young's modulus E_s and Poisson's ratio ν_s by the following equation:

$$E_s = \frac{E_{s,oed}(1+\nu_s)(1-2\nu_s)}{(1-\nu_s)}$$

Recent experiments conducted in CEA Marcoule show that the Young's modulus E_s of French BWPs is in the order of 4 MPa (non-published results). In order to match the experimental results on E_s, the elastic parameters of French BWPs are determined as: $E_s = 4.3$ MPa, $\nu_s = 0.495$.

APPENDIX E

SENSITIVITY STUDY OF BWP MATRIX'S DEVIATORIC VISCOSITY $\eta_{d,s}$

$\eta_{d,s} = 1.6 \times 10^7\ Pa.s$ was proposed for the BWP matrix's deviatoric viscosity in [1,2]. However, with this value of $\eta_{d,s}$, the current model may generate non-physical results or numerical divergence, especially for consolidation cases and leaching under confined conditions, where the mechanical part of the model is more involved than under free leaching conditions. In this appendix, sensitivity studies of the BWP matrix's deviatoric viscosity $\eta_{d,s}$ are presented for consolidation case (cf. 5.4.1), leaching under constant volume conditions, under constant counter-pressure, and under free leaching conditions.

Fig. E - 1 illustrates the temporal evolutions of volume change simulated for M20_NaNO3 BWPs consolidated under 1 Pa with deviatoric viscosity $\eta_{d,s}$ ranging from $\eta_{d,s} = 1 \times 10^6$ Pa. s to $\eta_{d,s} = 1 \times 10^{11}$ Pa. s. With this extremely small consolidation stress, tiny volume change values are expected. However, a volume change of about -0.3% after 90 days was obtained with $\eta_{d,s} = 1.6 \times 10^7\ Pa.s$. The numerical results show that the volume change approaches 0% as $\eta_{d,s}$ increases. For $\eta_{d,s} \geq 1 \times 10^9\ Pa.s$, the volume change under 1 Pa is almost 0.

Similarly, Fig. E - 2 illustrates the temporal evolutions of volume change simulated for M20_NaNO3 BWPs consolidated under 100 Pa with deviatoric viscosity $\eta_{d,s}$ ranging from $\eta_{d,s} = 1 \times 10^6$ Pa. s to $\eta_{d,s} = 1 \times 10^{11}$ Pa. s. As a reminder, experimental volume changes between -9% and -6% were recorded under a consolidation stress of 2.8 MPa (cf. 3.3.1). The volume change under 100 Pa should be much less. However, with $\eta_{d,s} = 1.6 \times 10^7\ Pa.s$, the volume change under 100 Pa is almost stabilized at about 7% after 90 days, which is clearly not consistent with the experimental results. For $\eta_{d,s} \geq 1 \times 10^{10}\ Pa.s$, the volume change under 100 Pa is almost 0.

Fig. E - 1 and Fig. E - 2 show that $\eta_{d,s} = 1.6 \times 10^7\ Pa.s$ can lead to numerical simulations inconsistent with the experimental results. Sensitivity studies are thus realized for leaching under constant volume conditions, under constant counter-pressure, and under free leaching conditions to determine the value of $\eta_{d,s}$.

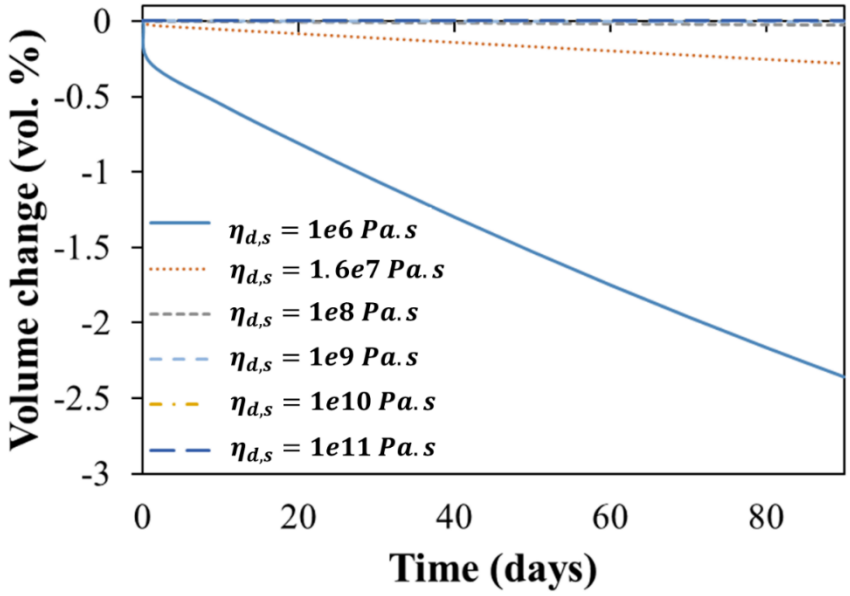

Fig. E - 1 Temporal evolutions of volume change simulated for M20_NaNO3 BWPs consolidated under 1 Pa with deviatoric viscosity $\eta_{d,s}$ ranging from $\eta_{d,s} = 1 \times 10^{6}\ Pa.s$ to $\eta_{d,s} = 1 \times 10^{11}\ Pa.s$.

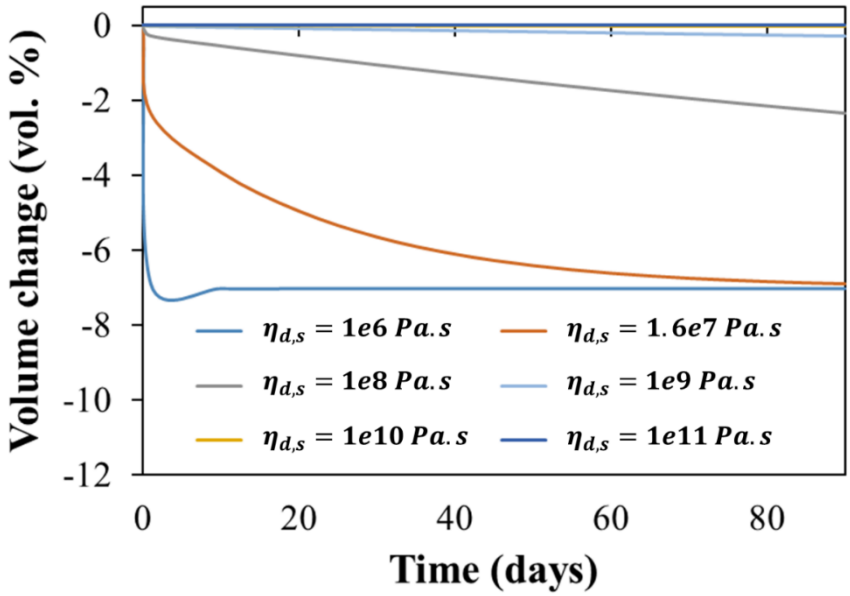

Fig. E - 2 Temporal evolutions of volume change simulated for M20_NaNO3 BWPs consolidated under 100 Pa with deviatoric viscosity $\eta_{d,s}$ ranging from $\eta_{d,s} = 1 \times 10^{6}\ Pa.s$ to $\eta_{d,s} = 1 \times 10^{11}\ Pa.s$.

Fig. E - 3 shows the generated stress simulated for M20_NaNO3 BWPs under constant volume conditions with deviatoric viscosity $\eta_{d,s}$ ranging from $\eta_{d,s} = 1 \times 10^{7}$ Pa.s to $\eta_{d,s} = 1 \times 10^{15}$ Pa.s. It should first be noted that the simulation diverges after 100 days with $\eta_{d,s} = 1 \times 10^{7}$ Pa.s. With $\eta_{d,s} = 1 \times 10^{8}$ Pa.s and $\eta_{d,s} = 1 \times 10^{9}$ Pa.s, the simulations also diverge since fluctuations with no physical meaning are observed. For $\eta_{d,s} \geq 1 \times 10^{10}\ Pa.s$, the simulations converge with physically meaningful numerical results. It is also worth noting that the numerical results generated with $\eta_{d,s} =$

$1 \times 10^{10}\ Pa.s$ coincide with the simulations generated with $\eta_{d,s} = 1 \times 10^{8}$ and $1 \times 10^{9}\ Pa.s$ before their divergence.

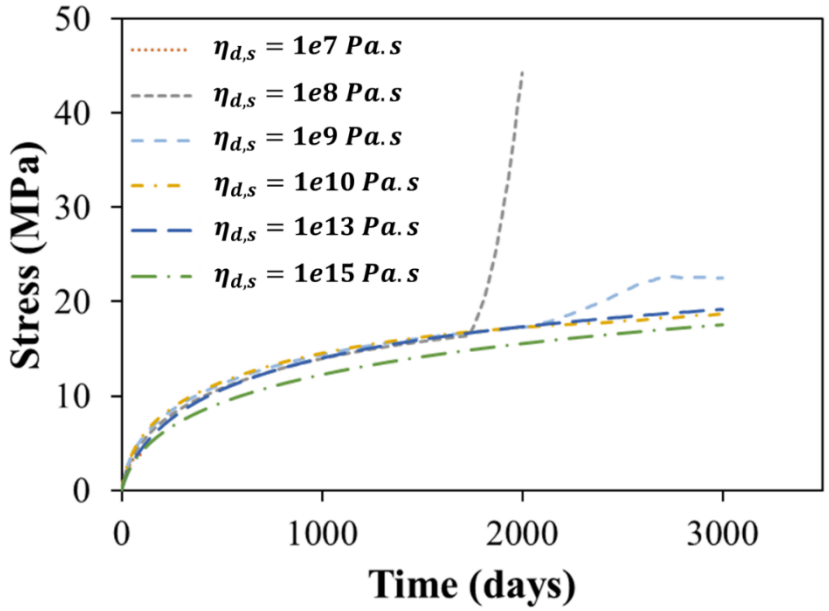

Fig. E - 3 Temporal evolutions of generated stress simulated for M20_NaNO3 BWPs under constant volume conditions with deviatoric viscosity $\eta_{d,s}$ ranging from $\eta_{d,s} = 1 \times 10^{7}\ Pa.s$ to $\eta_{d,s} = 1 \times 10^{15}\ Pa.s$.

Fig. E - 4 shows the temporal evolutions of swelling simulated for M30_NaNO3 BWPs under 2.8 MPa constant counter-pressure with deviatoric viscosity $\eta_{d,s}$ ranging from 1×10^{7} Pa. s to 1×10^{15} Pa. s. For $\eta_{d,s}$ ranging from 1×10^{7} Pa. s to 1×10^{10} Pa. s, the swelling increases as $\eta_{d,s}$ increases. On the other hand, the swelling decreases as $\eta_{d,s}$ increases for $\eta_{d,s}$ ranging from 1×10^{10} Pa. s to 1×10^{15} Pa. s. It is also worth noting that the simulations generated with different $\eta_{d,s}$ are quite close between them except the one generated with $\eta_{d,s} = 1 \times 10^{15}$ Pa. s.

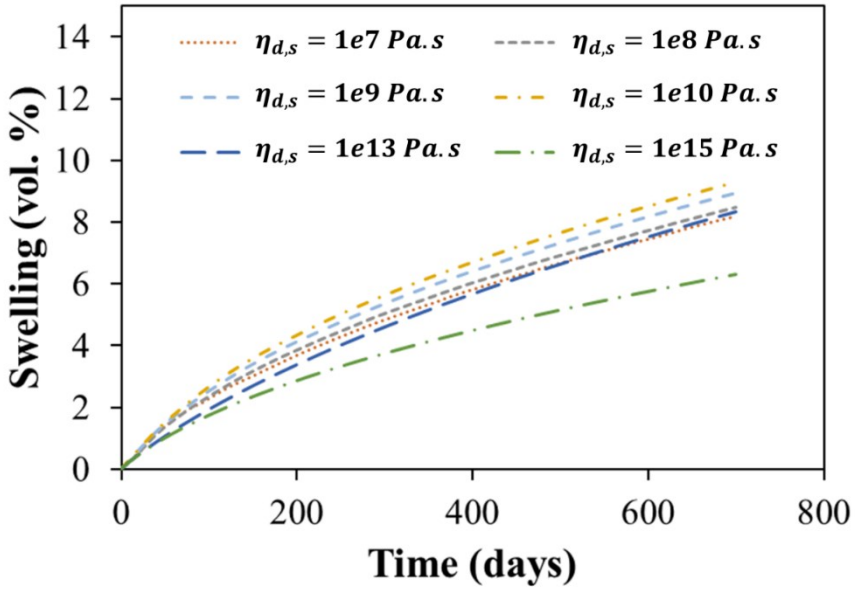

Fig. E - 4 Temporal evolutions of swelling simulated for M30_NaNO3 BWPs under 2.8 MPa constant counter-pressure with deviatoric viscosity $\eta_{d,s}$ ranging from $\eta_{d,s} = 1 \times 10^{7}\ Pa.s$ to $\eta_{d,s} = 1 \times 10^{15}\ Pa.s$.

Fig. E - 5 and Fig. E - 6 illustrate the temporal evolutions of swelling and water uptake amount simulated for M20_NaNO3 BWPs under free leaching conditions with deviatoric viscosity $\eta_{d,s}$ ranging from $\eta_{d,s} = 1 \times 10^{6}$ Pa. s to $\eta_{d,s} = 1 \times 10^{15}$ Pa. s . The simulations generated with $\eta_{d,s}$ ranging from 1×10^{6} Pa. s to 1×10^{10} Pa. s are almost overlapped. The numerical values simulated with $\eta_{d,s} = 1 \times 10^{13}$ Pa. s and $\eta_{d,s} = 1 \times 10^{15}$ Pa. s are significantly lower.

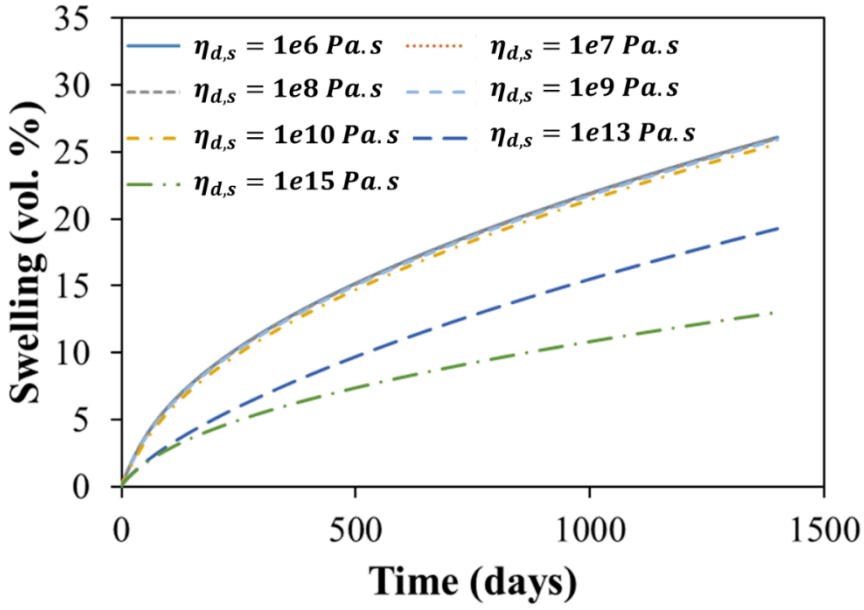

Fig. E - 5 Temporal evolutions of swelling simulated for M20_NaNO3 BWPs under free leaching conditions with deviatoric viscosity $\eta_{d,s}$ ranging from $\eta_{d,s} = 1 \times 10^{6}\ Pa.s$ to $\eta_{d,s} = 1 \times 10^{15}\ Pa.s$.

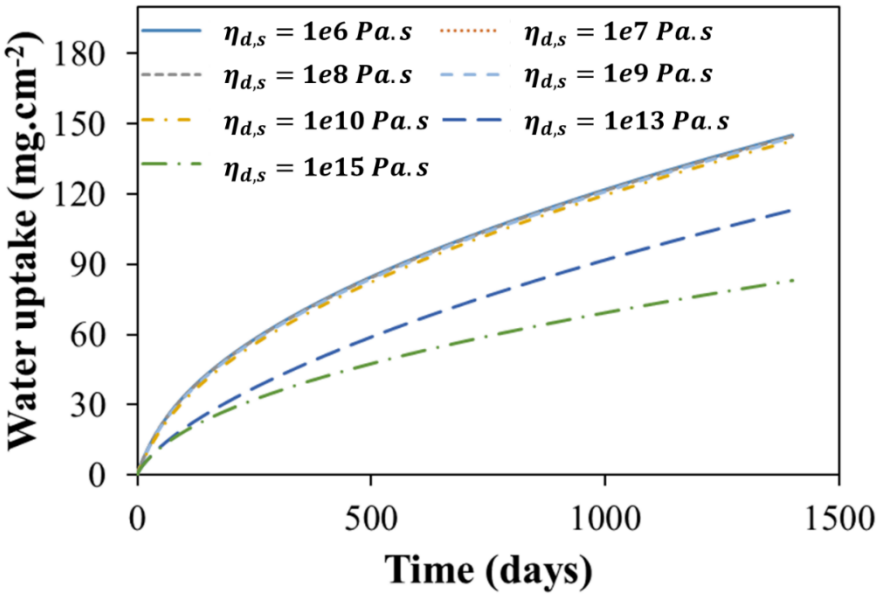

Fig. E - 6 Temporal evolutions of water uptake amounts for M20_NaNO3 BWPs under free leaching conditions with deviatoric viscosity $\eta_{d,s}$ ranging from $\eta_{d,s} = 1 \times 10^{6}\ Pa.s$ to $\eta_{d,s} = 1 \times 10^{15}\ Pa.s$.

In order to generate numerical results more consistent with the experimental data and to avoid numerical divergence, the BWP matrix's deviatoric viscosity $\eta_{d,s}$ is chosen based on the sensitivity studies presented above: $\eta_{d,s} = 1 \times 10^{10}\ Pa.s$.

APPENDIX F

SIMULATIONS IN 2D PLANE MODELING

Simulations in two-dimensional plane strain modeling are performed to verify the independence of the numerical results with respect to the dimension. 2D simulations using quadratic 8-node elements are compared to the simulations performed in 1D for several typical cases. A schematic representation of the two-dimensional configuration is presented in Fig. F - 1. The impact of the amount of mesh in width on numerical results is also investigated.

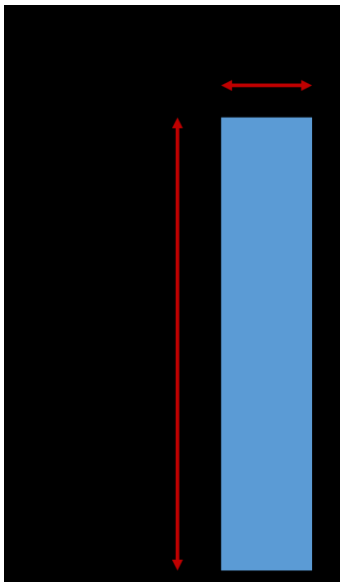

Fig. F - 1 Schematic representation of the two-dimensional configuration.

The numerical results simulated in 1D and 2D are compared for free leaching tests (cf. Fig. F – 2), leaching tests under constant counter-pressure (cf. Fig. F – 3 and Fig. F – 4), and leaching tests under constant volume conditions with a perfect semi-permeable bitumen matrix (cf. Fig. F – 5). Three 2D meshes are used for simulation : 2D - 1, 2D - 2, 2D – 5. They have the same amount of mesh in length as the 1D mesh and have respectively 1, 2 and 5 mesh in width.

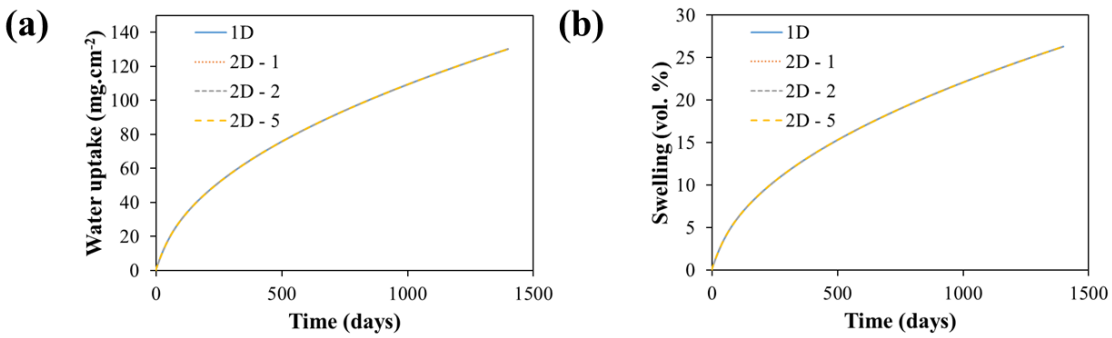

Fig. F – 2 Comparison of numerical results simulated in 1D and 2D for M20_NaNO3 under free leaching conditions.

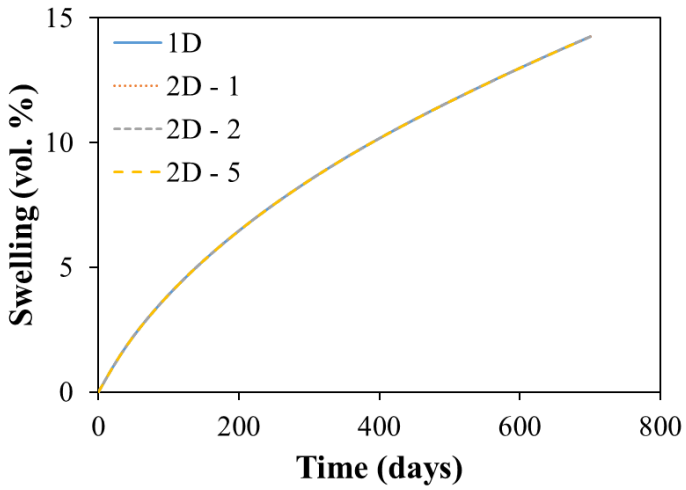

Fig. F – 3 Comparison of numerical results simulated in 1D and 2D for M30_NaNO3 under 176 kPa constant counter-pressure.

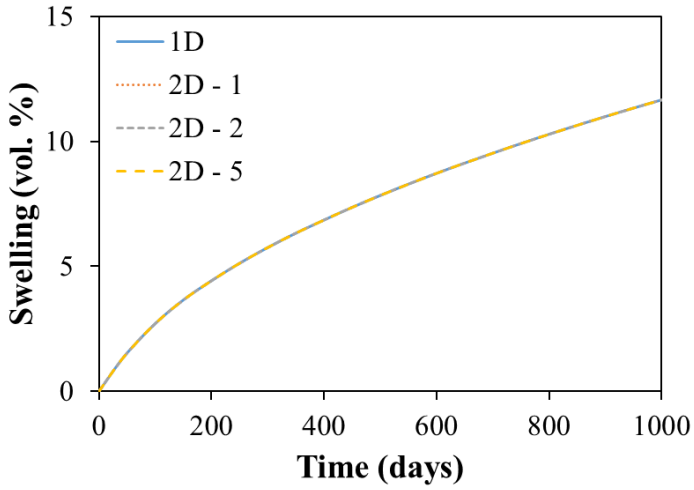

Fig. F – 4 Comparison of numerical results simulated in 1D and 2D for M30_NaNO3 under 2.8 MPa constant counter-pressure.

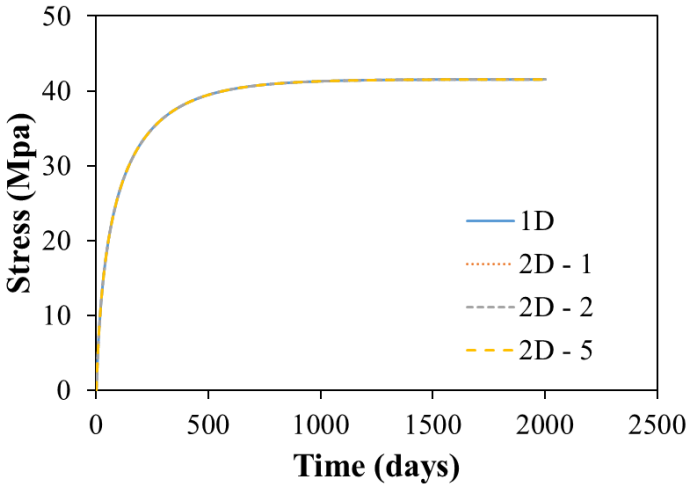

Fig. F – 5 Comparison of numerical results simulated in 1D and 2D for leaching tests under constant volume conditions with a perfect semi-permeable bitumen matrix.

The numerical results simulated in 2D are perfectly overlapped with those simulated in 1D for all the cases presented above. The numerical results are thus proven to be independent of the dimension. The simulations are thus performed only in 1D for the rest of this work.

REFERENCES

[1] G. Melot, P. Dangla, S. Granet, S. M'Jahad, J.B. Champenois, A. Poulesquen, Chemo-Hydro-Mechanical analysis of Bituminized waste swelling due to water uptake: Experimental and model comparisons, J. Nucl. Mater. 536 (2020) 152165. https://doi.org/10.1016/j.jnucmat.2020.152165.

[2] G. Mélot, Modélisation poromécanique du gonflement d'enrobés bitumineux par reprise d'eau, 2019.

[3] ANDRA, Pièce 20 : Plan de développement de l'installation de stockage Cigéo, 2022. https://www.andra.fr/sites/default/files/2023-04/Pièce 20-Plan de développement installation stockage Cigéo.pdf.

[4] Andra, Pièce 6 - Etude d'impact du projet global Cigéo - Volume I - Introduction et contexte réglementaire, 2022. https://www.andra.fr/sites/default/files/2023-04/Pièce 06-Etude impact-Vol1-Introduction et contexte.pdf (accessed May 15, 2023).

[5] ASN, Lettre ASN CODEP-DRC-2019-007552 - ASND/2019-00392, n.d.

[6] N. Bleyen, S. Smets, W. Verwimp, K. Hendrix, X. Sillen, E. Valcke, Hydration of Eurobitum bituminized waste under free swelling conditions: osmosis-induced swelling and NaNO3 leaching, MRS Adv. 1 (2016). https://doi.org/10.1557/adv.2017.196.

[7] A. Mariën, S. Smets, E. Valcke, Study of the Processes Related to the Water Uptake of Eurobitum Bituminized Radioactive Waste: Effect of Salt Concentration, MRS Proc. 1193 (2009) 513. https://doi.org/10.1557/PROC-1193-513.

[8] A. Mariën, E. Valcke, N. Bleyen, M. Van Geet, M. Wevers, The Use of µCT and ESEM in the Study of the Osmosis-Induced Water Uptake by Eurobitum Bituminized Radioactive Waste, Microsc. Microanal. 18 (2012) 1163–1180. https://doi.org/10.1017/S1431927612001092.

[9] E. Valcke, A. Marien, S. Smets, X. Li, N. Mokni, S. Olivella, X. Sillen, Osmosis-induced swelling of Eurobitum bituminized radioactive waste in constant total stress conditions, J. Nucl. Mater. 406 (2010) 304–316. https://doi.org/10.1016/j.jnucmat.2010.08.060.

[10] A. Mariën, N. Mokni, E. Valcke, S. Olivella, S. Smets, X. Li, Osmosis-induced water uptake by Eurobitum bituminized radioactive waste and pressure development in constant volume conditions, J. Nucl. Mater. 432 (2013) 348–365. https://doi.org/10.1016/j.jnucmat.2012.08.032.

[11] K. Irisawa, O. Ohsone, Y. Meguro, Effects of salt content on leaching properties of synthetic bituminized wastes, J. Nucl. Sci. Technol. 51 (2014) 323–331. https://doi.org/10.1080/00223131.2014.864959.

[12] K. Irisawa, Y. Meguro, Swelling pressure and leaching behaviors of synthetic bituminized waste products with various salt contents under a constant-volume condition, J. Nucl. Sci. Technol. (2017) 1–8. https://doi.org/10.1080/00223131.2016.1273143.

[13] J.B. Champenois, R. Blinder, A. Guillermo, M. Bardet, A. Poulesquen, Influence of Mineral Salts Content on Bituminous Waste Products Water Uptake, in: Poromechanics VI, American Society of Civil Engineers, Reston, VA, 2017: pp. 634–639. https://doi.org/10.1061/9780784480779.078.

[14] B. Gwinner, J. Sercombe, B. Simondi-Teisseire, F. Adenot, I. Felines, E. Favre, EXPERIMENTAL AND THEORETICAL STUDY OF THE PORE STRUCTURE AND DIFFUSION PROPERTIES OF AN EVOLVING HETEROGENEOUS MATERIAL: APPLICATION TO RADIOACTIVE BITUMINIZED WASTE, Chem. Eng. Commun. 194 (2007) 234–247. https://doi.org/10.1080/00986440600829747.

[15] B. Gwinner, J. Sercombe, C. Tiffreau, B. Simondi-Teisseire, I. Felines, F. Adenot, Modelling of bituminized radioactive waste leaching. Part II: Experimental validation, J. Nucl. Mater. 349 (2006) 107–118. https://doi.org/10.1016/j.jnucmat.2005.10.019.

[16] B. Gwinner, Comportement Sous Eau Des Dechets Radioactifs Bitumes : Validation Experimentale Du Modele De Degradation Colonbo, 2004.

[17] N. Bleyen, S. Smets, W. Verwimp, V. Van Gompel, E. Valcke, J. Lautru, A. Poulesquen, A. Leclerc, J.B. Champenois, Water uptake-induced pressure development by French bituminized radioactive waste products under nearly constant volume conditions, J. Nucl. Mater. 561 (2022) 153569. https://doi.org/https://doi.org/10.1016/j.jnucmat.2022.153569.

[18] S. Le Feunteun, O. Diat, A. Guillermo, A. Poulesquen, R. Podor, NMR 1D-imaging of water infiltration into mesoporous matrices, Magn. Reson. Imaging. 29 (2011) 443–455. https://doi.org/10.1016/j.mri.2010.10.001.

[19] R. Blinder, J.-B. Champenois, A. Leclerc, A. Poulesquen, A. Guillermo, J. Lautru, R. Podor, M. Bardet, NMR 1D-Imaging of Water Infiltration into Porous Bitumen-Salt Matrices: The Effect of Salt Solubility, J. Phys. Chem. C. 123 (2019) 27105–27115. https://doi.org/10.1021/acs.jpcc.9b09285.

[20] J. Sercombe, B. Gwinner, C. Tiffreau, B. Simondi-Teisseire, F. Adenot, Modelling of bituminized radioactive waste leaching. Part I: Constitutive equations, J. Nucl. Mater. 349 (2006) 96–106. https://doi.org/https://doi.org/10.1016/j.jnucmat.2005.10.014.

[21] N. Mokni, S. Olivella, E. Valcke, A. Mariën, S. Smets, X. Li, Deformation and Flow Driven by Osmotic Processes in Porous Materials: Application to Bituminised Waste Materials, Transp. Porous Media. 86 (2011) 635–662. https://doi.org/10.1007/s11242-010-9644-2.

[22] N. Mokni, Deformation and flow driven by osmotic processes in porous materials, Universitat Politècnica de Catalunya, 2011.

[23] N. Mokni, S. Olivella, X. Li, S. Smets, E. Valcke, A. Mariën, Deformation of bitumen based porous material: Experimental and numerical analysis, J. Nucl. Mater. 404 (2010) 144–153. https://doi.org/10.1016/j.jnucmat.2010.07.019.

[24] N. Mokni, S. Olivella, E.E. Alonso, Swelling in clayey soils induced by the presence of salt crystals, Appl. Clay Sci. 47 (2010) 105–112. https://doi.org/10.1016/j.clay.2009.01.005.

[25] P. Dangla, A. Bonnard, Ifsttar/bil: (v2.8.6) A Modeling Platform Based on Finite Volume/element Methods, (2022). https://doi.org/10.5281/ZENODO.6463236.

[26] S. Raude, Modèle de comportement LKR, (n.d.). https://code-aster.org/V2/doc/default/fr/man_r/r7/r7.01.40.pdf (accessed June 2, 2023).

[27] Electricité de France, Code_Aster Open Source - general FEA software, (n.d.). https://code-aster.org/ (accessed June 2, 2023).

[28] H. Sakamoto, S. Kobayashi, H. Tanabe, S. Kataoka, T. Yoshida, A. Takei, Y. Nakamori, M. Sugimoto, T. Kanno, A program to develop packages for long-lived ILW, (2001).

[29] S. Camaro, Long-term behavior of bituminized waste, in: Proc. Int. Work. Saf. Perform. Eval. Bituminization Process. Radioact. Waste (Radwaste Bituminization'99), 1999: pp. 157–160.

[30] W.M. Haynes, CRC handbook of chemistry and physics, CRC press, 2014.

[31] S. NAKAYAMA, Y. IIDA, T. NAGANO, T. AKIMOTO, Leaching Behavior of a Simulated Bituminized Radioactive Waste Form under Deep Geological Conditions, J. Nucl. Sci. Technol. 40 (2003) 227–237. https://doi.org/10.3327/jnst.40.227.

[32] H. Darcy, Les fontaines publiques de la ville de Dijon: exposition et application..., Victor Dalmont, 1856.

[33] L. Dormieux, D. Kondo, F.-J. Ulm, Microporomechanics, John Wiley & Sons, 2006.

[34] J.H. Hoff, R.A. Lehfeldt, Lectures on Theoretical and Physical Chemistry, 1900.

[35] Y.C. Moore, W.J. Hamer, Revised values of the osmotic coefficients and mean activity coefficients of sodium nitrate in water at 25°C, J. Phys. Chem. Ref. Data. 9 (1982) 513–518. https://doi.org/10.1063/1.555621.

[36] R.M. Barrer, Diffusion and permeation in heterogeneous media, Diffus. Polym. (1968) 165–217.

[37] J.C. Maxwell, A treatise on electricity and magnetism unabridged, Dover, 1954.

[38] J.D. Eshelby, The determination of the elastic field of an ellipsoidal inclusion, and related problems, Proc. R. Soc. London. Ser. A. Math. Phys. Sci. 241 (1957) 376–396.

[39] J. Li, G.J. Weng, Anisotropic stress-strain relations and complex moduli of a viscoelastic composite with aligned spheroidal inclusions, Compos. Eng. 4 (1994) 1073–1097. https://doi.org/10.1016/0961-9526(95)91284-N.

[40] Y.M. Wang, G.J. Weng, The Influence of Inclusion Shape on the Overall Viscoelastic Behavior of Composites, J. Appl. Mech. 59 (1992) 510–518. https://doi.org/10.1115/1.2893753.

[41] L.C. Brinson, W.S. Lin, Comparison of micromechanics methods for effective properties of multiphase viscoelastic composites, Compos. Struct. 41 (1998) 353–367. https://doi.org/10.1016/S0263-8223(98)00019-1.

[42] J.-F. Barthélémy, A. Giraud, F. Lavergne, J. Sanahuja, The Eshelby inclusion problem in ageing linear viscoelasticity, Int. J. Solids Struct. 97–98 (2016) 530–542. https://doi.org/10.1016/j.ijsolstr.2016.06.035.

[43] Y. Chen, J. Champenois, P. Dangla, S. Granet, J. Lautru, A. Leclerc, G. Melot, Investigation of bituminized waste products swelling behavior due to water uptake under free leaching conditions: Experiments and modeling, Int. J. Numer. Anal. Methods Geomech. (2023). https://doi.org/10.1002/nag.3624.

[44] M. Anoua, A. Ramirez-Martinez, F. Cherblanc, J.C. Bénet, The Use of Chemical Potential to Describe Water Transfer in Complex Media with Strong Solid–Liquid Bonding, Transp. Porous Media. 102 (2014) 111–122. https://doi.org/10.1007/s11242-013-0265-4.

[45] O. Coussy, Poromechanics, John Wiley & Sons, 2004.

[46] S.R. De Groot, P. Mazur, Non-equilibrium thermodynamics, Courier Corporation, 2013.

[47] K.S. Pitzer, G. Mayorga, Thermodynamics of electrolytes. II. Activity and osmotic coefficients for strong electrolytes with one or both ions univalent, J. Phys. Chem. 77 (1973). https://doi.org/10.1021/j100638a009.

[48] T. Mori, K. Tanaka, Average stress in matrix and average elastic energy of materials with misfitting inclusions, Acta Metall. 21 (1973). https://doi.org/10.1016/0001-6160(73)90064-3.

[49] R. Edgeworth, B.J. Dalton, T. Parnell, The pitch drop experiment, Eur. J. Phys. 5 (1984) 198–200. https://doi.org/10.1088/0143-0807/5/4/003.

[50] K.E. Brodersen, G. Brunel, R. Gens, F. Lambert, J.C. Nominé, A. Sneyers, P. Van Iseghem, Characteristics of bituminised radioactive waste, 1998.

[51] K.E. Brodersen, Hygroscopic materials in bituminized waste: experiments and modelling, in: Int. Work. Saf. Perform. Eval. Bituminization Process. Radioact. Waste, Nuclear Research Institute Rez plc, 1999: pp. 149–152.

[52] T. Nguhen, E. Byrd, D. Bentz, Measuring transport of liquid water through organic coatings adhered to a substrate, American Chemical Society, Washington, DC (United States), 1993.

[53] P.R. Herrington, J.P. Wu, L.C. van den Kerkhof, S.A. Bagshaw, Water diffusion in bitumen films, Constr. Build. Mater. 294 (2021) 123530. https://doi.org/https://doi.org/10.1016/j.conbuildmat.2021.123530.

[54] P. Atkins, P.W. Atkins, J. de Paula, Atkins' physical chemistry, Oxford university press, 2014.

[55] K.S. Pitzer, Activity Coefficients in Electrolyte Solutions, CRC Press, 2018. https://doi.org/10.1201/9781351069472.

[56] J.F. Zemaitis Jr, D.M. Clark, M. Rafal, N.C. Scrivner, Handbook of aqueous electrolyte thermodynamics: theory & application, John Wiley & Sons, 2010.